

# Modelling Solar Coronal Magnetic Field Evolution

Erin Elizabeth Goldstraw



University of  
St Andrews | FOUNDED  
1413 |

This thesis is submitted in partial fulfilment for the degree of  
Doctor of Philosophy (PhD)  
at the University of St Andrews

March 2019



## Abstract

---

Footpoint motions at the photosphere can inject energy into the magnetic field in the solar corona. This energy is then released in the corona as heat. There are many mathematical approaches to model the evolution of these magnetic fields. Magnetohydrodynamics (MHD) provides the most convenient and practical approach. However, there are many alternative approximate methods. It is difficult to know when an approximate method is valid and how well the assumptions need to be satisfied for the solutions to be accurate enough. To illustrate this, a simple experiment is performed. Four approximate methods, including Reduced MHD (RMHD), are used to model the evolution of a footpoint driven coronal loop through sequences of equilibria. The predicted evolution from each method is compared to the solution from full MHD simulations to test the accuracy of each method when the relevant assumptions are adjusted. After this initial test, the validity of RMHD is investigated for the particular case of the magnetic field evolution involving the development of the tearing instability. Full MHD simulations are used to argue the applicability of the assumptions and conditions of RMHD for this evolution. The potential of this setup to heat the corona is considered by performing full MHD simulations including thermodynamic processes of optically thin radiation and thermal conduction. These additional processes are not included in RMHD.





## **Candidate's declaration**

I, Erin Elizabeth Goldstraw, do hereby certify that this thesis, submitted for the degree of PhD, which is approximately 60,000 words in length, has been written by me, and that it is the record of work carried out by me, or principally by myself in collaboration with others as acknowledged, and that it has not been submitted in any previous application for any degree.

I was admitted as a research student at the University of St Andrews in September 2015.

I received funding from an organisation or institution and have acknowledged the funders in the full text of my thesis.

Date: ..... Signature of candidate: .....

## **Supervisor's declaration**

I hereby certify that the candidate has fulfilled the conditions of the Resolution and Regulations appropriate for the degree of PhD in the University of St Andrews and that the candidate is qualified to submit this thesis in application for that degree.

Date: ..... Signature of supervisor: .....



## Permission for publication

In submitting this thesis to the University of St Andrews we understand that we are giving permission for it to be made available for use in accordance with the regulations of the University Library for the time being in force, subject to any copyright vested in the work not being affected thereby. We also understand, unless exempt by an award of an embargo as requested below, that the title and the abstract will be published, and that a copy of the work may be made and supplied to any bona fide library or research worker, that this thesis will be electronically accessible for personal or research use and that the library has the right to migrate this thesis into new electronic forms as required to ensure continued access to the thesis.

I, Erin Elizabeth Goldstraw, confirm that my thesis does not contain any third-party material that requires copyright clearance.

The following is an agreed request by candidate and supervisor regarding the publication of this thesis:

### **Printed copy**

Embargo on all of print copy for a period of 1 year on the following ground(s):

- Publication would be commercially damaging to the researcher, or to the supervisor, or the University.

### **Supporting statement for printed embargo request**

Part of this thesis contains unpublished material, which could be used by fellow researchers before publication, which would be damaging for the researcher, supervisor and University.

### **Electronic copy**

Embargo on all of electronic copy for a period of 1 year on the following ground(s):

- Publication would be commercially damaging to the researcher, or to the supervisor, or the University.

### **Supporting statement for electronic embargo request**

Part of this thesis contains unpublished material, which could be used by fellow researchers before publication, which would be damaging for the researcher, supervisor and University.

### **Title and Abstract**

- I agree to the title and abstract being published.

Date: ..... Signature of candidate: .....

Date: ..... Signature of supervisor: .....



## Underpinning Research Data or Digital Outputs

### Candidate's declaration

I, Erin Elizabeth Goldstraw, understand that by declaring that I have original research data or digital outputs, I should make every effort in meeting the University's and research funders' requirements on the deposit and sharing of research data or research digital outputs.

Date: ..... Signature of candidate: .....

### Permission for publication of underpinning research data or digital outputs

We understand that for any original research data or digital outputs which are deposited, we are giving permission for them to be made available for use in accordance with the requirements of the University and research funders, for the time being in force.

We also understand that the title and the description will be published, and that the underpinning research data or digital outputs will be electronically accessible for use in accordance with the license specified at the point of deposit, unless exempt by award of an embargo as requested below.

The following is an agreed request by candidate and supervisor regarding the publication of underpinning research data or digital outputs:

No embargo on underpinning research data or digital outputs.

Date: ..... Signature of candidate: .....

Date: ..... Signature of supervisor: .....

## Financial Support

The research leading to the results presented within this thesis has received PhD funding from the UK Science and Technology Facilities Council (STFC) studentship, ST/I505999/1.

This work used the DIRAC 1, UKMHD Consortium machine at the University of St Andrews.

This work used the DiRAC@Durham facility managed by the Institute for Computational Cosmology on behalf of the STFC DiRAC HPC Facility ([www.dirac.ac.uk](http://www.dirac.ac.uk)). The equipment was funded by BEIS capital funding via STFC capital grants ST/P002293/1, ST/R002371/1 and ST/S002502/1, Durham University and STFC operations grant ST/R000832/1. DiRAC is part of the National e-Infrastructure.



## **Publications**

This thesis contains work which has been adapted from the following publications:

1. E. E. Goldstraw, A. W. Hood and P. K. Browning and P. J. Cargill. Comparison of methods for modelling coronal magnetic fields *A& A* 610:A48, February 2018. doi:10.1051/0004-6361/201731069,

## **Collaboration Statement**

The numerical simulations presented in this thesis were carried out by myself under the supervision of Prof. Alan Hood. I thank Klaus Galsgaard for useful discussions. I thank Sean Oughton for many useful and interesting discussions and feedback.





## Acknowledgements

When I received my offer of a PhD in the solar group in St Andrews, I was most of the way through my MSc in Edinburgh. This wonderful opportunity gave me something to look forward to and work towards as I prepared for a marathon of nine exams in one exam diet and a dissertation in MHD turbulence during the summer.

I would like to thank the solar group and the school for the last 3.5 years.

I would like to thank my supervisor, Alan, for his help, explanations and guidance during the course of my PhD.

I thank Zoe, Craig, Tom, James, Jack and Daniel for their help during these years.

I would like to thank Antonia for the support, occasional meetings for lunch and being someone I could always speak to even though I know you are very busy. Thank you.

I thank Sheila Kinnison, who has generously ensured I have some money for books.

I acknowledge our late family friend, Peter C. Macdougall, who was always interested in my studies and achievements.

Although I have not had the chance to get to know anyone very well in St Andrews, I would like to thank the town for being such a welcoming and friendly place. This is the first area I have felt comfortable enough to explore on my own, and have recently started swimming at East Sands leisure centre. I also regularly visit The Crystal Shop. It has been a tranquil and peaceful place to visit for a break from my studies.

I want to say a special big thank you to Sasha (Саша). Our Russian-English conversations have been a very welcome, interesting, fun and stimulating activity during the second half of my PhD. Большое спасибо! Давай общаться дальше.

I thank my mum for transport to and from the Mathematical Institute every day. I wish I could find an easier way for you.

I thank my parents for encouraging me to enjoy learning from the beginning.

A special acknowledgement and thank you to my late grandad, who passed away in 2000, and gran, who passed away recently in November 2018. I know you are very proud of your granddaughter.



For my parents.  
In loving memory of my gran and grandad.



Поехали! - Ю.А. Гагарин  
Let's go! - Y.A. Gagarin  
1961



# Contents

<b>1</b>	<b>Introduction</b>	<b>1</b>
1.1	Coronal Loops and Heating	2
1.2	Brief Description of Magnetic Confinement	3
1.3	Outline	5
<b>2</b>	<b>MHD Model</b>	<b>7</b>
2.1	Overview	7
2.2	Maxwell's Equations	8
2.3	MHD Assumptions	10
2.4	MHD Equations	10
2.5	MHD: Conservation laws	14
2.6	MHD Equilibria: Grad-Shafranov Equation	15
2.7	MHD: Waves and Polarisation	17
2.8	Tearing Instability Analysis	21
2.9	Summary	25
<b>3</b>	<b>RMHD Model</b>	<b>27</b>
3.1	Overview of RMHD	27
3.2	Brief History of RMHD in Fusion Devices	29
3.3	Original RMHD Derivations	30
3.3.1	Strauss' Derivation	30
3.3.2	Zank and Matthaeus' RMHD Equations	34
3.3.3	Montgomery's RMHD Equations	35
3.3.4	Discussion	36
3.4	RMHD Model	37
3.4.1	RMHD: Derivation	38
3.4.2	RMHD: Conservation Laws	42
3.4.3	RMHD: Properties	42
3.4.4	Validity	46
3.5	Validity Checks of RMHD	48
3.6	Coronal Loop Studies	50
3.6.1	MHD Studies	51
3.6.2	RMHD Studies	53
3.7	Similar Methods	57

3.8	Other Formulations of “Reduced” Models in MHD	57
3.9	Summary	60
<b>4</b>	<b>Shearing: Comparison of Methods</b>	<b>61</b>
4.1	Introduction	61
4.2	Experiment and Model Descriptions	62
4.2.1	MHD Equations	62
4.2.2	Experiment Description	64
4.2.3	Magnetofrictional Relaxation	66
4.2.4	One-Dimensional Equilibrium Equation	68
4.2.5	Linear and Weakly Nonlinear Expansion	70
4.2.6	Reduced MHD	77
4.3	Results	78
4.3.1	Comparison With Full MHD Results	80
4.3.2	Full MHD Dynamics	87
4.3.3	Full MHD Dynamics: Field Expansion	101
4.4	Summary	105
<b>5</b>	<b>Tearing Instability: Validity of RMHD</b>	<b>107</b>
5.1	Introduction	107
5.2	Experiment Overview	109
5.2.1	MHD Equations	109
5.2.2	Experiment Description	110
5.3	Results	112
5.3.1	Overview of Full MHD Simulations	113
5.3.2	Validity Tests of the RMHD Conditions	119
5.3.3	Qualitative Comparisons	122
5.3.4	MHD Dynamics	124
5.4	Summary	142
<b>6</b>	<b>Tearing Experiment: Thermodynamics</b>	<b>144</b>
6.1	Introduction	144
6.2	Experiment Overview	145
6.2.1	MHD Equations	146
6.2.2	Normalisation and Initial Conditions	146
6.2.3	Experiment Setup	147
6.3	Results	147
6.4	Discussion	165
<b>7</b>	<b>Summary and Further Work</b>	<b>171</b>
	<b>Appendices</b>	<b>174</b>
	<b>Appendix A Alternative RMHD Derivations</b>	<b>175</b>
	A.1 Zank and Matthaeus’ Derivation	175



A.2	Montgomery's Derivation	181
A.3	Van Ballegooijen's Equilibrium Derivation of RMHD	184
<b>Appendix B Similar Methods</b>		<b>187</b>
B.1	Kruger et al: Generalised RMHD	187
B.2	Gazol et al: RMHD including Alfvén dynamics	189
B.3	Zhukov: RMHD including slow waves	191
B.4	Zank and Matthaeus: Nearly Incompressible MHD	192
B.5	Bhattacharjee et al: Four Field MHD	194
B.6	Van Ballegooijen et al: RMHD for Alfvén wave turbulence	197
<b>Appendix C Second order Solution</b>		<b>200</b>
<b>Bibliography</b>		<b>215</b>

# Chapter 1

## Introduction

Plasma is made up of ions and electrons, which can move freely in space and are not confined together in an atom. The process of ionisation, where the electrons and protons in an atom are separated, requires a very high temperature. The plasma state is somewhat rare on Earth, but nevertheless, it is common throughout the universe and accounts for >90% of matter. The individual charged particles are acted on by electromagnetic forces, either external forces or internal forces produced by other particles in the plasma. In most cases the dynamics of a plasma can be suitably modelled as a fluid. This can be done when considering scales where forces from individual particles are negligible compared to the net force produced by all particles and external forces.

The mathematical framework that describes the fluid-like dynamics of a plasma is provided by the model of magnetohydrodynamics (MHD) (Priest 2014). This model makes a few key assumptions relating to charge neutrality and lengthscales. Despite these assumptions MHD is applicable in a vast range of plasmas from nuclear fusion to the solar corona. The MHD model involves solving a set of coupled, complex, nonlinear partial differential equations for eight unknown quantities. Analytical solutions to these equations are few and far between, usually only possible in very specific simple cases. In the majority of cases, a numerical solution is needed. However, numerical approaches require a significant amount of computational resources.

Due to the high demand on these resources, it is common to look for possible ways to reduce the complexity in the equations and make them computationally easier to solve. One way to simplify the equations is by applying additional assumptions. These could be related to the existence of a strong external magnetic field, invariance in a coordinate direction and/or vector field direction or compressibility. The important thing to consider when implementing such assumptions is whether they are valid for the current system under investigation. This is particularly crucial when applying a model designed for one application to another topic.

In this project we aim to illustrate the importance of this concept. To do this we consider the method of reduced MHD (RMHD), which was originally proposed for magnetic confinement plasmas and has been subsequently applied to plasma in coronal structures, called coronal loops. These two types of plasma and areas of research are very different as

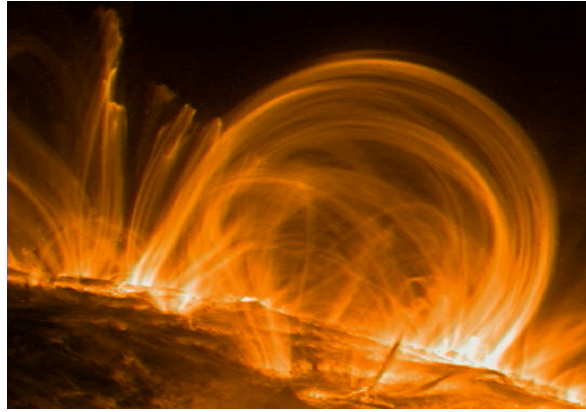


Figure 1.1: Image of coronal loops taken from <https://scied.ucar.edu/sun-coronal-loops> from TRACE/NASA.

will be briefly demonstrated in this chapter. In Section 1.1 the solar corona (Priest 1984) is introduced and a brief overview of magnetic confinement (Boyd and Sanderson 2003) is given in Section 1.2. Finally, in Section 1.3 an outline of this thesis is given.

## 1.1 Coronal Loops and Heating

The visible part of the sun, which consists of dense optically thick plasma, is known as the photosphere or surface of the sun. The photosphere is observed to have a temperature of  $\sim 6000\text{K}$ . This plasma is turbulent due to convective motions. These motions are typically of  $1\text{--}2\text{ km s}^{-1}$ . The upper atmosphere of the sun, which is the halo visible during an eclipse, is called the corona. The typical number density of particles in the corona is  $10^{14}\text{ m}^{-3}$  and typical magnetic field strength is  $100\text{G}$  ( $10^{-2}\text{T}$ ).

From the photosphere, strong magnetic fields emerge, extending into the corona before returning to the surface. These magnetic structures are visible in a broad spectrum of wavelengths due to the emission of the hot plasma that is confined on them and are called coronal loops and have a broad range of lengths of  $\sim 10 - 100\text{Mm}$ . An image of coronal loops taken in ultraviolet is shown in Figure 1.1.

Contrary to intuition, the temperature increases from the photosphere to the corona. The coronal temperature is around  $1 - 2\text{MK}$ . This unexpectedly high temperature requires a heat source. It is generally accepted that the source of heating is the convective motions of the photosphere. This energy can then be transferred to and stored in the coronal magnetic field. However, the mechanism to convert this reservoir of energy into internal energy, to heat the plasma, is still to be determined. The mystery of this process is one of the most challenging questions in solar physics, known as the coronal heating problem.

These motions move the footpoints of coronal loops which are rooted into the higher density photosphere. The resulting evolution of the loops depends on the timescale of the footpoint motions. For motions on a fast timescale, waves are generated and dissipated to heat the plasma. This is known as alternating current (AC) heating. For slower

timescales, the loops are moved as a whole through a series of approximate equilibrium states. These equilibria are non-potential and energy can be stored in the magnetic field until conditions for non-equilibrium or an instability are met, after which the stored energy is released. The release of the stored energy is by a process called reconnection where the magnetic field breaks and reconnects into a new lower energy state. This process is known as direct current (DC). Here we focus on DC heating.

The solar corona is full of loops with varying temperatures. These loops are likely to interact with each other. Thermodynamic processes, also, play an important part in the evolution of coronal loops and is essential for investigation of coronal heating.

Next, properties necessary for fusion are briefly discussed.

## 1.2 Brief Description of Magnetic Confinement

Fusion is a possible source of energy on Earth since a lot of energy can be released as a result of the nuclear reactions. A very high temperature of the order of  $10^8\text{K}$  with a number density of  $\sim 10^{20}$  particles  $\text{m}^{-3}$  is required for fusion to occur. Naturally, no physical material can contain a substance at such a high temperature. Fortunately, magnetic fields can be used to contain the plasma, which is possible due to the nature of charged particles, which are confined by electromagnetic forces to follow magnetic field lines. This process is called magnetic confinement.

The common magnetic field configuration contains the plasma in a ring with a circular cross section, or doughnut shape, called a torus. Such a toroidal shape can be achieved with a helical magnetic field threading the torus. This magnetic configuration requires a magnetic field in two directions. One is provided externally and the second is produced by the plasma itself. The former is obtained by using external magnetic coils to produce a strong field of about 10T along the axis of the plasma column called the toroidal direction. The second is produced by the resulting current induced in the plasma, which creates a smaller magnetic field acting in a circle perpendicular to the axis of the cylinder, known as the poloidal direction.

Fusion plasmas can only be maintained for a very short time of one or two minutes. The radius of the plasma, called the minor radius, is generally much less than a metre and the major radius from the centre of the plasma column to the centre of the torus is about a metre.

There are many pieces of equipment that are necessary for the successful and safe operation of a magnetically confined plasma. The entire system including the plasma and equipment is called a tokamak. This is an abbreviation of the Russian phrase meaning a: “toroidal chamber with magnetic coils” (Russian: **тороидальная камера с магнитными катушками**).

The main goal in magnetic confinement is to maintain the stability of the plasma for as long as possible to allow hydrogen ions to collide and fuse to form helium. This requires a high level of understanding of magnetic equilibria and nonlinear dynamics such as instabilities.

The necessary existence of an externally generated toroidal magnetic field,  $B_0$ ,

Table 1.1: Summary of typical coronal and tokamak plasma quantities: magnetic field  $B$ , temperature,  $T$ , length,  $L$  and number density,  $n$ . The Alfvén speed,  $V_A = \frac{B}{\sqrt{\mu_0 n m_p}}$ , and Alfvén time,  $\tau_A = \frac{L}{V_A}$ , are calculated, where  $m_p$  is the mass of a proton. The lengthscale of a tokamak is taken to be the major radius of JET.

System	$B$ (T)	$T$ (MK)	$L$ (m)	$n$ ( $\text{m}^{-3}$ )	$V_A$ ( $\text{m s}^{-1}$ )	$\tau_A$ (s)
Corona	$1 \times 10^{-2}$	1-2	$100 \times 10^6$	$10^{14}$	$7 \times 10^5$	145
Tokamak	10	100	3	$10^{20}$	$2 \times 10^7$	$3 \times 10^{-7}$

motivates the assumption of a dominant guide field in the full MHD equations. It follows that other quantities are smaller than and perpendicular to this field component. Further simplification results from variations being mainly perpendicular to the magnetic field direction. These assumptions lead to the equations of RMHD (Kadomtsev and Pogutse 1974; Strauss 1976). RMHD is a nonlinear, incompressible approximation of full 3D compressible MHD. The velocity and magnetic fields involve two components which are perpendicular to  $\mathbf{B}_0$  and depend fully on two coordinates and weakly on the third. Thus RMHD is neither fully 3D or 2D. A special feature of RMHD is that if the weak dependence on the third coordinate is dropped the equations simplify to those of 2D incompressible MHD.

There are two main reasons why the model of RMHD has become popular for investigations into magnetic confinement compared to full MHD and other approximate methods. First, the RMHD equations are much simpler than the full MHD equations, resulting in less demand on limited computational resources. Second, the equations still retain some nonlinear dynamics which linear methods do not.

We do not consider validity of RMHD in the context of fusion. This brief description of magnetic confinement is included for background context and motivation of this study. This approximate model has recently been applied in the context of solar physics. This is a very different type of plasma as was discussed in the previous section, Section 1.1.

In summary, fusion and coronal plasmas are fundamentally very different. These systems require very different timescales, lengthscales, temperatures and number densities, as summarised in Table 1.1. Fusion requires a number density  $10^6$  greater, a temperature 100 times hotter and a magnetic field 1000 times stronger than in the corona. Another intrinsic difference between these systems is that in the corona there are many coronal loops which can interact with each other whereas a fusion plasma is an isolated system. It may be arguable that the guide field threading a coronal loop dominates other quantities when a loop is in equilibrium. However, this seems unlikely during highly dynamic processes such as instabilities and reconnection. This argument also follows for quantities and variations being mainly restricted to perpendicular directions. It seems unlikely that the same assumptions which are generally applicable in tokamaks are also valid in the corona. This maybe is the case for a small subset of situations or special cases but seems unlikely in general. This raises the question of validity.

## 1.3 Outline

Validity is a very important question to ask when considering which method to use. If the assumptions are not valid at some point, the results are likely to be inaccurate, and may lead to false conclusions. These incorrect conclusions will only slow down the progress of new research as they need to be checked and corrected, as necessary.

The best procedure to verify the accuracy of an approximate solution is to compare it with results which are known to be accurate. For our purposes we take full compressible MHD to provide such accurate results. The assumptions of full MHD are also present in approximate models. There are countless systems to test the accuracy of a given approximate method. Each needs to be analysed on an individual basis. In this project we investigate one particular system with a focus on validity of RMHD.

We begin with a general illustration of validity. To do this, we choose four common approximate methods: linearisation, magnetofrictional relaxation, 1D approach and RMHD. Each is used to model the evolution of a coronal loop undergoing smooth footpoint motions. These results are then compared and contrasted with each other and with results from full 2.5D compressible MHD simulations. Full details and results are presented in Chapter 4 and were published in Goldstraw et al. 2018.

After this straightforward initial experiment, we focus our attention on checking validity of RMHD. This investigation was motivated by potential disagreement between studies in the literature using RMHD and full MHD and the lack of studies directly comparing these two models.

An example of this conflict is Rappazzo, Velli, and Einaudi (2010), who used RMHD to model the tearing instability in the context of coronal heating. Rappazzo et al (2010) applied footpoint motions, consisting of a smooth shearing and spatially random perturbation, to an initially uniform background field. These motions allow energy to be stored in the magnetic field before the development of the tearing instability and the subsequent release of the stored energy through reconnection. Their key result is that the energy storage and release only occurs once. Magnetic energy is not stored again, even though the motions are continued throughout the simulation. This is in contrast to the common picture in MHD, that this process would be cyclic: energy build up and release followed by subsequent energy build up and release.

It may be the case that, in general, both ideas are true since the dynamics depend crucially on the properties of footpoint motions. Nevertheless, the major area of doubt over Rappazzo et al's study is that it uses the approximate method of RMHD. This raises the question of whether their conclusion would still hold true if the same system was modelled using full MHD, which has not been tested. It is one of the aims of this study to check their conclusion using full 3D compressible MHD.

This is done by extending our simple 2.5D system in Chapter 4 to 3D and applying an additional symmetry-breaking perturbation. The application of a shear and perturbation results in the development of the tearing instability. Arguments concerning the validity of RMHD are made using our full 3D compressible MHD simulation results and qualitative comparisons to Rappazzo, Velli, and Einaudi (2010) are discussed in Chapter 5.

Despite the fact that RMHD has been used in the context of coronal heating, it cannot predict the thermodynamics of the system since there is no energy equation. Without the inclusion of radiation and conduction, little conclusion can be made about the coronal heating potential of this system. Such processes need to be investigated using full MHD. In Chapter 6 our system is extended to include the effects of radiation and conduction to enable new results which are not possible when restricted to using RMHD.

There are many further systems to test the validity of RMHD and several potentially useful conclusions to verify in the literature. There are also numerous similar models to RMHD that have been developed over the last few decades and could be investigated further. A summary of results and future work is given in Chapter 7.

The following chapters, Chapter 2 and Chapter 3, introduce the mathematical models of MHD and RMHD and the relevant properties and literature for this study.

## Chapter 2

# MHD Model

### 2.1 Overview

When studying the dynamics of a plasma, there are two main approaches: microscopic, where each particle is considered individually, and macroscopic, where the plasma is treated as a magnetised fluid, i.e MHD. The main focus will be on the macroscopic dynamics and evolution of the plasma in time. In the following sections, the mathematical model of MHD describing the fluid-like dynamics of plasma will be introduced.

A general fluid is described by the hydrodynamic fluid equations. A hydrodynamic fluid consists of neutral atoms which can undergo physical collisions described by classical physics. A plasma is distinct from a neutral hydrodynamic fluid due to the presence of charged ions. The electromagnetic forces produced by an individual particle can act on many others at a large distance, resulting in altering their trajectory and speed. Due to the importance of these electromagnetic forces the interactions of the particles' electric and magnetic fields must be included in the fluid equations. This is done by combining the equations describing electromagnetism, given by Maxwell's equations, and the equations of fluid mechanics. This results in a mathematical model describing an electrically conducting fluid.

In Section 2.2, Maxwell's equations of electromagnetism are described. In order to use the fluid approximation, a few assumptions are used to simplify Maxwell's equations, which determine when MHD is valid. These necessary assumptions are listed in Section 2.3 and when applied give the MHD equations in Section 2.4. It is important for a mathematical model to be physically meaningful and correctly capture all of the relevant physics. Full MHD conserves mass, momentum, magnetic flux and total energy. These conservation laws are presented in Section 2.5. An interesting and important topic is the class of equilibrium states, in which a system does not change in time unless perturbed. The Grad-Shafranov equation, which describes MHD equilibrium states with translational symmetry, is derived in Section 2.6. When an equilibrium is disturbed by a small perturbation, it evolves dynamically and is no longer stationary. An important feature of a medium is the propagation of these small perturbations, or waves, through the fluid. In a plasma, there are several types of waves, each with their own properties, which will be discussed in Section 2.7. On the other



hand, if an initial equilibrium is unstable, when a small perturbation is present, it can destroy the original equilibrium state through the development of an instability. In this work, we will model the evolution of the tearing instability. The linear analysis of the tearing mode is presented in Section 2.8. In Section 2.9, a common additional assumption is introduced.

## 2.2 Maxwell's Equations

In this section, we introduce the ideas of electromagnetism described by Maxwell's equations. Plasma consists of free electrons and protons. These charged particles produce an electric field,  $\mathbf{E}$ , measured in Newtons per Coulomb ( $\text{N C}^{-1}$ ) or volts per metre ( $\text{V m}^{-1}$ ). A flow of electrons is an electric current, which produces a magnetic field,  $\mathbf{H}$ , and magnetic induction,  $\mathbf{B}$ , in units of tesla, T.  $\mathbf{B}$  is commonly called the magnetic field, instead of  $\mathbf{H}$ . As the particles move, they interact with the magnetic and electric fields of other particles. The properties of electric and magnetic fields are described mathematically by Maxwell's four equations of electromagnetism, namely Gauss' laws for the electric and magnetic fields, Faraday's law of induction and Ampère's law.

### Gauss' Law for the Electric Field

The net electric flux through a closed surface,  $S$ , with unit normal,  $\hat{\mathbf{n}}$ , is proportional to the net amount of electric charge contained within the surface. This idea is described mathematically by Gauss' law, which in integral form is

$$\oint_S \mathbf{E} \cdot \hat{\mathbf{n}} dA = \frac{q}{\epsilon_0},$$

where  $q$  is the total charge in coulombs, C, inside the closed surface,  $S$ , and the constant  $\epsilon_0 = 8.85 \times 10^{-12} \text{C}(\text{V m})^{-1}$ , is known as the vacuum permittivity. Physically this equation means that protons with a positive charge are sources of an electric field and electrons with a negative charge are sinks of the field.

Gauss' law can be written in differential form as

$$\nabla \cdot \mathbf{E} = \frac{\rho_q}{\epsilon_0}, \quad (2.1)$$

where  $\rho_q$  is the charge density measured in  $\text{C m}^{-3}$ .  $q$  and  $\rho_q$  are related by

$$q = \int \rho_q dV,$$

where the volume  $V$  contains the surface,  $S$ . Similarly to the integral form, this shows that the electric field diverges away from a positive charge and converges towards a negative charge.

**Gauss' Law for the Magnetic Field**

There are no sources or sinks for a magnetic field. This means a magnetic field does not diverge from or converge to a single point in space. Gauss' law can be written for the magnetic field as

$$\nabla \cdot \mathbf{B} = 0. \quad (2.2)$$

**Faraday's Law of Induction**

If the magnetic flux contained in an open surface,  $S$ , bounded by a closed curve,  $C$ , changes in time then an electric field is induced along a closed path,  $C$ . Faraday's law describes this phenomenon mathematically, which can be written in integral form as

$$\oint_C \mathbf{E} \cdot d\mathbf{l} = -\frac{\partial}{\partial t} \int_S \mathbf{B} \cdot \hat{\mathbf{n}} dA. \quad (2.3)$$

Faraday's law describes the phenomenon that a changing magnetic field induces an electric field that acts against the change in  $\mathbf{B}$ . An induced electric field is fundamentally different from the intrinsic field of a charged particle. An induced electric field does not have sources or sinks, its fieldlines form closed loops. Faraday's law can be written in differential form as

$$\frac{\partial \mathbf{B}}{\partial t} = -\nabla \times \mathbf{E}. \quad (2.4)$$

Physically this means that the rate of change in time of the magnetic flux is equal and opposite to the induced rotation of the electric field.

**Ampère's Law**

There are two types of current: a physical current produced by the flow of electrons and a displacement current produced by a changing electric flux. A physical current density is given by the flow of charged particles with number density,  $n$  ( $\text{m}^{-3}$ ), charge,  $q$  (C), and average velocity,  $\mathbf{v}$  ( $\text{m s}^{-1}$ ) as

$$\mathbf{j} = nq\mathbf{v}, \quad (2.5)$$

with units of  $\text{C}(\text{m}^2 \text{s})^{-1} = \text{A m}^{-2}$ . Note that the current density has units of current per unit area. The displacement current, also in units of current density, is produced by a variation in time of the electric flux through  $S$ . This is analagous to Faraday's law and is described mathematically by Ampère's law, which can be written as

$$\nabla \times \mathbf{B} = \mu \left( \mathbf{j} + \epsilon_0 \frac{\partial \mathbf{E}}{\partial t} \right), \quad (2.6)$$

where the constant  $\mu_0 = 4\pi \times 10^{-7} \text{N A}^{-2}$  is the permeability of free space.

## 2.3 MHD Assumptions

In this section we will emphasise the assumptions of full MHD. These assumptions are present throughout all models considered in this study. Full MHD as the limit of a magnetised fluid is itself an approximation to the microscopic dynamics of individual particles. In the fluid limit only the average properties of many particles are considered rather than the dynamics of each individual one. Over large distances and times, such as are present in astrophysical and coronal systems, these assumptions provide an excellent description of the evolution and so the fluid equations of full MHD are taken to provide the “exact” and most accurate solutions throughout this work.

The assumptions of full MHD are:

1. The fluid approximation assumes the fluid is a continuum of particles compared to discrete particles. This is valid providing lengthscales are much greater than the mean free path - the average distance that collisions occur between particles.
2. Charge neutrality is assumed. This assumes that there are equal numbers of positive and negative charged particles evenly distributed throughout the plasma, resulting in no net charge locally anywhere. The individual particle properties, such as charge and mass, are neglected and assumed to be one species. This is possible since the mass of a proton is much greater than the mass of an electron  $m_p \gg m_e$ .
3. The viscous stress tensor is assumed isotropic. Although anisotropy is an important aspect in the current study, approximate methods considered in this study use an even simpler form of viscous dissipation. The main function of the viscosity is to dissipate waves and kinetic energy. Thus, this approximate form of viscosity is sufficient for the current investigation.
4. Nonrelativistic: Typical speeds are assumed to be much less than the speed of light,  $v \lll c$ .
5. Neglect displacement current. Removes electromagnetic waves at speed of light.

## 2.4 MHD Equations

A plasma is described by its density,  $\rho$ , in units of  $\text{kg m}^{-3}$ , pressure,  $p$ , in units of  $\text{N m}^{-2}$ ,  $\mathbf{v}$ , in units of  $\text{m s}^{-1}$  and magnetic field,  $\mathbf{B}$ , in tesla, T. Additional properties of the electric field and temperature can be calculated once these eight quantities are known. The MHD equations are found by combining the hydrodynamic equations with Maxwell's equations. First, the above assumptions are applied to Maxwell's equations to give fluid approximations of the electromagnetic equations

Assumption two of full MHD requires that the charge density is zero and hence Gauss' law, Equation (2.1), is simply  $\nabla \cdot \mathbf{E} = 0$ . Therefore, the electric field from individual particles are neglected and only the electric field induced by the changing magnetic field is considered.

The typical magnitude of the electric field,  $E$ , can be written in terms of the typical magnitude of the magnetic induction,  $B$ , by considering Faraday's law, Equation (2.4). Taking a typical length,  $\ell$ , and typical time,  $t$ , the electric field strength is

$$E = \frac{\ell B}{t} = vB, \quad (2.7)$$

where  $v$  is a typical speed. Now considering Ampère's law, Equation (2.6), the LHS is simply

$$\nabla \times \mathbf{B} \sim \frac{B}{\ell},$$

and the displacement current, substituting Equation (2.7) and using  $c^2 = (\mu\epsilon)^{-1}$ , can be written as

$$\frac{1}{c^2} \frac{\partial \mathbf{E}}{\partial t} \sim \frac{1}{c^2} \frac{E}{t} = \frac{v^2}{c^2} \frac{B}{\ell}.$$

Since  $c^2 \gg v^2$  the displacement current is small compared to the magnetic field, hence it can be neglected and Ampère's law is written as

$$\mu \mathbf{j} = \nabla \times \mathbf{B}. \quad (2.8)$$

The velocity and magnetic fields are related by Ohm's law, which is

$$\mathbf{j} = \sigma_c (\mathbf{E} + \mathbf{v} \times \mathbf{B}),$$

where  $\sigma_c$  is the conductivity in units of siemens per metre.

### Summary of MHD Equations

The full 3D compressible MHD equations, including gravity, thermal conduction and radiation, can be written as:

$$\text{Equation of Motion} \quad \rho \frac{\partial \mathbf{v}}{\partial t} + \rho (\mathbf{v} \cdot \nabla) \mathbf{v} = -\rho \mathbf{g} - \nabla p + \mathbf{j} \times \mathbf{B} + \nabla \cdot \mathbf{S}, \quad (2.9a)$$

$$\text{Continuity Equation} \quad \frac{\partial \rho}{\partial t} + \nabla \cdot (\rho \mathbf{v}) = 0, \quad (2.9b)$$

$$\text{Induction Equation} \quad \frac{\partial \mathbf{B}}{\partial t} = \nabla \times (\mathbf{v} \times \mathbf{B}) - \nabla \times (\eta \nabla \times \mathbf{B}), \quad (2.9c)$$

$$\text{Energy Equation} \quad \frac{\partial}{\partial t} \left( \frac{p}{\gamma - 1} \right) + \mathbf{v} \cdot \nabla \left( \frac{p}{\gamma - 1} \right) = -\frac{\gamma p}{\gamma - 1} \nabla \cdot \mathbf{v} - \mathcal{L}, \quad (2.9d)$$

$$\mathcal{L} = \mathcal{L}_{\text{conduction}} + \mathcal{L}_{\text{radiation}} - \eta j^2 - \epsilon_{ij} S_{ij},$$

Table 2.1: Values of  $\alpha$  and  $\chi$  for different temperature ranges used in the equation for optically thin radiation, Equation (2.11) taken from Klimchuk, Patsourakos, and Cargill (2008).

$\chi(10^{-13})$	$\alpha$	Temperature range (MK)
$1.09 \times 10^{-31}$	2	$10^4 \leq T \leq 10^{4.97}$
$8.87 \times 10^{-17}$	-1	$10^{4.97} < T \leq 10^{5.67}$
$1.90 \times 10^{-22}$	0	$10^{5.67} < T \leq 10^{6.18}$
$3.53 \times 10^{-13}$	$-\frac{3}{2}$	$10^{6.18} < T \leq 10^{6.55}$
$3.46 \times 10^{-25}$	$-\frac{1}{3}$	$10^{6.55} < T \leq 10^{6.90}$
$5.49 \times 10^{-16}$	-1	$10^{6.90} < T \leq 10^{7.63}$
$1.96 \times 10^{-27}$	$\frac{1}{2}$	$10^{7.63} \leq T$

where  $\mathcal{L}_{\text{conduction}} = \nabla \cdot \mathbf{q}$  is the effect of thermal conduction and  $\mathbf{q}$  is the associated heat flux, given by

$$\mathbf{q} = -\frac{\kappa}{B^2} (\mathbf{B} \cdot \nabla T) \mathbf{B}. \quad (2.10)$$

where  $\kappa = \kappa_0 T^{\frac{5}{2}}$  and  $\kappa_0 = 10^{-11} \text{W(mK)}^{-1}$  is a typical value for the parallel thermal conductivity in the corona. In reality there is also thermal conduction perpendicular to the magnetic field but it is much smaller than the conduction along the field and so is neglected.

$\mathcal{L}_{\text{radiation}}$  is the losses due to optically thin radiation in the solar corona. Optically thin radiation is given by

$$\mathcal{L}_{\text{radiation}} = \rho^2 \chi T^\alpha. \quad (2.11)$$

The constants,  $\chi$  and  $\alpha$ , depend on temperature, given in Klimchuk, Patsourakos, and Cargill 2008, as listed in Table 2.1. These values and formula are chosen to fit observations of solar emission. The current and solenoidal condition are given by

$$\mathbf{j} = \frac{\nabla \times \mathbf{B}}{\mu}, \text{ and } \nabla \cdot \mathbf{B} = 0. \quad (2.12)$$

In these equations  $\mathbf{v}$  is the plasma velocity,  $\rho$  the mass density,  $p$  the gas pressure,  $\mathbf{B}$  the magnetic induction and  $\mathbf{j}$  the current density.  $\eta$  is the magnetic diffusivity, equal to  $\frac{1}{\sigma\mu}$  with units of  $\text{m}^2 \text{s}^{-1}$

The equation of motion includes contributions from gravity,  $\mathbf{g}$ , mechanical pressure forces,  $\nabla p$ , Lorentz force,  $\mathbf{j} \times \mathbf{B}$ , and divergence of viscous stresses,  $\nabla \cdot \mathbf{S}$ . The energy equation includes effects of thermal conduction, optically thin radiation, ohmic and viscous dissipation. The viscous stress tensor is given by

$$S_{ij} = 2\rho\nu \left( \epsilon_{ij} - \frac{1}{3} \delta_{ij} \nabla \cdot \mathbf{v} \right), \quad (2.13)$$

where  $\nu$  is the kinematic viscosity with units  $\text{m}^2 \text{s}^{-1}$  and the strain rate is

$$\epsilon_{ij} = \frac{1}{2} \left( \frac{\partial v_i}{\partial x_j} + \frac{\partial v_j}{\partial x_i} \right). \quad (2.14)$$

This is the hydrodynamic viscous stress tensor as any effects of the magnetic field are neglected. Both shock and “real” viscosity are used in the computational code, Lare, that is used in this study. Shocks are perturbations that travel faster than the local wave speed. This causes sharp changes in pressure. A large value of viscosity is needed to quickly dissipate these. Real viscosity damps any other perturbations. Once the pressure is known, the temperature of the plasma can be calculated from the ideal gas law in a fully ionised plasma as

$$T = \frac{p}{\tilde{\mu} R \rho},$$

where  $R = 8.3 \times 10^3 \text{ J(K kg)}^{-1}$  is the gas constant and  $\tilde{\mu}$  is the molar mass in units of  $\text{kg mol}^{-1}$ . An important quantity in plasma physics is the plasma beta, given by the ratio of the gas pressure and magnetic pressure as

$$\beta = \frac{2\mu p}{B^2}. \quad (2.15)$$

There are many different limits which can be applied to these MHD equations, some of the resulting sets of equations are stated below.

#### Dissipative MHD Equations

In this study, the dissipative compressible MHD equations will be frequently used. In this case, thermal conduction and radiation are neglected. Gravity is neglected for simplicity.

$$\rho \frac{\partial \mathbf{v}}{\partial t} + \rho(\mathbf{v} \cdot \nabla) \mathbf{v} = -\nabla p + \mathbf{j} \times \mathbf{B} + \nabla \cdot \mathbf{S}, \quad (2.16a)$$

$$\frac{\partial \rho}{\partial t} + \nabla \cdot (\rho \mathbf{v}) = 0, \quad (2.16b)$$

$$\frac{\partial \mathbf{B}}{\partial t} = \nabla \times (\mathbf{v} \times \mathbf{B}) - \nabla \times (\eta \nabla \times \mathbf{B}), \quad (2.16c)$$

$$\frac{\partial}{\partial t} \left( \frac{p}{\gamma - 1} \right) + \mathbf{v} \cdot \nabla \left( \frac{p}{\gamma - 1} \right) = -\frac{\gamma p}{\gamma - 1} \nabla \cdot \mathbf{v} + \epsilon_{ij} S_{ij} + \eta j^2, \quad (2.16d)$$

$$\nabla \cdot \mathbf{B} = 0. \quad (2.16e)$$

where the rest of the notation is the same as in Equation (2.9).

#### Ideal MHD Equations

A second important form of the MHD equations is the ideal limit. This is found by setting  $\eta = \nu = 0$  in Equations (2.16). For simplicity gravity, thermal conduction and radiation

are also neglected. The set of ideal MHD equations is

$$\rho \frac{\partial \mathbf{v}}{\partial t} + \rho (\mathbf{v} \cdot \nabla) \mathbf{v} = -\nabla p + \mathbf{j} \times \mathbf{B}, \quad (2.17a)$$

$$\frac{\partial \rho}{\partial t} + \nabla \cdot (\rho \mathbf{v}) = 0, \quad (2.17b)$$

$$\frac{\partial \mathbf{B}}{\partial t} = \nabla \times (\mathbf{v} \times \mathbf{B}), \quad (2.17c)$$

$$\frac{\partial}{\partial t} \left( \frac{p}{\gamma - 1} \right) + \mathbf{v} \cdot \nabla \left( \frac{p}{\gamma - 1} \right) = -\frac{\gamma p}{\gamma - 1} \nabla \cdot \mathbf{v} \quad (2.17d)$$

$$\nabla \cdot \mathbf{B} = 0. \quad (2.17e)$$

### Ideal Incompressible MHD Equations

In this study, the form of the incompressible MHD equations will be important for comparison to approximate methods. In the ideal limit these are

$$\rho_0 \frac{\partial \mathbf{v}}{\partial t} = -\nabla p + (\mathbf{j} \times \mathbf{B}), \quad (2.18a)$$

$$\frac{\partial \rho}{\partial t} + \mathbf{v} \cdot \nabla \rho = 0. \quad (2.18b)$$

$$\frac{\partial \mathbf{B}}{\partial t} = \nabla \times (\mathbf{v} \times \mathbf{B}), \quad (2.18c)$$

$$\frac{\partial}{\partial t} \left( \frac{p}{\gamma - 1} \right) + \mathbf{v} \cdot \nabla \left( \frac{p}{\gamma - 1} \right) = 0. \quad (2.18d)$$

$$\nabla \cdot \mathbf{v} = 0, \quad \nabla \cdot \mathbf{B} = 0. \quad (2.18e)$$

In the next section the conservation laws of MHD are presented.

## 2.5 MHD: Conservation laws

It is a fundamental law that energy cannot be created or destroyed and so must be conserved. Here we state the conservation laws for full MHD. Some of the global conserved properties are different for compressible MHD and incompressible MHD and change depending on the dimension of the model considered. Nonetheless conservation of mass, momentum and total energy are always true in full MHD. This is not always strictly true when considering approximate methods.

The ability of a system to properly conserve a quantity is important. For a mathematical model this is determined by writing the equations in a conserved form. For example a quantity,  $Q$ , is conserved if

$$\frac{\partial Q}{\partial t} = -\nabla \cdot \mathbf{S},$$

where  $Q$  is a rank  $n$  tensor and  $S$  is a rank  $n + 1$  tensor.

The continuity equation, Equation (2.9b), is already in this form. This equation states the conservation of mass since the rate of change of  $\rho$  must be equal to the net flux of mass flowing out of or into the volume.

Conservation of total energy,  $E_{tot} = \frac{1}{2}\rho v^2 + \frac{1}{2\mu_0}B^2 + \rho\frac{p}{\gamma-1}$  is found by finding equations for the kinetic, magnetic and internal energy. This is done by multiplying the equation of motion, Equation (2.9a), by  $\mathbf{v}$ , continuity equation, Equation (2.9b) by  $\frac{1}{2}v^2$  and multiplying the induction equation, Equation (2.9c), by  $\frac{\mathbf{B}}{\mu_0}$ . Finally adding both of the resulting equations to the energy equation, Equation (2.9d), gives

$$\frac{\partial E_{tot}}{\partial t} = -\nabla \cdot \left( \frac{p}{\gamma-1}\rho\mathbf{v} + \frac{1}{2}\rho v^2\mathbf{v} + p\mathbf{v} - \mathbf{S} \cdot \mathbf{v} + \mathbf{q} + \frac{1}{\mu_0}\mathbf{E} \times \mathbf{B} \right) - \mathcal{L}_{\text{radiation}}, \quad (2.19)$$

where the Poynting flux is given by  $\frac{1}{\mu_0}(\mathbf{E} \times \mathbf{B})$ . In the following section, we derive the Grad-shafranov equation describing 2D MHD equilibria.

## 2.6 MHD Equilibria: Grad-Shafranov Equation

Another important topic of full MHD is the existence and properties of equilibria. These are states where quantities do not change in time. In certain situations, symmetry can be assumed, and an equation can be derived to describe the equilibrium magnetic field in a plasma. Here we derive the equation of equilibrium called the Grad-Shafranov equation for the case of translational symmetry, where invariance in  $z$  is assumed. We begin by considering the ideal MHD equations, Equations (2.17), in a static, ideal equilibrium with no variation in time and  $\mathbf{v} = 0$ . The static MHD equations are given by

$$\mathbf{j} \times \mathbf{B} = \nabla p, \quad (2.20a)$$

$$\nabla \times \mathbf{B} = \mu_0 \mathbf{j}, \quad (2.20b)$$

$$\nabla \cdot \mathbf{B} = 0. \quad (2.20c)$$

These are the force balance equation, current and the divergence-free condition respectively. Since the  $z$  direction is assumed invariant, the magnetic field,  $\mathbf{B}$ , can be written in terms of a vector potential,  $\mathbf{A}$ , as

$$\begin{aligned} \mathbf{B} &= \nabla \times \mathbf{A}, \\ &= \nabla A(x, y) \times \hat{\mathbf{e}}_z + B_z(x, y)\hat{\mathbf{e}}_z. \end{aligned} \quad (2.21)$$

where  $A$  is the  $z$  component of  $\mathbf{A}$ , known as the flux function.



Now calculating  $\mathbf{B} \cdot \nabla A$  using Equation (2.21) gives

$$\begin{aligned} \mathbf{B} \cdot \nabla A &= (\nabla A(x, y) \times \hat{\mathbf{e}}_z + B_z(x, y)\hat{\mathbf{e}}_z) \cdot \nabla A, \\ &= \underbrace{(\nabla A \times \hat{\mathbf{e}}_z) \cdot \nabla A}_{=0} + \underbrace{B_z \hat{\mathbf{e}}_z \cdot \nabla A}_{=0 \text{ since } \frac{\partial}{\partial z} = 0}, \\ &= 0. \end{aligned} \tag{2.22}$$

Thus  $A$  is constant along fieldlines of  $\mathbf{B}$ .

Taking the dot product of the force balance condition, Equation (2.20a), with  $\mathbf{B}$  and using Equation (2.21) gives

$$\begin{aligned} \mathbf{B} \cdot (\mathbf{j} \times \mathbf{B}) &= \mathbf{B} \cdot \nabla p, \\ 0 &= (\nabla A \times \hat{\mathbf{e}}_z) \cdot \nabla p, \\ &= \frac{\partial A}{\partial y} \frac{\partial p}{\partial x} - \frac{\partial A}{\partial x} \frac{\partial p}{\partial y}, \\ \Rightarrow p(x, y) &= p(A(x, y)). \end{aligned}$$

Hence  $p$  is a function of  $A$  and is also constant along fieldlines. It follows that

$$\nabla p(A) = \frac{dp(A)}{dA} \nabla A. \tag{2.23}$$

An expression for the current,  $\mathbf{j}$ , is found from Equation (2.20b) and substituting Equation (2.21) for  $\mathbf{B}$  gives

$$\nabla \times \mathbf{B} = -\nabla^2 A \hat{\mathbf{e}}_z + \nabla B_z \times \hat{\mathbf{e}}_z = \mu \mathbf{j}. \tag{2.24}$$

Substituting this equation for  $\mathbf{j}$  and Equation (2.21) for  $\mathbf{B}$  into the force balance condition, Equation (2.20a), gives

$$\mathbf{j} \times \mathbf{B} = \frac{1}{\mu} \left( -\nabla^2 A \nabla A - [(\nabla B_z \times \hat{\mathbf{e}}_z) \cdot \nabla A] \hat{\mathbf{e}}_z - B_z \nabla B_z \right) = \nabla p. \tag{2.25}$$

The  $z$  component of Equation (2.25) is

$$\begin{aligned} \frac{\partial A}{\partial y} \frac{\partial B_z}{\partial x} - \frac{\partial A}{\partial x} \frac{\partial B_z}{\partial y} &= 0, \\ \Rightarrow B_z &= B_z(A(x, y)). \end{aligned}$$

Hence  $B_z$  is a function of  $A$  and is also constant along fieldlines. It follows that

$$\nabla B_z(A) = \frac{dB_z(A)}{dA} \nabla A. \tag{2.26}$$

Using Equation (2.23) and Equation (2.26) for  $p(A)$  and  $B_z(A)$  in the  $x$  and  $y$  components

of Equation (2.25) allows them to be written as

$$\nabla^2 A + \mu \frac{dp}{dA} + \frac{1}{2} \frac{dB_z^2}{dA} = 0. \quad (2.27)$$

This equation is known as the Grad–Shafranov equation. It is a key equation in MHD and is a standard non-linear elliptic PDE. In general, a solution of this equation is a two dimensional equilibrium state. Here, the pressure is a function of  $A$ , which is determined by the ideal energy equation, Equation (2.17d), and  $B_z(A)$  is a known function of  $A$ . In general, a 2D analytic equilibrium can only be found for certain functions of  $p(A)$  and  $B_z(A)$ . In other cases, it is necessary to further simplify the Grad–Shafranov equation. One method of doing this, called the 1D approach, is presented in Chapter 4 in Section 4.2.4.

In the following section, we consider a small perturbation to an equilibrium state and describe the properties of the resulting waves.

## 2.7 MHD: Waves and Polarisation

The many forces that are present in a plasma perform a restoring force when the plasma is perturbed. In the present investigation MHD waves are not directly studied but can be important to the nonlinear dynamical evolution. Information about the complex nonlinear nature of these waves is contained in the full MHD equations, described in Section 2.4. The evolution of these waves results in a substantial requirement of computational time and resources to solve the full MHD equations. As will be shown, in Chapter 3, a significant simplification can be made by neglecting all high frequency waves and only following long wavelength, low frequency Alfvén waves, as is the case for RMHD. In this section, the ideal MHD equations, Equation (2.17), will be used to illustrate the three types of MHD waves. An ideal system is considered since dissipation effects only damp the wave amplitudes.

Consider an initial equilibrium with a constant, uniform background field,  $\mathbf{B}_0 = B_0 \hat{\mathbf{e}}_z$ , constant density,  $\rho_0$ , and pressure,  $p_0$ . The ideal MHD quantities are expanded about this equilibrium as

$$\mathbf{B} = \mathbf{B}_0 + \mathbf{B}, \quad \mathbf{v} = \mathbf{v}, \quad p = p_0 + p, \quad \rho = \rho_0 + \rho. \quad (2.28)$$

Linearising the continuity equation, Equation (2.17b), and energy equation, Equation (2.17d), gives two coupled equations given by

$$\frac{\partial \rho}{\partial t} + \rho_0 \nabla \cdot (\mathbf{v}) = 0, \quad (2.29)$$

$$\frac{\partial p}{\partial t} + \gamma p_0 \nabla \cdot (\mathbf{v}) = 0, \quad (2.30)$$

which can be combined to give the equation for sound waves as

$$\frac{\partial p}{\partial t} = c_s^2 \frac{\partial \rho}{\partial t},$$

where  $c_s = \sqrt{\frac{\gamma p_0}{\rho_0}}$  is the sound speed.

Linearising the equation of motion, Equation (2.17a), gives

$$\rho_0 \frac{\partial \mathbf{v}}{\partial t} = -\nabla \left( p + \frac{1}{\mu} \mathbf{B}_0 \cdot \mathbf{B} \right) + \frac{1}{\mu_0} (\mathbf{B}_0 \cdot \nabla) \mathbf{B}. \quad (2.31)$$

Linearising the induction equation, Equation (2.17c), gives

$$\frac{\partial \mathbf{B}}{\partial t} = B_0 \left( \frac{\partial \mathbf{v}}{\partial z} - \nabla \cdot \mathbf{v} \hat{\mathbf{e}}_z \right), \quad (2.32)$$

where  $\mathbf{B}_0 = B_0 \hat{\mathbf{e}}_z$  was substituted. Differentiating Equation (2.31), in time and substituting Equation (2.30) and Equation (2.32), gives

$$\frac{\partial^2 \mathbf{v}}{\partial t^2} = c_f^2 \nabla (\nabla \cdot \mathbf{v}) + V_A^2 \left( \frac{\partial^2 \mathbf{v}}{\partial z^2} - \frac{\partial \nabla \cdot \mathbf{v}}{\partial z} \hat{\mathbf{e}}_z - \nabla \frac{\partial v_z}{\partial z} \right), \quad (2.33)$$

where  $V_A = \sqrt{\frac{B^2}{\mu \rho_0}}$ , is the Alfvén speed and  $c_f^2 = c_s^2 + V_A^2$ , is the sum of the Alfvén and sound speeds, called the fast speed. Differentiating the  $z$  component of Equation (2.33) with respect to  $z$  gives

$$\frac{\partial^2}{\partial t^2} \frac{\partial v_z}{\partial z} = c_s^2 \frac{\partial^2 \nabla \cdot \mathbf{v}}{\partial z^2}. \quad (2.34)$$

The divergence of Equation (2.33) gives

$$\frac{\partial^2 \nabla \cdot \mathbf{v}}{\partial t^2} = c_f^2 \nabla^2 \nabla \cdot \mathbf{v} - V_A^2 \nabla^2 \frac{\partial v_z}{\partial z}. \quad (2.35)$$

Taking  $\frac{\partial^2}{\partial t^2}$  of Equation (2.35) and substituting Equation (2.34) gives a fourth order wave equation

$$\frac{\partial^4 \nabla \cdot \mathbf{v}}{\partial t^4} - c_f^2 \nabla^2 \frac{\partial^2 \nabla \cdot \mathbf{v}}{\partial t^2} + c_s^2 V_A^2 \nabla^2 \frac{\partial^2 \nabla \cdot \mathbf{v}}{\partial z^2} = 0. \quad (2.36)$$

Taking the curl of velocity gives the vorticity as,  $\omega = \nabla \times \mathbf{v}$ . The  $z$  component of vorticity,  $\omega_z = (\nabla \times \mathbf{v})_z$ , is found by taking the  $z$  component of the curl of Equation (2.33). This gives a wave equation with the Alfvén speed, as

$$\frac{\partial^2 \omega_z}{\partial t^2} = V_A^2 \frac{\partial^2 \omega_z}{\partial z^2}. \quad (2.37)$$

Assuming perturbations have the form

$$\exp(i(\mathbf{k} \cdot \mathbf{x} - \omega t)), \quad (2.38)$$

where  $\mathbf{k}$  is the wavevector which is the direction the wave propagates in, and  $\omega$  is the wave

frequency. Substituting Equation (2.38) into Equation (2.37) gives

$$[\omega^2 - k_z^2 V_A^2] \omega_z = 0. \quad (2.39)$$

and substituting Equation (2.38) into Equation (2.36) gives

$$[\omega^4 - k^2 c_f^2 \omega^2 + k^2 k_z^2 c_s^2 V_A^2] \nabla \cdot \mathbf{v} = 0. \quad (2.40)$$

There are two possible solutions to Equation (2.39) and Equation (2.40):  $\omega_z = 0$  and  $\omega_z \neq 0$ . Taking  $\omega_z \neq 0$  gives, from Equation (2.39), a dispersion relation for Alfvén waves of the form

$$\omega^2 = k_z^2 V_A^2 = k^2 V_A^2 \cos^2 \theta. \quad (2.41)$$

The phase speed of a wave is given by  $v_p = \frac{\omega}{k}$ . The phase speed given by Equation (2.41) is

$$v_p^2 = V_A^2 \cos^2 \theta. \quad (2.42)$$

This shows that an Alfvén wave can travel with an angle  $\theta$  to the magnetic field. The direction in which energy is transported is given by the group velocity which is given by  $v_g = \frac{\partial \omega}{\partial \mathbf{k}} = \pm V_A \hat{\mathbf{e}}_z$ . The sign indicates that Alfvén waves can travel parallel or anti-parallel to  $\mathbf{B}_0$ . In this case Equation (2.40) can only be satisfied by assuming incompressibility,  $\nabla \cdot \mathbf{v} = 0$ . Thus an Alfvén wave is an incompressible perturbation and travels at the Alfvén speed along  $\mathbf{B}_0$  and cannot travel across the field. It follows that there are no pressure or density perturbations. The components parallel to  $\mathbf{B}_0$ , namely:  $v_z$  and  $B_z$ , are also zero. The pressure force  $\nabla_{\perp} \left( p + \frac{\mathbf{B}_0 \cdot \mathbf{B}}{\mu} \right) = 0$ . The perpendicular components of the equation of motion, Equation (2.31), and the induction equation, Equation (2.32), are

$$\begin{aligned} \frac{\partial \mathbf{v}_{\perp}}{\partial t} &= V_A \frac{\partial \mathbf{B}_{\perp}}{\partial z}, \\ \frac{\partial \mathbf{B}_{\perp}}{\partial t} &= V_A \frac{\partial \mathbf{v}_{\perp}}{\partial z}. \end{aligned}$$

These can be combined to give the Alfvén wave equation.

For the second case,  $\omega_z = 0$ , Equation (2.39) is automatically satisfied. If  $\nabla \cdot \mathbf{v} \neq 0$  Equation (2.40) gives the dispersion relation

$$\omega^4 - k^2 c_f^2 \omega^2 + k^4 \cos^2 \theta c_f^2 c_t^2 = 0, \quad (2.43)$$

where  $c_t^2 = \frac{c_s^2 V_A^2}{c_s^2 + V_A^2}$  is called the slow wave speed. The phase speed can be written as

$$c^4 - c_f^2 c^2 + \cos^2 \theta c_f^2 c_t^2 = 0.$$

This has roots of

$$c_{\pm}^2 = \frac{c_f^2}{2} \left[ 1 \pm \sqrt{\left( 1 - 4 \frac{c_t^2}{c_f^2} \cos^2 \theta \right)} \right].$$

Perpendicular to  $\mathbf{B}_0$ ,  $\theta = \pi/2$ , and the two solutions are  $c_+^2 = c_f^2$  and  $c_-^2 = 0$ . Parallel to the magnetic field,  $\theta = 0$ , the solutions are  $c_s^2$  and  $V_A^2$ . One wave has a speed greater than or equal to the maximum of these two speeds and the second wave has a speed less than or equal to the minimum. Hence the first is the fast magnetoacoustic wave and the second is the slow magnetoacoustic wave.

In summary the fast wave propagates almost isotropically in all directions. The slow wave cannot travel across the magnetic field. Both magnetoacoustic waves are compressible while the Alfvén wave is incompressible and only travels along the field.

### Polarisation

Here we consider the frame of reference of a wave. This is separate from a spatial coordinate system. In this frame there are two known directions: the direction of propagation,  $\mathbf{k}$ , and the magnetic field,  $\hat{\mathbf{B}}_0$ . The direction of propagation is an intrinsic property of the wave and so is a basis vector. As a wave propagates there are fluctuations of the magnetic and velocity fields. These fluctuations can be restricted to be in a certain direction relative to these two vectors. This is called polarisation. Here we define the three possible wave polarisations. Since it has been shown that Alfvén waves involve fluctuations normal to both the direction of propagation and the magnetic field we can now simply write that these perturbations are in the direction

$$\hat{\mathbf{e}}_{\text{toroidal}} = (\mathbf{k} \times \hat{\mathbf{B}}_0). \quad (2.44)$$

This is called the toroidal direction. This property of Alfvén wave fluctuations to be perpendicular to  $\mathbf{k}$  and  $\hat{\mathbf{B}}_0$  can now be concisely written as: Alfvén waves are toroidally polarised.

Fluctuations along the direction of propagation are called longitudinal. Only velocity fluctuations can be longitudinal since the magnetic field must be incompressible:  $\mathbf{k} \cdot \mathbf{B} = 0$ .

In the wave frame we have found two fundamental directions for a given wavenumber to describe the direction of the perturbation: direction of propagation,  $\hat{\mathbf{k}}$ ; and the toroidal direction,  $\hat{\mathbf{e}}_{\text{toroidal}}$ . To complete the set of basis vectors in three dimensional space we need a third linearly independent vector. This can simply be found by taking the cross product of  $\mathbf{k}$  and  $\hat{\mathbf{e}}_{\text{toroidal}}$ . The unit vector in this direction can be written as

$$\hat{\mathbf{e}}_{\text{poloidal}} = (\mathbf{k} \times \hat{\mathbf{B}}_0) \times \mathbf{k}. \quad (2.45)$$

This is called the poloidal direction.

These three directions: toroidal, poloidal and longitudinal complete a set of linearly

independent basis vectors in the wave frame. Poloidal and toroidal refer to the basis directions which complete the triad with the wavevector. Since these directions are normal to  $\mathbf{k}$  the perturbations polarised along these directions are incompressible. The waves that are toroidally polarised are called shear Alfvén and those that are poloidally polarised are pseudo Alfvén waves, which is the slow magnetoacoustic wave in the incompressible limit.

In Chapter 3 we introduce RMHD, an approximate model of MHD, which only considers low frequency Alfvén waves. In the following section the development of the tearing instability from a small perturbation is considered.

## 2.8 Tearing Instability Analysis

A small perturbation to a stable equilibrium can produce waves as described in the previous section, however if the equilibrium is unstable, under the appropriate conditions, a small perturbation can grow in magnitude. This is the development of an instability. Similar to waves, properties of instabilities can be found from linear analysis. Here we sketch the linear analysis for the tearing instability for a general equilibrium, following the procedure taken in Chapter 5.3.1 of Boyd and Sanderson 2003.

In this section we use the resistive form of the momentum and induction equations, given by neglecting viscosity in Equation (2.16a) and Equation (2.16c). Nonzero resistivity is needed to allow the instability to develop. Assuming incompressibility,  $\nabla \cdot \mathbf{v} = 0$ , for simplicity, the momentum and induction equations are

$$\rho_0 \frac{\partial \mathbf{v}}{\partial t} = -\nabla p + (\mathbf{j} \times \mathbf{B}), \quad (2.46a)$$

$$\frac{\partial \mathbf{B}}{\partial t} = \nabla \times (\mathbf{v} \times \mathbf{B}) + \eta \nabla^2 \mathbf{B}, \quad (2.46b)$$

$$\nabla \cdot \mathbf{v} = 0, \quad \nabla \cdot \mathbf{B} = 0. \quad (2.46c)$$

The magnetic field is comprised of an equilibrium field,  $\mathbf{B}_{\text{equil}}$ , and a perturbation,  $\mathbf{B}_1$ , as

$$\mathbf{B} = \mathbf{B}_{\text{equil}} + \mathbf{B}_1.$$

Here the equilibrium magnetic field includes an initial constant background magnetic field,  $\mathbf{B}_0$ , and a spatially varying part, which is chosen to be a function of  $x$  only as

$$\mathbf{B}_{\text{equil}} = B_{\text{equil } y}(x) \hat{\mathbf{e}}_y + (B_0 + B_{\text{equil } z}(x)) \hat{\mathbf{e}}_z. \quad (2.47)$$

This equilibrium magnetic field, Equation (2.47), creates an equilibrium current of the form

$$\mathbf{j}_{\text{equil}} = -\frac{dB_{\text{equil } z}}{dx} \hat{\mathbf{e}}_y + \frac{dB_{\text{equil } y}}{dx} \hat{\mathbf{e}}_z.$$

This equilibrium magnetic field,  $\mathbf{B}_{\text{equil}}$ , satisfies a force balance equilibrium condition. Taking an equilibrium with  $\mathbf{v} = 0$ ,  $p = p_0$  and  $\rho = \rho_0$ , Equation (2.46a), gives the force balance equation,  $\mathbf{j}_{\text{equil}} \times \mathbf{B}_{\text{equil}} = 0$ . Only the  $x$  component is nonzero when considering a

nontrivial equilibrium field, which is

$$(B_0 + B_{\text{equil } z}(x)) \frac{dB_{\text{equil } z}(x)}{dx} + B_{\text{equil } y} \frac{dB_{\text{equil } y}}{dx} = 0.$$

Integrating gives

$$(B_0 + B_{\text{equil } z}(x))^2 + B_{\text{equil } y}^2 = \text{constant},$$

where  $B_0$  has been taken inside the derivative since it is constant.

Perturbations of the velocity,  $\mathbf{v}_1$ , and magnetic field,  $\mathbf{B}_1$ , are assumed to be of the form

$$\mathbf{B}_1(x, y, z, t) = \mathbf{B}_1(x) \exp(i(k_y y + k_z z) + \sigma t), \quad (2.48)$$

where  $k_y$  and  $k_z$  are wavenumbers and  $\sigma$  is the growth rate. This form of the magnetic and velocity perturbations is substituted in the incompressible equations, Equation (2.46a) and Equation (2.46b). The  $x$  dependence of variables is assumed henceforth for conciseness.

The  $x$  component of the incompressible induction equation, Equation (2.46b), using Equation (2.48), is

$$\sigma B_{1x} = B_{\text{equil } y} i k_y v_{1x} + (B_0 + B_{\text{equil } z}) i k_z v_{1x} + \eta \left( \frac{d^2}{dx^2} - k_y^2 - k_z^2 \right) B_{1x}. \quad (2.49)$$

This shows that if the perturbation is nonzero and  $\mathbf{k} \cdot \mathbf{B}_{\text{equil}} = 0$  at a point in  $x$ , say at  $x = \xi$ , then this equation gives a diffusion equation. The magnetic field diffuses when  $x$  derivatives are large. The dissipation term becomes large when the  $x$  derivative of  $B_{1x}$  is large. It follows that if  $\sigma$  is positive the initially small perturbation grows exponentially in time.

Since there is a nonzero  $B_{1x}$  there will be a corresponding nonzero  $v_{1x}$ . An equation for  $v_{1x}$  as a function of  $B_{1x}$ , can be found in the following way. Expanding Equation (2.46a) using Equation (2.48), gives the three components of the momentum equation as

$$\begin{aligned} \sigma \rho_0 v_{1x} = & - \frac{d}{dx} (B_{\text{equil } y} B_{1y} + (B_0 + B_{\text{equil } z}) B_{1z}) \\ & + i (\mathbf{k} \cdot \mathbf{B}_{\text{equil}}) B_{1x}, \end{aligned} \quad (2.50a)$$

$$\begin{aligned} \sigma \rho_0 v_{1y} = & B_{1x} \frac{dB_{\text{equil } y}}{dx} - i k_y B_{1z} (B_0 + B_{\text{equil } z}) \\ & + i k_z B_{1y} (B_0 + B_{\text{equil } z}), \end{aligned} \quad (2.50b)$$

$$\sigma \rho_0 v_{1z} = B_{1x} \frac{dB_{\text{equil } z}}{dx} + i k_y B_{1z} B_{\text{equil } y} - i k_z B_{1y} B_{\text{equil } y}. \quad (2.50c)$$

The incompressibility condition for velocity,  $\nabla \cdot \mathbf{v}_1 = 0$ , can be rearranged to give

$\frac{dv_{1x}}{dx}$  as a function of  $v_{1y}$  and  $v_{1z}$  as

$$-\frac{dv_{1x}}{dx} = ik_y v_{1y} + ik_z v_{1z}. \quad (2.51)$$

Multiplying by  $\sigma\rho_0$  and substituting Equation (2.50b) and Equation (2.50c) and using the solenoidal constraint on the perturbed magnetic field,  $\nabla \cdot \mathbf{B} = 0$ , Equation (2.51) gives

$$\begin{aligned} -\sigma\rho_0 \frac{dv_{1x}}{dx} &= \sigma\rho_0 (ik_y v_{1y} + ik_z v_{1z}), \\ &= i(\mathbf{k} \cdot \mathbf{B}_{\text{equil}}) B_{1x} + (k_y^2 + k_z^2) (B_{1z} (B_0 + B_{\text{equil } z}) + B_{1y} B_{\text{equil } y}) \\ &\quad - i(\mathbf{k} \cdot \mathbf{B}_{\text{equil}}) \frac{dB_{1x}}{dx}. \end{aligned} \quad (2.52)$$

Differentiating Equation (2.52) wrt  $x$  and combining with  $(k_y^2 + k_z^2)$  times Equation (2.50a) gives

$$\begin{aligned} \sigma\rho_0 \left( \frac{d^2 v_{1x}}{dx^2} - (k_y^2 + k_z^2) v_{1x} \right) &= i(\mathbf{k} \cdot \mathbf{B}_{\text{equil}}) \left[ \frac{d^2 B_{1x}}{dx^2} - (k_y^2 + k_z^2) B_{1x} \right] \\ &\quad - i \frac{d^2}{dx^2} [(\mathbf{k} \cdot \mathbf{B}_{\text{equil}})] B_{1x}. \end{aligned} \quad (2.53)$$

Equation (2.53) and Equation (2.49) give two coupled equations for  $v_{1x}$  and  $B_{1x}$ .

In summary the system of equations to solve is

$$\begin{aligned} \sigma\rho_0 \left( \frac{d^2 v_{1x}}{dx^2} - (k_y^2 + k_z^2) v_{1x} \right) &= i(\mathbf{k} \cdot \mathbf{B}_{\text{equil}}) \left[ \frac{d^2 B_{1x}}{dx^2} - (k_y^2 + k_z^2) B_{1x} \right] \\ &\quad - i \frac{d^2}{dx^2} [(\mathbf{k} \cdot \mathbf{B}_{\text{equil}})] B_{1x}. \\ \sigma B_{1x} &= i(\mathbf{k} \cdot \mathbf{B}_{\text{equil}}) v_{1x} + \eta \left( \frac{d^2}{dx^2} - k_y^2 - k_z^2 \right) B_{1x}. \end{aligned}$$

Assuming  $\frac{d}{dx} \gg k_y, k_z$ , these equations become

$$\sigma\rho_0 \frac{d^2 v_{1x}}{dx^2} = i(\mathbf{k} \cdot \mathbf{B}_{\text{equil}}) \frac{d^2 B_{1x}}{dx^2} - i \frac{d^2}{dx^2} [(\mathbf{k} \cdot \mathbf{B}_{\text{equil}})] B_{1x}. \quad (2.55a)$$

$$\sigma B_{1x} = i(\mathbf{k} \cdot \mathbf{B}_{\text{equil}}) v_{1x} + \eta \frac{d^2 B_{1x}}{dx^2}. \quad (2.55b)$$

The equilibrium field rapidly changes over a small region near  $x = \xi$ , with width  $\zeta$ . Since  $\mathbf{k} \cdot \mathbf{B}_{\text{equil}}(\xi) = 0$  but  $\mathbf{k} \cdot \frac{d\mathbf{B}_{\text{equil}}(\xi)}{dx} \neq 0$  we have

$$\mathbf{k} \cdot \mathbf{B}_{\text{equil}} \approx \zeta \mathbf{k} \cdot \frac{d\mathbf{B}_{\text{equil}}}{dx}. \quad (2.56)$$

Considering variations on small scales,  $\zeta$ , in  $x$  near  $x = \xi$  and neglecting terms varying on



the equilibrium lengthscale Equation (2.55b) gives

$$\frac{d^2 B_{1x}}{dx^2} = \frac{1}{\eta} i \mathbf{k} \cdot \mathbf{B}_{\text{equil}} v_{1x}. \quad (2.57)$$

Substituting Equation (2.57) into Equation (2.55a) gives

$$\begin{aligned} \sigma \rho_0 \frac{d^2 v_{1x}}{dx^2} &\approx i (\mathbf{k} \cdot \mathbf{B}_{\text{equil}}) \frac{d^2 B_{1x}}{dx^2}, \\ &\approx -\frac{1}{\eta} (\mathbf{k} \cdot \mathbf{B}_{\text{equil}})^2 v_{1x}, \end{aligned} \quad (2.58)$$

Taking  $\frac{d}{dx} \approx \frac{1}{\zeta}$  and using Equation (2.56) and Equation (2.58) gives

$$\frac{\sigma \rho_0 v_{1x}}{\zeta^2} \approx \frac{\zeta^2}{\eta} \left( \mathbf{k} \cdot \frac{d\mathbf{B}_{\text{equil}}}{dx} \right)^2 v_{1x}. \quad (2.59)$$

Thus, rearranging Equation (2.59) for  $\zeta$  gives

$$\zeta \approx \left( \frac{\sigma \rho_0 \eta}{\left( \mathbf{k} \cdot \frac{d\mathbf{B}_{\text{equil}}}{dx} \right)^2} \right)^{1/4}. \quad (2.60)$$

Since  $\mathbf{B}_{\text{equil}}(\xi) = 0$ ,  $\frac{d\mathbf{B}_{\text{equil}}}{dx}$  varies rapidly near  $x = \xi$  on lengthscale  $\zeta$ . The perturbation,  $B_{1x}$ , grows rapidly near  $\xi$ . Thus  $\frac{dB_{1x}}{dx}$  varies rapidly and appears discontinuous on large scales. It follows that  $\frac{d^2 B_{1x}}{dx^2}$  is very large. The magnitude of the second derivative of the perturbation can be measured by the dimensionless parameter,  $\Delta'$ , as

$$\Delta' = L \frac{\mathbf{B}'_{1x}(+\zeta/2) - \mathbf{B}'_{1x}(-\zeta/2)}{\mathbf{B}_{1x}(\xi)}, \quad (2.61)$$

where  $L$  is an equilibrium lengthscale. Using Equation (2.61) and Equation (2.55a), near  $x = \zeta$  can be written as

$$\begin{aligned} \sigma \rho_0 \frac{d^2 v_{1x}}{dx^2} &\approx (\mathbf{k} \cdot \mathbf{B}_{\text{equil}}) \frac{d^2 B_{1x}}{dx^2}, \\ &\approx (\mathbf{k} \cdot \mathbf{B}_{\text{equil}}) \frac{\frac{dB_{1x}(+\zeta/2)}{dx} - \frac{dB_{1x}(-\zeta/2)}{dx}}{\zeta}, \\ &\approx (\mathbf{k} \cdot \mathbf{B}_{\text{equil}}) \frac{\Delta' B_{1x}(\xi)}{\zeta L}, \end{aligned} \quad (2.62)$$

In the outer region, away from  $x = \xi$ , resistivity is negligible and the system can be treated as ideal. Setting  $\eta = 0$  in Equation (2.55b) gives

$$B_{1x} = \frac{(\mathbf{k} \cdot \mathbf{B}_{\text{equil}}) v_{1x}}{\sigma}. \quad (2.63)$$

Substituting Equation (2.63) into Equation (2.62) and using Equation (2.56) gives

$$\begin{aligned} \frac{\sigma \rho_0 v_{1x}}{\zeta^2} &\approx (\mathbf{k} \cdot \mathbf{B}_{\text{equil}})^2 \frac{\Delta' v_{1x}}{\zeta L \sigma}, \\ &\approx \left( \mathbf{k} \cdot \frac{d\mathbf{B}_{\text{equil}}}{dx} \right)^2 \frac{\Delta' \zeta v_{1x}}{L \sigma}, \end{aligned} \quad (2.64)$$

Rearranging for the growth rate,  $\sigma$ , gives

$$\sigma^2 = \frac{1}{\rho_0} \left( \mathbf{k} \cdot \frac{d\mathbf{B}_{\text{equil}}}{dx} \right)^2 \frac{\Delta' \zeta^3}{L} \quad (2.65)$$

Substituting for  $\zeta$ , Equation (2.60), and rearranging gives an expression for  $\sigma$  of

$$\sigma \sim \rho_0^{-1/5} L^{-4/5} \eta^{3/5} \Delta'^{4/5} \left( \mathbf{k} \cdot \frac{d\mathbf{B}_{\text{equil}}}{dx} \right)^{2/5}. \quad (2.66)$$

Expanding the dot product gives

$$\sigma \sim \rho_0^{-1/5} L^{-4/5} \eta^{3/5} \Delta'^{4/5} |\mathbf{k}|^{2/5} \left| \frac{d\mathbf{B}_{\text{equil}}}{dx} \right|^{2/5} \cos^{2/5} \theta. \quad (2.67)$$

where  $\theta$  is the angle between  $\mathbf{k}$  and  $\mathbf{B}_{\text{equil}}$ . This shows that the growth rate depends on the angle between  $\mathbf{k}$  and  $\mathbf{B}_{\text{equil}}$ .

In the special case of 2D incompressible MHD, when there is no variation in  $z$  and a strong uniform magnetic field in  $z$ , this analysis can be carried out in the same way, by setting  $k_z = 0$  and  $B_{\text{equil}} = B_0 \hat{\mathbf{z}} + B_{\text{equil } y}(x) \hat{\mathbf{y}}$ , hence the growth rate can be expressed in the 2D form

$$\omega_{2D} \sim \rho_0^{-1/5} k_y^{2/5} \eta^{3/5} \Delta'^{4/5} B_{\text{equil } y}^{2/5}. \quad (2.68)$$

## 2.9 Summary

In this chapter, the model of MHD has been introduced. The equations of full MHD are complex nonlinear PDEs involving eight unknown quantities. In many areas of research where it is wished to solve these equations, such as fusion devices or astrophysics, there is a strong background magnetic field present throughout the region of interest. Assuming such a guide field to be constant in time and space results in much simpler equations.

Montgomery and Turner 1981 show that in the limit of such a strong field the full incompressible MHD equations become essentially 2D. The only contribution parallel to the guide field being through a linear Alfvén wave equation. This form of the equations results in dynamics similar to incompressible 2D MHD with small contributions from three dimensional Alfvén waves. This implies that if there is an infinitely strong background field throughout the plasma, then a 3D system would be 2D in nature. This motivates the possibility for a significant simplification to the full MHD equations in the presence of a

strong guide field. This simple picture is described by the approximate model of reduced MHD (RMHD), which is introduced in the next chapter.

## Chapter 3

# RMHD Model

### 3.1 Overview of RMHD

MHD is a widely used model for the evolution of a plasma. However, as shown in Section 2.4, the full 3D compressible MHD equations are a set of nonlinear PDEs, which require a substantial amount of computational time and resources to solve and gain meaningful results. In some cases, it is possible that additional assumptions can reduce the full set of equations, Equation (2.9), to a more computationally manageable set and can provide useful insights into the dynamics of a system while requiring less resources. There are several possible assumptions that can be used to achieve this. Here we focus on the case of a strong unidirectional background magnetic field that is present throughout the plasma. Such a dominant field component is a common feature in many natural plasma systems, such as fusion and astrophysical plasmas.

It is well known in MHD turbulence theory that a strong background magnetic field,  $\mathbf{B}_0$ , creates anisotropy. One of the first analytic studies proposing this was Moffatt 1967 for small Reynolds numbers and later Montgomery and Turner 1981 for high Reynolds numbers. This global anisotropy is a clear large scale example that MHD turbulence is unlikely to be isotropic as is commonly assumed in hydrodynamic turbulence theory. Anisotropy is an intrinsic property of MHD turbulence.

The development of anisotropy has been modelled numerically in detail in many MHD turbulence investigations using the full MHD equations (Shebalin, Matthaeus, and Montgomery 1983; Oughton, Priest, and Matthaeus 1994; Oughton 1996; Oughton et al. 2016). Many aspects that characterise such anisotropic systems were found, such as the tendency of a three dimensional turbulent system to act like a 2D system in planes perpendicular to  $\mathbf{B}_0$ . This indicates that, providing  $\mathbf{B}_0$  is large enough, the system can be approximated as almost 2D in nature. The 2D MHD equations are much simpler than the 3D case. There is less agreement on the general manifestation of other characteristics, such as the importance of fluctuations parallel to  $\mathbf{B}_0$ , when a strong guide field is present.

Since a strong background field imposes such significant restrictions on the 3D dynamics, it is natural to assume anisotropy in the equations from the outset, when considering a system permeated by a strong background field. Anisotropic equations were used

for magnetically confined plasmas by Kadomtsev and Pogutse 1974 and Rosenbluth et al. 1976 using cylindrical geometry appropriate for fusion devices. These studies will be briefly discussed in Section 3.2 to provide a brief history and insight into the original motivation behind the assumptions that will be discussed in this study. Their equations have been derived and rederived many times over the years using several different approaches and have become known as the equations of reduced MHD (RMHD). Some of these approaches are mentioned in Section 3.3. A formal derivation of RMHD and properties of the equations are discussed in Section 3.4.

Once the RMHD equations have been derived, an important aspect of an approximate MHD model is to check how its solutions compare to those of full MHD. Some full MHD studies are similar, but not identical to, studies using RMHD. Without direct comparisons of simulations from both methods it is difficult to determine how well RMHD models a system. There are also many aspects, such as thermodynamics, that are not included in RMHD and thus cannot be predicted at all. There do not seem to be many comparisons or consistency checks between MHD and RMHD. Those that we know of are discussed in Section 3.5.

Since the original formulation of RMHD, this model has been used in many investigations. Due to the focus on nonlinearities in RMHD these studies have been predominantly in the context of turbulence. In general, the periodic boundary conditions which are used to model a turbulent system threaded by a strong background field are arguably similar to those used for a magnetically confined plasma. Our main focus is not on turbulence and hence no further argument of validity of RMHD for periodic turbulence is given. Over the last decade or so RMHD has also been used to model coronal loops. This would seem like a reasonable approximation, since these coronal structures consist of a dominant magnetic field component along the loop axis. However these systems may be different from triply periodic turbulence due to line-tied boundary conditions at the photospheric footpoints, and fundamentally distinct from fusion plasma as discussed in Chapter 1. In Section 3.6 we discuss a number of relevant full MHD and RMHD studies in solar physics, in the context of footpoint driven coronal loops. Although these studies are very similar, they are not exactly the same and direct comparisons are not possible. A discussion of the applicability of RMHD in the corona, with a focus on open magnetic regions, has recently been given in a review article by Oughton, Dmitruk, and Matthaeus 2003.

During the last few decades there have also been many similar models developed which attempt to simplify the MHD equations while retaining additional dynamics that are not included in the original model of RMHD. Another interesting area are the many models that predict similar dynamics to RMHD. Details of a selection of these models are briefly given in Section 3.7 and in Appendix B. There are also several models in other research areas of plasma physics which have similar acronyms to RMHD but which may or may not have any relation to the original RMHD model derived by Strauss 1976. These models are briefly listed in Section 3.8 in an attempt to resolve possible confusion.

We aim to present an informative summary of RMHD: including the original motivation and arguments leading to the development of this model, the properties of the equations, and recent relevant coronal loop studies. It is hoped that this provides a useful

overview of the RMHD model and the lack of direct comparisons and validity tests between RMHD and full MHD.

## 3.2 Brief History of RMHD in Fusion Devices

In this section the original motivation for the RMHD equations is discussed. The equations of RMHD were first proposed in cylindrical geometry for tokamaks. A brief summary is given of the research carried out in fusion devices when the assumptions of RMHD were first applied to the MHD equations.

Historically, the first article to use equations in the form of RMHD was Kadomtsev and Pogutse 1974. They investigate the nonlinear evolution of helical perturbations or kink modes in tokamaks and the possible development of disruptive instabilities. By taking into account toroidal geometry and characteristics of the kink instability, they simplify the MHD equations by assuming negligible gas pressure and a strong toroidal magnetic field. Curvature effects are neglected and the system is taken to be a straight cylinder of plasma. It is assumed that these assumptions are valid in general for tokamaks with large major radius and small plasma beta. The resulting equations were not presented as a general model, simply as an approximation of the MHD equations for the current system. They conclude that the helical perturbations create cavities on the surface of the plasma column. In order to reach a minimum energy state these cavities move inside the plasma, creating internal vacuums or “bubbles”. The number of these “bubbles” is the same as the mode number of the kink mode. It was found that over time these “bubbles” collect in the centre of the plasma column creating an internal vacuum column, whose volume increases in time, causing the radius of the column to increase as it expands to find an equilibrium. If there is no equilibrium the plasma is unstable and would continue to expand indefinitely. It was also suggested that under certain conditions this might lead to the disruptive instability. This is a major concern in magnetic confinement devices as such evolution must be avoided for safe operation. This result was confirmed by Rosenbluth et al. 1976.

Next, Strauss 1976 investigates the stability of kink modes in tokamaks with a non-circular cross-section. This motivates the formal derivation of RMHD in cartesian coordinates for a low- $\beta$  tokamak with a rectangular cross section. The derivation is presented in Section 3.3.1. He uses the RMHD equations to follow the nonlinear dynamics and confirm the potential development of fast-growing, fixed boundary kink modes in non-circular tokamaks. Strauss has contributed greatly to the development of the model of RMHD in many subsequent articles. In Strauss 1977, he extends his previous equations for low- $\beta$  tokamaks to high- $\beta$  devices and investigates equilibria, in Strauss 1982 the RMHD approach is used to find equations for mirror machines, in Strauss 1997 the equations are derived for near-potential magnetic fields. The equations have also been applied to stellarators, an early form of tokamak, Strauss 1980.

### 3.3 Original RMHD Derivations

In this section, we will describe three different approaches presented in the literature to derive the Reduced MHD (RMHD) equations from the full MHD ones. Sometimes, the derivations begin from the ideal MHD equations, Equations (2.17) for simplicity, but dissipation terms are easily added. Different forms of the RMHD equations are found depending on the value of  $\beta$ . We focus on low plasma beta. Here parallel and perpendicular directions are taken with respect to the background magnetic field,  $\mathbf{B}_0 = B_0 \hat{\mathbf{e}}_z$ , i.e parallel denotes the  $z$  direction and perpendicular denotes the  $x$  and  $y$  directions.

The main derivation in Section 3.3.1 is the original method used by Strauss (Strauss 1976), giving a brief straightforward derivation in terms of the magnetic flux function,  $A$ . For completeness, full details of a further three approaches to derive the RMHD equations are included in Appendix A. A second method is the more algebraic but physically motivated method used by Zank and Matthaeus 1992. The equations are summarised in Section 3.3.2 and derived in Appendix A.1.

In Section 3.3.3 and Appendix A.2, the third derivation of RMHD by Montgomery 1982 is discussed. In contrast, he begins from the incompressible MHD equations.

These three approaches to derive the RMHD equations, used by Strauss, Zank and Matthaeus and Montgomery, are included as each uses the assumptions of RMHD in a different way while arriving at the same equations. It is believed that discussing each of these approaches will help to clarify and emphasise the relation between a strong field and spectral anisotropy and that they are both necessary assumptions of RMHD.

A fourth derivation was presented independently by van Ballegooijen 1985. The approach used is very different from the other derivations included here as RMHD is derived from an equilibrium viewpoint. This reveals a subtle relationship between RMHD and magnetofrictional relaxation methods. This method is also included in Appendix A.3.

#### 3.3.1 Strauss' Derivation

In this section, the first formal derivation of RMHD by Strauss 1976 is given. This method was the first time RMHD had been derived in cartesian coordinates, thus enabling this model to be used in a wider range of applications. Strauss' article is widely regarded as the original derivation of RMHD, and the equations are occasionally referred to as the "Strauss equations" or "KPS equations" - Kadomtsev-Pogutse-Strauss - in the literature. A description of this derivation was given in Biskamp 1993, with slightly different or sometimes more detailed arguments which are included here for clarity.

The system is a long thin cylinder of plasma aligned with the  $z$  axis. It follows that the system is much longer in  $z$  than in  $x$  and  $y$  and so a large aspect ratio is assumed. The inverse of the aspect ratio is taken to give a small parameter  $\varepsilon_{\text{strauss}}$ .

$$\varepsilon_{\text{strauss}} = \frac{L_{\perp}}{L_z} \ll 1. \quad (3.1)$$

The final system is incompressible so constant density,  $\rho_0 = 1$ , is assumed throughout for

simplicity without loss of generality.

It is assumed that lengths over which variations take place are much longer in  $z$  than  $x$  and  $y$  by a factor of  $\varepsilon_{\text{strauss}}^{-1}$ . The  $z$  component of the magnetic field is similarly larger than the  $x$  and  $y$  components. Hence, following Biskamp 1993 we assume the ansatz

$$\frac{\partial}{\partial x}, \frac{\partial}{\partial y} \approx 1, \quad \frac{\partial}{\partial z} \approx \varepsilon_{\text{strauss}},$$

$$B_x, B_y \approx \varepsilon_{\text{strauss}}, \quad B_z \approx B_0 + \varepsilon_{\text{strauss}}^2,$$

which implies

$$j_x, j_y \approx \varepsilon_{\text{strauss}}^2, \quad j_z \approx \varepsilon_{\text{strauss}}.$$

The assumption that the background magnetic field strength,  $B_0$ , is strong means that the energy in  $B_0$  is much larger than the energy contained in the perpendicular field as  $B_0^2 \gg B_\perp^2$ . In a physical context, this assumption also implies that the thermal and kinetic energies are much smaller than the magnetic energy, which is dominated by the background field component,

$$\rho v^2 \sim p \lll B_z^2.$$

Since the thermal and kinetic energies and the magnetic energy contained in the perpendicular components are assumed smaller than the energy in the guide field we take them to be of the same magnitude as

$$v_\perp^2 \sim p \sim B_\perp^2.$$

Hence the pressure and velocity have the following ordering

$$p \approx \varepsilon_{\text{strauss}}^2, \quad \mathbf{v}_\perp \approx \varepsilon_{\text{strauss}}.$$

Time derivatives are chosen to be

$$\frac{\partial}{\partial t} \sim \mathbf{v} \cdot \nabla_\perp \sim \varepsilon_{\text{strauss}},$$

to ensure that the slow nonlinear dynamics, which evolve on a slow timescale, are retained.

The variation to the parallel field,  $B_z$ , denoted by  $\delta B_z$  can be determined since the variation in  $B_z$  is required to balance the pressure force

$$\delta B_z^2 \approx 2\delta B_z B_z \approx p.$$

It follows from this that  $\delta B_z \approx \varepsilon_{\text{strauss}}^2$  and so the parallel field is constant to lowest order. The total parallel component of the magnetic field is given by  $B_z = B_0 + \delta B_z$ , but  $\delta B_z$  is neglected here so that  $B_z \sim B_0$ .

Since the first order perturbation to the magnetic field only has perpendicular



components, it follows immediately that the magnetic field can be written in terms of the vector potential,  $\mathbf{A}$ , as

$$\begin{aligned}\mathbf{B} &= \nabla A \times \hat{\mathbf{e}}_z + (B_0 + \delta B_z) \hat{\mathbf{e}}_z, \\ &= \nabla A \times \hat{\mathbf{e}}_z + \left( B_0 + \left[ \frac{\partial A_y}{\partial x} - \frac{\partial A_x}{\partial y} \right] \right) \hat{\mathbf{e}}_z,\end{aligned}\quad (3.2)$$

where  $A$  is the  $z$  component of  $\mathbf{A}$ ,  $\delta B_z$  is the  $\varepsilon_{\text{strauss}}^2$  variation from the background field and  $z$  derivatives of  $A_x$  and  $A_y$  are neglected, since variations in  $z$  are small compared to those in  $x$  and  $y$ . The vector potential ensures that the solenoidal condition is automatically satisfied for the perpendicular components and leaves only the parallel contribution as

$$\nabla \cdot \mathbf{B} = \frac{\partial \delta B_z}{\partial z} \approx \varepsilon_{\text{strauss}}^3.$$

Higher order corrections to the perpendicular magnetic field, which are neglected here, are needed to satisfy the solenoidal constraint. The parallel magnetic field is assumed constant and the fluctuations are divergence-free.

Since parallel magnetic fluctuations are of higher order, the magnitude of the parallel velocity,  $v_z$ , can be found by looking at the  $z$  component of the momentum equation, Equation (2.17a),

$$\begin{aligned}\left( \frac{\partial}{\partial t} + \mathbf{v} \cdot \nabla \right) v_z &= j_{\perp} B_{\perp} - \frac{\partial p}{\partial z}, \\ \Rightarrow \varepsilon_{\text{strauss}} v_z &\approx \varepsilon_{\text{strauss}}^3, \quad \Rightarrow \quad v_z \approx \varepsilon_{\text{strauss}}^2.\end{aligned}$$

This shows  $v_z \lll v_{\perp}$ , analogous to the parallel magnetic field, and so no parallel flow is assumed:  $v_z = 0$ .

The induction equation, Equation (2.17c), can be integrated by substituting Equation (3.2) to get

$$\frac{\partial \mathbf{A}}{\partial t} = \mathbf{v}_{\perp} \times \mathbf{B} + \nabla U, \quad (3.3)$$

where  $U$  is a gauge potential. Next, the perpendicular components of Equation (3.3) are considered. Since  $\frac{\partial \delta B_z}{\partial t} = \frac{\partial \nabla \times \mathbf{A}_{\perp}}{\partial t} \approx \varepsilon_{\text{strauss}}^3$  it follows that  $\frac{\partial \mathbf{A}_{\perp}}{\partial t} \approx \varepsilon_{\text{strauss}}^3$ . This term is small and henceforth neglected. Therefore the perpendicular components of Equation (3.3) are

$$\frac{\partial \mathbf{A}_{\perp}}{\partial t} \approx 0 = -B_z \mathbf{v}_{\perp} + \nabla U \times \hat{\mathbf{e}}_z, \quad (3.4)$$

$$\begin{aligned}\Rightarrow -B_z \mathbf{v}_{\perp} &= -\nabla U \times \hat{\mathbf{e}}_z, \\ \Rightarrow \mathbf{v}_{\perp} &= \nabla \phi \times \hat{\mathbf{e}}_z, \quad \phi = \frac{U}{B_z}.\end{aligned}\quad (3.5)$$

where  $\phi$  is a stream function for  $\mathbf{v}$ . This results in the velocity field being incompressible

simply due to the fact that the perpendicular components of the induction equation are neglected.

To find an equation describing the dynamics of the perpendicular magnetic field, Equation (3.5) and a vector identity are used in the  $z$  component of Equation (3.3) which gives

$$\begin{aligned}\frac{\partial A}{\partial t} &= \nabla \phi \cdot (\nabla A \times \hat{\mathbf{z}}) + B_z \frac{\partial \phi}{\partial z}, \\ &= \nabla U \cdot \mathbf{B}.\end{aligned}\tag{3.6}$$

This equation can also be written as

$$\frac{\partial A}{\partial t} = -\mathbf{v} \cdot \nabla A + B_z \frac{\partial \phi}{\partial z}.\tag{3.7}$$

The final form of the RMHD induction equation is taken to be Equation (3.6).

Using Equation (3.2) the current is

$$\mathbf{j} = -\nabla^2 A \hat{\mathbf{e}}_z + \frac{\partial}{\partial z} \nabla_{\perp} A + \nabla B_z \times \hat{\mathbf{e}}_z.$$

Substituting the current into the momentum equation, Equation (2.17a),

$$\frac{d\mathbf{v}}{dt} = \left( -\nabla^2 A \hat{\mathbf{e}}_z + \frac{\partial}{\partial z} \nabla A + \nabla B_z \times \hat{\mathbf{e}}_z \right) \times (\nabla A \times \hat{\mathbf{e}}_z + B_z \hat{\mathbf{e}}_z) - \nabla p.$$

Using a vector identity and taking each term in turn gives

$$\begin{aligned}(-\nabla_{\perp}^2 A \hat{\mathbf{e}}_z) \times (\nabla A \times \hat{\mathbf{e}}_z) &= -\nabla_{\perp}^2 A \nabla_{\perp} A, \\ \frac{\partial}{\partial z} \nabla A \times B_z \hat{\mathbf{e}}_z &= B_z \frac{\partial}{\partial z} \nabla A \times \hat{\mathbf{e}}_z, \\ (\nabla B_z \times \hat{\mathbf{e}}_z) \times B_z \hat{\mathbf{e}}_z &= -\frac{1}{2} \nabla B_z^2.\end{aligned}$$

The momentum equation can be written as

$$\frac{d\mathbf{v}}{dt} = -\nabla_{\perp}^2 A \nabla_{\perp} A + B_z \frac{\partial}{\partial z} \nabla_{\perp} A \times \hat{\mathbf{e}}_z - \nabla_{\perp} \left( p + \frac{1}{2} B_z^2 \right).\tag{3.8}$$

Next, taking the curl of the velocity to give the vorticity as

$$\begin{aligned}\nabla \times \mathbf{v} &= \nabla \times (\nabla \phi \times \hat{\mathbf{e}}_z), \\ &= -\nabla^2 \phi.\end{aligned}\tag{3.9}$$

The equation for vorticity is found by taking the curl of Equation (3.8), giving

$$-\frac{\partial}{\partial t} \nabla_{\perp}^2 \phi - \mathbf{v} \cdot \nabla_{\perp} \nabla_{\perp}^2 \phi = -\nabla \times (\nabla_{\perp}^2 \nabla_{\perp} A) + \nabla \times \left( B_z \frac{\partial}{\partial z} \nabla_{\perp} A \right).\tag{3.10}$$

Taking each term in turn gives

$$\begin{aligned}\nabla \times (\nabla_{\perp}^2 A \nabla_{\perp} A) &= \mathbf{B}_{\perp} \cdot \nabla_{\perp} \nabla_{\perp}^2 A, \\ B_z \nabla \times \left( \frac{\partial}{\partial z} \nabla_{\perp} A \times \hat{\mathbf{e}}_z \right) &= -B_z \frac{\partial}{\partial z} \nabla_{\perp}^2 A.\end{aligned}$$

The resulting equation for vorticity is

$$\frac{\partial}{\partial t} \nabla_{\perp}^2 \phi + \mathbf{v} \cdot \nabla_{\perp} \nabla_{\perp}^2 \phi = \mathbf{B} \cdot \nabla \nabla_{\perp}^2 A. \quad (3.11)$$

This is the final form of the RMHD momentum equation.

### Summary

In summary the equations of RMHD in terms of potentials  $A$  and  $U$  have the form

$$\frac{\partial A}{\partial t} = \mathbf{B} \cdot \nabla \phi, \quad (3.12a)$$

$$\frac{\partial}{\partial t} \nabla_{\perp}^2 \phi + \mathbf{v} \cdot \nabla \nabla_{\perp}^2 \phi = \mathbf{B} \cdot \nabla \nabla_{\perp}^2 A, \quad (3.12b)$$

$$\nabla_{\perp} \cdot \mathbf{v} = 0, \quad \nabla_{\perp} \cdot \mathbf{B} = 0, \quad (3.12c)$$

where  $B_z = B_0 \hat{\mathbf{e}}_z$  and  $v_z = 0$ .  $A$  is the  $z$  component of the vector potential, and  $\phi$  is the velocity stream function.

$$\mathbf{B} = \nabla_{\perp} A \times \hat{\mathbf{e}}_z + B_z \hat{\mathbf{e}}_z, \quad \mathbf{v} = \nabla_{\perp} \phi \times \hat{\mathbf{e}}_z.$$

Two similar derivations by Zank and Matthaeus (Zank and Matthaeus 1992) and Montgomery (Montgomery 1982) are summarised in the next sections.

### 3.3.2 Zank and Matthaeus' RMHD Equations

Strauss' form of the RMHD equations, Equation (3.12), in terms of potentials, clearly displays the simplicity of the equations compared to full MHD. However it is potentially conceptually easier to understand the equations in terms of fields. Zank and Matthaeus 1992 use a different approach to derive the RMHD equations, from the compressible ideal MHD equations, Equations (2.17), in terms of the velocity and magnetic fields. A summary of the equations is given here, full details of their derivation are given in Appendix A.1.

Their RMHD equations are given by

$$\begin{aligned}\nabla_{\mathbf{x}} \cdot \mathbf{v} &= 0, & \nabla_{\mathbf{x}} \cdot \mathbf{B} &= 0, & \mathbf{x} &= (x, y), \\ \frac{\partial \mathbf{v}}{\partial t} + (\mathbf{v} \cdot \nabla_{\mathbf{x}}) \mathbf{v} &= -\nabla_{\mathbf{x}} p - \frac{1}{2} \nabla_{\mathbf{x}} (\mathbf{B}^2) + (\mathbf{B} \cdot \nabla_{\mathbf{x}}) \mathbf{B} + \frac{B_0}{\varepsilon_{zm}} \frac{\partial}{\partial z} \mathbf{B}, \\ \frac{\partial \mathbf{B}}{\partial t} + (\mathbf{v} \cdot \nabla_{\mathbf{x}}) \mathbf{B} &= \frac{B_0}{\varepsilon_{zm}} \frac{\partial}{\partial z} \mathbf{v} + (\mathbf{B} \cdot \nabla_{\mathbf{x}}) \mathbf{v}, \\ \frac{\partial p}{\partial z} &= -\frac{1}{2} \frac{\partial \mathbf{B}^2}{\partial z},\end{aligned}$$

where  $\mathbf{B} = (B_x(x, y, z, t), B_y(x, y, z, t))$  and  $\mathbf{v} = (v_x(x, y, z, t), v_y(x, y, z, t))$ . The Alfvén mach number,  $M_A$ , is the small parameter,  $\varepsilon_{zm}$ , given by

$$M_A = \frac{v_0^2}{V_A^2} = \frac{\mu v_0^2 \rho_0}{B_0^2}. \quad (3.13)$$

In the limit that quantities do not depend on the parallel coordinate,  $z$ , these equations are equivalent to the equations of 2D incompressible MHD, Equations (2.18). The parallel components,  $B_z = v_z = 0$ .

### 3.3.3 Montgomery's RMHD Equations

Montgomery 1982 derives the equations of RMHD from the incompressible MHD equations, Equations (2.18), including dissipation terms. Here the equations are stated, full details of their derivation are given in Appendix A.2

The equations for the perpendicular components are

$$\begin{aligned}\frac{\partial \mathbf{v}_{\perp}}{\partial t} + \mathbf{v}_{\perp} \cdot \nabla_{\perp} \mathbf{v}_{\perp} &= -\nabla_{\perp} p + \mathbf{B}_{\perp} \cdot \nabla_{\perp} \mathbf{B}_{\perp} + B_0 \frac{\partial \mathbf{B}_{\perp}}{\partial (\varepsilon_m z)} + \nu \nabla_{\perp}^2 \mathbf{v}_{\perp}, \\ \frac{\partial \mathbf{B}_{\perp}}{\partial t} + \mathbf{v}_{\perp} \cdot \nabla_{\perp} \mathbf{B}_{\perp} &= \mathbf{B}_{\perp} \cdot \nabla_{\perp} \mathbf{v}_{\perp} + B_0 \frac{\partial \mathbf{v}_{\perp}}{\partial (\varepsilon_m z)} + \eta \nabla_{\perp}^2 \mathbf{B}_{\perp},\end{aligned}$$

where the ratio of the background field to the fluctuations

$$\varepsilon_m = \frac{b}{B_0}, \quad (3.14)$$

is the small parameter used.

Their derivation is different from Strauss' and Zank and Matthaeus' in the previous two sections since the parallel components are not assumed zero and are evolved by

$$\begin{aligned}\frac{\partial v_z}{\partial t} + \mathbf{v}_{\perp} \cdot \nabla_{\perp} v_z &= \mathbf{B}_{\perp} \cdot \nabla_{\perp} B_z + B_0 \frac{\partial B_z}{\partial z} + \nu \nabla_{\perp}^2 v_z, \\ \frac{\partial B_z}{\partial t} + \mathbf{v}_{\perp} \cdot \nabla_{\perp} B_z &= \mathbf{B}_{\perp} \cdot \nabla_{\perp} v_z + B_0 \frac{\partial v_z}{\partial z} + \eta \nabla_{\perp}^2 B_z.\end{aligned}$$

These equations only involve coefficients of the perpendicular components. This means

that parallel fluctuations evolve passively, called “passive scalars” and do not affect the evolution of the perpendicular dynamics.

### 3.3.4 Discussion

In this section we show the equivalence between the three derivations of the RMHD equations discussed in the previous sections, Section 3.3.1, Section 3.3.2, Section 3.3.3 and presented in Strauss (1976), Zank and Matthaeus 1992 and Montgomery 1982, respectively. A substantial amount of work has been done to understand and clarify the assumptions and properties of RMHD in the two review articles by Sean Oughton et al (Oughton, Dmitruk, and Matthaeus 2003, Oughton, Matthaeus, and Dmitruk 2017). The arguments given in this section were first discussed in these reviews.

As shown in Oughton, Dmitruk, and Matthaeus 2003; Oughton, Matthaeus, and Dmitruk 2017 the three assumptions of RMHD are, namely, i)  $B_0^2 \gg b^2$ , ii) length-scale/spectral anisotropy:  $k_\perp \gg k_\parallel$ , and iii) variance anisotropy:  $b_z = v_z = 0$ . The first two naturally provide a small parameter to expand the full compressible (or incompressible) MHD equations. Considering the first assumption leads to the small parameter,  $\varepsilon_m$ , in Equation (3.14), used in Montgomery’s derivation. Consideration of the inverse of the large aspect ratio leads to the parameter,  $\varepsilon_{\text{strauss}}$ , as in Equation (3.1), used in Strauss’ original derivation, which is analogous to the second assumption. Zank and Matthaeus chose the Alfvén mach number as the small parameter,  $\varepsilon_{zm}$ , given in Equation (3.13), in their derivation, which does not immediately reflect an assumption of RMHD. In each case the other assumption(s) was (were) implied but not specifically defined. Each of these derivations provides the same equations for the perpendicular fields regardless of which small parameter is chosen. It follows that there must be a natural relation between these three parameters.  $\varepsilon_{zm}$  is equivalent to  $\varepsilon_m$  since the typical velocity fluctuations in Alfvén units, are assumed to be the same order as the magnetic fluctuations  $\delta v \sim \delta b$ .

It follows that there are two small parameters that describe the assumptions of RMHD. These are renamed as  $\varepsilon_a$  and  $\varepsilon_b$ , which will be used in the formal derivation of RMHD in Section 3.4.1.

$$\text{inverse aspect ratio: } \varepsilon_b \sim \varepsilon_{\text{strauss}} = \frac{L_\perp}{L_\parallel},$$

$$\text{ratio of fluctuations to background field: } \varepsilon_a = \varepsilon_m = \frac{\delta b}{B_0},$$

An important, but subtle, aspect of these small parameters:  $\varepsilon_a$  and  $\varepsilon_b$ , is that they are not independent of each other and it is not enough for each of them to be less than one individually, as  $\varepsilon_a \ll 1$  and  $\varepsilon_b \ll 1$ . The timescale condition for RMHD requires that the nonlinear time,  $\tau_{NL} \approx \frac{l_\perp}{|\mathbf{b}|}$ , is faster than the Alfvén time,  $\tau_A \approx \frac{l_\parallel}{B_0}$ . This relation can be rearranged to give

$$\tau_{NL} \leq \tau_A, \quad \Rightarrow \quad \frac{l_\perp}{|\mathbf{b}|} \leq \frac{l_\parallel}{B_0}, \quad \Rightarrow \quad \frac{l_\perp}{l_\parallel} \leq \frac{|\mathbf{b}|}{B_0}, \quad \Rightarrow \quad \varepsilon_b \leq \varepsilon_a \ll 1$$

Equivalently, in wavenumber space, with  $k = 2\pi l^{-1}$ , these quantities are defined as

$$\tau_A(\mathbf{k}) = \frac{1}{\mathbf{k} \cdot \mathbf{B}_0} = \frac{1}{|k_{\parallel}| |B_0|}, \quad \tau_{nl}(\mathbf{k}) = \frac{1}{k b_{\perp}(\mathbf{k})}, \quad \varepsilon_a = \frac{b_{\perp}(\mathbf{k})}{B_0}, \quad \varepsilon_b = \frac{k_{\parallel}}{k_{\perp}}, \quad (3.15)$$

where  $\tau_A(\mathbf{k})$  is called the Alfvén wave timescale and is defined as the time for a wave to travel a wavelength,  $k^{-1}$ , for the wavenumber. This Alfvén time is dependent on the wavevector  $\mathbf{k}$  and so is different for each wavevector. There is an important difference between the two Alfvén time definitions:  $\tau_A$  and  $\tau_A(\mathbf{k})$ . The first is the time it takes for an Alfvén wave to travel the parallel length of the box, and the second is the time taken for the Alfvén wave to travel a wavelength.

An important aspect is the value of the plasma  $\beta$ . The leading order equations for the perpendicular fluctuations remain the same regardless of this parameter, however the parallel fluctuations are zero for  $\beta \ll 1$  but may exist for larger values. Since our focus here is in the solar corona this discussion is mostly restricted to the  $\beta \ll 1$  limit.

It is important to emphasise that although Strauss does indeed define the inverse aspect ratio to be small this really means the ratio of the characteristic lengthscales rather than the physical length and width of the system. There is an important distinction between these lengthscales. In the limit of an infinite  $B_0$ , the Alfvén time becomes infinitely long,  $\tau_A \rightarrow \infty$ , which to satisfy the RMHD inequality requires the wavelength to become infinitely small,  $l_{\parallel} \rightarrow \infty$  ( $k_{\parallel} \rightarrow 0$ ). This means it will take an Alfvén wave with zero wavelength an infinite amount of time to travel a distance equal to its wavelength, hence the long-wavelength Alfvén waves that connect the infinite 2D planes of RMHD can no longer propagate. This reiterates the 2D nature of this model as emphasised by Zank and Matthaeus 1992.

In summary, in order to make the assumptions of RMHD a key feature of the derivation, both small parameters,  $\varepsilon_a$  and  $\varepsilon_b$ , are needed. This approach was taken by Oughton, Matthaeus, and Dmitruk 2017. A similar derivation is given in the next section.

### 3.4 RMHD Model

In this section, we demonstrate how certain assumptions can be applied to the full dissipative limit of the compressible MHD equations, Equations (2.16), derived in Section 2.4, to derive the equations of RMHD. This model retains some of the nonlinearity of the full MHD equations but is considerably computationally easier to solve. The aim here is to clearly present, from first principles, the necessary assumptions, and their consequences, to arrive at the equations of RMHD for a low  $\beta$  system. We present a derivation of RMHD in Section 3.4.1 and discuss some related features of the equations in Section 3.4.2 and Section 3.4.3. Where possible these are compared and contrasted to the equivalent relations in full MHD.

### 3.4.1 RMHD: Derivation

We now present a derivation of RMHD following the same method as in Oughton, Matthaeus, and Dmitruk 2017. In this section we consider a plasma in equilibrium with uniform density,  $\rho_0$ , pressure  $p_0$  and uniform background magnetic field,  $\mathbf{B}_0$ . The first assumption is that the background field is large and aligned with the  $z$  direction  $B_0 \hat{\mathbf{e}}_z$ . In this context the term “large” means that the energy in the background field is much larger than that of the fluctuations of the magnetic field,  $\mathbf{b}$ , as  $B_0^2 \gg \mathbf{b}^2$ . A small parameter,  $\varepsilon_a$ , is defined as

$$\varepsilon_a = \frac{|\mathbf{b}|}{B_0} \ll 1 \quad (3.16)$$

where the background field strength,  $|\mathbf{B}_0| = B_0$ , is used. Since  $\varepsilon_a$  depends on the strength of the background field,  $B_0$ , it can be thought of as a measure of how strong the field is. Thus, the larger  $\mathbf{B}_0$  is the smaller  $\varepsilon_a$ .

It is common to expand the fluctuations of velocity,  $\mathbf{v}$ , magnetic field,  $\mathbf{b}$  and pressure  $p$  in powers of  $\varepsilon_a$  using a linear expansion as

$$\mathbf{B}_0 + \mathbf{b} = \mathbf{B}_0 + \varepsilon_a \mathbf{b} + \varepsilon_a^2 \mathbf{b}_1 \cdots,$$

$$\mathbf{v} = \varepsilon_a \mathbf{v} + \varepsilon_a^2 \mathbf{v}_1 \cdots,$$

$$p = p_0 + \varepsilon_a p + \varepsilon_a^2 p_1 \cdots.$$

$$\rho = \rho_0 + \varepsilon_a \rho + \varepsilon_a^2 \rho_1 \cdots.$$

However a linear expansion separates the linear and nonlinear dynamics. Nonlinear terms, such as  $\mathbf{b} \cdot \nabla \mathbf{b}$ , will be considered less important, since they are  $O(\varepsilon_a^2)$ , compared to linear terms, such as  $\mathbf{B}_0 \cdot \nabla \mathbf{b}$ , which are  $O(\varepsilon_a)$ .

Our aim is to derive a set of equations that are simpler than the full MHD equations but retain some of the inherent nonlinearity. We wish to keep the fluctuations and nonlinear terms of  $O(1)$ . To do this we can rescale our variables. For example the background field can be rescaled as  $\mathbf{B}'_0 = \mathbf{B}_0 \varepsilon_a$ . Thus the expansion that will be used here is

$$\mathbf{B}_0 + \mathbf{b} = \frac{\mathbf{B}'_0}{\varepsilon_a} + \mathbf{b}' + \varepsilon_a \mathbf{b}'_1 \cdots,$$

$$\mathbf{v} = \mathbf{v}' + \varepsilon_a \mathbf{v}'_1 \cdots,$$

$$p = \frac{p'_0}{\varepsilon_a} + p' + \varepsilon_a p'_1 \cdots,$$

$$\rho = \frac{\rho'_0}{\varepsilon_a} + \rho' + \varepsilon_a \rho'_1 \cdots.$$

The primed quantities with no subscript are  $O(1)$  and a subscript “1” denotes quantities of  $O(\varepsilon_a)$ . As mentioned, this expansion allows the nonlinear and linear terms for the fluctuations to be the same order. A second advantage of this ordering is that as  $B_0 \rightarrow \infty$ ,  $\varepsilon_a \rightarrow 0$  and the leading order fluctuations remain of  $O(1)$  whereas in the linear expansion they would go to zero.

Another simplification that can be made when focusing on nonlinear effects is to

eliminate any high frequency waves. This requires two further assumptions. First, consider Alfvén and slow magnetoacoustic waves, whose anisotropic dispersion relations were found to be  $\omega_A = \pm k_{\parallel} V_A$  where the wavenumber  $k_{\parallel}$  is parallel to the background magnetic field  $\mathbf{B}_0$ . In order to ensure the wave frequencies,  $\omega$ , are small we must restrict the value of the parallel wavenumber,  $k_{\parallel}$ , to be small. There is no restriction on the perpendicular wavenumber. This gives low frequency, long wavelength waves along the magnetic field. This is required by  $k_{\parallel} \ll k_{\perp}$ . Thus the second assumption is spectral anisotropy, or equivalently lengthscale anisotropy as  $l_{\perp} \ll l_{\parallel}$ . The requirement of lengthscale anisotropy motivates the definition of a second small parameter,  $\varepsilon_b$ , as

$$\varepsilon_b = \frac{l_{\perp}}{l_{\parallel}} \ll 1, \quad (3.17)$$

where  $l_{\parallel}$  and  $l_{\perp}$  are characteristic lengthscales along  $\mathbf{B}_0$  and perpendicular to it, respectively. This is equivalent to the inverse aspect ratio if  $l_{\parallel}$  and  $l_{\perp}$  are the system sizes. Second, fast magnetoacoustic waves have a nearly isotropic dispersion relation. In order to eliminate high frequency fast waves variance anisotropy must be imposed. This is the third and final assumption for RMHD. Variance anisotropy results in the magnetic and velocity fluctuations being perpendicular to the background field,  $\mathbf{B}_0$ ,  $v'_z = b'_z = 0$ . It should also be noted that this requirement removes all fast waves, including low frequencies. This condition can be written mathematically as  $\mathbf{B}_0 \cdot \mathbf{v}' = \mathbf{B}_0 \cdot \mathbf{b}' = 0$ .

To summarise the three assumptions of RMHD, given in Oughton, Matthaeus, and Dmitruk 2017, are

- (i) A strong background magnetic field: The magnetic energy associated with the background magnetic field,  $\mathbf{B}_0 = B_0 \hat{\mathbf{e}}_z$ , is much larger than the magnetic energy associated with the perturbed field,  $\mathbf{b}$ , as  $B_0^2 \gg \mathbf{b}^2$ . This can be expressed, using the small parameter,  $\varepsilon_a$  in Equation (3.16).
- (ii) Spectral/lengthscale anisotropy: Derivatives parallel to  $\mathbf{B}_0$  are smaller than derivatives perpendicular to  $\mathbf{B}_0$ . This can be expressed, using the small parameter,  $\varepsilon_b$ , in Equation (3.17).
- (iii) Variance anisotropy: There are no components parallel to  $\mathbf{B}_0$ . This is expressed as  $\mathbf{v} \cdot \mathbf{B}_0 = \mathbf{b} \cdot \mathbf{B}_0 = 0$ .

The two small parameters,  $\varepsilon_a$  and  $\varepsilon_b$ , are not independent of each other. It is not enough for each of the inequalities to be satisfied individually. The fastest timescale left after removing high frequency waves is the Alfvén time,  $\tau_A \approx \frac{l_{\parallel}}{B_0}$ , and we are interested in dynamics occurring on nonlinear timescales,  $\tau_{NL} \approx \frac{l_{\perp}}{|\mathbf{b}|}$ . Thus nonlinear processes must occur on timescales shorter or equal to the Alfvén time. This can be written as

$$\tau_{NL} \leq \tau_A \quad \Rightarrow \quad \frac{l_{\perp}}{|\mathbf{b}|} \leq \frac{l_{\parallel}}{B_0} \quad \Rightarrow \quad \frac{l_{\perp}}{l_{\parallel}} \leq \frac{|\mathbf{b}|}{B_0} \quad \Rightarrow \quad \varepsilon_b \leq \varepsilon_a \ll 1.$$

Since we have imposed spectral anisotropy, we need to take into account that the parallel direction may be “slowly varying”: derivatives in  $z$  are small, i.e.  $\frac{\partial}{\partial z} \approx \varepsilon_b \frac{\partial}{\partial z'}$ . Thus we



take a “slowly varying” parallel coordinate  $z' = \varepsilon_b z$ . In general, there are dynamics occurring on fast timescales, measured by the Alfvén time,  $\tau_A$ , corresponding to large time derivatives. As a final constraint to filter out these fast variations produced by high frequency waves we define a fast timescale,  $t'$ , as a rescaled time coordinate,  $t' = \frac{t}{\varepsilon_a}$ . This gives a large derivative as  $\frac{\partial}{\partial t} \approx \frac{1}{\varepsilon_a} \frac{\partial}{\partial t'}$ . We use the small parameter  $\varepsilon_a$  since  $\tau_A$  depends on the strength of  $B_0$ . Derivatives with respect to  $t'$  are set to zero,  $(\frac{\partial}{\partial t'} = 0)$  to completely remove fluctuations on this fast timescale.

Initially all quantities are assumed functions of the three unscaled spatial and time coordinates and the scaled parallel and time coordinates as  $(x, y, z, z', t, t')$ . Expanding the dissipative induction equation, Equation (2.16c), and keeping terms up  $O(1)$  gives

$$\frac{\partial \mathbf{b}'_{\perp}}{\partial t} = \nabla \times \left( \mathbf{v}'_{\perp} \times \frac{\mathbf{B}'_0}{\varepsilon_a} \right) + \nabla \times (\mathbf{v}'_{\perp} \times \mathbf{b}'_{\perp}) + \eta \nabla_{\perp}^2 \mathbf{b}'_{\perp}. \quad (3.18)$$

The  $O(\varepsilon_a^{-1})$  term gives one perpendicular term and one parallel term. These are

$$\nabla \times \left( \mathbf{v}'_{\perp} \times \frac{\mathbf{B}'_0}{\varepsilon_a} \right) = \left( \frac{B'_0}{\varepsilon_a} \frac{\partial}{\partial z} \right) \mathbf{v}'_{\perp} - (\nabla_{\perp} \cdot \mathbf{v}'_{\perp}) \frac{\mathbf{B}'_0}{\varepsilon_a}.$$

The LHS of this equation is zero. Perpendicular components indicate that the velocity fluctuations are independent of  $z$ , the unscaled coordinate along the parallel direction. The component of this equation along  $\mathbf{B}_0$  implies the velocity is incompressible perpendicular to  $\mathbf{B}_0$ .

The  $O(1)$  terms from Equation (3.18) is the RMHD induction equation

$$\frac{\partial \mathbf{b}'_{\perp}}{\partial t} + (\mathbf{v}'_{\perp} \cdot \nabla_{\perp}) \mathbf{b}'_{\perp} = (\mathbf{b}'_{\perp} \cdot \nabla_{\perp}) \mathbf{v}'_{\perp} + \left( \frac{B'_0}{\varepsilon_a} \right) \left( \varepsilon_b \frac{\partial}{\partial z'} \right) \mathbf{v}'_{\perp} + \eta \nabla_{\perp}^2 \mathbf{b}'_{\perp}. \quad (3.19)$$

Similarly, expanding the equation of motion, Equation (2.16a), and keeping terms up to  $O(1)$  gives

$$\frac{\partial \mathbf{v}'_{\perp}}{\partial t} + (\mathbf{v}'_{\perp} \cdot \nabla) \mathbf{v}'_{\perp} = -\nabla (p + |\mathbf{b}'_{\perp}|^2) + (\nabla \times \mathbf{b}'_{\perp}) \times \frac{\mathbf{B}'_0}{\varepsilon_a} + (\mathbf{b}'_{\perp} \cdot \nabla_{\perp}) \mathbf{b}'_{\perp} + \nu \nabla_{\perp}^2 \mathbf{v}'_{\perp}. \quad (3.20)$$

The only  $O(\varepsilon_a^{-1})$  contribution from Equation (3.20) is in the second term on the RHS as

$$\frac{B'_0}{\varepsilon_a} \frac{\partial \mathbf{b}'_{\perp}}{\partial z} = 0. \quad (3.21)$$

This shows that the perpendicular magnetic fluctuations are also independent of the unscaled  $z$  coordinate. The  $O(1)$  terms in Equation (3.20) give the equation of motion for RMHD as

$$\frac{\partial \mathbf{v}'_{\perp}}{\partial t} + (\mathbf{v}'_{\perp} \cdot \nabla) \mathbf{v}'_{\perp} = -\nabla (p + |\mathbf{b}'_{\perp}|^2) + \left( \frac{B'_0}{\varepsilon_a} \right) \left( \varepsilon_b \frac{\partial}{\partial z'} \right) \mathbf{b}'_{\perp} + (\mathbf{b}'_{\perp} \cdot \nabla_{\perp}) \mathbf{b}'_{\perp} + \nu \nabla_{\perp}^2 \mathbf{v}'_{\perp}. \quad (3.22)$$

Equations (3.19) and (3.22) make up the main equations of RMHD. The term

$$\left(\frac{B'_0}{\varepsilon_a}\right) \left(\varepsilon_b \frac{\partial}{\partial z'}\right),$$

that is present in both of these equations explicitly contains both small parameters,  $\varepsilon_a$  and  $\varepsilon_b$ . This is to make the magnitude of these terms clear. This term consists of the very large magnetic field and the very small slowly varying parallel derivative. These two extremes at most cancel and the magnitude of this term is  $O(1)$ . The chosen scaling makes this apparent. If we now substitute for  $B_0$  and  $z$ , which are the physical variables, this is simply

$$B_0 \frac{\partial}{\partial z}.$$

In this case it is not clear whether this term is large or small. This is the only term that contains the background field or small parallel variations. Physically this term is related to the low frequency Alfvén waves that remain, travelling along the  $z$  direction. Thus, as emphasised in Zank and Matthaeus 1992, these waves connect the otherwise independent 2D planes of MHD. Without this term Equation (3.19) and Equation (3.22) are equivalent to 2D incompressible MHD.

The total pressure can be found by taking the divergence of the RMHD equation of motion, Equation (3.22), since  $\mathbf{v}'_{\perp}$  is incompressible, to give

$$\nabla_{\perp}^2 (p + |\mathbf{b}'_{\perp}|^2) = \nabla_{\perp} (\mathbf{b}'_{\perp} \cdot \nabla_{\perp} \mathbf{b}'_{\perp}) - \nabla_{\perp} (\mathbf{v}'_{\perp} \cdot \nabla_{\perp} \mathbf{v}'_{\perp}). \quad (3.23)$$

In summary the RMHD equations are given by

$$\frac{\partial \mathbf{b}'_{\perp}}{\partial t} + (\mathbf{v}'_{\perp} \cdot \nabla_{\perp}) \mathbf{b}'_{\perp} = (\mathbf{b}'_{\perp} \cdot \nabla_{\perp}) \mathbf{v}'_{\perp} + \left(\frac{B'_0}{\varepsilon_a}\right) \left(\varepsilon_b \frac{\partial}{\partial z'}\right) \mathbf{v}'_{\perp} + \eta \nabla_{\perp}^2 \mathbf{b}'_{\perp}. \quad (3.24a)$$

$$\begin{aligned} \frac{\partial \mathbf{v}'_{\perp}}{\partial t} + (\mathbf{v}'_{\perp} \cdot \nabla) \mathbf{v}'_{\perp} &= -\nabla (p + |\mathbf{b}'_{\perp}|^2) \\ &+ \left(\frac{B'_0}{\varepsilon_a}\right) \left(\varepsilon_b \frac{\partial}{\partial z'}\right) \mathbf{b}'_{\perp} + (\mathbf{b}'_{\perp} \cdot \nabla_{\perp}) \mathbf{b}'_{\perp} + \nu \nabla_{\perp}^2 \mathbf{v}'_{\perp}. \end{aligned} \quad (3.24b)$$

These two equations are much simpler than the full MHD equations, Equation (2.16). In these equations there are only four unknowns compared to eight in full MHD.

The simplicity of the RMHD equations is made even more evident when using magnetic and velocity potentials:  $\mathbf{b}_{\perp} = \nabla_{\perp} A \times \hat{\mathbf{e}}_z$  and  $\mathbf{v}_{\perp} = \nabla_{\perp} \phi \times \hat{\mathbf{e}}_z$ , as done in Section 3.3.1, Equations (3.12).

The appealing aspect of RMHD is that these equations only involve two scalars:  $\phi$  and  $A$ , whereas the MHD equations involve eight unknown quantities. Solving the RMHD equations requires significantly less computational resources compared to solving the full MHD equations, however, since this is a considerable simplification, RMHD cannot contain all of the features of full MHD.

In the next section, the conservation laws in RMHD are compared to full MHD.

### 3.4.2 RMHD: Conservation Laws

Here we state the conserved quantities in RMHD and highlight the similarities and differences from full 3D and 2D MHD. A detailed discussion of this can be found in Oughton, Matthaeus, and Dmitruk 2017.

The total energy and cross helicity in RMHD are

$$E = \int \frac{1}{2}(|\mathbf{v}'|^2 + |\mathbf{b}'|^2)dV,$$

$$H_c = \int \mathbf{v}' \cdot \mathbf{b}'dV.$$

Conservation of the total energy of the fluctuations, in the ideal case, is the same as for full MHD, except for a few important simplifications. RMHD only involves perpendicular components of the magnetic and velocity fields. The internal energy is not considered so the effects of viscous and ohmic heating cannot be taken into account. A further consequence of this is that no additional thermodynamic effects, such as thermal conduction and radiation, can be considered. The cross helicity,  $H_m$ , is a conserved quantity as in full MHD. If magnetic fluctuations are written as  $\mathbf{b}'_{\perp} = \nabla_{\perp} \times (\mathbf{A}e_z)$ , where  $\mathbf{A}$  is the magnetic vector potential, the magnetic helicity is trivially conserved in RMHD, as

$$H_m = \int \mathbf{A} \cdot \mathbf{B}_0 dV = B_0 \int \mathbf{A} dV = 0,$$

where the second equality comes from  $B_0$  being constant. The magnetic helicity is a proper conserved quantity in full 3D MHD. The quantity  $\int dV A_z^2$  is conserved in 2.5D MHD but not in either 3D MHD or RMHD.

In the next section, additional properties of the RMHD equations are presented.

### 3.4.3 RMHD: Properties

In the following sections, we will discuss several properties of the RMHD equations. Many of these properties were presented in Oughton, Matthaeus, and Dmitruk 2017. These properties highlight unusual characteristics that are specific to RMHD, including conservation of Elsässer energy in 2D planes. It will also be shown that RMHD fluctuations are toroidally polarised. An interesting similarity of the equation for RMHD equilibria to Euler's equation is discussed.

#### RMHD: Conservation of Elsässer Energies

It is occasionally useful, when discussing literature related to RMHD, to consider the MHD and RMHD equations in terms of fluctuations that travel parallel or antiparallel to the magnetic field. This can be achieved by using the Elsässer fields:  $\mathbf{z}_{\pm} = \mathbf{v} \pm \mathbf{B}$ , where the fluctuating fields are used for RMHD and the general fields for full MHD. The definition of the Elsässer fields uses the magnetic field in nondimensional units of the Alfvén speed.

The RMHD equations, Equations (3.24), in terms of the Elsässer fields are

$$\frac{\partial \mathbf{z}_{\pm}}{\partial t} \mp B_0 \frac{\partial \mathbf{z}_{\pm}}{\partial z} = -\mathbf{z}_{\mp} \cdot \nabla_{\perp} \mathbf{z}_{\pm} - \nabla_{\perp} p + \nu \nabla_{\perp}^2 \mathbf{z}_{\pm}, \quad (3.25)$$

where  $\nu = \eta$  is assumed.

The energies, defined as

$$W_{\pm}(z', t) = \frac{1}{2} \int |\mathbf{z}_{\pm}(x, y, z', t)|^2 dx dy,$$

satisfy a wave equation of the form

$$\left( \frac{\partial}{\partial t} \mp B_0 \frac{\partial}{\partial z'} \right) W_{\pm} = 0.$$

This shows that the total energy in RMHD modes is conserved for every value of the parallel coordinate,  $z'$ . When space is taken as a continuum, instead of discrete values, this provides an infinite number of invariants which are not generally present in full MHD.

The absence of these invariants in full MHD is due to the existence of parallel fluctuations in full MHD. In full 3D, incompressible MHD, the above wave equation is non-zero and the RHS is equal to

$$-\frac{\partial}{\partial z} \int dx dy z_{\pm \parallel} p \pm z_{\mp \parallel} \frac{z_{\pm \parallel}}{2}.$$

This does tend to zero in the special cases that the parallel fluctuations are zero or small or in the limit of RMHD where quantities are slowly varying in the parallel direction and a large magnetic field is present. Then these invariants are present in full 3D MHD. The energy is also conserved in time  $\int |W_{\pm}(z', t)|^n dz'$ , where  $n \geq 1$  is an integer. Due to finite computational resolution this is generally only true for  $n = 1$ .

### RMHD: Polarisation

To discuss polarisation it is useful to write the RMHD equations in wavenumber space. Fourier transforming the RMHD equations, Equation (3.25), using  $\mathbf{k} = k_{\perp} + k'_{\parallel} B_0$ .

$$\left( \frac{\partial}{\partial t} \mp i k'_{\parallel} B_0 \right) \mathbf{z}_{\pm}(\mathbf{k}) = -i \int \mathbf{z}_{\mp}(\mathbf{p}) \cdot \mathbf{q}_{\perp} \mathbf{z}_{\pm}(\mathbf{q}) dp dq - i k_{\perp} p(\mathbf{k}) - \nu k_{\perp}^2 \mathbf{z}_{\pm}(\mathbf{k}), \quad (3.26)$$

where  $\mathbf{p}$  and  $\mathbf{q}$  are wavevectors, such that  $\mathbf{k} = \mathbf{p} + \mathbf{q}$ . As we have shown in Section 2.7 there are three possible polarisations: toroidal, poloidal and longitudinal. In fourier space the velocity and magnetic fields can be decomposed into these polarisations

$$\mathbf{v} = v_T(\mathbf{k}) \hat{\mathbf{e}}_{\text{toroidal}} + v_P(\mathbf{k}) \hat{\mathbf{e}}_{\text{poloidal}} + v_{\text{longitudinal}}(\mathbf{k}) \hat{\mathbf{k}}.$$

$$\mathbf{b} = b_T(\mathbf{k}) \hat{\mathbf{e}}_{\text{toroidal}} + b_P(\mathbf{k}) \hat{\mathbf{e}}_{\text{poloidal}}.$$

Only the velocity can be longitudinally polarised. There is no longitudinal polarisation for the magnetic field since it must be incompressible. These directions can be defined similarly using the Elsässer fields as  $\mathbf{z}_{\pm} = \mathbf{z}_{\pm T} + \mathbf{z}_{\pm P}$ . Since RMHD requires incompressibility:  $\mathbf{k} \cdot \mathbf{v} = \mathbf{k} \cdot \mathbf{b} = 0$  and variance anisotropy:  $\mathbf{B}_0 \cdot \mathbf{v} = \mathbf{B}_0 \cdot \mathbf{b} = 0$  it follows that RMHD fluctuations are toroidally polarised. The RMHD equation, Equation (3.26) can be dotted with the toroidal direction, and defining  $z_{\pm \text{ RMHD}} = \mathbf{z}_{\pm} \cdot \hat{\mathbf{e}}_{\text{toroidal}}$ , becomes

$$\left( \frac{\partial}{\partial t} \mp ik'_{\parallel} \right) z_{\pm \text{ RMHD}}(\mathbf{k}) = -i \int \mathbf{z}_{\mp}(\mathbf{p}) \cdot \mathbf{q}_{\perp} \mathbf{z}_{\pm}(\mathbf{q}) \cdot \hat{\mathbf{e}}_{\text{toroidal}} dp dq - \nu k_{\perp}^2 z_{\pm \text{ RMHD}}(\mathbf{k}). \quad (3.27)$$

It is illustrative to compare this with the equation for full incompressible 3D MHD, which includes both toroidal and poloidal polarisation denoted by  $\mathbf{z}_{\pm T}$  and  $\mathbf{z}_{\pm P}$ . Longitudinal components are zero due to the assumption of incompressibility. Setting the poloidal component to zero, the toroidal polarisation gives the equation for full MHD

$$\left( \frac{\partial}{\partial t} \mp ik_{\parallel} B_0 \right) \mathbf{z}_{\pm T}(\mathbf{k}) = -i \int \mathbf{z}_{\mp T}(\mathbf{p}) \cdot \mathbf{q}_{\perp} \mathbf{z}_{\pm T}(\mathbf{q}) \cdot \hat{\mathbf{e}}_T dp dq - \nu k^2 \mathbf{z}_{\pm T}(\mathbf{k}). \quad (3.28)$$

The important differences between Equation (3.28) for full MHD and Equation (3.27) for RMHD are that in the former the dissipation terms include parallel dissipation and there is no restriction to the size of  $B_0$  compared to the fluctuating fields, nor to variations along the parallel direction. These equations are deceptively similar and these differences could make a big difference to the dynamics and evolution.

#### RMHD: Relation to Euler's Equation

Just as in full MHD, an important topic is equilibria. In the case of RMHD equilibria there is an interesting similarity between the RMHD equations and Euler's equation in hydrodynamics. This analogy has been discussed in a few articles (van Ballegooijen 1985, Rappazzo 2015). The latter will be followed here.

Setting  $\frac{\partial}{\partial t} = 0$  and  $\mathbf{v} = 0$  in Equations (3.24) gives the RMHD equation for equilibria

$$\mathbf{B} \cdot \nabla j_{\parallel} = 0. \quad (3.29)$$

Note only the current component parallel to  $\mathbf{B}_0$  is present in RMHD. Expanding the magnetic field as  $\mathbf{B}_0 + \mathbf{b}$  and rearranging, Equation (3.29) gives

$$\frac{\partial j_{\parallel}}{\partial z} + \frac{\mathbf{b}}{B_0} \cdot \nabla_{\perp} j_{\parallel} = 0. \quad (3.30)$$

This equation describes the balance of the magnetic tension force along  $z$  and the perpendicular Lorentz force. Thus if the magnetic field is known at the boundary  $z = 0$

Equation (3.30) can be solved to find the equilibria at a height in  $z$  away from the boundary, as done by van Ballegoijen 1985. It has been noted by several authors that this equation is of the same form as the 2D incompressible Euler equation in hydrodynamics, which is

$$\frac{\partial \omega}{\partial t} + \mathbf{v} \cdot \nabla \omega = 0, \quad (3.31)$$

where the parallel vorticity is  $\omega = -\nabla^2 \phi$  and  $\mathbf{v} = \nabla \phi \times \hat{\mathbf{e}}_z$ . The RMHD equilibrium equation, Equation (3.30), and Euler's equation, Equation (3.31), are equivalent under the transform

$$t \rightarrow z, \quad \mathbf{v} \rightarrow \frac{\mathbf{b}_\perp}{B_0}, \quad \omega \rightarrow \frac{j}{B_0}$$

This analogy does not seem to take into account the slowly varying nature of parallel derivatives in RMHD. The similarity of these equations allows possible results from hydrodynamics to be applied to RMHD equilibria and, when appropriate, full MHD. In hydrodynamics there are two conserved quantities: kinetic energy,  $\frac{v^2}{2}$ , and enstrophy,  $\omega^2$ . It is well known that in 2D incompressible turbulence that a dual cascade exists: an inverse cascade of energy and direct cascade of enstrophy. Due to the similarity of the 2D incompressible Euler equation and the equilibrium RMHD equation the same analysis can be applied for the magnetic energy and square parallel current,  $j_\parallel^2$ . It then follows that there is an inverse cascade of magnetic energy and a direct cascade of  $j_\parallel^2$ .

Dimensional analysis can be done using Equation (3.30). Using a typical parallel lengthscale,  $Z$ , typical background field,  $B_0$ , typical fluctuations,  $b$  and typical perpendicular lengthscale,  $l$ , Equation (3.30) gives the relation  $Z = \frac{B_0 l}{b}$ . This ratio gives the distance in  $z$  over which a magnetic feature will be deformed and produce a strong variation along the parallel field. It should be noted here that strong variations in  $z$  are not valid in RMHD as the parallel direction is assumed slowly varying. Thus we must require that  $Z$  is much larger than the box length,  $L_z$ , as  $Z > L_z$ . If  $B_0$  and  $l$  are held constant  $Z$  depends on the value of the fluctuating magnetic field. Small fluctuations result in a large  $Z$  and satisfy both the first assumption of RMHD and this new relation. However for large fluctuations  $Z$  is small and reiterates the breakdown of the RMHD assumptions. This allows a threshold value to be determined for the fluctuations to satisfy  $Z \sim L_z$ , which is  $b \sim \frac{B_0 l}{L_z}$ . Values that are smaller than this threshold are close to satisfying the equilibrium equation. It is then expected that the system is near an equilibrium that it can relax to. On the other hand, a system with larger  $b$  does not satisfy the equilibrium condition and nonlinearities are important and lead to the creation of current structures. The excess energy must be dissipated to reach an equilibrium. This was presented and investigated numerically by Rappazzo 2015. Bowness, Hood, and Parnell 2013 have also shown some support for this in their full MHD simulations.

### 3.4.4 Validity

When considering an approximate model, it is important to check that the assumptions remain valid for the current system. If inappropriate assumptions are used, the results may be inaccurate and lead to false conclusions. This will only slow down progress in research as these potentially false conclusions need to be identified, checked and verified or corrected as necessary. Validity should be considered for each system on a case by case basis for any approximate method. Simply because the method was assumed, or proved, to be accurate for one system does not imply it is valid in general. There are many aspects of validity, including accuracy and consequences of the assumptions and the possible implications on the dynamics of including some effects and excluding others.

In this study we illustrate this concept by focusing on the method of RMHD. There are many subtleties of this model that make it difficult to determine whether it is valid for a given application or not. The following sections illustrate the difficulty in determining validity of RMHD following the discussions presented in Oughton, Dmitruk, and Matthaeus 2004; Oughton, Dmitruk, and Matthaeus 2003; Oughton, Matthaeus, and Dmitruk 2017.

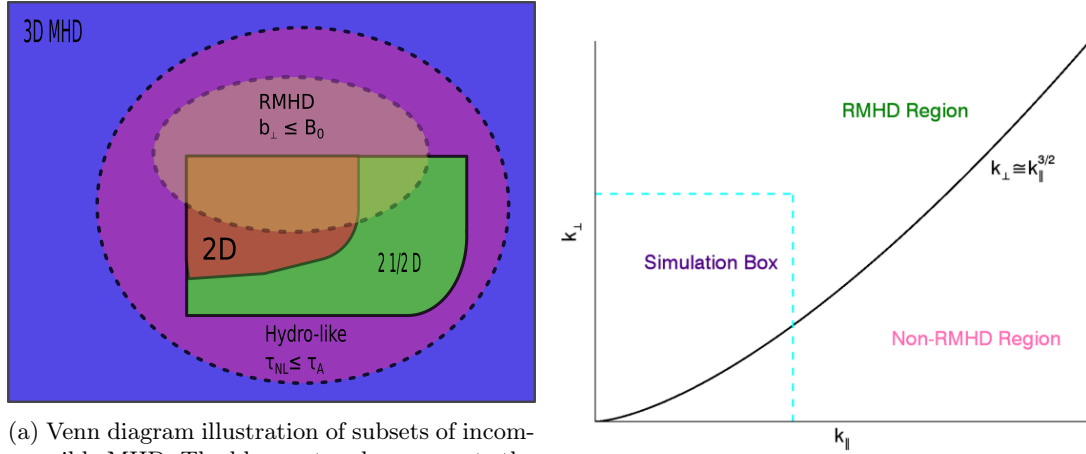
#### Subsets of 3D incompressible MHD

Here we consider the space consisting of all full 3D incompressible MHD fluctuations with an external magnetic field. The focus is on incompressible MHD since this is the case for RMHD. These modes can be divided depending on the relation of the nonlinear and Alfvén timescales. In the case  $\tau_{NL} \leq \tau_A$ , nonlinear dynamics are dominant and thus hydro-like effects dominate the effect of the magnetic field. The fluctuations that satisfy this condition are called hydro-like. If the opposite is true,  $\tau_{NL} \geq \tau_A$ , then the magnetic field dominates the nonlinear dynamics. If in addition, to the hydro-like condition, fluctuations also satisfy  $\delta b \ll B_0$  they are called RMHD fluctuations. Since both of these conditions must be true RMHD modes form a proper subset of hydro-like modes.

Models of MHD with lower dimension are common due to their simplicity compared to full 3D MHD. These models also form subsets of full 3D MHD and hydro-like modes. The two subsets considered here are 2.5D and 2D MHD. The former involves three vector field components depending on two coordinates. The latter involves two field components depending on two coordinates. A one dimensional model is also possible but not considered in this section since RMHD fields depend on more than one coordinate.

A natural question is to ask what dimension RMHD is. RMHD quantities depend fully on two coordinates and weakly on the third. Hence RMHD is neither completely three dimensional, nor two and a half or two dimensional. This question was discussed in detail in Oughton, Matthaeus, and Dmitruk 2017.

These subsets are illustrated by a venn diagram in Figure 3.1a. A similar representation is given in Figure 8 of Oughton, Dmitruk, and Matthaeus 2004. In this figure the hydro-like and RMHD regions bordered by dashed lines depend on the strength of the guide field,  $B_0$ . Although this is only an illustration, it clearly shows the indeterminate nature of the dimensionality of RMHD as it sits somewhere between 2D MHD and 2.5D MHD while



(a) Venn diagram illustration of subsets of incompressible MHD. The blue rectangle represents the space of full 3D MHD. The purple ellipse represents the subset of hydro-like region. The green shape represents the subspace of 2.5D MHD. The red shape represents the subspace of 2D MHD. The pale transparent ellipse represents the space of RMHD. The RMHD and hydro-like regions are drawn using dashed lines to indicate that the area they enclose will change with the background magnetic field strength,  $B_0$ .

(b) Illustration of RMHD and non-RMHD modes in  $k$ -space using the RMHD condition. The “simulation box” region is a sketch of the wavenumbers accessible in a simulation.  $k_\perp$  and  $k_\parallel$  are restricted by the number of grid points. This illustration shows that a general computational box will contain both RMHD and non-RMHD fluctuations.

Figure 3.1: Illustrations of RMHD validity.

still forming its own subset of full 3D MHD and hydro-like modes.

#### Validity region in wavenumber space

Another way to illustrate the complex nature of RMHD is to consider wavenumber space. In this section we take the wavenumber space of full 3D MHD and determine an approximate relation for the boundary between RMHD modes and non-RMHD modes. RMHD focuses on nonlinear evolution that happens on timescales faster than the Alfvén time. The boundary between RMHD and non-RMHD fluctuations is found by equating the nonlinear and Alfvén times,  $\tau_{NL} = \tau_A$ , as is also the case for critical balance (Goldreich and Sridhar 1995).

By making a few assumptions, it is possible to find an approximate relation between the perpendicular and parallel wavenumbers. Assuming that energy is contained at lengthscales,  $\lambda$ , with typical velocity fluctuations,  $\delta v$ , the nonlinear timescale is  $\tau_{NL} = \frac{\lambda}{\delta v}$ . The timescale inequality,  $\tau_{NL} \leq \tau_A$  can be rearranged to give  $k_\parallel \leq \frac{\delta v}{\lambda B_0}$ . At smaller inertial range scales, it is necessary to assume a functional form for the spectrum, such as the Kolmogorov spectrum of  $k^{-5/3}$ .

Oughton, Dmitruk, and Matthaeus 2003 assume the form  $\tau_{NL} = \frac{\lambda}{\delta v} \left( \frac{1}{k\lambda} \right)^{2/3}$ . The inequality gives  $k_\parallel^3 \leq \lambda^{-1} \left( \frac{\delta b}{B_0} \right)^3 (k_\perp^2 + k_\parallel^2)$ , where we have assumed  $\delta v \sim \delta b$ . Assuming  $k_\perp \gg k_\parallel$  and now taking the RHS and LHS to be equal gives the relation  $k_\perp \sim k_\parallel^{3/2}$ .

An illustration of this relation is shown in Figure 3.1b and figure 7a of Oughton, Dmitruk, and Matthaeus 2003 and figure 1a of Oughton, Dmitruk, and Matthaeus 2004. Modes above this relation are valid in RMHD and those under are non-RMHD modes.



The line has been plotted down to the origin although this is not physically correct. It should be noted that in the non RMHD region couplings are likely to include those between RMHD and non-RMHD fluctuations as well as those between non-RMHD fluctuations. The dashed lines illustrate a typical simulation box. Such a region is normally rectangular, and, thus will include both RMHD and non-RMHD fluctuations. This is a good example of the importance of checking self consistency and validity of an approximate model, especially one like RMHD.

### 3.5 Validity Checks of RMHD

One important aspect of any approximate method is how accurate its results are compared to the correct solution. This can be done by measuring the accuracy of the prediction against the exact solution. In the case of RMHD, when the assumptions and their implications are more subtle, it is important to consider validity of both the initial conditions and system properties and also whether the system under investigation is likely to invalidate the original assumptions during the evolution.

The best way to verify the applicability of a method is to undertake simple tests using both the approximate and exact methods and directly compare the results of both methods. As far as we are aware there do not seem to be many direct comparisons of full MHD and RMHD. Here we discuss the validity checks of RMHD that we are aware of.

The first direct comparisons of RMHD and 3D compressible MHD are presented in Dmitruk, Matthaeus, and Oughton 2005 for simulations of freely decaying turbulence with a  $64^3$  computational box with periodic boundaries.

Three sets of initial conditions are chosen which gradually relax the conditions of RMHD. The background magnetic field strength, in units of the initial fluctuations, is varied. They investigate how well the assumptions of spectral anisotropy, variance anisotropy and strong background field need to be satisfied for RMHD to be accurate compared to full MHD. The use of full compressible MHD also allows the evolution of non-RMHD modes to be investigated.

The three types of initial conditions for the full MHD simulations are

- (i) anisotropic, plane polarised (transverse) ICs,
- (ii) isotropic, large scale (small  $k$ ) plane polarised (transverse) ICs,
- (iii) isotropic ICs including parallel fluctuations,

for both velocity and magnetic fluctuations. The initial conditions used for RMHD simulations were slightly modified in some cases, to ensure the assumptions were satisfied initially. The first set of initial conditions are completely valid in RMHD and it is expected that the two methods should agree well. For a fairly large field, with a magnitude of  $B_0 = 4$  times the initial fluctuations, and  $\beta \sim 1.0$ , RMHD and MHD are found to be virtually indistinguishable. This indicates that if the initial conditions satisfy the RMHD conditions and  $B_0$  is strong enough RMHD is a good approximation of full MHD for freely decaying turbulence. However the agreement deteriorates as  $B_0$  is decreased. A value of  $B_0 = 1.0$ ,

which has a magnitude similar to the fluctuations, results in very poor agreement. This shows that if the background field is similar in magnitude to the fluctuations, there are noticeable differences since assumption (i) of RMHD is not satisfied. It is found that the agreement can be improved by increasing the degree of spectral anisotropy in the initial conditions. For the second type of ICs good agreement is found for a value of  $B_0 = 8.0$  ( $\beta = 0.25$ ). This shows that spectral isotropic initial conditions do not have a significant effect on the evolution in full MHD when a large enough background field is present. It is found that RMHD tracks the Alfvén wave dynamics well. For the third set of ICs the amount of parallel fluctuation present initially is varied. It is found that even if parallel fluctuations are absent initially in full MHD a small amount is generated dynamically. If such fluctuations are present initially the amount stays approximately constant throughout the simulations. It is concluded that providing  $\beta \ll 1$  and  $B_0 \gg \delta b$  RMHD is likely to be fairly accurate, providing compressible effects from parallel fluctuations are small.

Some higher resolution (up to  $2048^3$  for RMHD and  $2048^2 \times 512$  for MHD) simulations are presented by Mason et al. 2012 and Perez et al. 2012 where the main focus is spectral scaling laws in incompressible, driven MHD turbulence. Since comparison between RMHD and full MHD is not the main focus of these studies there is not much detail. The results are likely to be inaccurate as they have simply taken the toroidal polarisation of the MHD equations, without setting parallel dissipation to zero: leaving dissipation terms as  $\nabla^2$  instead of  $\nabla_{\perp}^2$  as in RMHD. This approach may create large parallel dissipation which does not exist in RMHD. It is unclear how this might affect the dynamics but it could have implications on the energy cascades. Details of polarisation were discussed in Section 3.4.3 for RMHD and MHD. Henceforth, the study by Dmitruk, Matthaeus, and Oughton 2005 is considered here as the only detailed, systematic, direct comparison of RMHD and MHD.

As well as direct comparisons, another important aspect of validity is to ensure the method is self consistent. This question is addressed, in relation to non-RMHD fluctuations, those that do not fit within the RMHD formalism, in Oughton, Dmitruk, and Matthaeus 2004.

RMHD fluctuations are defined to satisfy  $\delta b, \delta v \ll B_0$  and  $\tau_{NL}(\mathbf{k}) \leq \tau_A(\mathbf{k})$ . One issue with RMHD is that there is no constraint on the fluctuations to satisfy these relations. Therefore non-RMHD fluctuations, those that do not satisfy the above conditions, could exist in the initial conditions or be generated during the evolution. The third key assumptions of RMHD is that variations along the background field are small compared to perpendicular ones. However there is nothing in the RMHD equations which formally inhibits the formation of small lengthscales in this parallel direction, since the transfer of energy in this direction is not prevented and there is no parallel dissipation. This is a potential issue of how accurate RMHD models dissipation along the background field direction. Sometimes, in the literature, “artificial” dissipation terms have been added to the equations to limit the parallel transfer of energy, however this ad-hoc choice is not a proper solution. This issue is also only an aesthetic problem related to the RMHD equations, in reality it is well known that a strong guide field suppresses the parallel cascade in full MHD turbulence when parallel dissipation is present.

Oughton, Dmitruk, and Matthaeus 2004 focus on the interactions of fluctuations

in the turbulent cascade. The parallel spectrum is investigated by performing a set of forced turbulence RMHD simulations, varying the guide field,  $\mathbf{B}_0$ , and the resolution. Only one wavevector, namely  $\mathbf{k} = (1, 1, 1)$ , is forced and initially a subset of wavenumbers  $k_z$ ,  $k_\perp$ , are excited. It is found that the parallel energy spectrum,  $E(k_z) = \sum_{k_x, k_y} E(k_x, k_y, k_z)$ , has an exponential dependence which becomes steeper as  $B_0$  is increased. An exponential parallel spectrum was also suggested in Kinney and McWilliams 1998. In contrast the 2D spectrum at  $k_z = 0$  varies very little with the magnitude of the guide field. The computational region of validity of RMHD in fourier space is defined, as was discussed in Section 3.4.4 and Figure 3.1b. They derive a dependence between the maximum parallel and perpendicular wavenumbers and the magnitude of the background field. They argue that if this relation is not satisfied the system is not resolved fully. This means that the entire RMHD domain is not included in the computational domain, resulting in the dynamics potentially being incorrectly evolved.

In the next section we discuss some coronal loop studies using MHD and RMHD that are relevant to the present study.

### 3.6 Coronal Loop Studies

RMHD has been applied to a wide range of systems from general turbulence to the solar corona. There are only a few direct validity tests or consistency checks, as discussed in Section 3.5, which highlights a lack of knowledge and understanding of the importance of these aspects for any approximate method. The tests that have been performed are limited to turbulence studies. Nevertheless, RMHD has also been used to model coronal loops, which is distinct from general turbulence due to the line-tied boundary conditions imposed at the loop footpoints.

In this section an overview of relevant coronal loop studies using full MHD and RMHD over the last few decades is given. Particular attention is given to coronal loops since there are many phenomena, such as instabilities, where the applicability of RMHD is questionable. An important aspect of solar physics, as introduced in Section 1.1, is the effect that motions at the photosphere have on the evolution of the coronal magnetic field. One important consequence of line tied boundary conditions is that large boundary layers can be created, Scheper and Hassam 1999 argued that RMHD is invalid when these boundary layers are present, however this argument concerns the higher order RMHD equations derived by van Ballegooijen 1985, details can also be found in Appendix A.3. This is not an issue when using the original RMHD equations, where the background field remains constant throughout.

As detailed in Wilmot-Smith 2015, there are several ways of studying the evolution of a coronal loop subject to footpoint motions. A uniform background field can be driven in two ways by moving the footpoints incrementally and allowing the system to relax after each step or by moving the footpoints continually. In this section, we focus our attention on studies of full MHD involving continuous driving in Section 3.6.1. This approach is commonly used in RMHD, which will be discussed in Section 3.6.2.

RMHD is appealing in this context since a coronal loop can be approximated as

a strong, uniform field in the vertical direction perturbed by motions at the boundaries of a low  $\beta$  plasma. However, RMHD enforces many extra constraints on the system, such as incompressibility and no parallel velocity or magnetic fluctuations, which may or may not remain valid in the subsequent evolution. It is essential to investigate this system using full MHD in order to model the resulting evolution as accurately and completely as possible. It is difficult to compare existing studies of RMHD and full 3D MHD, due to the different velocity boundary conditions used or even to investigate the validity since variance and spectral anisotropy are rarely tested. Nonetheless, it is useful to compare the general features in these studies. This system is commonly characterised by states where quantities oscillate around a constant value. These states will be referred to as turbulent, however this is meant in a solar context taking into account any consequences of the line tied boundary conditions at the photospheric ends that create differences from triply periodic turbulence.

### 3.6.1 MHD Studies

One of the first investigations into the effect of different velocity profiles in a 3D box was presented in Galsgaard and Nordlund 1996. They apply a sinusoidal shearing on both boundaries which randomly changes in time between orthogonal directions. Tests are made where the boundaries are mirror images of each other or independent. Two different aspect ratios are tested: one where the domain is a cube and one where the guide field direction is ten times longer than the other directions. It is concluded that if the field is stressed in one direction, then further stressed in the orthogonal direction, small lengthscales are created and reconnection begins. It is found that the evolution depends on the relation between the driving duration and Alfvén times. If the driver period is short, only small scale current sheets are created. On the other hand if driving is longer, the magnetic energy builds up and large scale current sheets are formed.

Bowness, Hood, and Parnell 2013 perform 3D compressible MHD simulations investigating the formation and evolution of a single current sheet in a coronal loop. Although their box has dimensions of  $[0.3, 0.3, 0.5]$ , which does not give a large enough aspect ratio for validity of RMHD, their study is relevant here. They begin with an analytic sheared field in the  $y$  direction, given by

$$\mathbf{B} = \left[ 0, \lambda \sin\left(\frac{\pi x}{0.3}\right), \sqrt{1 + \lambda^2 \cos^2\left(\frac{\pi x}{0.3}\right)} \right]. \quad (3.32)$$

Subsequently, a second shear is performed in the  $x$  direction. given by

$$v_x(x, y, \pm 0.5) = \pm \sin\left(\frac{\pi y}{0.3}\right). \quad (3.33)$$

A twisted current layer is formed and reconnection is triggered. There are a number of aspects which would not be picked up in RMHD. It is shown that inside the current layer the parallel field component is very small compared to the perpendicular ones. It is also shown that there is fast outflow from the reconnection sites in the perpendicular directions. It is unclear whether RMHD would predict this as perpendicular components must be smaller

than the parallel field and if the guide field was dominant the flow may be expected in the parallel direction. However there can be no parallel flow in RMHD.

Galsgaard and Nordlund 1996; Bowness, Hood, and Parnell 2013 explain that if a system already contains current layers further driving in a second direction results in reconnection rather than continued storing of magnetic energy. This agrees with results found in RMHD: Rappazzo, Velli, and Einaudi 2013; Rappazzo 2015.

The effect of the helicity and complexity of the photospheric driver is investigated in Ritchie, Wilmot-Smith, and Hornig 2016. They test a driver that changes periodically in time. First, it consists of a vortical rotation, given by

$$\begin{aligned} v_x &= 0.15ky \exp\left(\left(-x^2 - y^2\right)/2\right), \\ v_y &= -0.15kx \exp\left(\left(-x^2 - y^2\right)/2\right), \end{aligned}$$

this then changes to a vortex of the form

$$\begin{aligned} v_x &= 0.15y \exp\left(\left(-(x - x_0)^2 - y^2\right)/2\right), \\ v_y &= -0.15(x - x_0) \exp\left(\left(-(x - x_0)^2 - y^2\right)/2\right). \end{aligned}$$

where  $k$  controls the helicity and  $x_0$  controls the centre of the second vortex. It is shown that a driver with low helicity results in a magnetically dominated steady state whereas a driver with high helicity results in the build up of magnetic energy in a repeated fashion with smaller oscillations. This seems to be a similar approach to Galsgaard and Nordlund 1996 as the driver varies in time and/or changes direction. They argue that their simulations are run for longer ( $\sim 900$  Alfvén times) than those carried out using RMHD: Rappazzo, Velli, and Einaudi 2010; Rappazzo, Velli, and Einaudi 2013, which ran for  $\sim 600$  and  $2000$  Alfvén times respectively, and that is why no further storage of magnetic energy is found in Rappazzo et al's studies. However, as will be discussed in more detail in Section 3.6.2, these RMHD studies implement a different driving profile, namely: a steady constant driving in the form of a one dimensional shear and a single vortex, respectively, which is likely to involve different dynamics compared to the case of two interacting drivers as in Ritchie, Wilmot-Smith, and Hornig 2016.

Ritchie, Wilmot-Smith, and Hornig 2016 find that the perpendicular field components are  $\sim \frac{1}{3}$  of the uniform background field. The parallel field has increased between 10% – 20% from its initial value. These are noticeable differences to what is assumed in RMHD. Similarly Ng, Lin, and Bhattacharjee 2012 found magnitudes of the perpendicular field components as large as 50% of the background field in their RMHD simulations.

Recently a numerical code HYPERION has been developed for compressible 3D MHD including conduction, radiation and gravity in Dahlburg, Rappazzo, and Velli 2010; Dahlburg et al. 2012; Dahlburg et al. 2016. Their studies focus on the thermodynamic properties of systems, previously investigated using RMHD. The first two studies test the thermodynamic properties of a coronal loop subject to shearing motions similar to Rappazzo, Velli, and Einaudi 2010, which is discussed in the next section. They state general agreement for the time dependent evolution between a RMHD simulation and their MHD code but

this is not shown in detail and direct comparisons are needed to verify this. They also do not give details of what is not in agreement between these two methods.

Dahlburg et al. 2016 analyse the thermal properties of a coronal loop undergoing rotational motions at its footpoints. The conclusions they make, in addition to those previously made using RMHD, are that the internal energy also has a turbulent evolution and that coronal loops are of a multithermal nature. They briefly show that the maximum temperature tracks the maximum current. They argue that increasing  $B_0$  brings the system closer to RMHD.

In summary, the type of footpoint motions applied are very important to the evolution of a coronal loop. When the field is stressed in one direction small scales are created which leads to the build up of currents. If the field is further driven in such a way that perturbs these initial current structures then reconnection begins. It seems that there are many aspects of this secondary shear which determine how effectively the system is able to store magnetic energy after reconnection starts. This gives a clearer idea of what is happening when random footpoint motions are used that results in a turbulent state. Similar evolution is found in studies of RMHD, which are discussed next.

### 3.6.2 RMHD Studies

An initially stable equilibrium is perturbed by footpoint motions to generate reconnection in a cylindrical flux tube by Strauss 1990. The initial magnetic field

$$\mathbf{B} = \nabla A_0 \times \hat{\mathbf{e}}_z + B_0 \hat{\mathbf{e}}_z,$$

is used where the equilibrium,  $A_0$ , is determined by a current profile of the type

$$J_0(r) = \frac{2}{q_0} \left( 1 - \left( \frac{r}{R} \right)^2 \right)^5.$$

where  $q_0$  is an inverse measure of the twist and  $R$  is the radius of the flux tube. This equilibrium is maintained by an equilibrium flow. Simulations are done of a flux tube with the above equilibrium with its footpoints rotated in time. When this above equilibrium is twisted at its footpoints current sheets are formed and reconnection occurs where the velocity flow is parallel to the field.

Another study by Longcope and Sudan 1994 involves a similar system using random footpoint motions to investigate the properties of the current sheets and reconnection that form as a result of the turbulence. It has not been made clear if the applied boundary motions are incompressible, which is required for validity of RMHD. The general steady state has current concentrated in structures that extend the entire length in  $z$  with varying magnitude. The range of  $\eta$  tested is extended in Ng, Lin, and Bhattacharjee 2012, who argue that the heating rate is independent of  $\eta$  in the limit of small resistivity.

Reconnection is studied using RMHD in Milano et al. 1999; Gómez et al. 2001 by simulating the merging of two flux tubes. The flux tubes are driven at the boundaries with a stationary velocity. Since the process of coalescence results in compression of the

magnetic field and plasma it is currently unclear how important these compressible effects are to the dynamics, which raises the question of whether RMHD is valid for this system.

A scaling law for coronal heating has been proposed by Dmitruk et al (Dmitruk and Gómez 1999; Gomez, Dmitruk, and Milano 2000) using dimensional analysis. RMHD simulations of a coronal loop with stationary driving motions at its footpoints were carried out to determine the unknown functional dependence. The resulting scaling law found using RMHD is the same as that previously found in Dmitruk and Gómez 1997; Dmitruk, Gómez, and DeLuca 1998 using 2D MHD simulations of a 2D plane perpendicular to the axis of a coronal loop. This agreement between the RMHD and 2D incompressible MHD simulations is not surprising as nondimensionalisation requires approximating the terms involving derivatives along the loop axis as constant to provide an energy input, which results in the RMHD equations being equivalent to 2D incompressible MHD.

A footpoint driven coronal loop is investigated in a series of articles by Rappazzo et al. The degree of understanding of the assumptions of RMHD varies greatly in the literature. These articles are a good example where the requirements and limitations of RMHD are not always made clear. The RMHD equations are written so that the terms involving parallel derivatives are  $B_0 \frac{\partial}{\partial z} \Rightarrow \frac{V_A}{v_{ph}} \frac{\partial}{\partial z}$ , where  $v_{ph}$  is the boundary velocity. Since  $V_A \gg v_{ph}$  this would seem to be a very large gradient along the length of the loop, however for RMHD parallel derivatives are slowly varying. Thus as discussed before the product of a large velocity and small gradient combine to give a term equal in magnitude to the nonlinear terms in the equations.

Initially in Rappazzo, Velli, and Einaudi 2008; Rappazzo et al. 2007; Rappazzo et al. 2008 a random velocity stream function is applied at the boundaries of a coronal loop

$$\phi(x, y) = \frac{1}{\sqrt{\sum_{mn} \alpha_{mn}^2}} \sum_{k,l} \frac{l \alpha_{kl}}{2\pi \sqrt{k^2 + l^2}} \sin \left[ \frac{2\pi}{l} (kx + ly) + 2\pi \xi_{kl} \right], \quad (3.34)$$

where the amplitudes,  $\alpha_{kl}$ , and phases,  $\xi_{kl}$ , are random numbers between 0 and 1 and are independent for each boundary. This driver is constant in time but random amplitude and phase so it does not necessarily vary smoothly in space. It is found that steady state turbulence is achieved for both magnetic and kinetic energies. In the final turbulent state current layers are aligned with the background field.

The statistical properties of ohmic dissipation and reconnection of the same system is studied by Wan et al. 2014 using the same footpoint motions as in Rappazzo et al. 2008 and Equation (3.34). They argue that a consequence of the result found by Servidio et al. 2014: that the general flux function does not always define flux surfaces, is that x-type points are not always found inside current sheets in RMHD as would be expected in full MHD. This effect reduces the overall efficiency of the reconnection. The largest reconnection rates are found when the locations of x-points and current sheets coincide. Similar results were found using periodic boundary conditions by Zhdankin, Boldyrev, and Chen 2016; Zhdankin et al. 2017. It is not currently known if this is also the case in MHD or a feature specific to RMHD.

The previous studies carried out by Rappazzo et al used a vortical type driver which

gave a non-vanishing Lorentz force, naturally allowing nonlinear terms to grow in time and establish a steady turbulent state. A further study investigates whether a similar turbulent state can be created using smooth footpoint motions. in Rappazzo et al. 2006; Rappazzo, Velli, and Einaudi 2010 uses a driver which is only a function of  $x$ . This is a special type of boundary velocity which gives a vanishing Lorentz force, which allows magnetic energy to be stored rather than dissipated in a turbulent cascade. The sheared boundary condition, Rappazzo, Velli, and Einaudi 2010, is

$$u(x, y, L) = \sin\left(4\frac{2\pi}{l_{\perp}}x + 1\right) \hat{\mathbf{e}}_y,$$

$$u(x, y, 0) = 0.$$

The question addressed here is whether a smooth one dimensional driver can also lead to a turbulent state of magnetic energy as was found for a two dimensional random driver previously in Rappazzo et al. 2007; Rappazzo et al. 2008; Rappazzo, Velli, and Einaudi 2008. This question was already verified in forced 2D MHD (see Einaudi et al. 1996; Romeou, Velli, and Einaudi 2004; Romeou, Velli, and Einaudi 2007; Romeou, Velli, and Einaudi 2009). As well as the shear driver, a perturbation, in the form of white noise, is also applied throughout the simulations. This is the required setup for the tearing instability which triggers reconnection and allows the stored magnetic energy to be released. They find in this case the kinetic energy reaches a steady state as in the previous studies using a random driver. In contrast to these previous studies the magnetic energy continues to increase in time initially, until the tearing instability develops after which the stored magnetic energy is dissipated and there is a peak in the kinetic energy, After the instability the energies oscillate about a steady value. It is concluded that this configuration does lead to a turbulent state through the development of the tearing instability. The final state is similar to that found using a spatially random driver. The surprising thing is that the magnetic energy does not build up again, even though the system is still being driven. The system remains in a statistically steady turbulent state maintained by the continued footpoint motions. This is not expected in MHD as it does not agree with the “sequences of equilibria” picture, in which the storage and release of energy occurs cyclically. The time taken for the field to relax back to a lower energy is longer than the driving timescale. This needs to be verified using full MHD and will be the focus of Chapter 5.

The direction of spectral transfer between the magnetic and velocity fields is investigated in Rappazzo and Velli 2011 where Alfvén waves are injected into the system using the same forcing as in Rappazzo et al. 2008 (Equation (3.34)). Similar results were found in decaying and driven incompressible periodic MHD turbulence in Alexakis et al. 2007; Alexakis 2011; Teaca et al. 2009 .

Rappazzo et al. 2012 investigate “interchange” reconnection; reconnection of magnetic fields along the boundary between a closed loop and open fieldlines. Footpoint motions are applied as in Rappazzo et al. 2008 to one end of the closed fieldlines, resulting in the field reconnecting where some closed fieldlines become open and vice versa. This is a considerably more complex system for which validity of RMHD is difficult to ascertain without



further investigation.

Rappazzo, Velli, and Einaudi 2013 investigated another type of footpoint motion which leads to a turbulent system through the development of the kink instability. This is done by forcing the system with a single non-circular vortex in a central region at the boundary which twists the magnetic fieldlines. The non-circular nature of the streamlines acts as a perturbation leading to the onset of the kink instability. It is concluded that the kink instability only occurs once like the tearing mode previously investigated in Rappazzo, Velli, and Einaudi 2010. The driver is only applied in a finite region at the boundary which allows the twisted field to expand into the region where there is no driver applied. Further energy release occurs due to the interaction of fieldlines through the transverse periodic boundary conditions. The final system oscillates between energy states. Similarly to Rappazzo, Velli, and Einaudi 2010 the magnetic energy is stored initially until the kink instability develops, causing the release of magnetic energy and increase in kinetic energy before the system settles to a steady state.

Rappazzo and Parker 2013 and Rappazzo 2015 continue their investigation into the conditions for current sheet formation and reconnection in decaying turbulence. An initial random magnetic potential is used to give a disordered perpendicular magnetic field that depends on all three coordinates and is constant in time to mimic the perpendicular field resulting from disordered footpoint motions without applying boundary motions to reach this initial state. The magnetic field is initially not in equilibrium and attempts to reach such a state. Whether the field is in equilibrium or not is determined by the RMHD equilibrium condition, Equation (3.30), which balances the Lorentz force components. The evolution of the system is investigated by varying the distribution of energy in the parallel modes of the magnetic field. A 2D periodic system is found to relax to a force-free equilibrium state with no  $z$  variation. In contrast to a 3D line-tied system which does not give a force-free final state. In the case that energy is present in parallel modes other than  $k_{\parallel} = 0$  mode, an inverse cascade develops to transfer energy to the 2D mode so that it can be dissipated through the direct perpendicular cascade. The threshold value for magnetic fluctuations needed to satisfy the equilibrium condition, described in Section 3.4.3, was argued and tested by varying the magnetic fluctuations present initially. They choose  $0.01 < b/B_0 < 0.1$ , which, in theory, satisfies the first assumption of RMHD. It is found that if magnetic fluctuations are greater than this threshold, reconnection occurs to allow the field to reach an equilibrium. Otherwise, the system relaxes to an equilibrium state, with no extra dissipation. A similar final state is found in all cases.

The effect of the timescale of footpoint motions on the dynamics is tested in Rappazzo et al. 2018. The boundary velocity used in Rappazzo et al. 2007; Rappazzo et al. 2008, in Equation (3.34), is modified, such that the coefficients,  $\alpha_{rs}$ , are changed from one value to another on a forcing timescale,  $t_p$ . For large values of  $t_p \geq 10 - 24$  the energy dynamics are found to be very similar to the stationary driver used previously Rappazzo et al. 2007; Rappazzo et al. 2008 with  $t_p = \infty$ . Smaller values result in smaller energy in the fields as the creation of current sheets and dissipation is less effective. Rappazzo et al. 2018 also present full compressive MHD simulations, similar to Dahlburg et al. 2016, to investigate the effect of the forcing timescale on the temperature evolution. It is concluded

that smaller  $t_p$  results in less variation and overall smaller maximum temperature in time. The probability density of the temperature is shown to be increasingly narrow, centered around much lower values than  $10^6 K$  for small  $t_p$ . This is used to argue the requirement of low frequency motions to produce X-ray and EUV emissions.

### 3.7 Similar Methods

The original model of RMHD, derived by Strauss 1976, is very simple compared to that of full MHD, and as a consequence it does neglect a number of potentially interesting dynamical effects. Such dynamics happen on fast timescales and so neglecting them removes much of the complexity in the full MHD equations and considerably decreases the computational resources needed to solve the equations. Although validity is always an important question, RMHD has been widely used for its advantages over MHD. Due to the simplicity of RMHD, there are several aspects which are not permitted in the RMHD picture that one may like to include. Examples include: inhomogeneous Alfvén speeds, arbitrary non-constant background fields, Alfvén wave dynamics and slow waves.

As a result several other approximate MHD methods have been derived over the years in an attempt to include some additional dynamics while retaining reasonable demand on resources compared to the full MHD equations. As with RMHD, it is difficult to determine when any approximate method is valid. Hence the validity of each of these models needs to be investigated individually in future work.

In this section we will give an overview of these models. A number of these adapted models are listed in Table 3.1 and Table 3.2, giving the model name, if it has a unique name, and the associated articles and appendix number where the equations and further details can be found.

### 3.8 Other Formulations of “Reduced” Models in MHD

There are a number of models that have been developed for MHD to simplify the full nonlinear equations to account for the anisotropy of a strong background field. These range from two-fluid to kinetic models. Most of which have little to do with the original single fluid RMHD model derived by Strauss 1976 except for the assumptions of a strong background field and the idea of a “reduced” model.

Although the main focus of this work is on the original fluid version of RMHD derived for fusion plasma in tokamaks by Strauss 1976, these additional models are mentioned here in order to make the reader aware of such models in the literature and their similar acronyms which could lead to considerable confusion. Considering how natural the choice of a strong background field is in fusion devices and astrophysics there are numerous models of this type. No attempt at completeness is made. Details of a number of these models are given in Table 3.3.

Table 3.1: List of adapted RMHD models. These do not have a unique name to distinguish them from the original RMHD model derived by Strauss (Strauss (1976)).

Article(s)	Appendix	Notes
Strauss and Lawson 1989	-	<ul style="list-style-type: none"> <li>• resonant absorption</li> <li>• includes density gradients.</li> </ul>
<ul style="list-style-type: none"> <li>• Dmitruk, Milano, and Matthaeus 2001</li> <li>• Dmitruk et al. 2001</li> <li>• Dmitruk et al. 2002</li> <li>• Dmitruk and Matthaeus 2003a</li> <li>• Dmitruk and Matthaeus 2003b</li> </ul>	-	<ul style="list-style-type: none"> <li>• Alfvén speed profile</li> <li>• Alfvén turbulence</li> <li>• open magnetic fields</li> </ul>
<ul style="list-style-type: none"> <li>• Gazol, Passot, and Sulem 1999</li> <li>• Gazol, Passot, and Sulem 2000</li> </ul>	B.2	2D dynamics (RMHD) plus nonlinear Alfvén waves
<ul style="list-style-type: none"> <li>• van Ballegooijen et al. 2011</li> <li>• Asgari-Targhi and van Ballegooijen 2012</li> <li>• Asgari-Targhi et al. 2013</li> <li>• van Ballegooijen, Asgari-Targhi, and Berger 2014</li> </ul>	B.6	<ul style="list-style-type: none"> <li>• Alfvén wave turbulence in coronal loops</li> <li>• includes lower atmosphere</li> <li>• variable Alfvén speed</li> </ul>

Table 3.2: List of approximate MHD models which have similar properties to the original model of RMHD derived by Strauss (Strauss (1976)).

Name	Article(s)	Appendix	Notes
generalised RMHD	Kruger, Hegna, and Callen 1998	B.1	<ul style="list-style-type: none"> <li>• does not require large aspect ratio</li> <li>• inhomogeneous <math>\mathbf{B}_0</math></li> </ul>
slow MHD	Zhukov 2001	B.3	RMHD plus slow wave dynamics in cylindrical coords
NIMHD	Zank and Matthaeus 1992	B.4	<ul style="list-style-type: none"> <li>• nearly incompressible MHD</li> <li>• incompressible limit gives RMHD</li> </ul>
MHD4field	<ul style="list-style-type: none"> <li>• Bhattacharjee, Ng, and Spangler 1998</li> <li>• Bhattacharjee and Ng 1999</li> <li>• Bhattacharjee et al. 1999</li> <li>• Bhattacharjee and Ng 2001</li> </ul>	B.5	<ul style="list-style-type: none"> <li>• inhomogeneous <math>\mathbf{B}_0</math></li> <li>• 4 scalars</li> <li>• if <math>\beta \ll 1</math> and/or <math>\mathbf{B}_0 = B_0 \hat{\mathbf{e}}_z</math> then =RMHD.</li> </ul>

Table 3.3: Additional models which may or may not be the same RMHD.

Acronym	Full name	article	notes
QGMHD	quasigeostrophic MHD	Kinney and McWilliams 1997	stratified, rotating system
RMHD	reduced MHD	Denton, Rogers, and Lotko 2007	Auroral plasma
RHMHD	reduced hall MHD	Gómez, Mahajan, and Dmitruk 2008	turbulence, coronal loops
KRMHD	kinetic RMHD	Schekochihin et al. 2009	Alfvén dynamics (RMHD) plus passive compressional effects
ERMHD	electron RMHD	Schekochihin et al. 2009	interaction of Alfvén and compressional dynamics
HRMHD	hall RMHD	Schekochihin et al. 2009	low $\beta$ cold plasma limit of KRMHD and ERMHD
NRMHD	noisy RMHD	<ul style="list-style-type: none"> <li>• Ruffolo and Matthaeus 2013</li> <li>• Ruffolo and Matthaeus 2015</li> <li>• Shalchi and Hussein 2014</li> </ul>	fieldline random walk model

### 3.9 Summary

In this chapter the approximate MHD model of reduced MHD was introduced. The RMHD equations are considerably simpler than the full MHD ones. For this reason RMHD has been used to model many different systems, in addition to fusion plasma, which RMHD was derived for. It is unclear whether RMHD is valid in other areas of research, such as the solar corona. There are very few comparisons or validity checks between RMHD and full MHD. In this study we take the first step in investigating the validity of RMHD by considering one particular example in solar physics. We choose to verify the conclusion made, using RMHD, by Rappazzo, Velli, and Einaudi (2010). To do this, a full MHD model of their system is developed in two stages, which will be described in the following two chapters, Chapter 4 and Chapter 5.

## Chapter 4

# Shearing: Comparison of Methods

### 4.1 Introduction

In this chapter, we investigate the evolution of an initially uniform magnetic field driven at its footpoints. Slow, smooth footpoint motions allow the build up of magnetic energy. This is the first stage in the coronal heating picture. The magnetic energy will continue to build up until such time as the necessary conditions for an instability or non-equilibrium are satisfied, which allow the subsequent release of the stored energy.

Ideally, one would like to model this build up of energy using full MHD. As demonstrated in Chapter 2, the full MHD equations are very complex and require a substantial amount of computational time and resources to achieve solutions. For such a simple system, such as the one studied here, there are many additional assumptions, which can be made to simplify the full MHD equations. These could be related to the magnitude of the plasma beta or the distance the footpoints are moved or the strength of the initial magnetic field. The resulting equations create an approximate method of MHD. There are many different types of approximate methods. Some assume the magnetic field evolves through sequences of equilibria and some consider the time evolution of the system. We will focus on four common models, two of each type. First, we consider the relaxation or magneto-frictional method, (Yang, Sturrock, and Antiochos 1986; Yang 1989; Yang 1990; Yang 1992; Klimchuk and Sturrock 1992), which is a quasi-static method which—together with a flux transport model (Mackay and van Ballegooijen 2006a; Mackay and van Ballegooijen 2006b)—can be used to follow the evolution of the force-free, coronal magnetic field. This is discussed in Section 4.2.3. Second, 2D equilibria can be calculated by solving the Grad-Shafranov equation for the magnetic flux function,  $A$ , derived in Section 2.6. In general, it is difficult to determine the unknown functional dependencies of the gas pressure and the driven component of the magnetic field on  $A$ . Lothian and Hood 1989 and Brown-ing and Hood 1989 simplify the 2D Grad-Shafranov equation to a 1D equation, discussed in Section 4.2.4. Third, linear dynamics of the system can be investigated in time using the method of linearised MHD. Linearising about an initial state is a useful approach, as it can allow important insights into the dynamics. Nonlinear effects can be considered by expanding the MHD equations to higher order. The first and second order solutions given

by this method, described in detail in Section 4.2.5 and in Appendix C, reveal features that help to justify the use of the 1D solution mentioned above, as well as important information about this system. Another method which can be used to investigate the time evolution of the system is reduced MHD (RMHD), which was introduced in Chapter 3.

Although these approximate models can be useful, it is, nevertheless, difficult to know when a certain approximate method is valid and when it is not. This is due to the nature of the assumptions, which, generally, require a certain quantity to be very large or small. It is not usually known exactly when such conditions are satisfied. If the assumptions of an approximate method are not sufficiently satisfied, the results could be misleading and false conclusions could be made. To illustrate the importance of considering validity of approximate methods, we will use each of the above methods: magnetofrictional relaxation, 1D approach, linearisation and RMHD to model the evolution of a footpoint driven coronal loop. The solution from each method will be directly compared with each other and judged against the full MHD solution from the Lare code (see Arber et al. (2001)) which is taken to be the “exact” solution.

Direct comparisons of these methods have not been done before, in this context. There are many studies, where a few models are compared to a known solution. One example is Dmitruk, Matthaeus, and Oughton 2005, where RMHD and full MHD are directly compared in the context of MHD turbulence. Properties of footpoint driven coronal loops have been frequently modelled. Examples of footpoint driven simulations include Murawski and Goossens 1994; Meyer et al. 2011; Meyer, Mackay, and van Ballegooijen 2012; Meyer et al. 2013.

This chapter is organised as follows. Section 4.2 describes the simple footpoint driving experiment, and outlines the details of the four approximate models we examine. Section 4.3.1 presents a comparison between these models and benchmarks them against solutions to the full MHD equations. In Section 4.3.2 a more detailed analysis of our full MHD results is presented. A summary of our results is given in Section 4.4.

## 4.2 Experiment and Model Descriptions

In this section, we present the full MHD equations used in this chapter and the full details of our experiment and each approximate method.

### 4.2.1 MHD Equations

The time evolution of our simple experiment is determined by solving the MHD equations, Equations (2.9), described in Chapter 2, using the Lare code (Arber et al. 2001). The viscous form of the MHD equations, neglecting resistivity, gravity, radiative losses and

conduction, are expressed as

$$\rho \frac{\partial \mathbf{v}}{\partial t} + \rho(\mathbf{v} \cdot \nabla) \mathbf{v} = -\nabla p + \mathbf{j} \times \mathbf{B} + \nabla \cdot \mathbf{S}, \quad (4.1a)$$

$$\frac{\partial \rho}{\partial t} + \nabla \cdot (\rho \mathbf{v}) = 0, \quad (4.1b)$$

$$\frac{\partial \mathbf{B}}{\partial t} = \nabla \times (\mathbf{v} \times \mathbf{B}), \quad (4.1c)$$

$$\frac{\partial}{\partial t} \left( \frac{p}{\gamma - 1} \right) + \mathbf{v} \cdot \nabla \left( \frac{p}{\gamma - 1} \right) = -\frac{\gamma p}{\gamma - 1} \nabla \cdot \mathbf{v} + \epsilon_{ij} S_{ij}, \quad (4.1d)$$

together with

$$\mathbf{j} = \frac{\nabla \times \mathbf{B}}{\mu} \text{ and } \nabla \cdot \mathbf{B} = 0$$

where the  $z$  direction is assumed invariant. Notation is the same as in Chapter 2. The viscous stress tensor is given by Equation (2.13) and the strain rate is given by Equation (2.14). This set of equations (4.1) conserve the total energy,  $E = \frac{1}{2} \rho v^2 + \frac{B^2}{2\mu} + \rho \frac{p}{\gamma - 1}$ , so that the dissipation of kinetic energy must go either into an increase in magnetic energy or an increase in internal energy (i.e. the gas pressure) defined as  $e = \frac{p}{\gamma - 1}$ .

It is normal to express the variables in the MHD equations in terms of non-dimensional ones. This allows the system to be described by dimensionless parameters. Then, it may be possible to determine approximate solutions by considering the special cases when these parameters are very large or very small. To do this, we take three typical reference quantities, which describe all of the system quantities: a length scale,  $R$ , a density,  $\rho_0$ , and a magnetic field strength,  $B_0$ . The dimensionless speed is the Alfvén speed,  $V_A = B_0 / \sqrt{\mu \rho_0}$ , and time is expressed in terms of the Alfvén travel time,  $t_0 = R / V_A$ . Hence

$$(x, y, z) = R(\tilde{x}, \tilde{y}, \tilde{z}), \quad t = \frac{R}{V_A} \tilde{t}, \quad \mathbf{B} = B_0 \tilde{\mathbf{B}},$$

$$p = \frac{B_0^2}{\mu} \tilde{p}, \quad \mathbf{v} = V_A \tilde{\mathbf{v}}, \quad \rho = \rho_0 \tilde{\rho}. \quad (4.2)$$

Substituting these expressions into Equation (4.1) and dropping the tildes, the equations remain exactly the same, except that  $\mu = 1$  and  $\nu$  is a non-dimensional viscosity that is the inverse of the Reynolds number. For the values  $R = 180 \times 10^3$  m,  $\rho_0 = 1.67 \times 10^{-4}$  kg m<sup>-3</sup>, and  $B_0 = 0.03$  T, the Alfvén speed is  $V_A = 2070$  m s<sup>-1</sup> and the Alfvén travel time is  $t_0 = 87$  s. This also gives a reference temperature of 516.7 K.

We take solutions of the MHD equations as the exact solutions. These are solved using Lare2d, see Arber et al. 2001, since an invariant direction will be chosen in this experiment. Next the simple experiment that these equations are applied to is described.



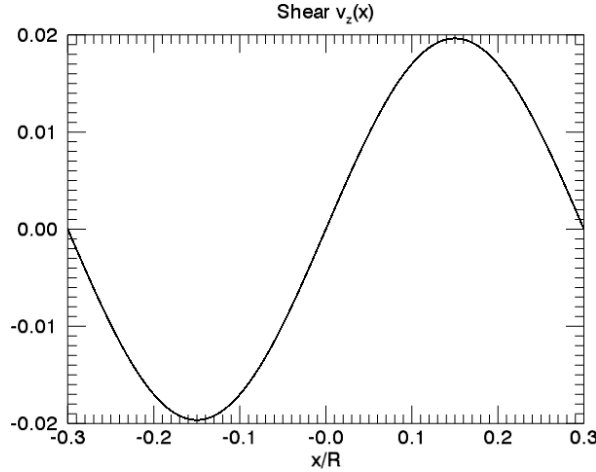


Figure 4.1: Plot showing the shear driver,  $v_z$ , as a function of  $x$  at the bottom boundary,  $z = -3$ , once it has reached its full amplitude.

#### 4.2.2 Experiment Description

We consider a computational box  $-l \leq x \leq l$  and  $-L \leq y \leq L$  with an initial uniform magnetic field,  $\mathbf{B} = B_0 \hat{\mathbf{e}}_y$ , uniform density,  $\rho_0$ , and uniform pressure,  $p_0$ . This can be thought of as a coronal loop of length  $2L$  and width  $2l$  with a dimensionless plasma  $\beta$  equal to  $2p/B^2$ . The magnetic field is line tied at the boundaries in  $y$ . Periodic boundary conditions are used in  $x$ . We will use the term “loop” though the results are valid in general. In our dimensionless variables,  $B_0 = 1$ ,  $\rho_0 = 1$ , and  $p_0$  is a constant related to the initial plasma beta,  $\beta_0$ , by  $\beta_0 = 2p_0$  and initial internal energy by  $e_0 = \frac{p_0}{\gamma-1}$ .

At the loop ends, zero gradient boundary conditions are used for all quantities except velocity. A driving velocity is imposed in the  $z$  direction at the two photospheric ends ( $y = \pm L$ ) of the form

$$v_z(x, \pm L, t) = \pm F(t) \sin kx, \quad (4.3)$$

where  $k = \pi/l$  and  $v_z(\pm l, y, t) = 0$ . The time dependent amplitude,  $F(t)$ , is used to ramp up the driver from rest to a constant speed in time.  $F(t)$  is taken as

$$F(t) = \frac{V_0}{2} \left\{ \tanh \left( \frac{t - t_1}{\tau_0} \right) + 1 \right\}, \quad (4.4)$$

where  $t_1 > \tau_0$  is the switch-on time. We use  $t_1 = 6$  and  $\tau_0 = 2$ , corresponding to times of  $t_1 \approx 8.5$  minutes and  $\tau_0 \approx 3$  minutes. If the parameter  $\tau_0$  is small, then  $F(t)$  can be approximated by

$$F(t) = \begin{cases} 0, & t < t_1, \\ V_0, & t_1 \leq t. \end{cases}$$

The driver can be switched off by using a similar function to ramp down the velocity. The driver is always switched on in the simulations presented here. The other two velocity

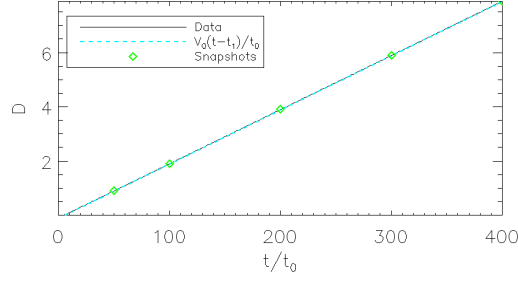


Figure 4.2: Maximum footpoint displacement,  $D$ , given by Equation (4.5) (dashed line) and actual Lare2D data (solid line) from Simulation 1 in Table 4.1 on page 79 plotted as a function of time  $t$ . The symbols indicate the values of  $D$  and  $t$  that are used for the comparisons in the results section, Section 4.3.

components are zero at the loop ends:  $v_x = v_y = 0$ .

This form of the velocity on the boundary given by Equation (4.3) will cause the photospheric footpoints to be displaced by a distance

$$d(x) = D \sin kx.$$

The maximum footpoint displacement,  $D$ , can be calculated by integrating the velocity amplitude in time as

$$D = \int_0^t F(t) dt = \frac{V_0 \tau}{2} \left( \log \left\{ \cosh \left( \frac{t - t_1}{\tau} \right) \right\} + \frac{t}{\tau} \right) \approx V_0(t - t_1), \quad (4.5)$$

for times greater than the driving start time,  $t_1$ .

Thus, we have three distinct lengths in this problem: the half-length of the loop,  $L$ ; the half-width of the loop,  $l$ ; and the photospheric footpoint displacement,  $d(x)$ , of a magnetic fieldline from its initial position. In all cases, we take  $L = 3$  and  $l = 0.3$  so that  $l/L = 0.1 \ll 1$ . However, we allow  $D/L$  to vary from low to high values. The approximation for the maximum displacement,  $D$ , Equation (4.5), is plotted along with the data from one of the full MHD simulations in Table 4.1 on page 79 for the driver as a function of  $t$  in Figure 4.2. The symbols denote the values of  $D$  and corresponding  $t$  that are used in the results section, Section 4.3.

Next, we consider the various speeds in our system. These are the Alfvén speed,  $V_A$ ; sound speed,  $c_s = \sqrt{\gamma p_0 / \rho_0}$  ( $\gamma = 5/3$  is the ratio of specific heats); the speed of the driving motions at the photospheric ends,  $V_0$ ; and a maximum diffusion speed,  $V_{visc} = \nu / l$ , based on the horizontal lengthscales. Typically we take  $\nu = 10^{-3}$  so that  $V_{visc} \approx 3 \times 10^{-3}$ . A smaller value of  $\nu$  could be used, but a value that is too small results in numerical diffusion being more important than the specified value. In order to pass through sequences of equilibria, we require

$$V_{visc} \ll V_0 \ll c_s. \quad (4.6)$$

The driving speed is also slow and sub-Alfvénic if  $V_0 \ll 1$  from Equation (4.2). Accordingly, we choose  $V_0$  as 0.02, corresponding to a value of  $V_0 \approx 44.4 \text{ m s}^{-1}$ . Equation (4.6) requires that the pressure should be higher than a minimum value of  $p_0 \gg 2.4 \times 10^{-4}$ . We consider the range  $10^{-3} < p_0 < 1.0$ . Equivalently, this can be written in terms of the initial plasma  $\beta_0$  as  $2 \times 10^{-3} < \beta_0 < 2.0$  or in terms of the initial internal energy as  $\frac{3 \times 10^{-3}}{2} < e_0 < \frac{3}{2}$ .

In the following sections, we describe each of the approximate models. First, we describe the magnetofrictional relaxation model in Section 4.2.3, and, second, in Section 4.2.4 we present the derivation of the 1D equilibrium approach. Third, in Section 4.2.5, we derive the first and second order linear MHD equations using the method of linearisation and describe the analytic solutions. Lastly in Section 4.2.6, we discuss the similarities and differences between the linear and RMHD methods.

### 4.2.3 Magnetofrictional Relaxation

Here we introduce the magnetofrictional relaxation method. Magneto-frictional, relaxation methods solve the induction equation, Equation (4.1c), with the velocity given by the unbalanced Lorentz force. To ensure that  $\nabla \cdot \mathbf{B} = 0$ , we express the magnetic field in terms of a vector magnetic potential,  $\mathbf{A} = (A_x(x, y), A_y(x, y), A(x, y))$ , so that

$$\mathbf{B} = \nabla \times \mathbf{A} = \left( \frac{\partial A}{\partial y}, -\frac{\partial A}{\partial x}, \frac{\partial A_y}{\partial x} - \frac{\partial A_x}{\partial y} \right).$$

The equations to be solved are

$$\mathbf{v} = \frac{\mathbf{j} \times \mathbf{B}}{B^2}, \quad (4.7a)$$

$$\frac{\partial \mathbf{A}}{\partial t} = \mathbf{v} \times \mathbf{B}. \quad (4.7b)$$

The time evolution is not physical but leads to a final state in which the magnetic field has relaxed to a force-free equilibrium. Once the relaxation process is complete and since invariance in  $z$  is assumed for the final equilibrium, the  $z$  component of  $\mathbf{A}(x, y)$  is a flux function and the final  $z$  component of the magnetic field,  $B_z = \partial A_y / \partial x - \partial A_x / \partial y$ , will be a function of the flux function,  $A(x, y)$ , i.e.  $B_z = B_z(A)$ . Boundary conditions are chosen for the vector potential to give a magnetic field that results from the driving motions in Equation (4.3) and the initial uniform field. These are

$$A_x(x, \pm L) = \mp B_0 D \sin(\pi x / l) \quad \text{and} \quad A(x, \pm L) = -B_0 x. \quad (4.8)$$

Without loss of generality, the gauge function is chosen so that  $A_y(x, \pm L) = 0$  and, once the field has relaxed, this implies that  $A_y(x, y) = 0$ . Then,  $A_x$  is a function of  $A$  since  $B_z = -\frac{\partial A_x}{\partial y}$ . Note that while the equation for equilibrium, given by the Grad-Shafranov Equation, Equation (2.27) on page 17, involves only  $A$ , the evolution towards equilibrium requires calculation of  $A_x$  also.

We select a physical time,  $t$ , and use Equation (4.5) to determine the maximum

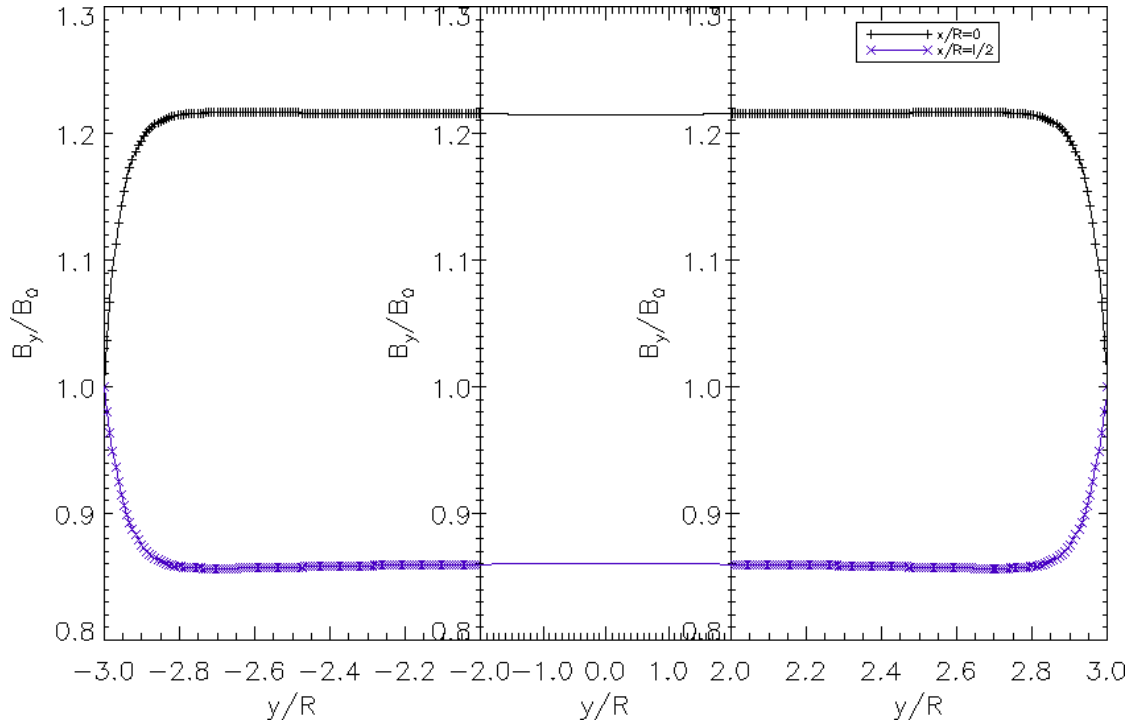


Figure 4.3: An example of the final state of  $B_y$  found using the magnetofrictional relaxation method, Equation (4.7) with the footpoint displacement,  $D$ , equal to the loop length,  $L$ .  $B_y/B_0$  is plotted as a function of  $y$  along the loop axis at  $x = 0$  (upper) and  $x = l/2$  (lower). The horizontal scale is expanded at the two ends to illustrate the resolved boundary layers at  $y = \pm L$  and compressed in the middle to demonstrate that there is no variation with  $y$  there.

footpoint displacement,  $D$ . Given this value of  $D$ , Equations (4.7) can be solved with the boundary conditions in Equation (4.8) to determine the resulting force-free equilibrium field. As an example, we choose  $D = 3.0$  so that  $D$  is equal to the half-length,  $L$ , and solve Equations (4.7). The final state for the background field,  $B_y$ , is shown in Figure 4.3. There are two important points. Firstly, there are sharp boundary layers at the photospheric boundaries in  $y$ , where  $B_y$  rapidly changes from the imposed constant boundary value of  $B_0 = 1$  over a short distance that is comparable to the half-width,  $l$ . Derivatives with respect to  $y$  are large in the boundary layers. The width of the boundary layer is controlled by the width to length ratio,  $l/L$ , but not dependent on the value of  $D/L$ . This fact is also found analytically using the linearisation method in Section 4.2.5 and used in Section 4.2.4. Secondly, in the middle of the layer, away from the boundaries,  $B_y$  is almost independent of  $y$ . It is found analytically by the 1D approach in Section 4.2.4 and linearisation in Section 4.2.5 and shown in the results discussed in Section 4.3 that  $B_y$  does vary with  $x$  as  $\cos(2kx)$  when  $D/L$  is small. Figure 4.3 shows that the magnitude of  $B_y$  has changed by at least 10% from its uniform value of one, when the footpoint displacement is comparable to the loop length,  $L$ . These properties will be found to be general characteristics of this system.

#### 4.2.4 One-Dimensional Equilibrium Equation

Here the two dimensional Grad–Shafranov equation, Equation (2.27), derived in Chapter 2, Section 2.6, is used to find an equation describing a one dimensional equilibrium.

When  $l/L \ll 1$  a simple estimate of the final equilibrium state is possible, even when the footpoint displacement,  $D$ , is larger than the half-length,  $L$ , i.e.  $D/L \geq 1$ , by solving the 1D form of the Grad–Shafranov equation. Following the approach of Lothian and Hood 1989; Browning and Hood 1989, and Mellor et al. 2005, we can use the fact that the 2D equilibrium can be expressed in terms of the flux function,  $A(x, y)$ , which satisfies the Grad–Shafranov equation, Equation (2.27).

For shearing motions defined in Equations (4.3)–(4.5), the photospheric footpoint displacement is given by integrating a fieldline from its initial position,  $(x_0, y_0)$ , to its final one at  $(x, y)$ . Consider the equation for magnetic fieldlines which can be written as

$$\frac{dx}{B_x} = \frac{dy}{B_y} = \frac{dz}{B_z} = \frac{ds}{B},$$

where  $s$  is a parameter along the fieldline and  $B = |\mathbf{B}|$ . Since the velocity at the boundary moves the fieldlines in the  $z$  direction, the distance moved is simply the footpoint displacement,  $D$ . We can write

$$\begin{aligned} \frac{dz}{B_z} &= \frac{dy}{B_y}, \\ \Rightarrow \frac{dz}{dy} &= \frac{B_z}{B_y}. \end{aligned} \quad (4.9)$$

We can now integrate both sides of Equation (4.9) with respect to  $y$ . Thus the LHS simply gives the displacement of a fieldline in the  $z$  direction, i.e the displacement of the footpoints. Since  $B_y = -\frac{\partial A}{\partial x}$  and  $A$  are both functions of  $x$ , it follows that we can write  $B_y$  as a function of  $A$  as  $B_y(A)$ . Also since  $B_z = B_z(A)$  is a function of  $A$ , so is the footpoint displacement, denoted by  $D(A)$ . Since  $A$  is constant along fieldlines, the integrals are evaluated at a constant value of  $A$ . Rearranging Equation (4.9) gives

$$\begin{aligned} \int dz &= \int_0^{+L} \left( \frac{B_z}{B_y} \right) \Big|_{A=\text{const}} dy, \\ \Rightarrow D(A(x, L)) &= \int_{y=0}^{y=+L} \left( \frac{B_z(A)}{B_y} \right) \Big|_{A=\text{const}} dy, \\ &= B_z(A) \int_{y=0}^{y=+L} \left( \frac{1}{-\partial A / \partial x} \right) \Big|_{A=\text{const}} dy. \end{aligned} \quad (4.10)$$

As shown in the above articles and from the magneto-frictional relaxation results in Section 4.2.3 and Figure 4.3, away from the boundaries we can ignore the boundary layers and assume that the fieldlines are essentially straight over most of the loop length. A value of  $l/L \ll 1$  is always assumed. Away from the boundary layers  $A$  is independent of  $y$  and this implies that the integrand in Equation (4.10) is independent of  $y$ . Therefore, we can

determine  $B_z(A)$  in terms of the footpoint displacement by integrating Equation (4.10). This gives

$$B_z(A) = -\frac{D(A)}{L} \frac{dA}{dx}. \quad (4.11)$$

For the shearing motion in Equation (4.3), we have at  $y = L$  that  $D(A) = V_0(t - t_1) \sin kx$ , where  $k = \pi/l$  and  $A(x, L) = -B_0x$ . Hence,  $D(A) = V_0(t - t_1) \sin(kx) = -D \sin(kA/B_0)$ , where  $D = V_0(t - t_1)$  is the maximum footpoint displacement.

The gas pressure can also be written as a function of  $A$ . Conservation of flux and mass between any two fieldlines implies that

$$\frac{B_y}{\rho} = \frac{B_0}{\rho_0}, \quad (4.12)$$

where  $B_0$  and  $\rho_0$  are the initial unsheared values. Next, if the effect of viscous heating is small, the entropy remains constant between any two fieldlines so that

$$\frac{p}{\rho^\gamma} = \frac{p_0}{\rho_0^\gamma}. \quad (4.13)$$

Rearranging the last two equations, Equation (4.12) and Equation (4.13), gives the pressure in terms of  $B_y$  as

$$p = \frac{p_0}{B_0^\gamma} B_y^\gamma = \frac{p_0}{B_0^\gamma} \left( -\frac{dA}{dx} \right)^\gamma, \quad (4.14)$$

where  $-\frac{dA}{dx} > 0$ .

The Grad–Shafranov equation, Equation (2.27), can be written as a 1D pressure balance equation of the form

$$\begin{aligned} & \frac{d^2 A}{dx^2} + \frac{d}{dA} \left( \frac{B_z^2(A)}{2} + \mu p(A) \right) = 0, \\ \Rightarrow & \frac{d^2 A}{dx^2} + \frac{dx}{dA} \frac{d}{dx} \left( \frac{B_z^2(A)}{2} + \mu p(A) \right) = 0, \\ \Rightarrow & \frac{dA}{dx} \frac{d^2 A}{dx^2} + \frac{d}{dx} \left( \frac{B_z^2(A)}{2} + \mu p(A) \right) = 0, \\ \Rightarrow & \frac{d}{dx} \left( \frac{1}{2} \left( \frac{dA}{dx} \right)^2 \right) + \frac{d}{dx} \left( \frac{B_z^2(A)}{2} + \mu p(A) \right) = 0, \\ \Rightarrow & \frac{d}{dx} \left( \left( \frac{dA}{dx} \right)^2 + B_z^2(A) + 2\mu p(A) \right) = 0, \end{aligned} \quad (4.15)$$

where  $B_z(A)$  and  $p(A)$  are given by Equation (4.11) and Equation (4.14). This implies that the total pressure is constant away from the boundary layers and there is no magnetic tension. It is computationally easier to express all variables in Equation (4.15) in terms of

the flux function,  $A$ , and solve

$$\frac{d^2 A}{dx^2} \left( 1 + \left( \frac{D}{L} \right)^2 \sin^2(kA/B_0) + \frac{2\mu\gamma p_0}{B_0^\gamma} \left( -\frac{dA}{dx} \right)^{\gamma-2} \right) = -\frac{k}{2B_0} \left( \frac{D}{L} \right)^2 \sin(2kA/B_0) \left( \frac{dA}{dx} \right)^2, \quad (4.16)$$

subject to  $A(\pm l) = \mp B_0 l$ . The value of the constant total pressure is determined as part of the solution.

It is useful to investigate analytic solutions of Equation (4.16) in the extreme cases of low and high  $D/L$ . For small displacement,  $D/L \ll 1$ , the solution to Equation (4.16) is

$$A = -B_0 \left( x + \left( \frac{D}{L} \right)^2 \frac{\sin(2kx)}{8k(1 + 2c_s^2/V_A^2)} \right) + O\left(\frac{D^4}{L^4}\right), \quad (4.17a)$$

$$B_y = B_0 \left( 1 + \left( \frac{D}{L} \right)^2 \frac{\cos(2kx)}{4(1 + 2c_s^2/V_A^2)} \right) + O\left(\frac{D^4}{L^4}\right). \quad (4.17b)$$

Hence, the correction to  $B_y$  is small (of order  $(D/L)^2$ ). For large displacement,  $D/L \gg 1$ , the LHS of Equation (4.16) is dominated by the middle term, away from  $x = 0$  and  $x = \pm l$ . In this case the equation to solve is

$$\frac{d}{dx} \left( \left( \frac{D}{L} \right)^2 \sin^2(kA/B_0) \left( \frac{dA}{dx} \right)^2 \right) = 0. \quad (4.18)$$

This gives solutions for  $A$ ,  $B_y$  and  $B_z$  as

$$A = -\frac{B_0}{k} \cos^{-1} \left( 1 - \frac{2|x|}{l} \right), \quad B_z = B_0 \frac{D}{L} \frac{2}{\pi} \frac{\sin(kA/B_0)}{|\sin(kA/B_0)|}$$

and  $B_y = B_0 \frac{2}{\pi} \frac{1}{|\sin(kA/B_0)|}, \quad (4.19)$

thus  $B_z$  has the form of a square wave with amplitude  $B_0(2/\pi)(D/L)$ . The minimum value of  $B_y$  is  $B_0(2/\pi)$ . The variation of the axial field with  $x$  is discussed along with the other approaches in Section 4.3.

#### 4.2.5 Linear and Weakly Nonlinear Expansion

A simple way to gain insight into the properties of solutions of the MHD equations is to linearise the equations about an initial equilibrium state. The equilibrium considered here consists of a uniform background magnetic field,  $B_0$ . In this section, we consider small perturbations to this state. The expansion is for the case  $B_\perp \ll B_0$ , which we expect to be valid when  $D/L \ll 1$  and which will be checked a posteriori. Thus, the linear expansion

is

$$\mathbf{B} = B_0 \hat{\mathbf{e}}_y + B_{1z}(y, t) \sin kx \hat{\mathbf{e}}_z + (B_{2x}(x, y, t) \hat{\mathbf{e}}_x + B_{2y}(x, y, t) \hat{\mathbf{e}}_y) \cdots, \quad (4.20a)$$

$$\mathbf{v} = V_{1z}(y, t) \sin kx \hat{\mathbf{e}}_z + (V_{2x}(x, y, t) \hat{\mathbf{e}}_x + V_{2y}(x, y, t) \hat{\mathbf{e}}_y) \cdots, \quad (4.20b)$$

$$p = p_0 + p_2(x, y, t) \cdots, \quad (4.20c)$$

$$\rho = \rho_0 + \rho_2(x, y, t) \cdots, \quad (4.20d)$$

where  $B_0$ ,  $p_0$ , and  $\rho_0$  are the constant initial state quantities. The subscript “1” denotes first-order terms. Since, in general, incompressible shearing motions, such as Equation (4.3) used here, initially only produce Alfvén waves, there are no first-order variations in  $\rho$  and  $p$ . The subscript “2” indicates terms that are second order in magnitude and thus driven by products of the first-order terms. Such terms are weakly nonlinear. The higher order corrections to the Alfvén wave terms will come in at third order, which is not considered here. This expansion, Equation (4.20), breaks down when the magnitude of higher order terms is equal to the next lowest order terms, i.e when the second-order terms become as large as the first-order terms. When this happens, full MHD must be used to capture all nonlinear effects.

The MHD equations, Equations (4.1), can now be expanded using Equation (4.20). We consider terms up to and including second-order. To first-order, we have the equation for damped Alfvén waves

$$\rho_0 \frac{\partial V_{1z}}{\partial t} = B_0 \frac{\partial B_{1z}}{\partial y} + \rho_0 \nu \nabla^2 V_{1z}, \quad (4.21a)$$

$$\frac{\partial B_{1z}}{\partial t} = B_0 \frac{\partial V_{1z}}{\partial y}. \quad (4.21b)$$



The second-order, weakly nonlinear equations are

$$\begin{aligned} \rho_0 \frac{\partial v_{2x}}{\partial t} = & -\frac{\partial}{\partial x} \left( p_2 + B_0 B_{2y} + \frac{1}{2} B_{1z}^2 \sin^2 kx \right) + B_0 \frac{\partial B_{2x}}{\partial y} \\ & + \rho_0 \nu \left( \frac{\partial^2 v_{2x}}{\partial x^2} + \frac{\partial^2 v_{2x}}{\partial y^2} + \frac{1}{3} \frac{\partial}{\partial x} \left( \frac{\partial v_{2x}}{\partial x} + \frac{\partial v_{2y}}{\partial y} \right) \right), \end{aligned} \quad (4.22a)$$

$$\begin{aligned} \rho_0 \frac{\partial v_{2y}}{\partial t} = & -\frac{\partial}{\partial y} \left( p_2 + \frac{1}{2} B_{1z}^2 \sin^2 kx \right) \\ & + \rho_0 \nu \left( \frac{\partial^2 v_{2y}}{\partial x^2} + \frac{\partial^2 v_{2y}}{\partial y^2} + \frac{1}{3} \frac{\partial}{\partial y} \left( \frac{\partial v_{2x}}{\partial x} + \frac{\partial v_{2y}}{\partial y} \right) \right), \end{aligned} \quad (4.22b)$$

$$\frac{\partial p_2}{\partial t} = -\rho_0 \left( \frac{\partial v_{2x}}{\partial x} + \frac{\partial v_{2y}}{\partial y} \right), \quad (4.22c)$$

$$\frac{\partial B_{2x}}{\partial t} = B_0 \frac{\partial v_{2x}}{\partial y}, \quad (4.22d)$$

$$\frac{\partial B_{2y}}{\partial t} = -B_0 \frac{\partial v_{2x}}{\partial x}, \quad (4.22e)$$

$$\begin{aligned} \frac{\partial p_2}{\partial t} = & -\gamma p_0 \left( \frac{\partial v_{2x}}{\partial x} + \frac{\partial v_{2y}}{\partial y} \right) \\ & + (\gamma - 1) \rho_0 \nu \left( k^2 V_{1z}^2 \cos^2 kx + \left( \frac{\partial V_{1z}}{\partial y} \right)^2 \sin^2 kx \right). \end{aligned} \quad (4.22f)$$

In Equation (4.22a), Equation (4.22b), and Equation (4.22f), the linear Alfvén wave terms appear as quadratic sources for the second-order variables.

Next, analytic solutions of these first- and second-order equations are discussed.

### First-order Solutions

Once the shearing motion starts, an Alfvén wave is excited. This wave is damped due to the small viscosity and a steady state is reached. The solution to the first-order, linear equations, Equation (4.21a) with the initial condition:  $v_{1z} = B_{1z} = 0$  when the driver is switched on at  $t = t_1$ , is given by a steady state solution and a Fourier series representation of a damped standing Alfvén wave. The solution for  $V_{1z}$  is of the form

$$\left( \frac{V_{0y}}{L} + \sum_{n=1}^{\infty} \alpha_n \sin(n\pi y/L) e^{i\omega(t-t_1)} \right) \sin kx,$$

where  $\omega$  satisfies the appropriate dispersion relation. Due to viscosity,  $\omega$  is complex and the Fourier series terms decay to zero for large time leaving the steady state solution for  $V_{1z}$ , given by

$$V_{1z} = \begin{cases} 0, & t < t_1, \\ \frac{V_{0y}}{L} \sin kx, & t_1 < t, \end{cases} \quad (4.23)$$

This gives a steady state solution for  $B_{1z}$  in Equation (4.21b), given by

$$B_{1z} = \begin{cases} 0, & t < t_1, \\ B_0 \left( \frac{V_0(t-t_1)}{L} + \frac{\nu k^2 L V_0}{2V_A^2} \left( \frac{y^2}{L^2} - 1 \right) \right) \sin kx, & t_1 < t. \end{cases} \quad (4.24)$$

These solutions for  $v_{1z}$  and  $B_{1z}$  will be modified once the nonlinearities develop. Corrections to these steady state solutions are third-order which are neglected, thus in the following we refer to  $B_{1z}$  as  $B_z$ . The final steady state for  $B_{1z}$ , given in Equation (4.24) consists of two terms. The first term depends on the footpoint displacement,  $D = V_0(t - t_1)$ , and the second is due to viscosity and is independent of time. When the footpoints of the magnetic field are being moved at a speed  $V_0$  in a viscous fluid, the central part will lag behind. Hence,  $B_z$  is smaller in magnitude at  $y = 0$  compared to  $y = \pm L$ . This term produces a gradient along the loop length. Although small this term will contribute to the magnetic pressure produced by the sheared magnetic field and play an important part in the dynamics of this system, which will be discussed in Section 4.3. The 1D approach, derived in Section 4.2.4, in the limit of large displacement, Equation (4.19), and the first order solution, Equation (4.24), can be used to give upper and lower bounds for the maximum of  $B_z$ . Taking the maximum value of  $B_z$  from Equation (4.19) and Equation (4.24), the maximum value lies between

$$B_0 \frac{2D}{\pi L} \leq B_{\max} \leq B_0 \frac{D}{L}. \quad (4.25)$$

The maximum value of  $B_z$  from the full MHD data in Table 4.1, on page 79, and these upper and lower bounds are plotted as a function of  $t$  in Figure 4.4 on page 74. This shows that the actual maximum of the sheared magnetic field,  $B_z$ , agrees with the first-order linear solution for small  $t$  and becomes more like a square wave, as predicted by the 1D approach, for large  $t$ . The  $x$  dependence of  $B_z$  is discussed in the results section, Section 4.3, where it is shown that  $B_z$  does indeed have a square wave profile at large  $t$  or large  $D$ .

The leading order surface integrated kinetic energy can be calculated as a function of time by using the first-order solution, Equation (4.23), given by

$$\int_{x=-l}^l \int_{y=-L}^L \frac{1}{2} \rho_0 V_{1z}^2 dy dx = \frac{1}{3} \rho_0 V_0^2 l L. \quad (4.26)$$

Hence, to leading order the kinetic energy is constant in time. This indicates that the system is in a steady state. This will be compared to the full MHD results in Section 4.3. The leading order change to the integrated magnetic energy requires knowledge of second-order variables. It will be shown that the second order contributions to the magnetic field integrate to zero leaving only the first order term in Equation (4.24). The leading order change in the surface integrated magnetic energy, including the viscosity terms, up to second

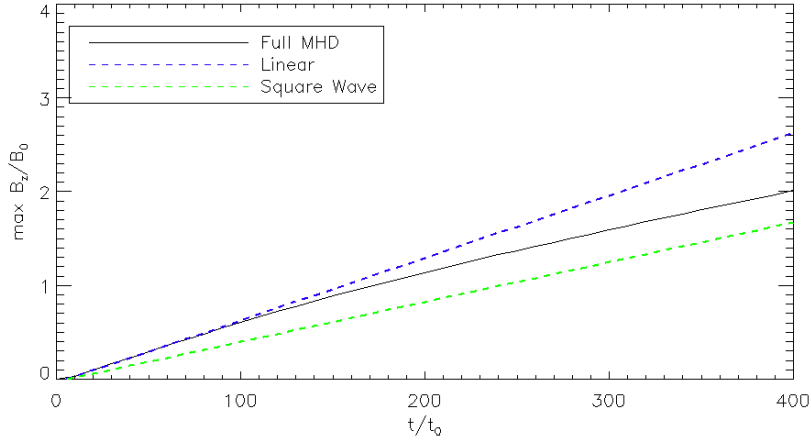


Figure 4.4: The maximum of  $B_z$  for simulation 1 data in Table 4.1 on page 79 and the upper and lower bounds for the maximum of  $B_z$  in Equation (4.25) given by the maximum of the 1D solution for  $B_z$  in the limit of large shear, Equation (4.19) and the first-order linear prediction for  $B_{1z}$ , Equation (4.24), as a function of time  $t$ .

order is given by

$$\begin{aligned}
 & \int_{x=-l}^l \int_{y=-L}^L \frac{1}{2} B_{1z}^2 dy dx, \\
 &= B_0^2 l L \left( \frac{V_0^2 (t - t_1)^2}{L^2} - \frac{2}{3} \frac{k^2 \nu V_0^2}{V_A^2} (t - t_1) + \frac{2}{15} \frac{k^4 \nu^2 V_0^2 L^2}{V_A^4} \right), \\
 &\approx B_0^2 l L \left( \frac{D^2}{L^2} - \frac{2}{3} \frac{D}{L} \frac{k^2 \nu V_0 L}{V_A^2} + \frac{2}{15} \left( \frac{k^2 \nu V_0 L}{V_A^2} \right)^2 \right). \tag{4.27}
 \end{aligned}$$

For high  $D/L$  or equivalently large time, the magnetic energy is proportional to  $(D/L)^2$ .

## Second-order Solutions

Now that the first-order steady state solutions for  $v_{1z}$  and  $B_z$  in Equation (4.23) and Equation (4.24), are known, the second-order equations, Equation (4.22), can be solved. The solutions are complex. Although, the steps to generate them are straightforward, it is a lengthy derivation. For brevity, full details of the solutions and derivation are given in

Appendix C. The basic forms of the solutions are given by

$$v_{2x}(x, y, t) = (B(y)(t - t_1) + C(y)) \sin(2kx) , \quad (4.28a)$$

$$v_{2y}(x, y, t) = (F(y)(t - t_1) + E(y)) \cos(2kx) + G(y) , \quad (4.28b)$$

$$B_{2x}(x, y, t) = B_0 \left( B'(y) \frac{(t - t_1)^2}{2} + C'(y)(t - t_1) \right) \sin(2kx) , \quad (4.28c)$$

$$B_{2y}(x, y, t) = -2kB_0 \left( B(y) \frac{(t - t_1)^2}{2} + C(y)(t - t_1) \right) \cos(2kx) , \quad (4.28d)$$

$$\frac{\rho_2(x, y, t)}{\rho_0} = -G'(y)(t - t_1) \quad (4.28e)$$

$$+ \left( [2kB(y) + F'(y)] \frac{(t - t_1)^2}{2} + (2kC(y) + E'(y))(t - t_1) \right) \cos(2kx) ,$$

$$p_2(x, y, t) = \frac{\gamma p_0}{\rho_0} \rho_2$$

$$+ (\gamma - 1) \rho_0 \nu (t - t_1) \left( k^2 V_{1z}^2 \cos^2 kx + \left( \frac{\partial V_{1z}}{\partial y} \right)^2 \sin^2 kx \right) . \quad (4.28f)$$

Here ' denotes a derivative with respect to  $y$ . The functions  $G(y)$ ,  $B(y)$ ,  $C(y)$ ,  $F(y)$ , and  $E(y)$  are determined in Appendix ?? . A key point to note is that averaging  $v_{2y}$  over  $x$  gives a function of  $y$ , namely  $G(y)$ , which is

$$G(y) = \frac{\nu k^2 V_0^2 (2\gamma - 1)}{12c_s^2} y \left( \frac{y^2}{L^2} - 1 \right) . \quad (4.29)$$

For a fixed value of viscosity,  $\nu$ , the magnitude of  $G(y)$  increases when the initial pressure,  $p_0$ , is reduced (decrease in sound speed,  $c_s$ ). The solution for  $\rho_2$  also involves  $y$  derivatives of  $G(y)$ , which results in a change in density that is independent of  $x$ , given by

$$-\rho_0 G'(y)(t - t_1) = \rho_0 \frac{\nu k^2 V_0^2 (2\gamma - 1)}{12c_s^2} \left( 1 - 3 \frac{y^2}{L^2} \right) (t - t_1) . \quad (4.30)$$

Integrating  $\rho_2(x, y, t)$  over  $x$  and  $y$ , shows that mass is conserved. So the variations of  $\rho$  from its uniform initial state are simply a redistribution of the mass as a result of the magnetic pressure created by the sheared field,  $B_z$ , along  $x$  and  $y$ . From Equation (4.30), the magnitude of this term is proportional to  $\frac{\nu k^2 V_0^2}{c_s^2} (t - t_1)$ . Defining a diffusion length as  $l_d = \sqrt{\nu(t - t_1)}$ , the change in density depends on the ratio of two lengthscales and two velocities, as

$$\pi^2 \left( \frac{l_d}{l} \right)^2 \frac{V_0^2}{c_s^2} .$$

As  $l_d$  increases with time,  $G'(y)$  will eventually become important. In addition, it becomes important for faster driving speeds,  $V_0$ , and/or slower sound speed,  $c_s$ .

### Second-order Solutions: Neglect Viscosity

As an example, we illustrate the weakly nonlinear dynamics by neglecting viscosity in the second order equations, Equation (4.22). Setting  $\nu = 0$  the functions,  $G(y)$ ,  $B(y)$ ,  $C(y)$ ,  $E(y)$  and  $F(y)$ , become

$$G(y) = C(y) = E(y) = 0, \quad (4.31a)$$

$$B(y) = \frac{\delta}{4k} \left( \frac{\cosh(2ky)}{\cosh(2kL)} - 1 \right), \quad (4.31b)$$

$$F(y) = \frac{\delta}{4k} \left( \tanh(2kL) \frac{y}{L} - \frac{\sinh(2ky)}{\cosh(2kL)} \right), \quad (4.31c)$$

$$\delta = \frac{V_0^2}{L^2} \frac{1}{1 + c_s^2/V_A^2 (1 - \tanh(2kL)/2kL)}. \quad (4.31d)$$

The terms,  $\cosh(2ky)/\cosh(2kL)$  and  $\sinh(2ky)/\cosh(2kL)$ , in  $B(y)$  and  $F(y)$  clearly show that boundary layers are present in the solutions. The width of the boundary layer is controlled by the magnitude of  $2kL = 2\frac{\pi}{l}L$ . Hence, the ratio of the half-width to half-length,  $l/L$ , is important for the size of the boundary layer, as mentioned in Section 4.2.3.

### Second-order Solutions: Away from Boundaries

These solutions can be further simplified by neglecting the boundary terms. Away from the boundary layers, namely for  $2kL \gg 1$ ,  $B(y) \approx -\delta/4k$ ,  $F(y) \approx O(1/2kL)$ , and  $(1 + c_s^2/V_A^2)\delta \approx (V_0^2/L^2)$ . In this case the second-order solutions, Equations (4.28), also neglecting viscosity, can be expressed as

$$v_{2x} = -\frac{D}{L} \frac{V_0}{4kL(1 + c_s^2/V_A^2)} \sin(2kx), \quad (4.32a)$$

$$v_{2y} = \frac{D}{L} \frac{V_0}{4kL(1 + c_s^2/V_A^2)} \frac{y}{L} \cos(2kx), \quad (4.32b)$$

$$B_{2y} = \frac{D^2}{L^2} \frac{B_0 \cos(2kx)}{4(1 + c_s^2/V_A^2)}, \quad B_{2x} = 0, \quad (4.32c)$$

$$\rho_2 = \rho_0 \frac{B_{2y}}{B_0}, \quad p_2 = c_s^2 \rho_2 = \frac{c_s^2}{V_A^2} B_0 B_{2y}. \quad (4.32d)$$

We note that Equation (4.32c) and Equation (4.32d) agree with the linearised forms of Equation (4.12) and Equation (4.13) and Equation (4.17b) from the 1D equilibrium method in Section 4.2.4. In addition, the second-order total pressure,  $p_2 + B_{1z}^2/2 + B_0 B_{2y}$  is independent of  $x$  and equals  $(D^2/L^2)(B_0^2/4)$ .

From the first- and second-order magnetic field components, Equation (4.24) and Equation (4.32c), the magnitudes of these terms are in powers of  $D/L$ , making this the appropriate expansion parameter. Hence, these solutions are only strictly valid provided  $D/L \ll 1$ . When viscosity is included, from Equation (4.24) the ordering of the terms remains the same provided  $\nu < (2V_A^2/k^2 LV_0)(D/L)$ .

### 4.2.6 Reduced MHD

RMHD was discussed in detail in Chapter 3. This model is discussed in the context of the current  $2\frac{1}{2}$ D geometry. The RMHD equations, Equations (3.24), with  $\mathbf{B}_0 = B_0 \hat{\mathbf{e}}_y$  and assuming invariance in  $z$ , are

$$\rho_0 \frac{\partial v_x}{\partial t} + \rho_0 v_x \frac{\partial v_x}{\partial x} = -\frac{\partial}{\partial x} \left( p + \frac{b_x^2}{2} + \frac{b_z^2}{2} \right) + B_0 \frac{\partial b_x}{\partial y} + \rho_0 \nu \frac{\partial^2 v_x}{\partial x^2}, \quad (4.33a)$$

$$\rho_0 \frac{\partial v_z}{\partial t} + \rho_0 v_x \frac{\partial v_z}{\partial x} = b_x \frac{\partial b_z}{\partial x} + B_0 \frac{\partial b_z}{\partial y} + \rho_0 \nu \frac{\partial^2 v_z}{\partial x^2}, \quad (4.33b)$$

$$\frac{\partial b_x}{\partial t} + v_x \frac{\partial b_x}{\partial x} = b_x \frac{\partial v_x}{\partial x} + B_0 \frac{\partial v_x}{\partial y}, \quad (4.33c)$$

$$\frac{\partial b_z}{\partial t} + v_x \frac{\partial b_z}{\partial x} = b_x \frac{\partial v_z}{\partial x} + B_0 \frac{\partial v_z}{\partial y}, \quad (4.33d)$$

$$\frac{\partial v_x}{\partial x} = 0, \quad \frac{\partial b_x}{\partial x} = 0. \quad (4.33e)$$

As the footpoint displacement increases, the magnetic energy increases, as shown using linearisation in Equation (4.27). After a certain time the injected magnetic energy will exceed the initial energy contained in the background field. At this time the first assumption of RMHD, given in Section 3.4.1, will no longer be satisfied. This will happen when the footpoint displacement becomes comparable to the loop length,  $L$ . It was shown in Section 4.2.3 that there are steep gradients in the boundary layers created at the two photospheric boundaries. The second assumption of RMHD, requires small gradients along the loop length, will hold everywhere, except in these boundary layers. In our current system we have assumed  $z$  is invariant, leading to zero gradients in  $z$ . RMHD requires that derivatives along the background field, in  $y$ , are smaller than derivatives in  $x$  and  $z$ . It is likely that our assumption of invariance results in RMHD not being valid for this system.

Equations (4.33e) state that  $v_x$  and  $b_x$  are independent of  $x$ . It is not physically realistic for these components to be functions of time, hence they simply reduce to  $v_x = 0$  and  $b_x = 0$ . Hence, the RMHD equations, Equations (4.33), simplify to

$$0 = -\frac{\partial}{\partial x} \left( p + \frac{b_z^2}{2} \right), \quad (4.34a)$$

$$\rho_0 \frac{\partial v_z}{\partial t} = B_0 \frac{\partial b_z}{\partial y} + \rho_0 \nu \frac{\partial^2 v_z}{\partial x^2}, \quad (4.34b)$$

$$\frac{\partial b_z}{\partial t} = B_0 \frac{\partial v_z}{\partial y}. \quad (4.34c)$$

Equation (4.34b) and Equation (4.34c) are similar to the first-order solutions in Equation (4.21) and describe the propagation of damped Alfvén waves. Once the Alfvén waves introduced by the shearing motions have damped, the field passes through sequences of steady state solutions that are the same as those described by the first-order linear MHD solutions, Equation (4.23) and Equation (4.24). In fact, the first-order linear MHD solu-

tions are exact solutions of the RMHD equations. However, an important part is that, as mentioned in an appendix of Oughton, Dmitruk, and Matthaeus 2003, it is incorrect to linearise the RMHD equations. This equivalence with first order linear MHD is simply due to the linear coupling of the 2D planes by Alfvén waves. Solutions of  $v_z$  and  $b_z$  will be in agreement with the linearised, first-order solution.

From Equation (4.34a),  $p + b_z^2/2$  is constant in the horizontal direction,  $x$ . However, this total pressure is only constant in space and will still depend on time, as in the 1D method presented in Section 4.2.4. Hence, the gas pressure must balance the  $x$  variations in  $b_z^2/2$ . This implies that as the sheared magnetic field,  $b_z$ , increases the magnitude of the pressure will increase. After a certain time the pressure may be large. Such a high gas pressure may not be compatible with a low  $\beta_0$  plasma, as assumed in RMHD.

In contrast, the 1D approach and second-order solutions, discussed in Section 4.2.4 and Section 4.2.5, include the contribution from the magnetic pressure due to the modification of the background magnetic field,  $B_y$ , namely  $B_0 + b_y$  in the equations. This is a second-order change to the uniform background magnetic field, which is not included in RMHD. Hence, the assumption that the axial field does not change, must be dropped when the footpoint displacement is sufficiently large. In this case, the total pressure that is constant in  $x$ , namely

$$p + \frac{B_0^2}{2} + B_0 b_y + \frac{b_z^2}{2} = C(t) . \quad (4.35)$$

### 4.3 Results

Now we briefly summarise each method and clearly distinguish between the many related parameters ( $p_0$ ,  $\beta_0$ ,  $e_0$ ,  $D$ ,  $t$ ) before comparing the results of all the methods in Section 4.3.1 and analysing the full MHD dynamics in Section 4.3.2.

#### Full MHD:

For full MHD, we solve Equations (4.1) using the MHD code, Lare2D (see Arber et al. 2001), in  $2\frac{1}{2}$ D ( $\partial/\partial z = 0$ ) for the system described in Section 4.2.2 with the driven boundary condition in Equation (4.3) and Equation (4.4). The half width and half length of the loop are  $l = 0.3$  and  $L = 3$  respectively. The driving speed is  $V_0 = 0.02$  and the switch-on time  $t_1 = 6$ . Viscosity and resistivity are  $\nu = 10^{-3}$  and  $\eta = 0$ .

The driving amplitude is subsonic and subalfvénic and satisfies Equation (4.6), which means the magnetic field passes through a sequence of equilibria. We performed four full MHD simulations, each with a different value of  $\beta_0$ , or equivalently  $p_0$  or  $e_0$ , shown in Table 4.1. In the following, simulation 1 is referred to as high  $\beta_0$  and simulation 3 as low  $\beta_0$  unless otherwise stated. This choice was made for the majority of the results since the other two simulations are qualitatively the same and agree with our understanding in relation to their initial conditions. The maximum displacement,  $D$ , is related to time,  $t$ , by

Table 4.1: The initial internal energy,  $e_0$ , and  $\beta_0$  for our four full MHD simulations.

Simulation	$\beta_0 = 2p_0$	$e_0 = 3/2p_0$
1	4/3	1.0
2	4/30	0.1
3	4/300	0.01
4	4/3000	0.001

Equation (4.5)

$$D = V_0(t - t_1). \quad (4.36)$$

We choose various times, or equivalently footpoint displacements,  $D$ , using Equation (4.36), both smaller than and larger than  $L$ , such that  $0.29 \lesssim D/L \lesssim 2.63$ . The chosen values of  $D$  and  $t$  corresponding to snapshots of the full MHD simulations are shown as symbols in Figure 4.2 on page 65.

**Relaxation:**

- As described in Section 4.2.3, Equations (4.7) are solved to evolve the vector potential,  $\mathbf{A}$ , from an initial state perturbed by the footpoint displacement on the boundaries to a force-free equilibrium.
- Since the actual time evolution of this method is not physical, only the magnetic field components for the final state can be compared, hence there are no quantities as functions of time, such as the kinetic energy.
- The perturbation, Equation (4.8), is determined by the maximum displacement,  $D$ .

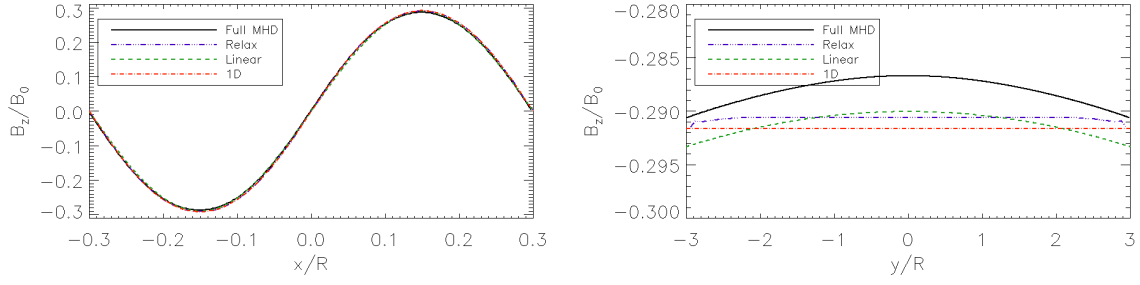
**One-dimensional equilibrium approach:**

- The 1D equilibrium approach, described in Section 4.2.4, involves solving Equation (4.16) for the flux function,  $A(x, y)$ .
- Equation (4.16) is determined by the maximum displacement,  $D$ , and initial pressure,  $p_0$ .
- This approach gives results for  $B_y$ ,  $B_z$ ,  $p$ ,  $j_y$ ,  $j_z$ , and  $\rho$  as functions of  $x$ .

**Linearisation:**

- The first- and second-order equations and their analytic solution of each variable are described in detail in Section 4.2.5 and in Appendix ??.
- These expressions are dependent on time,  $t$ , and the initial pressure,  $p_0$ .
- The solution for each variable consists of the linear first-order and second-order terms in order to take into account weakly non-linear effects. These results from the linearisation method are denoted “linear” in the results section.




 (a)  $B_z$  as a function of  $x$  at the midpoint in  $y$ .

 (b)  $B_z$  as a function of  $y$  at  $x = 0.15$ .

 Figure 4.5: Sheared magnetic field,  $B_z$ , for simulation 2 in Table 4.1 on page 79 at  $t = 50$ . The footpoint displacement is  $D/L \approx 0.29$ .

#### RMHD:

- As discussed in Section 4.2.6, RMHD is not applicable to this problem, but it does agree with the first-order terms in linear MHD.
- The first-order linear terms are an exact solution to the RMHD equations, Equation (4.34b) and Equation (4.34c).

We discuss comparisons of each of these methods in Section 4.3.1 and then describe the full MHD dynamics of the system in more detail in Section 4.3.2.

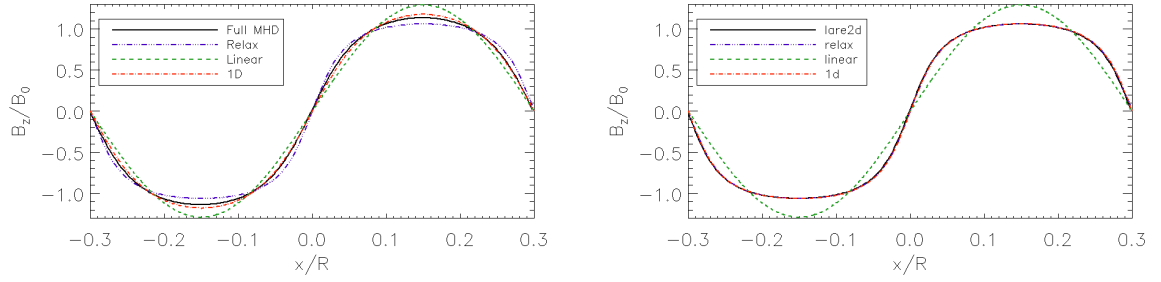
### 4.3.1 Comparison With Full MHD Results

#### Comparison of $B_z$

First, we consider the magnetic field component,  $B_z$ , introduced by the shearing motion. Figure 4.5, on page 80, shows  $B_z$  as a function of  $x$ , at the midpoint at  $y = 0$  (Figure 4.5a) and a function of  $y$  at  $x = -l/2$  (Figure 4.5b) at  $t = 50$ , corresponding to  $D/L \approx 0.29$  using Equation (4.36). This is for simulation 2 in Table 4.1 on page 79, which has a reasonably small plasma  $\beta_0$  and the resulting magnetic field will be approximately force-free. All of the approximations are shown in Figure 4.5. In fact, the agreement of the  $x$  dependence of  $B_z$  (Figure 4.5a) between the methods is remarkably good. This is surprising since the ratio of  $D/L$  is 0.29, which is not particularly small. Hence, one would expect the nonlinear terms to be important and the first- and second-order linear MHD solutions to be less accurate when compared to full MHD.

Full MHD and linearisation results are compared in Figure 4.5b, for  $B_z$  as a function of  $y$  at  $x = -l/2$ . As predicted by the linearised MHD expressions in Section 4.2.5, there is a slight variation of  $B_z$  with  $y$  which agrees with the full MHD results. However, the linear results do not include the slight slippage of  $B_z$  at the boundaries due to the strong boundary layer currents and so the two curves are slightly displaced. This  $y$  variation is not predicted by the 1D and relaxation methods, because they do not include viscosity.

When the footpoint displacement,  $D$ , is larger than the loop length,  $L$ , the shape of the  $B_z$  profile in  $x$  changes due to nonlinear effects and takes on an almost square wave



(a) Simulation 1.

(b) Simulation 3.

Figure 4.6: Plots of  $B_z$  against  $x$  at the midpoint,  $y = 0$ , for each method for time  $t = 200$  and footpoint displacement,  $D/L \approx 1.3$  for simulations in Table 4.1 on page 79.

shape, as predicted by the 1D approach (Section 4.2.4) when taking the limit of large  $D$  in Equation (4.19). The profile of  $B_z$  in  $x$  given by full MHD is shown in Figure 4.6, on page 81, for  $D/L \approx 3.9/3.0 = 1.3$  ( $t = 200$ ) for both high (Figure 4.6a) and low  $\beta_0$  (Figure 4.6b). The large gradients near  $x = 0$  and the boundaries correspond to an enhanced current component,  $j_y$  (shown in Figure 4.12 and discussed later in this section).

Solutions for  $B_z$  from each of the approximate methods are shown in Figure 4.6. For high plasma  $\beta_0$ , Figure 4.6a, the relaxation method predicts a magnitude of  $B_z$  slightly different compared to the full MHD results. However, this discrepancy is not present in Figure 4.6b, which is for low  $\beta_0$ . This is expected as the relaxation method assumes a low  $\beta$ . For both values of  $\beta_0$  the linear approximation is still remarkably good, even though it does not predict the square wave shape. The 1D approximation is essentially the same as the full MHD results for low  $\beta_0$  and is slightly different for high  $\beta_0$ . The maximum value of  $B_z$  is now about unity for both values of  $\beta_0$  and so it is definitely comparable in magnitude to the initial background field strength. RMHD results would be the same as the linear MHD results, however, since  $B_z \sim B_0 = 1$  the first RMHD assumption is not satisfied.

### Comparison of $B_y$

Initially,  $B_y$  is the only magnetic field component, which is subsequently modified during the time evolution. Figure 4.7, on page 82, shows  $B_y$  as a function of  $x$  at the midpoint,  $y = 0$ , for  $D/L \approx 0.63$  ( $t = 100$ ) in the top row and  $D/L \approx 1.3$  ( $t = 200$ ) in the bottom row and high  $\beta_0$  in the left column and low  $\beta_0$  in the right column.

For the full MHD results with low  $D/L \approx 0.63$  the maximum value of  $B_y$  has increased from the initial value of one by about 5% for high  $\beta_0$ , and 10% for low  $\beta_0$  where nonlinear effects are becoming important. Hence, for footpoint displacements smaller than the loop length the variations in  $B_y$  are small. For the case of high  $D/L \approx 1.3$  the maximum of  $B_y$  has increased by about 20% for high  $\beta_0$  and 30% for low  $\beta_0$ . It can be concluded that for high values of  $D$  any assumption that the background field remains constant is not valid.

The full MHD and 1D approaches agree extremely well for both values of  $D/L$  for low  $\beta_0$ , however there is a small discrepancy for high  $\beta_0$ . For the high plasma  $\beta_0$  case,

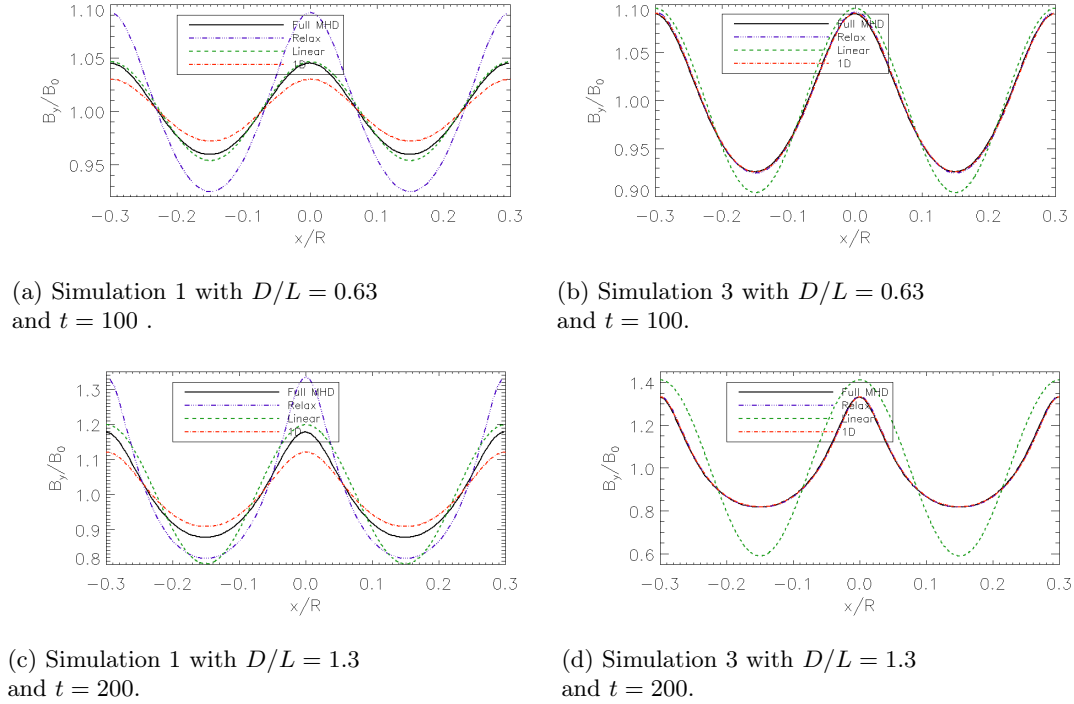


Figure 4.7: Plots of  $B_y$  against  $x$  at the midpoint,  $y = 0$ , for simulations in Table 4.1 on page 79.

(left column), only the relaxation results are significantly different from the others for both low and high  $D/L$ , as expected, since this method assumes the field is force-free. Similarly to  $B_z$ , in the low  $\beta_0$  regime in the right column, the relaxation method agrees with the full MHD and the 1D approaches regardless of the value of the footpoint displacement,  $D$ . Interestingly, the predictions for  $B_z$ , the shear component, from the relaxation method are consistently better than the  $B_y$  component, whereas one may expect the same accuracy for both components.

The first- and second-order linearised MHD solutions agree reasonably well with the full MHD results for low  $D/L \approx 0.63$  and high  $\beta_0$ . For low  $\beta_0$  the linear MHD results show a more noticeable discrepancy for small displacement. For large footpoint displacements,  $D/L \approx 1.3$  ( $t = 200$ ) in the bottom row, the second-order linearised MHD results predict a minimum value of  $B_y$  that is too low by about 10% for high  $\beta_0$ , and 25% for low  $\beta_0$  as the non-linear terms become more important.

#### Comparison of integrated energies

The surface integrated magnetic energy for all methods is shown in Figure 4.8, on page 83, as a function of time for high (Figure 4.8a) and low plasma  $\beta_0$  (Figure 4.8b). The Poynting flux associated with the shearing motion results in the magnetic energy increasing nearly quadratically in time for both values of  $\beta_0$ . The relaxation approach does not directly give quantities as functions of time. In order to calculate and compare the magnetic energy the magnetic field needs to relax for every value of the displacement. This is limited by resources so the magnetic energy is only calculated for a few values of  $D$ . These values of  $D$

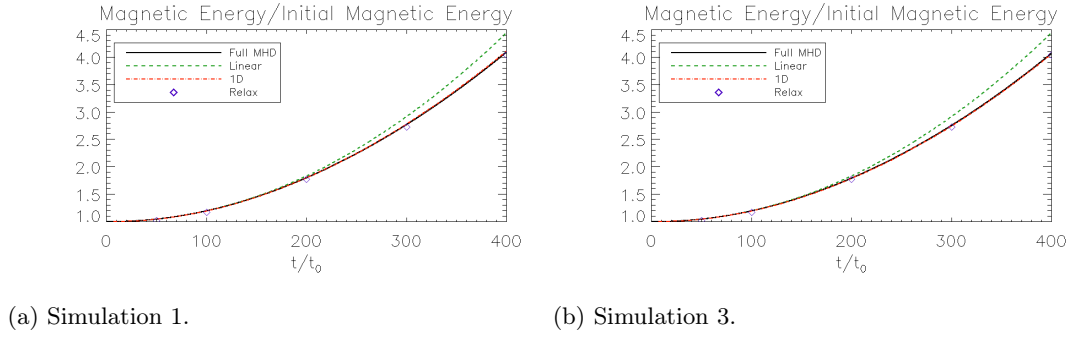


Figure 4.8: Surface integrated magnetic energy as a function of time,  $t$ , for simulations in Table 4.1 on page 79.

correspond to specific values of  $t$  as described in Equation (4.36). The resulting magnetic energy for the relaxation approach is shown as symbols in Figure 4.8. These data points agree well with the full MHD results. As noted for the other quantities, there is a marginal discrepancy for high  $\beta_0$  which is not present for low  $\beta_0$ . It is interesting to note that the 1D approach correctly matches the results from full MHD for all times, even when the footpoint displacement is larger than the half-length,  $L$ , for example, at  $t = 400$ ,  $D/L \approx 2.6$  using Equation (4.36). The analytical estimate from the linearised MHD equations, given in Equation (4.27), shows very good agreement up to  $t = 200$ ,  $D/L \approx 1.3$  when  $D \sim L$  and the linear solution is only in error by 10% at  $t = 400$ , when  $D/L \approx 2.6$ .

Thus, in comparison to full MHD, we can conclude that the slow magnetic field evolution is correctly modelled by the relaxation method and 1D approach for all times, provided the width-to-length ratio,  $l/L$ , is small, and by the linearised MHD method until the footpoint displacement becomes comparable to the loop half-length, regardless of the size of the plasma  $\beta_0$ . This is notable since once  $D \sim L$  one might not have expected the linearisation approach to be valid.

The surface integrated kinetic energy is shown in Figure 4.9, on page 84, as a function of time for each of the four different values of the initial plasma  $\beta_0$  for simulations given in Table 4.1 on page 79. The dashed lines are the kinetic energy estimates given by the first-order linearised MHD method in Equation (4.26). The constant value predicted by linearisation is only obtained by the full MHD system when the Alfvén waves, those excited when the boundary driving velocities are switched on, are dissipated. There are no estimates from either the relaxation method or the 1D approach, as they are assumed to be in equilibrium, hence do not involve velocity. The driving velocities are slow, hence the integrated kinetic energy is five orders of magnitude lower than the magnetic energy.

What is surprising is that the full MHD results only really match the prediction from linearisation, Equation (4.26), for an initial high  $\beta_0$  plasma. As  $\beta_0$  is reduced, the departure from the constant kinetic energy is much more significant. Note that simulation 4 did not run for as long as the other simulations due to computational problems, however, in fact, it has a lower final kinetic energy than the simulations which have run for longer.

The reason for this departure is due to the flow,  $v_y$ , along the loop length (as shown analytically by the linearised MHD method in Section 4.2.5), which is a consequence of the magnetic pressure gradient in  $y$  due to the  $y$  variation in  $B_z$  (see Equation (4.24)). The size

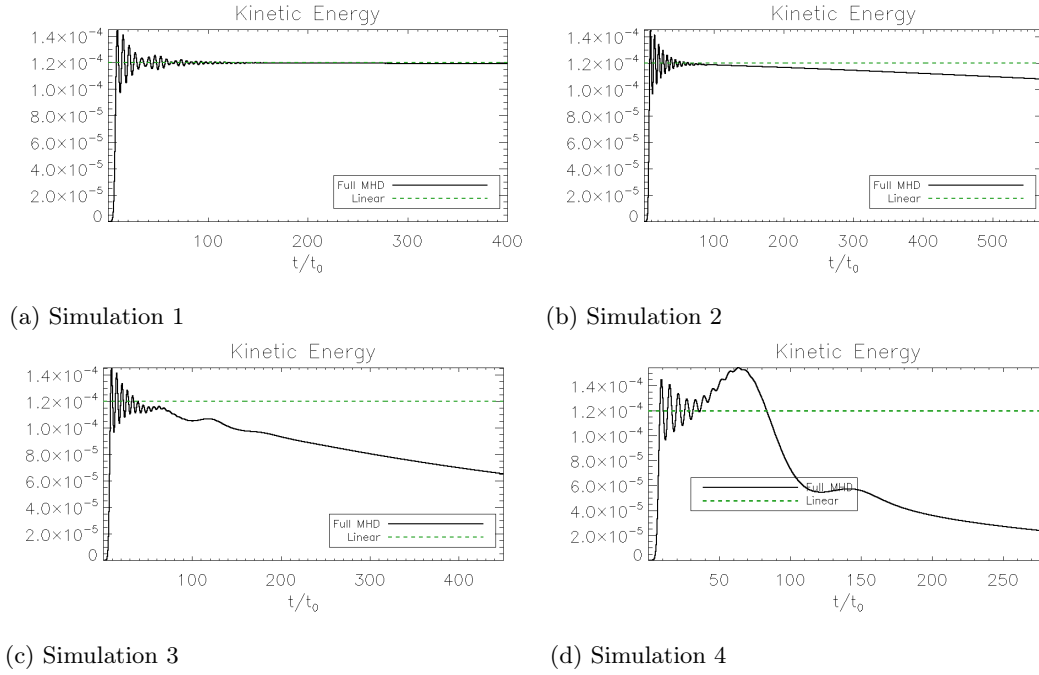


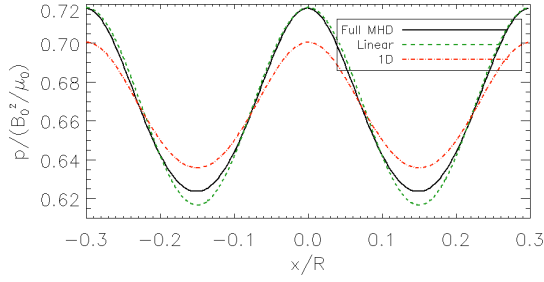
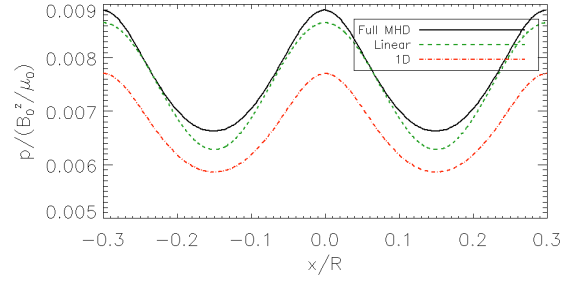
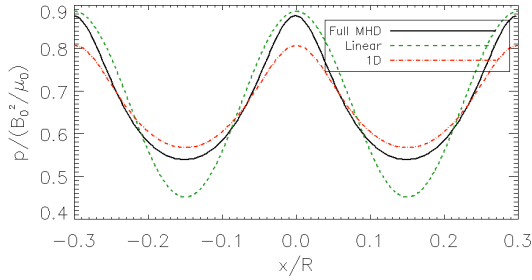
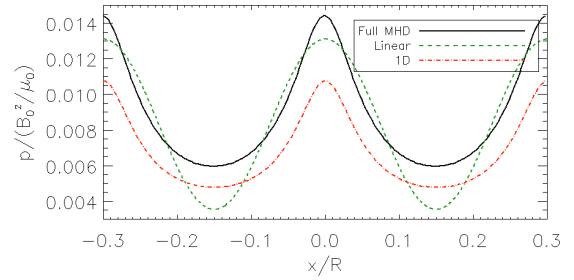
Figure 4.9: Surface integrated kinetic energy as a function of time,  $t$ , for simulations in Table 4.1 on page 79.

of the constant flow,  $G(y)$ , in the second-order solution (Section 4.2.5 and Equation (4.30) on page 75), is proportional to  $(l_d/l)^2(V_0/c_s)^2$ , where the diffusion lengthscale,  $l_d$ , is defined above in Section 4.2.5 under Equation (4.30) and  $c_s^2 = \gamma p_0/\rho_0$  is proportional to the initial gas pressure. The viscosity may be either real or due to numerical dissipation. In both cases, the viscosity damps out both the fast and Alfvén waves generated when the driving is switched on.

Once these waves are damped, the plasma can pass through sequences of equilibria. Although  $\nu$  is low, as time increases  $l_d$  will eventually become large, which means that  $p_0$  cannot be too low or else this change in density will occur sooner. This steady flow is due to the magnetic pressure gradients introduced by viscosity in the sheared component of the magnetic field,  $B_z$  (see the first-order equation for  $B_z$ , Equation (4.24)). Although the magnitude of this flow is small, it is constant in time and it will eventually modify the plasma density (see below and the second-order solution, Equation (4.30)). In turn, the change in the density will influence the integrated kinetic energy.

### Comparison of pressure

Since we vary the initial plasma  $\beta_0$  the initial pressure,  $p_0$ , varies accordingly. Figure 4.10, on page 85, shows  $p$  as a function of  $x$  at the midpoint in  $y$  for high  $\beta_0$  (left column) and low  $\beta_0$  (right column) for footpoint displacement  $D/L \approx 0.63$  in the top row and  $D/L \approx 1.3$  in the bottom row. The predicted pressure from linearisation and the 1D approach is compared to full MHD. The relaxation method assumes a force-free equilibrium so does not predict the pressure. The 1D approach gives a magnitude for  $p$  that is too small for high  $\beta_0$  for both low and high  $D$ .

(a) Simulation 1 with  $D/L = 0.63$  and  $t = 100$ .(b) Simulation 3 with  $D/L = 0.63$  and  $t = 100$ .(c) Simulation 1 with  $D/L = 1.3$  and  $t = 200$ .(d) Simulation 3 with  $D/L = 1.3$  and  $t = 200$ .Figure 4.10: Plots of  $p$  against  $x$  at the midpoint,  $y = 0$ , for simulations in Table 4.1 on page 79.

However, in the low  $\beta_0$  case it seems the underlying assumptions used in the 1D approach for the relationship between  $p$  and  $B_y$ , Equation (4.14), is no longer valid so the pressure is lower than for full MHD. This is notable since the 1D approach predicts  $B_y$  very accurately.

For both low and high  $\beta_0$  and small footpoint displacement  $D/L \approx 0.63$  ( $t = 100$ ), the linear MHD solution agrees reasonably well with the full MHD results. The discrepancy becomes larger for larger values of displacement,  $D/L \approx 1.3$ . Variations in pressure are not usually considered in RMHD.

The profile of  $p$  in  $x$  is similar to  $B_y$ . In the following section, Section 4.3.2, it is shown that the total pressure,  $p + \frac{1}{2}(B_y^2 + B_z^2)$ , at a certain time is spatially constant.

### Comparison with $\rho$

The plasma density as a function of  $x$  for the full MHD results, the linearised MHD method, and the 1D approach is shown in Figure 4.11, on page 86, at the midpoint in  $y$  for high plasma  $\beta_0$  (left column), low  $\beta_0$  (right column) and footpoint displacement of  $D/L \approx 0.63$  (top row) and  $D/L \approx 1.3$  (bottom row). The relaxation and RMHD methods are not considered as they do not account for variations in density.

For high  $\beta_0$  and small  $D/L$ , in Figure 4.11a, the agreement among the three methods is very good. The density variations in the  $x$  direction are of the order of 4% of the initial uniform value of one for the full MHD data and all three methods give essentially the same results for  $\rho$ . However, when the plasma  $\beta_0$  is low for small  $D/L$ , in Figure 4.11b, the density variations are between 10% and 20% of the initial uniform value. There is a

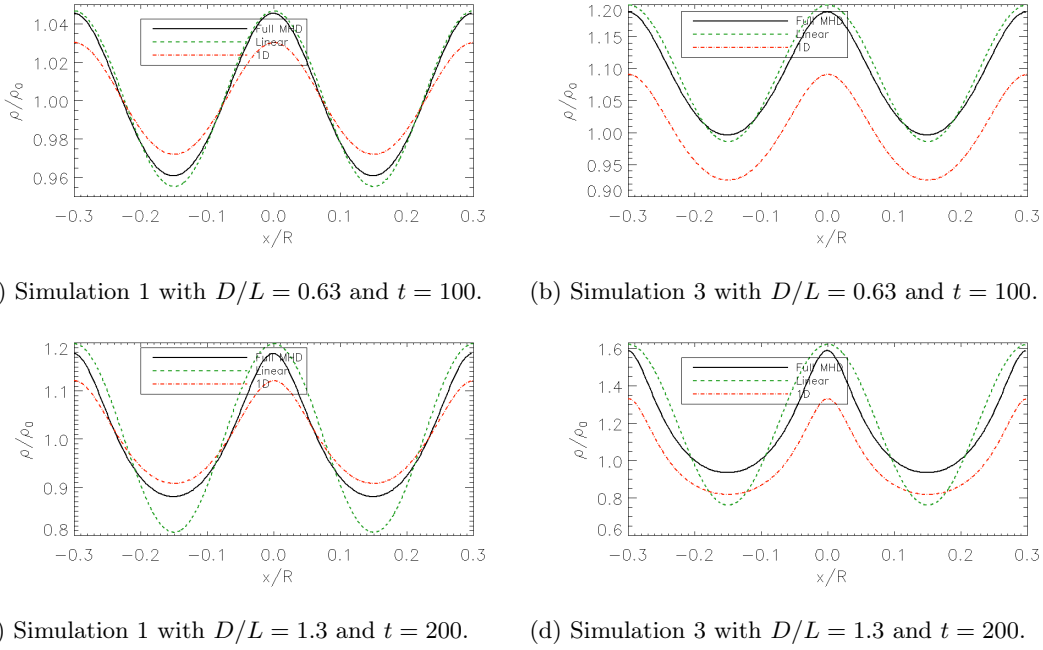


Figure 4.11: Plots of  $\rho$  against  $x$  at the midpoint,  $y = 0$ , for simulations in Table 4.1 on page 79.

general increase in the average value at  $y = 0$ . This is due to the variation in  $y$  of  $B_z$ . These large variations show that nonlinear effects are already becoming important.

For high  $\beta_0$  and larger footpoint displacement of  $D/L \approx 1.3$ , in Figure 4.11c, the variations are similar to the low  $\beta_0$  case for low  $D/L$ . This shows that the high  $\beta_0$  plasma will eventually evolve in the same way, but over a much longer time. Once the footpoint displacement has become large the variations in  $\rho$  for low  $\beta_0$  are nearly 60% of the initial uniform value of one, thus are very significant.

The 1D approach, as before, shows a smaller magnitude compared to  $\rho$  compared with full MHD for high  $\beta_0$  for both high and low  $D/L$ . In the case of low  $\beta_0$  this method predicts the same variation as full MHD, but is displaced slightly because the velocity and viscosity effects are not included in this approximation. These effects lead to the redistribution of density which is not as important for the high  $\beta_0$  and low  $D/L$  case.

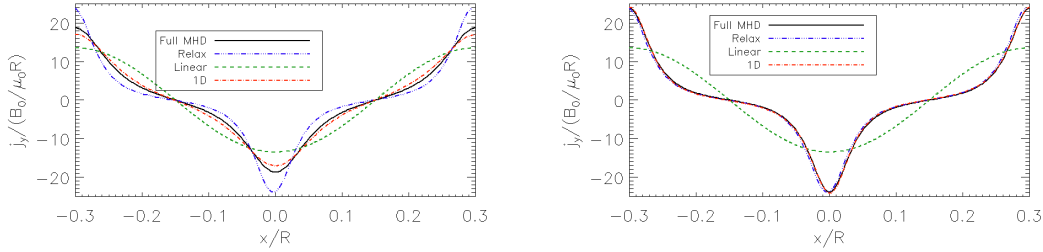
The first- and second-order linearised MHD results agree reasonably well for small displacement for both high and low  $\beta_0$ . In the case of higher  $D/L$ , nonlinear effects become important and the linear results now show a difference with the full MHD results for both high and low  $\beta_0$ . In RMHD, density is not evolved and hence, assumed to remain at the initial value, which is clearly not the case in the full MHD results. The evolution of  $\rho$  is described in more detail later in Section 4.3.2.

### Comparison with $j_y$

The dominant component of the current density is the  $y$  component, parallel to the background magnetic field. The results of  $j_y$  for full MHD, relaxation, the 1D approach, and linearisation are shown in Figure 4.12, on page 87, for  $D/L \approx 1.3$  for the case of high  $\beta_0$  (Figure 4.12a) and low  $\beta_0$  (Figure 4.12b). It is clear that the 1D approach matches the



full MHD results, with only a small discrepancy for high  $\beta_0$ , and that the magnitude of the current exceeds the linear MHD solution (which would be equal to RMHD) by almost a factor of 2 in Figure 4.12b for low  $\beta_0$  values. In general, the magnitude of the current increases as  $\beta_0$  decreases. The relaxation method agrees well with the 1D approach and full MHD results for  $j_y$  for low  $\beta_0$ , but gives a magnitude for  $j_y$  a little to large for high  $\beta_0$ . The other components of the current,  $j_z$  and  $j_x$ , are smaller than  $j_y$ . RMHD does not



(a) Simulation 1

(b) Simulation 3

Figure 4.12: Comparison of  $j_y$  against  $x$  at the midpoint,  $y = 0$ , for  $D/L \approx 1.3$  ( $t = 200$ ) for simulations in Table 4.1 on page 79.

predict a value for either  $j_z$  or  $j_x$ .

In the following section the full MHD dynamics are described in more detail.

#### 4.3.2 Full MHD Dynamics

In light of the interesting dynamics visible in the full MHD results discussed in the last section in this section we analyse our full MHD simulations in more detail. The main aim is to explain the dynamics in our system and how the initial value of the plasma  $\beta_0$  affects the evolution. We shall use the same full MHD data in Table 4.1 on page 79, as in the previous section. Additional simulations were also done to test if the magnetic field would expand, and by how much, if there was enough room in the simulation box. This was done by applying the driver across different fractions of the loop width. Details of these extra simulations will be given in the next section, Section 4.3.3.

##### Evolution of Density

Figure 4.9, on page 84, showed that the kinetic energy decreases more rapidly as  $\beta_0$  is decreased. It was briefly argued that this is due to a redistribution of density.

A parabolic dependence of density in  $y$ , related to the initial pressure, was predicted by the second-order solution in Equation (4.30), on page 75. This variation is clearly seen in the full MHD results, shown as a 2D surface of  $\rho$  in Figure 4.13, on page 88, at the end of the simulation ( $D/L \approx 2.6$ ), for the high  $\beta_0$  case (Figure 4.13a) and the low  $\beta_0$  case (Figure 4.13b). The final state of these simulations are strikingly different, considering they began from the same initial uniform density of 1.0 and the only difference is the value of  $\beta_0$ . In the final state, shown in Figure 4.13b, there is a 15% difference between the maximum and minimum values at  $x = 0$  for low  $\beta_0$ . On the other hand the high  $\beta_0$  case, in



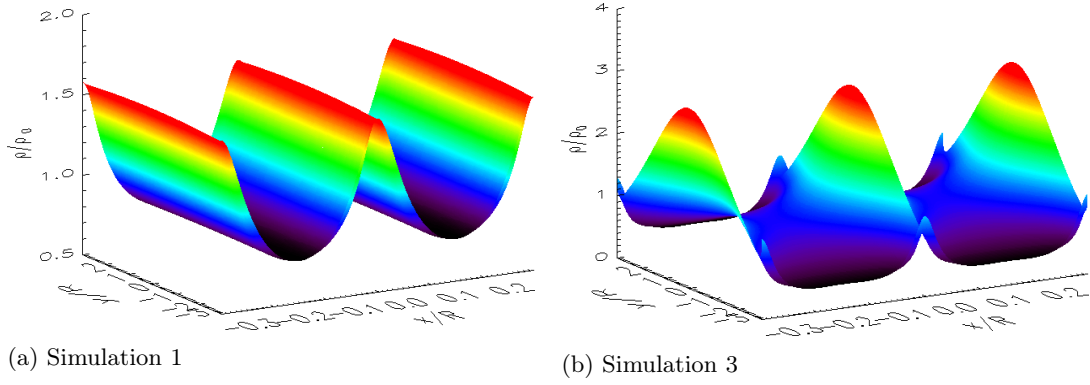


Figure 4.13: Surfaces of density at  $t = 400$  ( $D/L \approx 2.6$ ) for simulations in Table 4.1 on page 79.

Figure 4.13a,  $\rho$  has almost no visible  $y$  dependence. This figure clearly illustrates the large variation of density along  $x$  at  $y = 0$  as shown in Figure 4.11 on page 86. This variation of  $\rho$  in  $x$  and  $y$  is what causes the kinetic energy to decrease.

It is important to check conservation of mass, to ensure that no density has been gained or lost numerically during the evolution. This is done by calculating the surface integrated density

$$\frac{1}{4lL} \int dA \rho, \quad (4.37)$$

in time as shown in Figure 4.14, on page 89, for high (Figure 4.14a) and low  $\beta_0$  (Figure 4.14b). Here the line integrals of  $\rho$  in  $x$  are also shown along  $y = 0$  and  $y = \pm 3/4L$  as

$$\frac{1}{2l} \int_{-l}^l dx \rho(x, y = 0, \pm \frac{3}{4}L). \quad (4.38)$$

Figure 4.14 clearly illustrates that although the total density is conserved the spatial distribution is changing in time: increasing quickly in the middle ( $y = 0$ ) and decreasing elsewhere,  $y = \pm \frac{3}{4}L$ . The change in  $\rho$  is very small for high  $\beta_0$  but as the plasma beta is decreased the rate of change of  $\rho$  increases rapidly. The integral of  $\rho$  at  $y = 0$  increases by  $\approx 40\%$  for low  $\beta_0$  compared to  $< 1\%$  for high  $\beta_0$  by the end of the simulations. These figures show that the final state of the density is significantly different for different values of  $\beta_0$ .

We have already shown, in Section 4.2.5, that the linear solution for  $\rho$  has a term that is dependent on  $y$  and  $t$  but independent of  $x$ . The analytic expression, Equation (4.30), reveals that the size of this term is related to a ratio of  $\frac{\nu}{p_0}t = \frac{2\nu}{\beta_0}t$ . Since the viscosity is the same for these simulations  $t$  can be rescaled showing that the timescale of this phenomenon depends on  $\beta_0$ .

This can be explained as follows: If a value of  $\beta_0$  is chosen, say  $\beta_{0a}$  and a second value is chosen to be simply a fraction,  $c$ , of the first value as  $\beta_{0b} = c\beta_{0a}$ . Then we can

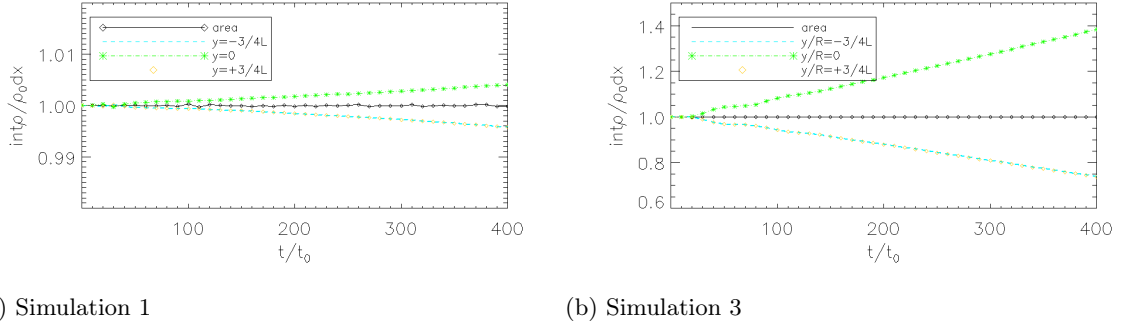


Figure 4.14: Plots showing the total mass for, (i) area integral of  $\rho$ , Equation (4.37) (black curve) and, (ii) the  $x$  integral at  $y = 0$  and  $\pm 3/4L$ , Equation (4.38), as functions of  $t$  for simulations in Table 4.1 on page 79. A different  $y$ -range has been used for each figure.

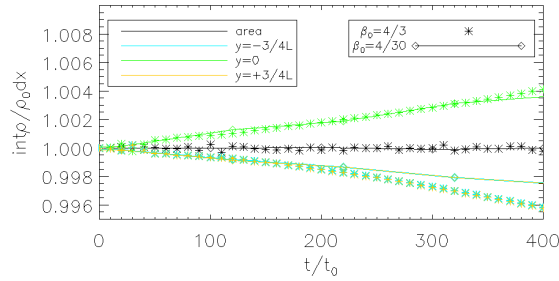


Figure 4.15: Plot showing the total area integral of  $\rho$  and the  $x$  integral at  $y = 0$  and  $\pm 3/4L$  as a function of  $t$ . Star symbols: high  $\beta_0$  (simulation 1). Diamond symbols: low  $\beta_0$  (simulation 2).  $t$  for low  $\beta_0$  is redefined as  $10t$ . Simulations are in Table 4.1 on page 79.

write this ratio for both values and equate them as

$$\frac{t_a}{\beta_{0a}} = \frac{t_b}{\beta_{0b}} = \frac{t_b}{c\beta_{0a}},$$

$$\Rightarrow t_a = \frac{t_b}{c}.$$

Since  $c \leq 1$  then  $t_a \geq t_b$ . This explains why the redistribution of density in  $y$  is less noticeable for high  $\beta_0$ ; since it will take much longer for this term to become important in a system with larger  $\beta_0$  than a system with small  $\beta_0$ . This can be illustrated using the high and reasonably low  $\beta_0$  ( $\beta_0 = 4/30$ ) data from simulations 1 and 2 in Table 4.1 on page 79. Setting  $t_a$  equal to our high initial plasma  $\beta_0$  of  $4/3$  as  $t_a = t_{\beta_0=4/3}$  and taking  $c = 0.1$  to give the value of  $t_b = t_{\beta_0=4/30}$  for  $\beta_0$  of  $4/30$ . We can plot the density integrals for these two simulations together by rescaling  $t'_{\beta_0=4/30} = t_{\beta_0=4/30}/c = 10(t_{\beta_0=4/30} - \tau_{\text{driver}}) = t_{\beta_0=4/3}$ . The  $\beta_0 = 4/30$  data is plotted against this rescaled  $t$  in Figure 4.15, on page 89, alongside the  $\beta_0 = 4/3$  data against the original time values.  $\tau_{\text{driver}}$  is the time taken for the driver to reach its maximum, which for these simulations equals 8.0 (ramp up time = 2.0, switch on time = 6.0). Now both data sets are similar in magnitude, illustrating that a lower value of  $\beta_0$  causes this redistribution of density in  $y$  to happen more rapidly in time.

The evolution of  $\rho$  is further investigated by calculating the maximum and min-

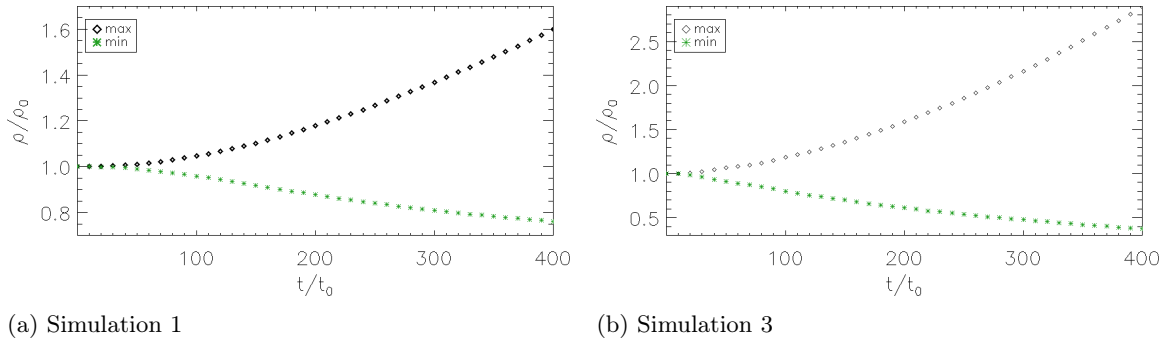


Figure 4.16: Plot showing the maximum and minimum of  $\rho$  as a function of  $t$  for simulations in Table 4.1 on page 79.

imum values of  $\rho$  throughout the volume at each timestep. These values are plotted in Figure 4.16, on page 90, for high (Figure 4.16a) and low  $\beta_0$  (Figure 4.16b). It is clear that the maximum of  $\rho$  is larger for low  $\beta_0$ . For high  $\beta_0$  the maximum of  $\rho$  increases by  $\sim 60\%$  and the minimum has decreased by  $\sim 25\%$  of the initial uniform value of one. In contrast for the simulation with low  $\beta_0$  the maximum has increased by more than 200% and the minimum has reduced by  $\sim 60\%$  of the initial uniform value of one. These are substantial changes in density, showing that any assumption that the density remains constant, such as used in RMHD, would be broken very quickly in the evolution. This is a consequence of the perpendicular magnetic field magnitude being of the order of the background field.

### Evolution of Pressure

Similarly to  $\rho$  there is a significant variation in the pressure. The maximum and minimum values of  $p$  at each timestep are plotted in Figure 4.17, on page 91, for high (Figure 4.17a) and low  $\beta_0$  (Figure 4.17b). For high  $\beta_0$  the maximum pressure increases by  $\sim 120\%$  and the minimum decreases  $\sim 40\%$  of the initial uniform value of  $\frac{2}{3}$  for this simulation. For low  $\beta_0$  the maximum value increases from its initial value of  $\frac{2}{300}$  by nearly 500% and decreases by 20%. This broad range of pressure indicates that the plasma  $\beta$  varies throughout the domain and changes significantly from the initial value. Since, in the low  $\beta_0$  case, the initial pressure was small, this decrease in pressure results in the minimum value approaching zero. This could cause numerical problems. It is found for simulation 4 with an even lower initial plasma  $\beta_0$  value of  $\beta_0 = 4/3000$  that the pressure does become essentially zero in some places. This potentially explains why this run encountered computational problems. This large change in the plasma  $\beta$  could have significant consequences on the evolution of the system. Any assumption about the pressure or  $\beta$  being small, such as in RMHD, would not be satisfied in these cases.

### Total Pressure and Ratio of Density and Magnetic Field

Since the variation in pressure is large, the pressure force is likely to be large. An important quantity is the total pressure,  $p + B^2/2\mu$ . If the total pressure at a time,  $t$ , equals a constant, meaning that it is independent of spatial coordinates, then the pressure forces

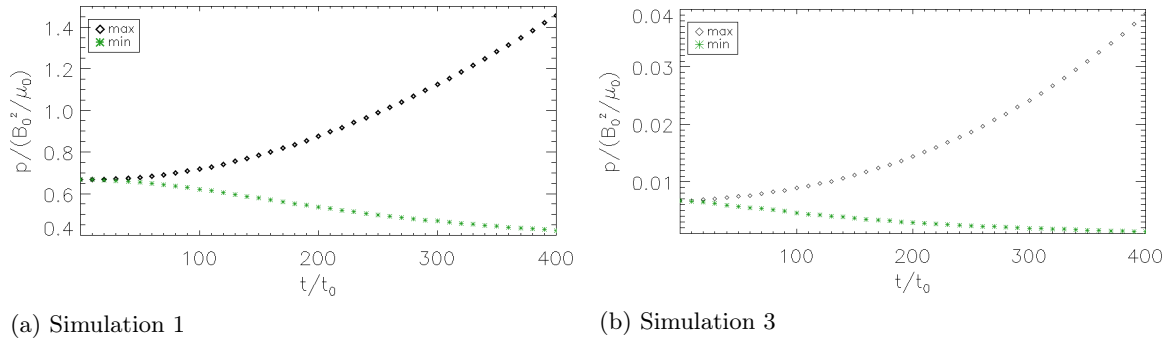


Figure 4.17: Plot showing the maximum and minimum of  $p$  as a function of  $t$  for simulations in Table 4.1 on page 79.

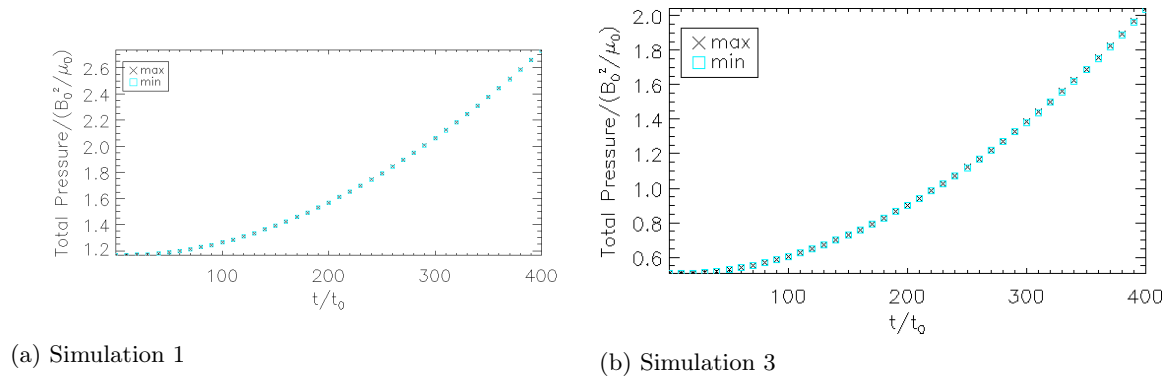


Figure 4.18: Plot showing the maximum and minimum of the total pressure,  $p + B^2/2\mu$ , along  $y = 0$  as a function of  $t$  for simulations in Table 4.1 on page 79.

are balanced and the system is in pressure balance. The maximum and minimum along  $y = 0$  of the total pressure is shown as a function of time in Figure 4.18, on page 91, for both high (Figure 4.18a) and low  $\beta_0$  (Figure 4.18b). The points lie on top of each other but the actual value of the total pressure increases in time. This shows that, away from boundaries, at a given time,  $t$ , the system is in equilibrium. This confirms the assumption that the system evolves through a sequence of equilibrium states. For low  $\beta_0$  the constant value of the total pressure is smaller than for high  $\beta_0$  since the initial value of the pressure is smaller and the magnetic pressure does not need to be as large to balance the pressure.

A second important quantity is the ratio of the density and magnetic field,  $\rho/B \approx \rho/B_y$ , which indicates the relation between density and magnetic flux. The axial field is assumed to be the dominant component here even though for large  $D$  the sheared field is similar in magnitude to the background field. This is chosen as the profile in  $x$  of  $\rho$  is the same as the axial field,  $B_y$ , showing that the density and axial field are compressed in the same regions. Figure 4.19 on page 92, shows the maximum and minimum values of  $\rho/B_y$  along  $y = 0$  for both high (Figure 4.19a) and low  $\beta_0$  (Figure 4.19b) as a function of time. This ratio stays about one for high  $\beta_0$ , indicating that the amount of flux per unit density remains approximately constant. In contrast the ratio is increasing a little for low  $\beta_0$ , which means that the density is increasing more than the axial field. In this case the other field components are becoming important.

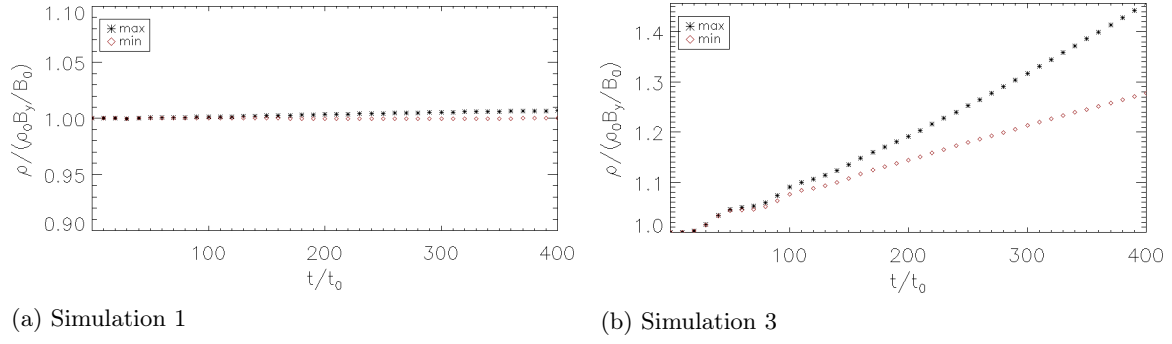


Figure 4.19: Plot showing the maximum and minimum of  $\rho/B_y$  as a function of  $t$  along  $y = 0$  for simulations in Table 4.1 on page 79.

### $y$ variation in $\rho$

It has been shown that the density is redistributed in  $x$  and  $y$ . The redistribution in  $x$  leads to a  $\cos(2kx)$  shape, as predicted by linearisation in Section 4.2.5, which is clearly present in the full MHD data for both high and low  $\beta_0$ , shown in Figure 4.13 on page 88. The redistribution in  $y$  is significantly different for the high and low  $\beta_0$  cases. A parabolic profile in  $y$  is created for low  $\beta_0$  in Figure 4.13b, however there is comparatively no  $y$  variation for high  $\beta_0$  in Figure 4.13a.

There are two distinct contributions to this  $y$  variation: boundary layers and a parabolic profile. The parabolic profile, if present, is significant over the entire loop length and so, is not an effect only found in the boundaries, and therefore is distinct from the boundary layer, previously mentioned in Section 4.2.3 when discussing the magneto-frictional method. This parabolic variation in  $y$  is due to viscosity, predicted in Section 4.2.5 using the analysis of the linear and weakly nonlinear solutions.

Both  $y$  variations are due to boundary effects but boundary layers are only present near the  $y$  boundaries and negligible in the centre of the domain. The parabolic variation is due to viscosity, which results in a spatial delay of the shearing between the magnetic footpoints and the middle of the fieldline. This delay causes significant variation along the loop length, as shown in surfaces of  $\rho$  in Figure 4.13b for low  $\beta_0$ . The aim of this section is to illustrate the  $y$  variation and how it varies with  $\beta_0$ .

Examples of the variation of  $\rho$  against  $y$  for high  $\beta_0$  and low  $\beta_0$  are given in Figure 4.20, on page 94, and Figure 4.21, on page 95, respectively, for three points along  $x$ , namely  $x = 0.0$ ,  $x = -l/2 = -0.15$  and  $x = -3l/4 = -0.225$  (top, middle and bottom row respectively). The left column in these two figures shows  $\rho$  over the full range in  $y$  and the right column shows a close-up of the region near the boundary of the same figure with a smaller range in  $y$  of  $2.7 \leq y \leq 3.0$ . These two ranges in  $y$  have been chosen to clearly illustrate the boundary layers and the parabolic variation.

Three things are evident in these figures. First, there is a clear  $y^2$  profile present in most of these plots for both high and low  $\beta_0$ , which is dominant for low  $\beta_0$ . This parabolic variation corresponds to that found using the linearisation method in Section 4.2.5 due to viscosity. Second, near the boundaries there is a narrow boundary layer which is more dominant for high  $\beta_0$  (for example Figure 4.20f) than low  $\beta_0$ . Third, the variation and

magnitude of  $\rho$  is very different for the two  $\beta_0$  values. This shows that the parabolic variation is present in the high  $\beta_0$  case, for example Figure 4.20c, but on a very small scale. This explains why it is not visible in the surface of  $\rho$  for high  $\beta_0$  but is very prominent for low  $\beta_0$ .

There is also a large difference in the magnitude of  $\rho$  at different  $x$  positions. At the midpoint  $x = 0$  there are narrow boundary layers present in  $y$  for both high and low  $\beta_0$ , shown in Figure 4.20b and Figure 4.21b. In contrast, the boundary layers are dominant in Figure 4.20f for high  $\beta_0$  but are not present at all for low  $\beta_0$  in Figure 4.21f at  $x = 3l/4$ . Only the parabolic variation is visible at the other two positions in  $x$  for low  $\beta_0$  in Figure 4.21b and Figure 4.21d. This shows that the viscous effect is dominant in the case of low  $\beta_0$ . However, for high  $\beta_0$ , at  $x = -3l/4$  the boundary layers clearly dominate over the parabolic variation. These examples are typical of the  $y$  variation throughout the entire domain: the high  $\beta_0$  case is dominated by boundary layers with a very small parabolic profile, in contrast, for the low  $\beta_0$  case the parabolic variation is dominant. It is also found the width of the boundary layers is approximately  $l/L$ , in agreement with the prediction made from the magnetofrictional method, in Section 4.2.3.

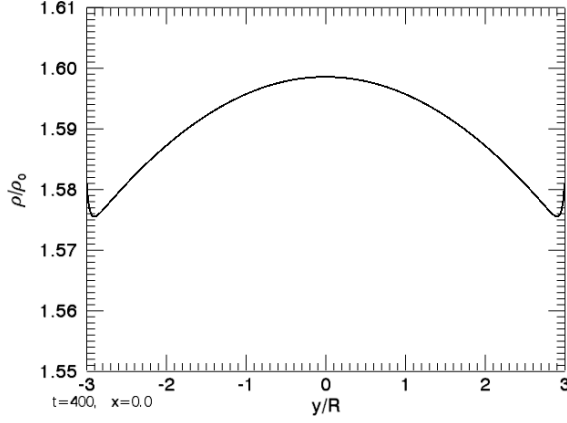
### Forces

Since it has been found that there are large spatial gradients present in the system, it is a natural next step to analyse the forces acting on our system.

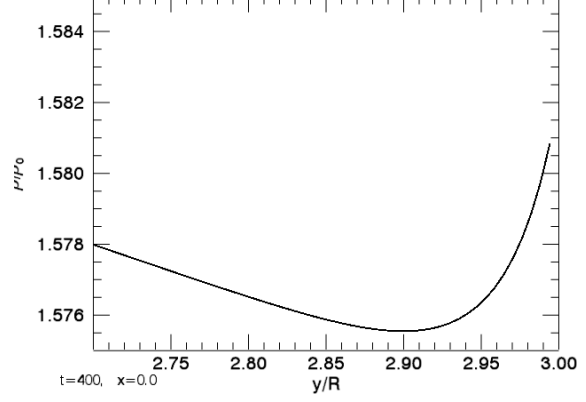
The contributions of the pressure gradient, magnetic pressure and magnetic tension acting in the  $y$  direction are plotted at  $y = -L$  in Figure 4.22, on page 96, and the  $y$  component total force in Figure 4.23, on page 96, as functions of  $x$  at the end of the simulations at the two boundaries  $y = \pm L$  where this force is largest, for high and low  $\beta_0$ .

Consider the forces on the boundary at  $y = -L$ . For high  $\beta_0$  the pressure force is marginally larger than and opposite in direction to the Lorentz force, which is mainly negative, resulting in a very small positive total force. For low  $\beta_0$ , the pressure force is accordingly smaller and the balancing magnetic pressure is also smaller thus the remaining magnetic tension term results in the Lorentz force being positive. This adds to the unbalanced part of  $\frac{\partial p}{\partial y}$  resulting in a larger positive total force. The analogous story is true at the other boundary  $y = L$  with a negative total force. This results in a ponderomotive force acting inward, creating the parabolic shape of  $\rho$  in  $y$ .

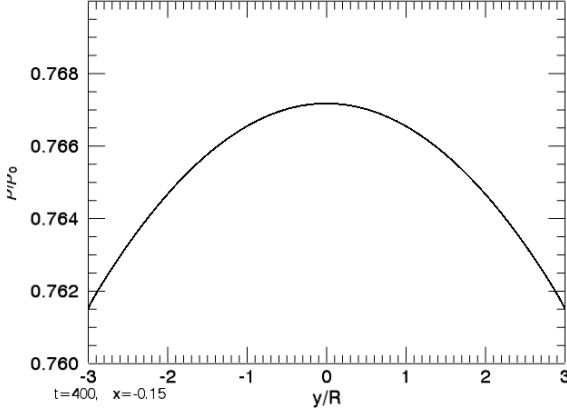
Similarly, the  $x$  component of the total force and the pressure gradient, magnetic pressure and magnetic tension are shown in Figures 4.24, on page 96, and 4.25, on page 97, as functions of  $x$  at  $y = 0$  for high and low  $\beta_0$ . In both cases the total force is small with steep peaks showing the plasma is compressed, creating strong currents. The magnetic pressure force is the dominant component, which results in a localised force compressing the plasma about  $x = 0$  and pushing outward towards the boundaries in  $x$ . This suggests that if the plasma was not confined to the simulation box it would expand. This is indeed the case and this is investigated later in the next section, Section 4.3.3.



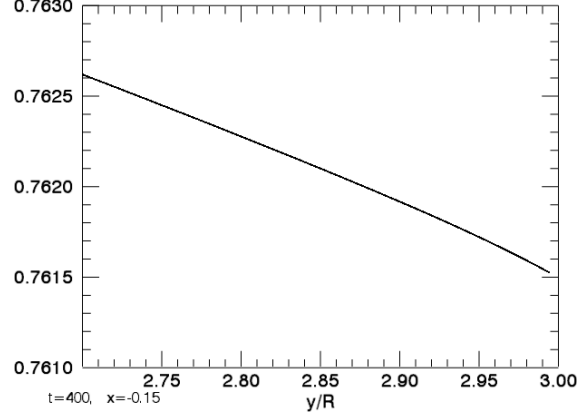
(a) Full range of  $y$  at  $x = 0.0$ .



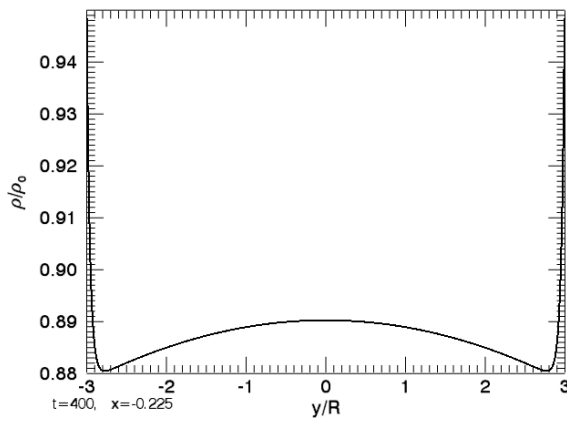
(b) Close up of boundary layers between  $y = 2.7$  and  $y = 3.0$  at  $x = 0.0$ .



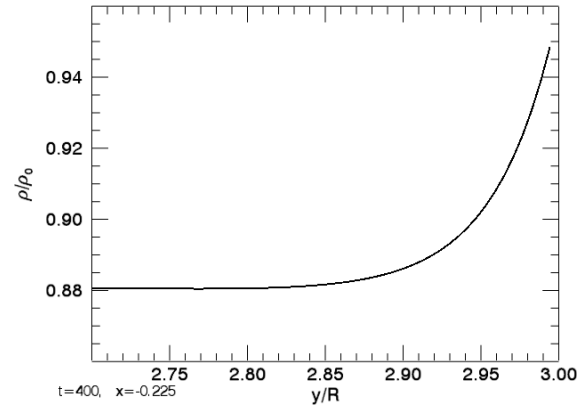
(c) Full range in  $y$  at  $x = -l/2 = -0.15$ .



(d) Close up of boundary layers between  $y = 2.7$  and  $y = 3.0$  at  $x = -l/2 = -0.15$ .



(e) Full range in  $y$  at  $x = -3l/4 = -0.225$ .



(f) Close up of boundary layers between  $y = 2.7$  and  $y = 3.0$  at  $x = -3l/4 = -0.225$ .

Figure 4.20: Plots of  $\rho$  as a function of  $y$  at the end of the simulation  $t = 400$  for simulation 1 in Table 4.1 on page 79 at different points along  $x$ .

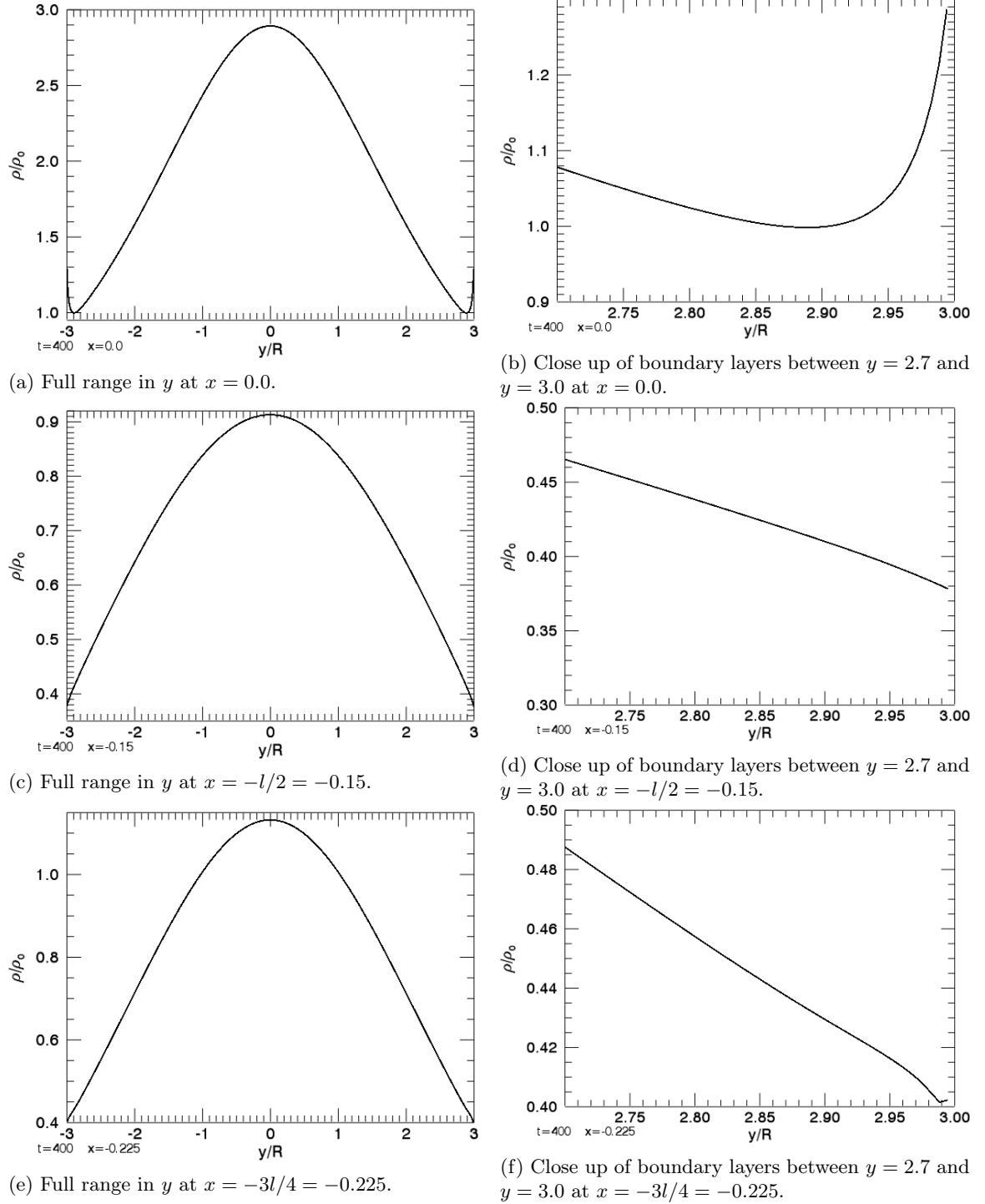


Figure 4.21: Plots of  $\rho$  as a function of  $y$  at the end of the simulation  $t = 400$  for simulation 3 in Table 4.1 on page 79 at different points along  $x$ .



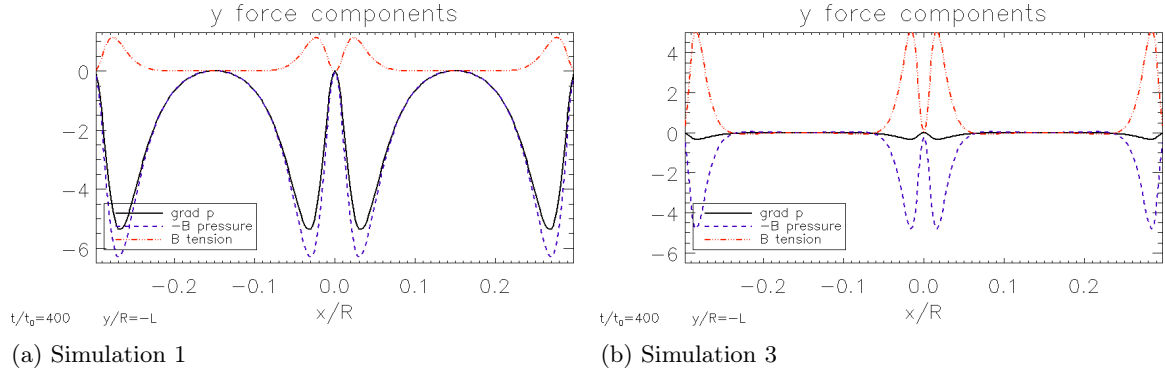


Figure 4.22: Plots of the  $y$  component of the forces: pressure gradient, magnetic pressure and magnetic tension as a function of  $x$  at the bottom boundary  $y = -L$  at  $D \approx 7.9$  ( $t = 400$ ) for simulations in Table 4.1 on page 79.

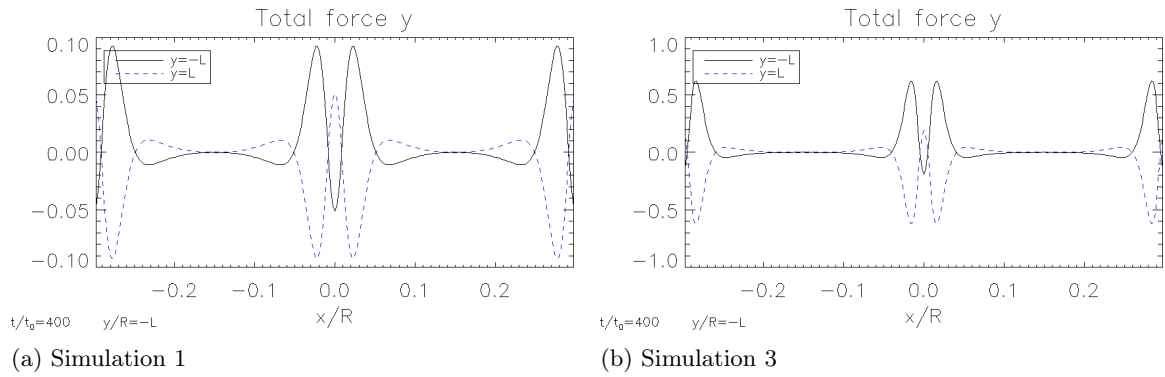


Figure 4.23: Plots of the  $y$  component of the total force as a function of  $x$  at the two boundaries at  $y = \pm L$  at  $D \approx 7.9$  ( $t = 400$ ) for simulations in Table 4.1 on page 79.

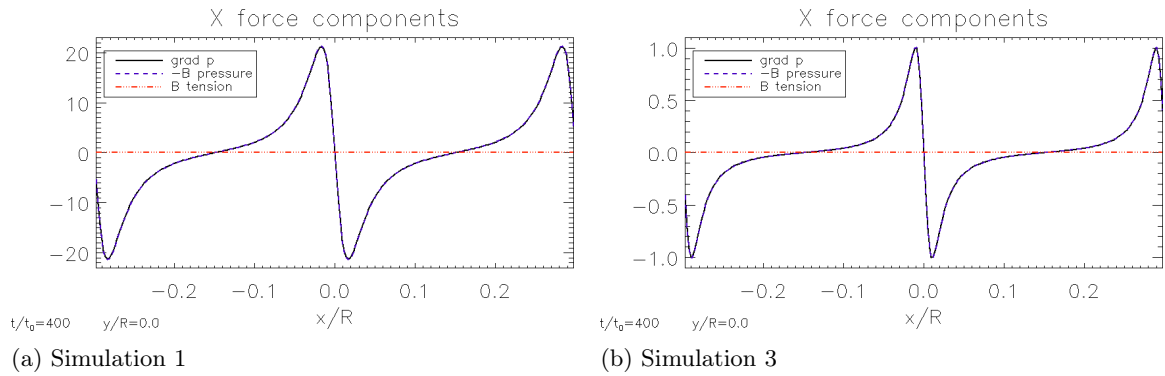


Figure 4.24: Plots of the  $x$  components of the forces: pressure gradient, magnetic pressure and magnetic tension as a function of  $x$  in the midpoint in  $y$  at  $D \approx 7.9$  ( $t = 400$ ) for simulations in Table 4.1 on page 79.

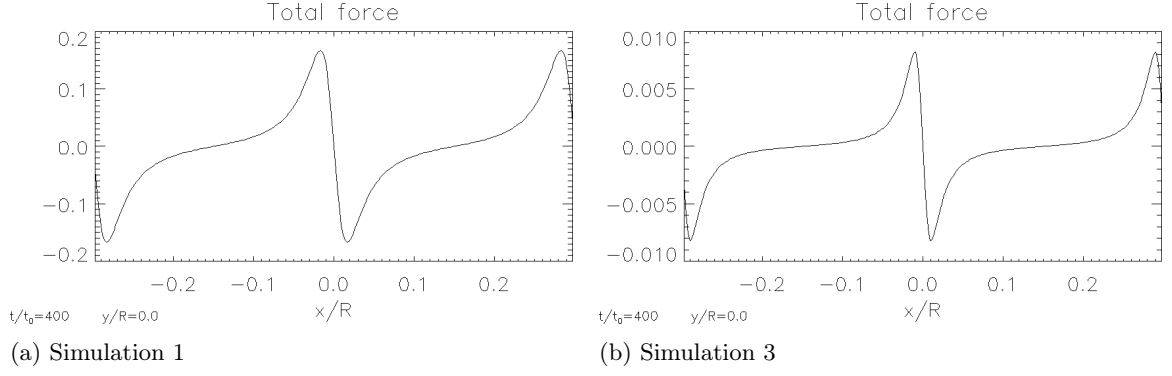


Figure 4.25: Plots of the  $x$  component of the total force as a function of  $x$  in the midpoint in  $y$  at  $D \approx 7.9$  ( $t = 400$ ) for simulations in Table 4.1 on page 79.

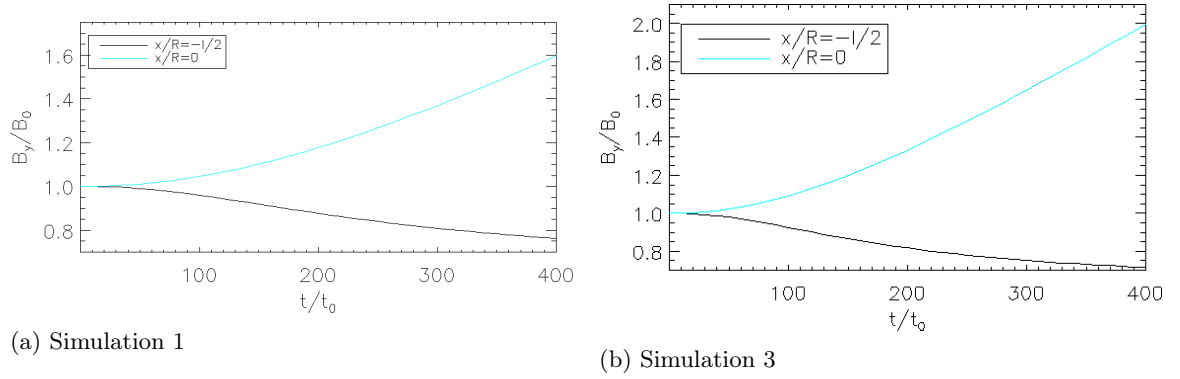


Figure 4.26: Two points are chosen at the midpoint  $y = 0$ , corresponding to  $x = 0$  and  $x = -l/2$ , and the magnitude of  $B_y$  is plotted against  $t$  for simulations in Table 4.1 on page 79.

### Variation of the Axial Field

The compression and expansion of the plasma is mainly seen in the background field,  $B_y$ . To illustrate this, two points,  $x = 0$  and  $x = -l/2 = -0.15$  are chosen at  $y = 0$ . The magnitude of  $B_y$  at these points is plotted as a function of  $t$  in Figure 4.26, on page 97, for high (Figure 4.26a) and low  $\beta_0$  (Figure 4.26b). This shows that, at  $x = -l/2$ ,  $B_y$  decreases from its initial value of one by about 20% for both values of  $\beta_0$  by the end of the simulation. At  $x = 0$  the magnitude of  $B_y$  increases by  $\sim 60\%$  for high  $\beta_0$  and 100% for low  $\beta_0$ . This shows significant changes in the parallel magnetic field which, as previously mentioned, illustrates that one of the assumptions of RMHD, namely, that the axial field remains constant, is not valid for this system. This change in  $B_y$  indicates that the parallel field is expanding and compressing.

Figure 4.27 on page 98 shows the maximum of  $B_y$  at  $y = 0$  for all four values of  $\beta_0$ . This shows that for small  $t$  the axial field in all cases is similar. On the other hand as time increases the high  $\beta_0$  case is much smaller than the other three values. This shows that the axial field has not been compressed very much yet for high  $\beta_0$  compared to the other simulations. The two lowest values of  $\beta_0$  give essentially the same maximum value for  $B_y$ , indicating there is a limit to how much the field can be compressed.

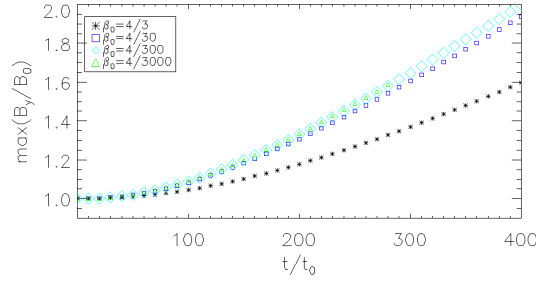


Figure 4.27: Plot showing the maximum of the axial field,  $B_y$ , as a function of  $t$  for the four values of  $\beta_0$  corresponding to simulations 1-4 in Table 4.1 on page 79.

### Fieldlines

The compression and expansion of the magnetic field can be visualised by considering fieldlines. Figure 4.28 on page 99, shows the fieldlines for high (Figure 4.28a) and low  $\beta_0$  (Figure 4.28b), corresponding to contours of the flux function,  $A$ , calculated by integrating  $B_y$  as  $A = \int B_y dx$ . The fieldlines at the end of the simulation are shown along with the fieldlines of the initial uniform background field  $B_0$  at  $t = 0$ . It is evident that the field is compressed around  $x = 0$  and has expanded away from  $x = \pm l/2$ .

It is difficult to tell from the fieldlines whether the field is compressed more for low  $\beta_0$  as suggested earlier. This can be investigated by calculating the distance these fieldlines have moved from their initial positions at  $t = 0$ . Note that this displacement is due to the compression or expansion of the plasma in  $x$  and not that imposed by the driver, which acts in the  $z$  direction, that simply moves the fieldlines. The displacement of the fieldlines at the end of the simulations is plotted against their initial position in  $x$  in Figure 4.29, on page 99, for high (Figure 4.29a) and low  $\beta_0$  (Figure 4.29b). As expected, in a low  $\beta$  plasma, magnetic forces dominate and the distance the fieldlines are displaced by is larger than for high  $\beta_0$ . Hence, the field has been compressed more than the high  $\beta_0$  case, even though the footpoint displacement is the same in both cases, as suggested in the last section and Figure 4.27 and Figure 4.29.

### Parallel Velocity, $v_y$

Since the plasma is being moved around there must be a corresponding velocity. The surface integral of squared velocity

$$\frac{1}{4lL} \int_{-l}^l \int_{-L}^L (v_x^2 + v_y^2 + v_z^2) dy dx,$$

was calculated as a function of time for high and low  $\beta_0$ . It is found that the integrated velocity is constant for low  $\beta_0$  however it is slightly increasing for the high  $\beta_0$  case. Since  $v_x$  is symmetric in  $x$  ( $v_x \propto \sin(2kx)$  see Section 4.2.5) it integrates to zero. However,  $v_y$  is not symmetric and does not integrate to zero. The maximum of the integral of  $v_y$  in  $x$ ,

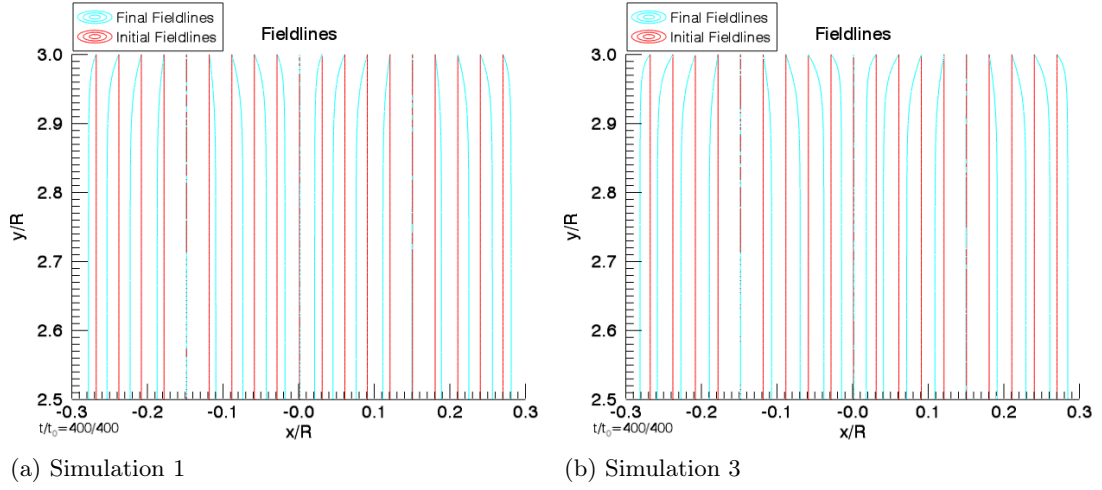


Figure 4.28: Fieldline plots showing the initial straight fieldlines (dashed lines) and final positions of the fieldlines at  $D \approx 7.9$  ( $t = 400$ ) for simulations in Table 4.1 on page 79. The  $y$  range has been restricted to  $2.5 \leq y \leq 3.0$  to clearly show the fieldlines at the boundaries. The fieldlines are straight in the middle of the box.

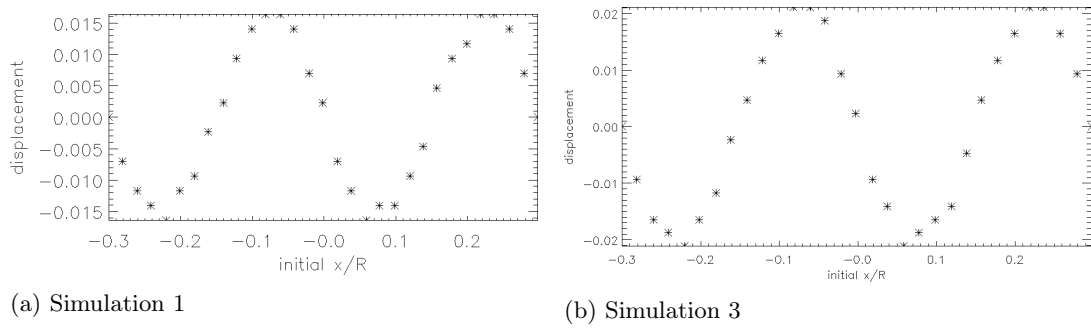


Figure 4.29: Displacement for fieldlines against their initial  $x$  position for simulations in Table 4.1 on page 79.

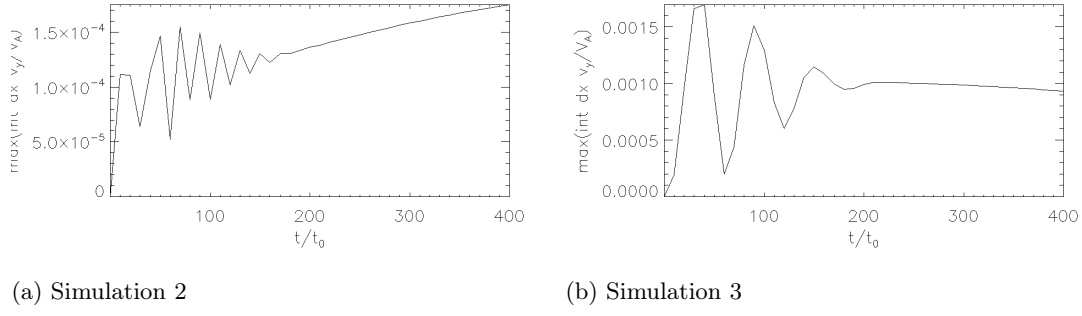


Figure 4.30: Maximum integrated  $v_y$  in  $x$ , Equation (4.39), as a function of time for simulations in Table 4.1 on page 79.

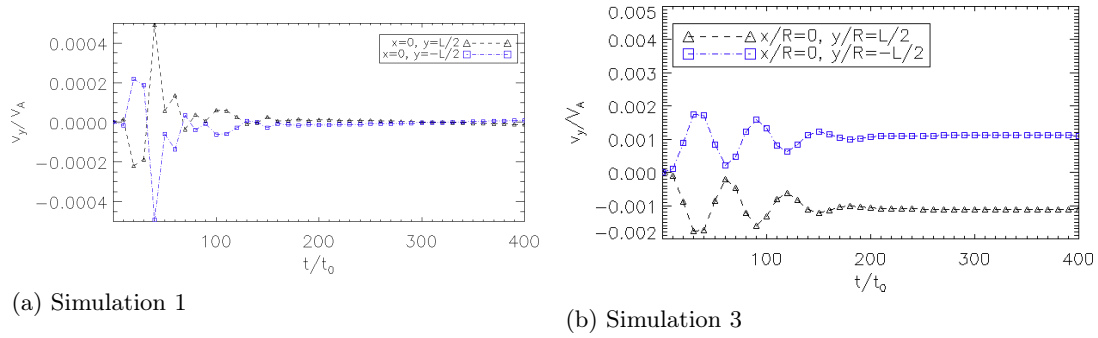


Figure 4.31: Two points in  $y$ , corresponding to  $y = \pm L/2$  at  $x = 0$  are followed in time. The magnitude of,  $v_y$ , the parallel flow is plotted against time at these points for simulations in Table 4.1 on page 79.

given by

$$Q(t) = \max \left( \frac{1}{2l} \int_{-l}^l v_y(x, y, t) dx \right). \quad (4.39)$$

$Q(t)$  is shown in Figure 4.30 on page 100 for both fairly high (Figure 4.30a) and low  $\beta_0$  (Figure 4.30b). For high  $\beta_0$  this quantity is near zero but starting to increase, explaining the increasing velocity integral. For low  $\beta_0$  this quantity reaches a steady state and this is why the integrated velocity is constant in this case.

It has been shown that there is a force pushing the plasma inwards in  $y$ , along the loop length. It follows that there is a corresponding parallel velocity. The parallel flow,  $v_y$ , is measured at  $x = 0$  and  $y = \pm 1/2L$  and shown as a function of time in Figure 4.31, on page 100, for high (Figure 4.31a) and low  $\beta_0$  (Figure 4.31b). The value of the parallel velocity,  $v_y$ , at the two points  $y = \pm L/2$  is equal and opposite in both cases but the sign is reversed for the different  $\beta_0$  values. In the low  $\beta_0$  case the velocity is negative for  $y = L/2$  and positive for  $y = -L/2$ . This clearly illustrates the inward flow parallel to the background magnetic field which transports the density. For the high  $\beta_0$  case the parallel flow is smaller and in the opposite direction: towards the boundaries, until a time near the end when the sign of  $v_y$  changes, indicating that the same inward flow seen in the case of low  $\beta_0$  would also occur if this simulation was continued for longer.

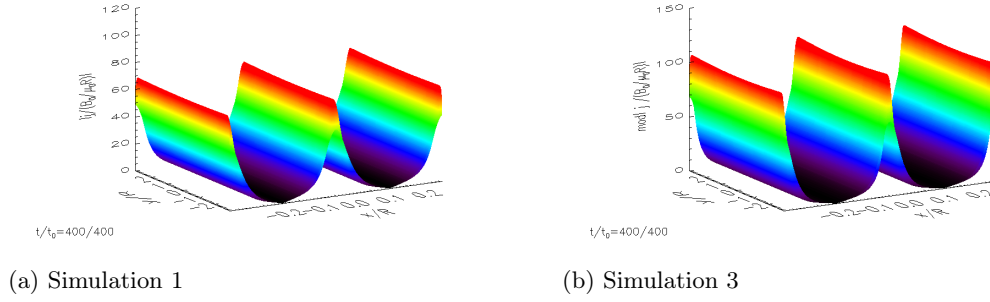


Figure 4.32: 2D surfaces of  $|j|$  for  $D \approx 7.9$  ( $t = 400$ ) for simulations in Table 4.1 on page 79.

### Current

It has been shown that the magnitude of the parallel and sheared components of the magnetic field change significantly, leading to large gradients. This indicates that there is a large current present. The magnitude of the current  $|j|$  is calculated and is shown as a surface in Figure 4.32, on page 101, at the end of the simulations ( $t = 400$ ) for high (Figure 4.32a) and low  $\beta_0$  (Figure 4.32b). The large localised structures in the surfaces indicate strong currents in both cases. The maximum is larger for the low  $\beta_0$  case which agrees with the higher derivatives due to the fieldlines being compressed more in this case.

#### 4.3.3 Full MHD Dynamics: Field Expansion

It was suggested earlier that the magnetic field could expand if there was extra room in the computational box. In this section we investigate how much the field expands depending on how much space there is for the magnetic field to expand. This is done by varying how much of the domain the driver is applied over. The plasma  $\beta_0$  is chosen to be  $4/30$  (as in Simulation 2 in Table 4.1 on page 79) as this value is not too low as to cause computational problems yet small enough that the redistribution of  $\rho$  is visible towards the end of the simulation but does not affect the dynamics significantly.

For clarity, we redefine the velocity on the boundaries at  $y = \pm L$ . In this section, we choose the half-width to be  $l' = 2l = 0.6$  and define the driver to be

$$v_z(x, \pm L, z, t) = \begin{cases} \pm F(t) \sin(\frac{kx}{a}) & \text{if } -al' \leq x \leq al' \\ 0 & \text{elsewhere} \end{cases} \quad (4.40)$$

where  $F(t)$  is the same as before, given in Equation (4.4) on page 64. The constant  $a$  is the fraction of  $l'$ , ( $a \leq 1$ ), that the driver is applied over. For example, if the driver is applied over a quarter of the domain,  $a = \frac{1}{4}$ . The boundary velocity given in Equation (4.40) is

$$v_z(x, \pm L, z, t) = \begin{cases} \pm F(t) \sin(4kx) & \text{if } \frac{1}{4}l' \leq x \leq \frac{1}{4}l' \\ 0 & \text{elsewhere} \end{cases}$$

Table 4.2: The initial internal energy,  $e_0$ , and  $\beta_0$  for our three full MHD simulations. The quantity  $a$  is the fraction of the boundary in  $x$  that the driver is applied over.

Simulation	$\beta_0 = 2p_0$	$e_0 = 3/2p_0$	$a$
e1	4/30	0.1	3/4
e2	4/30	0.1	1/2
e3	4/30	0.1	1/4

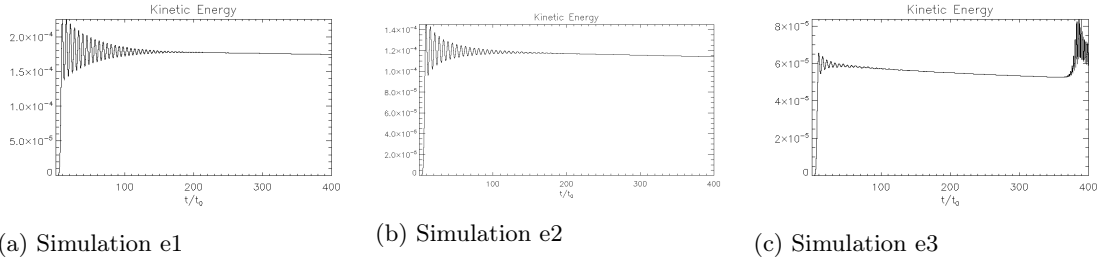


Figure 4.33: Plots of the kinetic energy when varying the fraction  $a$  of  $l'$  that the driver is applied over for simulations in Table 4.2 on page 102.

This ensures that a smooth continuous sinusoidal profile is used while  $a$  is varied, allowing extra room in the domain for the field to expand. Simulations have been done with  $a = \frac{3}{4}$ ,  $\frac{1}{2}$  and  $\frac{1}{4}$ , as summarised in Table 4.2 on page 102.

#### Effect on Kinetic Energy of Field Expansion

The kinetic energy for the three values of  $a$  are shown in Figure 4.33 and can be compared to the main full MHD results in Figure 4.9 on page 84. These figures show that as  $a$  is decreased the kinetic energy decreases more rapidly. This is a consequence of changing the argument of the sine in the driver equation: the kinetic energy decreases inversely proportionally to  $a$  even though the initial  $\beta_0$  and  $\nu$  are held constant. This can be understood algebraically using the linear solution derived in Section 4.2.5 and Appendix C as follows. The driver is  $v_z \propto \sin\left(\frac{kx}{a}\right)$ , thus the viscous term of the sheared magnetic field  $B_z \propto \frac{1}{a^2}$ . Hence the  $x$  independent term,  $G(y)$ , in  $v_y$  and  $\rho$  are modified by the same amount  $\frac{1}{a^2}$ . This is the term responsible for the density redistribution in  $y$ . Therefore  $G(y)$  is proportional to  $\frac{1}{a^2}$ . For our chosen values this corresponds to  $\frac{16}{9}$ , 4, 16, showing that this process becomes increasingly important as  $a$  is decreased. For  $a = \frac{1}{4}$  a problem has occurred towards the end of the simulation which may be related to the consequences of this and has caused the code to breakdown due to numerical problems. This is interesting as a similar evolution of kinetic energy has occurred for small  $a$  as for very low  $\beta_0$  (simulation 4 in Table 4.1 on page 79) shown in Figure 4.9d. This could be a very useful feature as it would allow for this effect to be investigated more easily for lower  $\beta_0$  values by decreasing  $a$  instead of  $\beta_0$ .

#### Effect on $\rho$ of Field Expansion

Allowing the field to expand has a significant effect on  $\rho$  as shown as a surface in  $x$  and  $y$  in Figure 4.34, on page 103, for  $t = 400$  at the end of the simulations. The parabolic shape of  $\rho$  becomes more noticeable as  $a$  is decreased, becoming very pronounced for  $a = \frac{1}{4}$  the

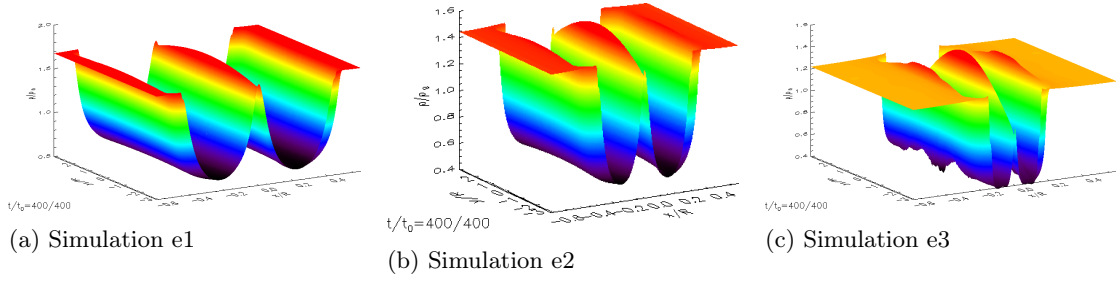


Figure 4.34: Surfaces of  $\rho$  in  $x$  and  $y$  when varying the fraction  $a$  of  $l'$  that the driver is applied over for simulations in Table 4.2 on page 102.

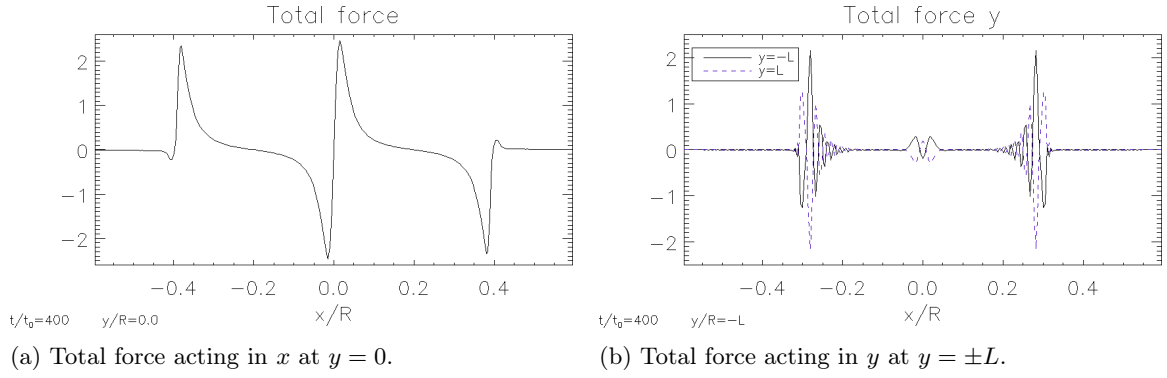


Figure 4.35: Plots of the total force components as a function of  $x$  at  $D \approx 7.9$  ( $t = 400$ ) for simulation e2 in Table 4.2 on page 102.

lowest value chosen here. These surfaces are similar to those found previously for the main full MHD data in Table 4.1 on page 79 for different values of  $\beta_0$  shown in Figure 4.13. Simulation 3 with low  $\beta_0$  has a final state similar to small values of  $a$ . The spiked parts in the surface for  $a = \frac{1}{4}$  indicates the system has encountered numerical problems for the smallest value of  $a$ .

### Forces in Field Expansion

It is interesting to see how applying the driver over part of the  $x$  range affects the forces in the  $x$  and  $y$  directions. This, of course, will show if the field is expanding and how this change affects the density. The  $x$  component of the total force is shown in Figure 4.35a, on page 103, as a function of  $x$ , for  $a = 1/2$ . It is initially surprising to see that the force in  $x$  has the opposite sign compared to the main simulations analysed previously. In the previous cases where there was no room for the plasma to expand the magnetic force dominated the pressure gradient. However, now the field can expand which means the magnetic pressure does not build up at the boundary and less pressure force is needed to balance it. It may be the case that the plasma is not as compressed in the middle either. Here the  $x$  component of the force has a small magnitude at the boundary of the driven region in  $x$  which acts toward the boundaries. This shows that the force is acting to expand the plasma. Around  $x = 0$  the  $y$  component of the total force, in Figure 4.35b, is similar to before. In contrast in the region where the field is expanding the force shows rapid oscillations. This may indicate that these simulations are under-resolved.



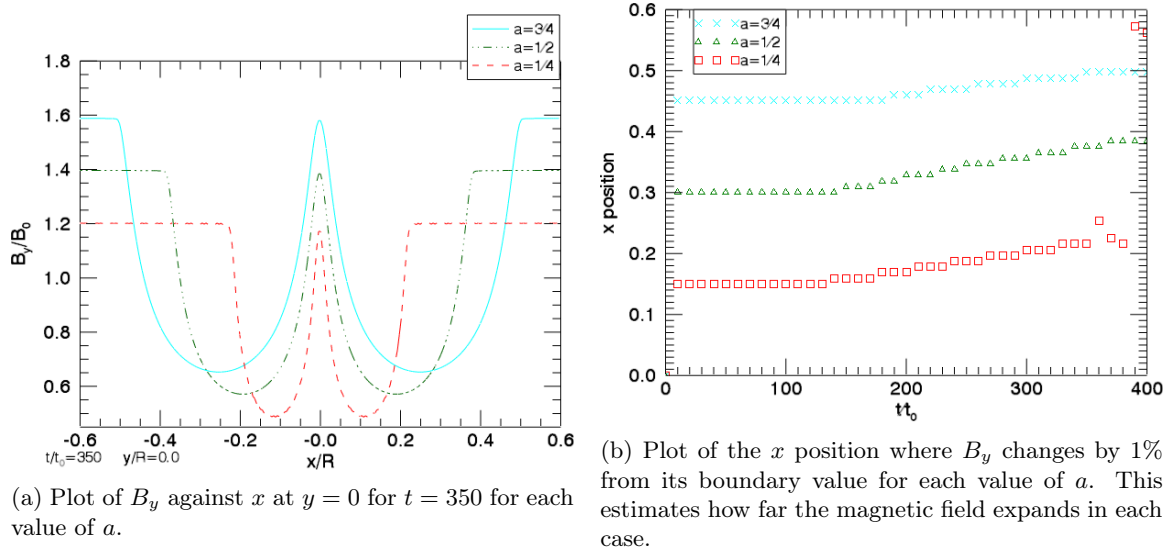


Figure 4.36: The values of  $a$  are those used in the simulations in Table 4.2 on page 102.

#### Effect on Fieldlines and Flux Conservation of Field Expansion

It is interesting to consider how driving a perpendicular magnetic field component results in compression or expansion of the background field when different amount of the field are driven. The process is as follows: the driver creates a sheared field which produces a magnetic force  $\nabla \frac{B_z^2}{2}$ . This force acts on the plasma density to compress or expand it. A good illustration of flux conservation is given by this change in the background field,  $B_y$ , when the field is allowed to expand. Flux is conserved as

$$\frac{1}{2l} \int_{-l}^l B_y dx = 1.0,$$

for all  $y$  and time. This shows that the total flux along  $x$  remains the same throughout the simulation. Initially the flux is divided equally between the regions where the shearing is applied and where it is not. Thus, when the field (and flux) decreases due to the magnetic pressure in a certain region, the area of this region must increase (expand) in order to contain the same amount of flux and thus maintain flux conservation. It follows that the unsheared region loses area and, hence flux, and so the constant value of the unsheared region must increase. The more flux that is contained in the unsheared region, the lower  $B_y$  is where the driver is applied. This idea is shown in Figure 4.36a, on page 104, for each value of  $a$  considered. Here  $B_y$  is plotted against  $x$  at  $y = 0$  at the end of the simulations ( $t = 350$ ). Note here that the smaller  $a$  the smaller  $B_y$  everywhere and, in each case, the field expands by a different amount. In Figure 4.36b the amount the field has expanded, defined as the point where the field has changed by 1% from the value at the boundary, is shown as a function of time for each  $a$ . The last couple of points for  $a = \frac{1}{4}$  show a significant jump in magnitude, so, again, the sign that this simulation has encountered problems.

Figure 4.37a shows the initial and final fieldlines for  $a = 1/2$ . This illustrates that

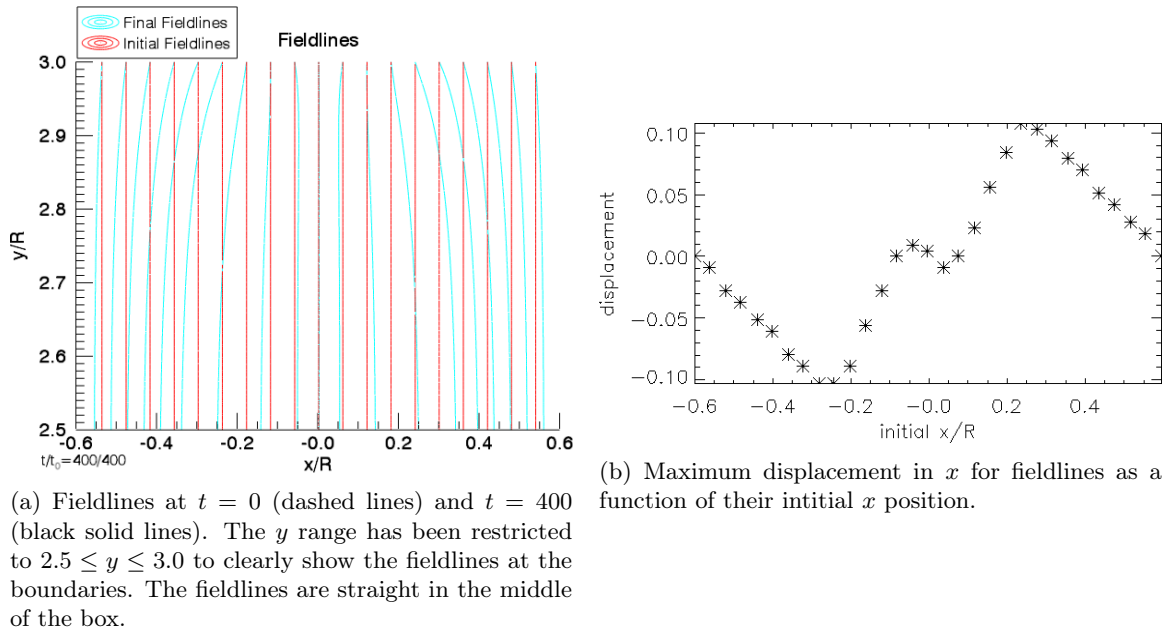


Figure 4.37: Figures for simulation e2 in Table 4.2 on page 102.

the magnetic fieldlines are allowed to expand into the region where there is no shear. It is difficult to tell by the fieldlines alone that the magnetic field is compressed in the middle as for the main MHD data previously discussed in Figure 4.28 on page 99. This is because the field expands a lot into the region with no shearing applied. To see if the fieldlines in the middle are still compressed, we calculate the maximum displacement for fieldlines starting at different initial  $x$  values in Figure 4.37b. This shows that the field is indeed still compressed in the center about  $x = 0$  but the displacement at other  $x$  values is much larger.

## 4.4 Summary

A simple footpoint shearing experiment has been investigated in this chapter to test four different methods: magnetofrictional relaxation, 1D approach, linearisation and RMHD, against full MHD results. The relaxation method provides an excellent match to the full MHD results for  $\mathbf{B}$  for low  $\beta_0$ , regardless of the footpoint displacement. The inclusion of the gas pressure and plasma density is possible (see Hesse and Birn 1993), but this has not been done here.

Solutions of the 1D approach give outstanding agreement with the Lare2D results for  $B_y$ ,  $B_z$ ,  $p$ ,  $\rho$ ,  $j_y$ , and  $j_z$  for all footpoint displacements and low values of  $\beta_0$  investigated. There are small discrepancies for higher values of  $\beta_0$  and the pressure and density predictions are displaced for low  $\beta_0$ . The 1D approach is, of course, derived with this specific experiment in mind. Unlike the relaxation method, it is not readily extendable to more complex photospheric footpoint displacements, but it does do exceptionally well for this particular problem.

The simplest dynamical approach, linearisation was used to expand the MHD

equations in powers of  $D/L$ . In principal, this should only be valid for  $D \ll L$ . Surprisingly, it has been found that this method provides good agreement for  $D/L \lesssim 1$ . One strength of this model is that it can provide useful insights into the dynamics. The MHD equations can always be linearised, but the existence of an analytic solution for more complex boundary conditions is not certain.

For this 2.5D system, RMHD is identical to the first-order linear MHD results, and thus is not capable of reproducing the results from full MHD. This is primarily because its main assumptions do not hold in this situation. While RMHD has the same parallel current component  $j_y$  as linear MHD, it does not provide any information about  $j_z \approx (\partial B_y / \partial x)$  since there can be no change to  $B_y$ . Hence, force balance can only be maintained by balancing the magnetic pressure due to  $B_{1z}^2/2$  by the gas pressure instead of through a change in the axial field,  $B_y$ . RMHD can, in theory, be applied to more complex incompressible photospheric motions, but it is uncertain whether the resulting evolution would satisfy the assumptions of RMHD, even if valid initially. Hence further investigation into validity of RMHD is required.

Solving the full MHD equations remains the preferred approach, provided sufficient computing resources are available to generate the long time evolution of the magnetic field.

There are many possible choices to extend this investigation to more complex systems and to explore the dependencies of this system in more detail. One interesting direction is to test different driving motions.

The main message to be taken from this work is that care should be taken not to simply implement a method without first establishing whether the assumptions are valid.

As mentioned, the driving motions used in this chapter are very similar to that used with RMHD in Rappazzo, Velli, and Einaudi 2010. In order to motivate qualitative comparisons with their study and discuss validity of RMHD, our simple system must be extended to 3D and a perturbation needs to be added. This is done in the next chapter.

## Chapter 5

# Tearing Instability: Validity of RMHD

### 5.1 Introduction

In the last chapter, we modelled the evolution of a footpoint driven coronal loop. The slow continuous driving applied at the loop ends allows the magnetic field to evolve through sequences of equilibria, during which the magnetic energy is stored. The build up of magnetic energy is the first stage of the coronal heating model. The next stage is the release of this stored energy. This can be done by reconnection. One mechanism to trigger reconnection is the tearing instability.

Conditions for the onset of the tearing instability are well known analytically, Furth, Killeen, and Rosenbluth 1963, and have been investigated analytically and numerically, using a stationary equilibrium magnetic field in full MHD (for example Velli and Hood 1989; Steinolfson 1983; van Hoven 1979; Einaudi and Rubini 1986; Einaudi and Rubini 1989) and RMHD (for example: Huang and Zweibel 2009; Strauss 1988).

Validity of using the RMHD equations for insights into the tearing mode, depends on the approach used. If complete invariance, i.e no slow variation, along the background field direction is assumed the equations and subsequent analysis are equivalent to that found for 2D incompressible MHD, and the growth rate is given by Equation (2.68) on page 25. On the other hand, if the slow parallel variation is retained in the equations which are then linearised, solutions are likely to be inaccurate. As noted in the appendix of Oughton, Dmitruk, and Matthaeus 2003, it is inappropriate to linearise the RMHD equations, since RMHD assumes the nonlinear and linear terms are of the same order of magnitude and the method of linearisation seeks to separate these processes.

Generally, the onset of the tearing mode in an initially stationary equilibrium containing current layers is studied. A more realistic approach is to consider the onset while strong currents are forming in time. Recently a modification to the fundamental tearing analysis was proposed which takes into account the time dependent formation of current by Uzdensky and Loureiro 2016; Tolman, Loureiro, and Uzdensky 2018.

The focus of most of these previous studies has been on understanding the growth rates, onset conditions and reconnection properties of the tearing instability. Another aspect of the phenomenon is to consider the overall time evolution of the system: evolution

through sequences of equilibria, formation of current sheets, development of the instability, subsequent energy release and further, yet unknown evolution after the instability.

Recently, Rappazzo, Velli, and Einaudi (2010) used RMHD to investigate the time evolution of a driven coronal loop in which the tearing mode occurs. They impose a driver of the form

$$v_{y \text{ RMHD}} = \sin \left( \frac{8\pi}{l}x + 1 \right).$$

This is very similar to the driver, Equation (4.3), applied in the previous chapter. An additional spatially random perturbation is imposed in  $v_x$ , to excite the tearing mode. Further details are given in Section 3.6.2. They concluded that the build up of energy and the release due to the tearing mode only occurred once. This does not agree with the coronal heating picture in full MHD, in which the build up and release of energy happens cyclicly. It is unclear whether RMHD is valid for the development of the tearing instability, since steep gradients are involved and the dynamics are likely to be 3D.

It is the aim of this chapter to check this conclusion of Rappazzo, Velli, and Einaudi 2010 using full MHD. To do this, our 2.5D system described in Chapter 4, is extended to 3D and an additional-symmetry-breaking perturbation is applied at the boundaries. Ideally, both the full MHD and RMHD equations would be solved to enable direct comparisons of these methods. Unfortunately, it has not been possible to do this. Nevertheless, the general evolution of our full MHD simulations can be qualitatively compared to results found using RMHD in Rappazzo, Velli, and Einaudi 2010 and enable us to confirm or disprove their conclusion. Our full MHD results can also be analysed to investigate whether the assumptions and constraints of RMHD are valid or not during the evolution.

This chapter is organised as follows. In Section 5.2 the full MHD equations and additional experimental set up is discussed. Results are presented in Section 5.3; in Section 5.3.1 our set of full 3D MHD simulations are briefly discussed, in Section 5.3.2 the assumptions and constraints of RMHD are tested using our full MHD data. in Section 5.3.3 we discuss the qualitative similarities and differences between our full MHD simulations. In Section 5.3.4 the dynamical evolution of one of our full 3D MHD simulations is described. In Section 5.4 a summary is given.

## 5.2 Experiment Overview

### 5.2.1 MHD Equations

The full 3D dissipative compressible MHD equations, described in Chapter 2 in Equation (2.16), on page 13. are

$$\rho \frac{\partial \mathbf{v}}{\partial t} + \rho(\mathbf{v} \cdot \nabla) \mathbf{v} = -\nabla p + \mathbf{j} \times \mathbf{B} + \nabla \cdot \mathbf{S}, \quad (5.1a)$$

$$\frac{\partial \rho}{\partial t} + \nabla \cdot (\rho \mathbf{v}) = 0, \quad (5.1b)$$

$$\frac{\partial \mathbf{B}}{\partial t} = \nabla \times (\mathbf{v} \times \mathbf{B}) - \nabla \times (\eta \nabla \times \mathbf{B}), \quad (5.1c)$$

$$\frac{\partial}{\partial t} \left( \frac{p}{\gamma - 1} \right) + \mathbf{v} \cdot \nabla \left( \frac{p}{\gamma - 1} \right) = -\frac{\gamma p}{\gamma - 1} \nabla \cdot \mathbf{v} + \epsilon_{ij} S_{ij} + \eta j^2, \quad (5.1d)$$

together with

$$\mathbf{j} = \frac{\nabla \times \mathbf{B}}{\mu}, \text{ and } \nabla \cdot \mathbf{B} = 0. \quad (5.2)$$

As before, in Chapter 2, the viscous stress tensor is given by Equation (2.13) and the strain rate is given by Equation (2.14). For the current experiment nonzero resistivity is necessary in order to study the nonlinear tearing mode. Care needs to be taken to ensure that  $\eta$  is not too large with respect to the driving velocity. As shown in Bowness, Hood, and Parnell 2013 a nonzero value of  $\eta$  will cause the driven magnetic field component to saturate to a maximum footpoint displacement where the footpoints cannot be driven any further. To ensure that this is not a problem we take  $\eta$  to have the form

$$\eta = \eta_b + \eta_{\text{anom}},$$

where  $\eta_b$  is a background resistivity which allows dissipation throughout the domain and  $\eta_{\text{anom}}$  is an anomalous resistivity which is only locally switched on once the modulus of the current exceeds a threshold value,  $j_{\text{crit}}$ , as

$$\eta_{\text{anom}} = \begin{cases} 0 & |j| < j_{\text{crit}}, \\ \eta_{\text{anom}} & |j| \geq j_{\text{crit}}. \end{cases} \quad (5.3)$$

Anomalous resistivity is used so that localised dissipation only occurs in regions of high current density.

The MHD equations are normalised in the same way as discussed in Section 4.2.1. Thermal effects are not considered in this chapter. Quantities simply scale accordingly when changing the normalisation,  $\rho_0$ ,  $R$  or  $B_0$ . The values used in this chapter are the same as for the previous chapter, namely  $B_0 = 0.01\text{T}$ ,  $\rho_0 = 1.67 \times 10^{-4}\text{kg/m}^3$  and  $R = 180,000\text{m}$ . This normalisation gives an Alfvén speed of  $V_A = 2070\text{m s}^{-1}$ , Alfvén travel time of  $t_0 = 87\text{s}$  and a reference temperature of  $516.7\text{K}$ .

### 5.2.2 Experiment Description

As in Chapter 4, Section 4.2.2, we consider a computational box of size  $0 \leq x, y \leq 2\ell$ , and  $0 \leq z \leq 2L$ . In this 3D box we have an initial, uniform magnetic field,  $\mathbf{B} = B_0 \hat{\mathbf{e}}_z$ , uniform density,  $\rho_0$  and uniform pressure,  $p_0$ . In our dimensionless variables,  $B_0 = 1$ ,  $\rho_0 = 1$  and  $p_0$  is a constant. We take  $L = 2.5$  and  $\ell = 0.5$ , which gives the ratio  $\ell/L = 0.2 \ll 1$ . This large aspect ratio satisfies the second RMHD assumption. Line tied boundary conditions are used at the loop ends in  $z$  and periodic boundary conditions are used in  $x$  and  $y$ . All quantities, except velocity, have zero gradients at the loop ends. The parallel velocity,  $v_z$ , is zero at the loop ends. The remaining two velocity components are given a specific driving profile as follows.

Two types of velocity motions are required at the loop footpoints in order to investigate the evolution of the nonlinear tearing instability in an initial uniform background field. First, we need to create a spatially varying equilibrium magnetic field which changes sign over a small distance. This is done by applying a driving velocity,  $v_y$ , that shears the initial uniform background field. This motion is considered to be sub-sonic and sub-Alfvénic and it has been shown before, in Goldstraw et al. 2018 and Chapter 4, that this system would evolve through sequences of equilibria if it is not disturbed. Second, a small symmetry-breaking perturbation is needed to produce a wavevector which satisfies  $\mathbf{k} \cdot \mathbf{B}_e = 0$  (where here  $\mathbf{B}_e$  is the equilibrium field, such as Equation (2.47) on page 21, in Section 2.8 for the tearing analysis). This is achieved by injecting waves in  $v_x$ .

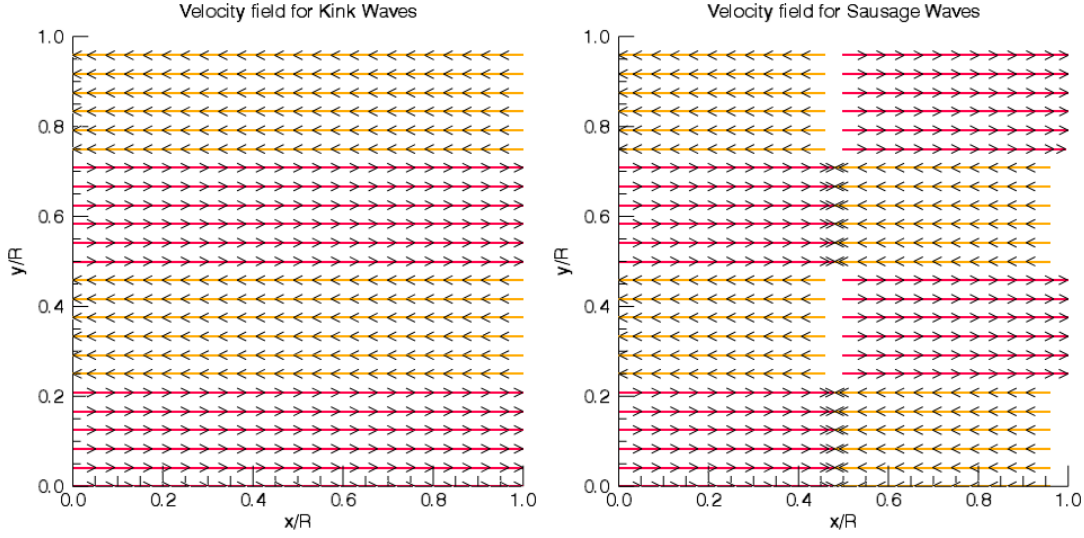
Following on from Chapter 4, we choose the same driving motions as in Equation (4.3) on page 64. In this chapter the size of the box has been altered, and so the adjusted driving velocity is given by

$$v_y(x, y, z = 0; z = 2L, t) = \pm F(t) \sin kx, \quad (5.4)$$

where  $k = \pi/\ell$ . The time-dependent amplitude,  $F(t)$ , is given by Equation (4.4) on page 64 with amplitude  $V_{0 \text{ shear}}$ . We use  $t_1 = 6$  and  $\tau_0 = 2$ , as in Chapter 4. The second type of velocity fluctuations are symmetry-breaking perturbations. These perturbations are taken to be waves in  $v_x$ . In order to ensure the system setup is, theoretically, valid in the RMHD formalism it is necessary to ensure the footpoint motions are incompressible. Two possible boundary conditions that satisfy this are chosen: one involving kink waves and the second involving sausage waves. The boundary conditions for kink waves are of the form

$$v_x(x, y, z = 0; z = 2L, t) = V_{0 \text{ waves}} \sin(2ky) \sin\left(\frac{2\pi t}{\tau_{\text{waves}}}\right), \quad (5.5)$$

where  $V_{0 \text{ waves}}$  is the amplitude of the waves and  $\tau_{\text{waves}}$  is the period of the kink waves. The boundary conditions for kink waves, Equation (5.5), and the driving velocity, Equation (5.4), are incompressible. The second type of boundary conditions for  $v_x$  used is in the form of sausage waves. In this case a small modification to the shear velocity, Equation (5.4), is needed to ensure incompressibility. The boundary conditions for a sausage



(a) Vector field of Equation (5.5) for a perturbation in the form of kink waves.

(b) Vector field of Equation (5.7) for a perturbation in the form of sausage waves.

Figure 5.1: Vector field representation of the two types of perturbations used.

wave perturbation are given by

$$v_y(x, y, z = 0, 2L) = \pm F(t) \sin(kx) + V_{0 \text{ waves}} \cos(2ky) \sin\left(\frac{2\pi t}{\tau_{\text{waves}}}\right) \cos(kx), \quad (5.6)$$

$$v_x(x, y, z = 0, 2L) = V_{0 \text{ waves}} \sin(2ky) \sin\left(\frac{2\pi t}{\tau_{\text{waves}}}\right) \sin(kx). \quad (5.7)$$

We consider the case  $V_{0 \text{ shear}} \gg V_{0 \text{ waves}}$  only for sausage waves. The correction to the shear velocity to maintain incompressibility on the boundaries for the sausage waves is small compared to the size of the shear. The wave amplitude for the kink waves is varied with respect to the driver amplitude. These two types of perturbations in Equation (5.5) and Equation (5.7) are represented as vector fields in the  $x - y$  plane in Figure 5.1.

The footpoint displacement is given by Equation (4.5) on page 65. The maximum displacement is taken to be equal to the displacement due to the driving,  $D_{\text{shear}}$ , only. The displacement due to the waves,  $D_{\text{wave}}$ , is neglected since the displacement due to the waves is orthogonal to the driving motion. Furthermore the displacement in  $y$  due to the driver,  $D_{\text{shear}}$ , increases indefinitely as a function of time, whereas  $D_{\text{wave}}$  has a maximum possible distance before reversing direction. Thus  $D_{\text{shear}} > D_{\text{waves}}$  after only a couple of timesteps, hence we shall write  $D = D_{\text{shear}}$ .

The relevant amplitude in this system are very similar to Chapter 4, discussed in Section 4.2.2, with the addition of the wave amplitude,  $V_{0 \text{ waves}}$ . A reference velocity,  $V_0$ , is taken for the driving and wave amplitudes. In order to pass through sequences of equilibria, we require

$$V_{\text{diss}} \ll V_{0 \text{ shear}}, V_{0 \text{ waves}} \ll c_s. \quad (5.8)$$

The driving and wave amplitudes are also slow and sub-Alfvénic if  $V_{0 \text{ shear}} \ll 1$  from



Table 5.1: The values for our full MHD simulations.  $V_0 = 0.02$ .  $\eta$  and  $\nu$  are the order of  $10^{-4}$ .

Simulation	$\beta_0 = 2p_0$	$e_0 = \frac{3}{2}p_0$	$\nu$	$\eta_0$	$\eta_{\text{anom}}$	$ j $	$V_0$ shear	$V_0$ waves	$\tau_{\text{waves}}$	waves
MHD:A	4/30	0.1	1	1	0.0	-	$V_0$	$V_0/10$	4.0	kink
MHD:B1	4/30	0.1	1	1	0.0	-	$V_0$	$2V_0$	4.0	kink
MHD:B2	4/30	0.1	1	1	0.0	-	$V_0$	$V_0$	4.0	kink
MHD:B3	4/30	0.1	1	1	0.0	-	$V_0$	$V_0/100$	4.0	kink
MHD:B4	4/30	0.1	1	1	0.0	-	$V_0/2$	$2V_0$	4.0	kink
MHD:C	4/300	0.01	1	1	0.0	-	$V_0$	$V_0/10$	4.0	kink
MHD:D	4/30	0.1	1	1	0.0	-	$V_0$	$V_0/10$	9.0	kink
MHD:saus	4/30	0.1	1	1	0.0	-	$V_0$	$V_0/10$	4.0	sausage
MHD:anom1	4/30	0.1	1	0.0	1	30	$V_0$	$V_0/10$	4.0	kink
MHD:anom2	4/30	0.1	1	0.0	10	30	$V_0$	$V_0/10$	4.0	kink
MHD:shear	4/30	0.1	1	1	0.0	-	$V_0$	0.0	0.0	-
MHD:ideal	4/30	0.1	0.0	0.0	0.0	-	$V_0$	$V_0/10$	4.0	kink

Equation (4.2) on page 63. Accordingly we take a reference speed of  $V_0$  as 0.02. As before, in Chapter 4, Equation (4.6) on page 65 then requires that the pressure is larger than a minimum value of  $p_0 \gg 2.4 \times 10^{-4}$ . This is satisfied in the simulations presented here. The driving and wave amplitudes are allowed to vary relative to the reference speed,  $V_0$ , and each other. The important parameters that will be varied in this study are:  $V_0$  shear,  $V_0$  waves,  $\tau_{\text{waves}}$ ,  $\beta_0$ ,  $\eta_b$ ,  $\eta_{\text{anom}}$ . The two types of perturbation: kink and sausage waves, are also tested.

In the next section we discuss the results of our full MHD simulations.

### 5.3 Results

As an initial test, two simple 3D simulations, MHD:ideal and MHD:shear in Table 5.1 on page 112, were done to ensure the general evolution is as expected and similar to our previous 2.5D MHD simulations, discussed in Chapter 4, Section 4.3. First, an ideal simulation, simulation MHD:ideal, with  $\nu = \eta = 0$ , uses the shearing, given by Equation (5.4), and kink waves, given by Equation (5.5). Energies are shown in Figure 5.2. The magnetic energy, shown in Figure 5.2b, increases quadratically, in agreement with Chapter 4 results presented in Figure 4.8 on page 83. The kinetic energy, shown in Figure 5.2a, oscillates about an approximately steady state, in agreement with results from Chapter 4, in Figure 4.9 on page 84. The kink waves make little difference and the evolution of the magnetic and kinetic energies are very similar to the previous 2.5D case. From this it is confirmed that the tearing instability does not occur in an ideal system. This simulation also provides a useful reference of an ideal evolution. A second test was done for a system very similar to Chapter 4 using the driver, Equation (5.4) and nonzero viscosity. Simulation MHD:shear also uses nonzero resistivity to check the effect this has on the evolution. The magnetic and kinetic energy, Figure 5.2, evolve similarly to the above ideal case, except that the magnetic energy does not increase as quickly as the ideal and previous 2.5D cases, which is a consequence of non zero  $\eta$ . This simulation allows us to check that the perturbation applied at the boundary is necessary for the onset of the tearing mode and provides a useful benchmark for the dynamics of a resistive system if the instability did not develop.

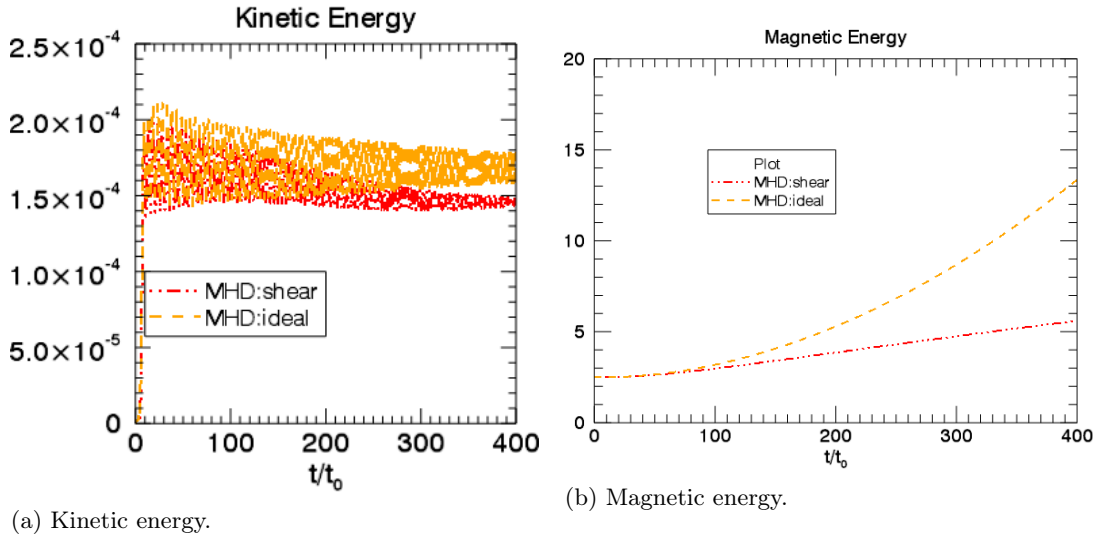
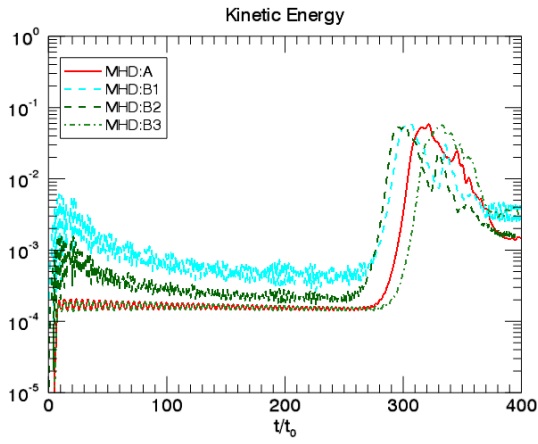


Figure 5.2: Plots of volume integrated instantaneous energy as functions of time. The legends refer to the simulation names in Table 5.1 on page 112.

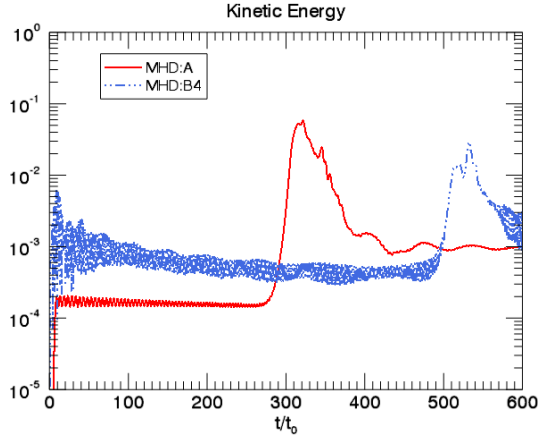
### 5.3.1 Overview of Full MHD Simulations

Several full MHD simulations, detailed in Table 5.1 on page 112, were done for different system parameters. A number of parameters are varied to investigate how the footpoint motions affect the evolution of the system. These parameters include: the wave and driving amplitudes,  $V_0$  waves and  $V_0$  shear (simulations MHD:A, B1-4), wave period,  $\tau_{waves}$  (simulation MHD:D) and the initial plasma beta,  $\beta_0$  (simulation MHD:C). Simulation MHD:A is used as the reference case. For most simulations one parameter was changed with respect to this reference case.

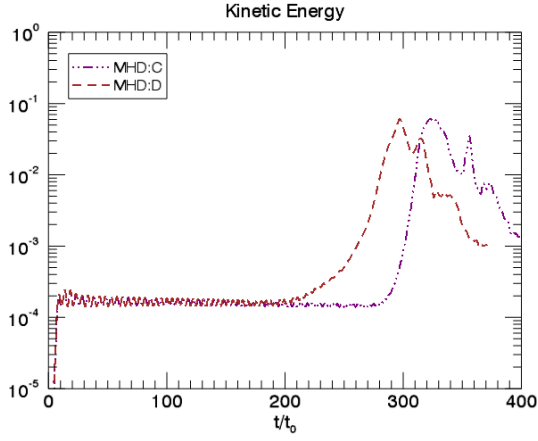
Two sets of boundary conditions are chosen so that the perturbations are incompressible to keep the initial setup within the RMHD formalism. This way any compressible effects are dynamically created during the evolution. It is then possible to investigate if the system remains in a state similar to RMHD or whether additional effects are important. In simulation MHD:saus, a driving profile and perturbation in the form of sausage waves, given in Equation (5.6) and Equation (5.7) is applied at the loop ends. The driver and perturbation in the form of kink waves, given by Equation (5.4) and Equation (5.5), are applied in all other simulations, except simulation MHD:shear, where no perturbation is applied as discussed above. The majority of the simulations, in Table 5.1 on page 112, use background resistivity,  $\eta_0$ , however it was difficult to test the effect of varying  $\eta$  this way. A larger value of  $\eta$  causes the footpoints to slip (Bowness, Hood, and Parnell 2013). Once this happens the field cannot be driven any further and the instability may not develop. A value of  $\eta$  that is too small results in numerical resistivity dominating the physical value. Thus, in order to circumvent this problem and investigate the effect of changing  $\eta$ , two simulations, MHD:anom1 and MHD:anom2, are done using two different values of anomalous resistivity,  $\eta_{anom}$ , which is locally turned on where  $|\mathbf{j}|$  exceeds a specified threshold. Both of these simulations use the same threshold.



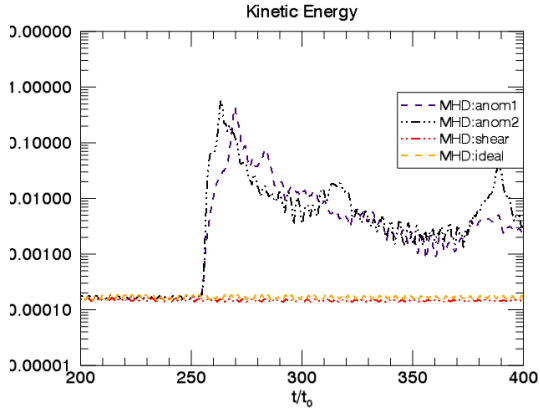
(a) The perturbation amplitude,  $V_0$  wave is varied.



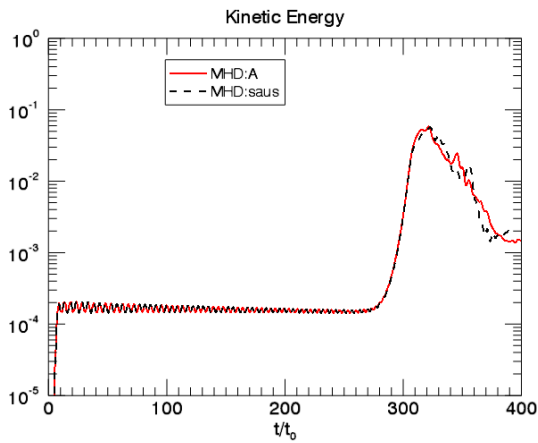
(b) The perturbation and driver amplitude,  $V_0$  waves and  $V_0$  shear, are varied.



(c) The perturbation period,  $\tau_{\text{waves}}$  and initial  $\beta_0$  are varied.

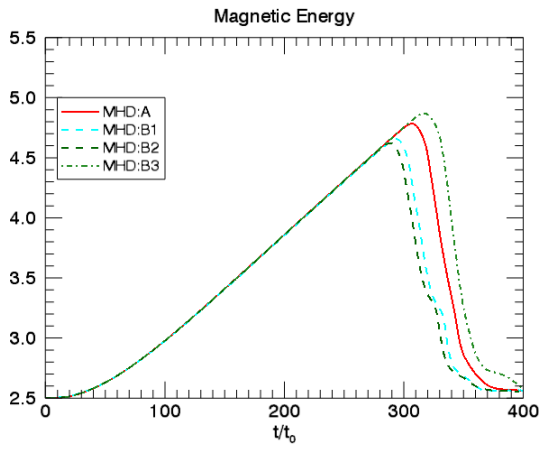
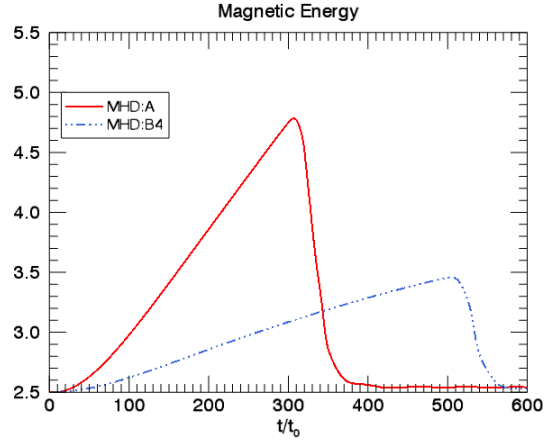
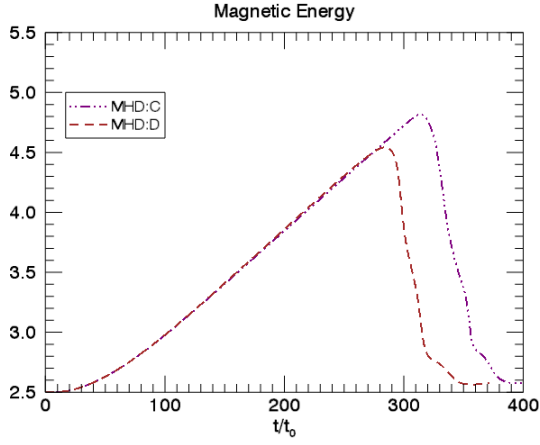
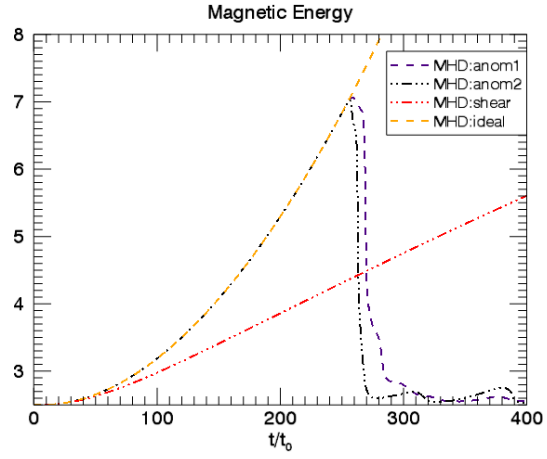
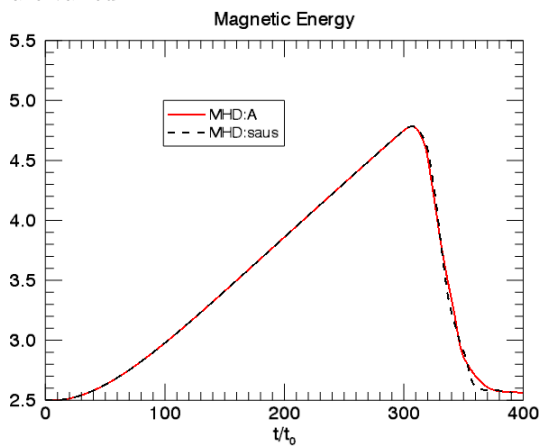


(d) Anomalous resistivity,  $\eta_{\text{anom}}$  is varied.



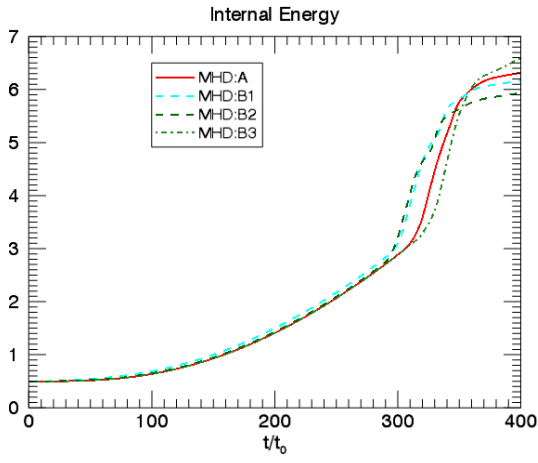
(e) Type of perturbation is varied.

Figure 5.3: Plots of volume integrated instantaneous kinetic energy against time for all of the simulations on a logarithmic  $y$  axis. The legends refer to the simulation names in Table 5.1 on page 112.

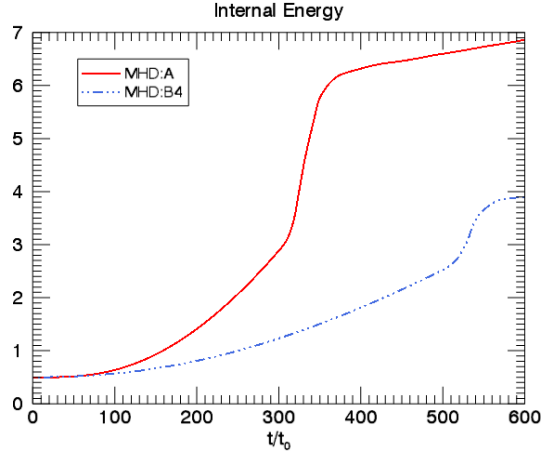
(a) The perturbation amplitude,  $V_{0 \text{ wave}}$  is varied.(b) The perturbation and driver amplitude,  $V_{0 \text{ waves}}$  and  $V_{0 \text{ shear}}$ , are varied.(c) The perturbation period,  $\tau_{\text{waves}}$  and initial  $\beta_0$  are varied.(d) Anomalous resistivity,  $\eta_{\text{anom}}$  is varied.

(e) Type of perturbation is varied.

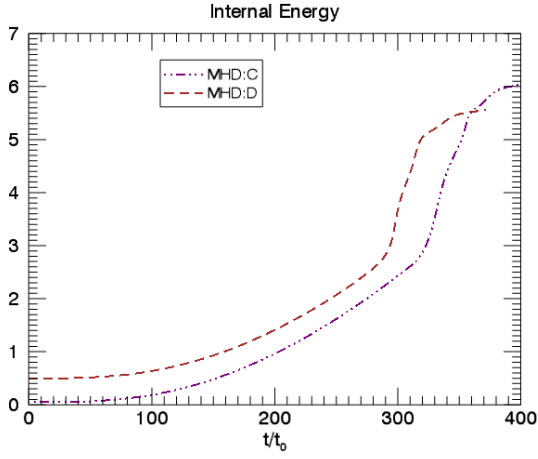
Figure 5.4: Plots of volume integrated instantaneous magnetic energy against time for all of the simulations. The legends refer to the simulation names in Table 5.1 on page 112.



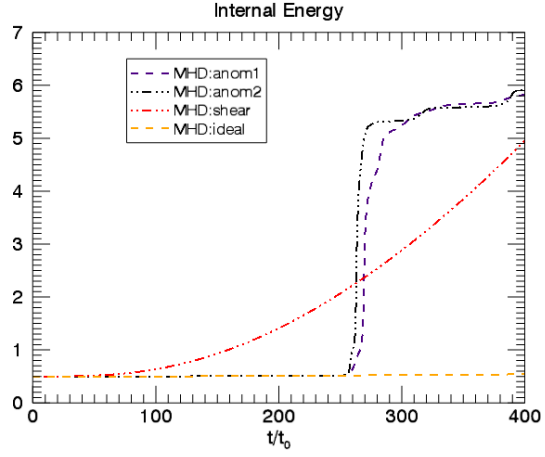
(a) The perturbation amplitude,  $V_0$  wave is varied.



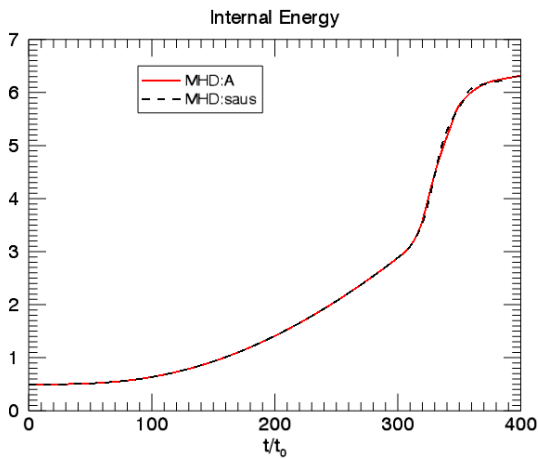
(b) The perturbation and driver amplitude,  $V_0$  waves and  $V_0$  shear, are varied.



(c) The perturbation period,  $\tau_{\text{waves}}$  and initial  $\beta_0$  are varied.

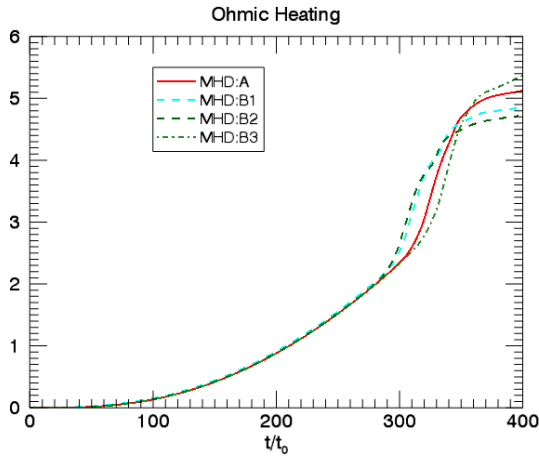
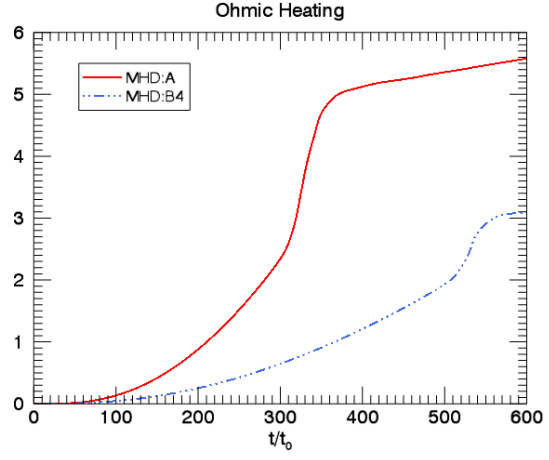
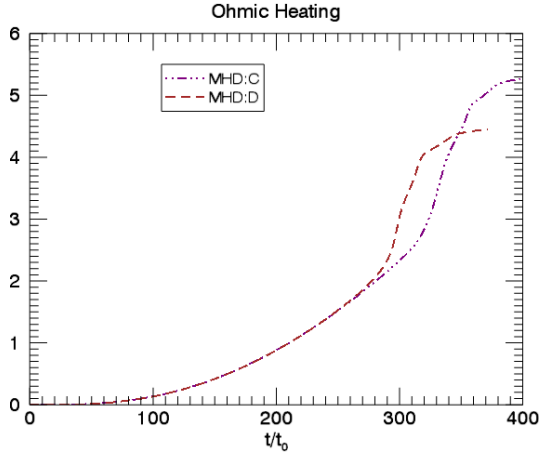
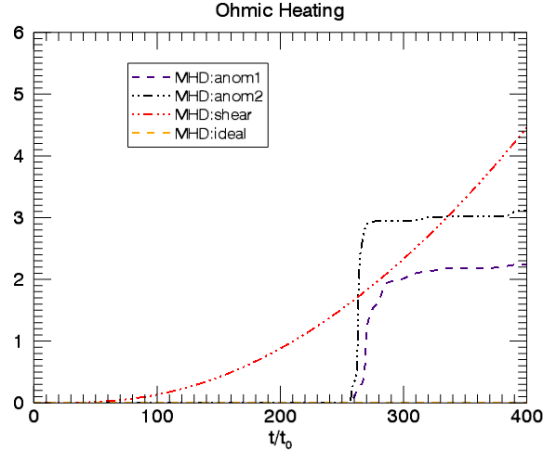
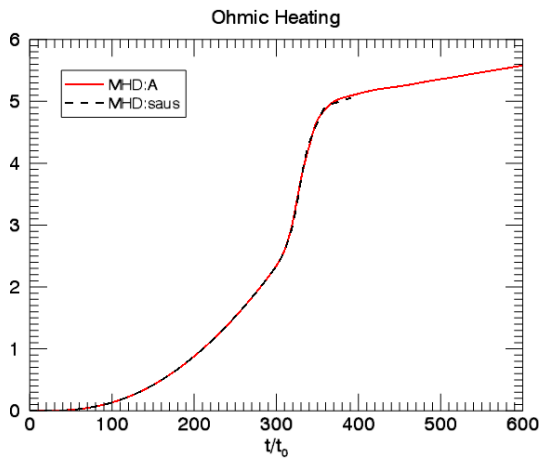


(d) Anomalous resistivity,  $\eta_{\text{anom}}$  is varied.



(e) Type of perturbation is varied.

Figure 5.5: Plots of volume integrated instantaneous internal energy against time for all of the simulations. The legends refer to the simulation names in Table 5.1 on page 112.

(a) The perturbation amplitude,  $V_0$  wave is varied.(b) The perturbation and driver amplitude,  $V_0$  waves and  $V_0$  shear, are varied.(c) The perturbation period,  $\tau_{\text{waves}}$  and initial  $\beta_0$  are varied.(d) Anomalous resistivity,  $\eta_{\text{anom}}$  is varied.

(e) Type of perturbation is varied.

Figure 5.6: Plots of volume integrated and time integrated ohmic heating against time for all of the simulations. The legends refer to the simulation names in Table 5.1 on page 112.

## Energies

The kinetic, magnetic and internal energy are plotted in Figure 5.3 (page 114), Figure 5.4 (page 115) and Figure 5.5 (page 116), respectively. The volume and time integrated ohmic heating is shown in Figure 5.6 on page 117. These figures show the energies for all simulations in Table 5.1. Initially, all of these simulations have generally the same energy evolution, which also agrees with the energy evolution of the 2.5D simulations in Figure 4.8 (page 83) and Figure 4.9 (page 84): kinetic energy oscillates around a steady value and magnetic energy is stored. Then, once the shearing exceeds a critical value, the tearing instability develops. For this shearing motion the instability occurs at about  $t = 280$ , in all cases presented in this chapter, except simulations MHD:ideal and MHD:shear as discussed earlier. The subsequent evolution differs from those discussed previously. After the instability develops the general evolution is as follows: the magnetic energy decreases, as it is converted to kinetic and internal energy, corresponding to a peak in kinetic energy and a large increase in internal energy and a rapid increase in the ohmic heating.

For simulations MHD:B1-3, which vary the perturbation amplitude,  $V_{0 \text{ waves}}$ , the time that the instability develops varies slightly compared to simulation MHD:A, as shown in Figure 5.3a. Varying  $V_{0 \text{ waves}}$  does not affect the rate of increase of magnetic energy, shown in Figure 5.4a. This means that the amount of energy stored depends on the onset time. Simulation MHD:B3, the smallest perturbation amplitude, develops the instability last. Simulations, MHD:B1 and MHD:B2, where the perturbation amplitude is larger than the driving, have a similar onset time which is smaller than MHD:A. For simulation MHD:B4, the driving speed is much less than the wave speed:  $V_{0 \text{ waves}} = 4V_{0 \text{ shear}}$ . Magnetic energy builds up significantly more slowly, shown in Figure 5.4b, compared to the other simulations, since the driving amplitude,  $V_{0 \text{ shear}}$ , is smaller. When the tearing instability does develop, at about  $t = 500$ , there is not as much magnetic energy stored and the peak in kinetic energy is smaller. This shows that the onset of the instability does depend on the relevant speeds of the waves and driver.

The energy evolution for simulations MHD:A and MHD:saus, Figure 5.3e, Figure 5.4e and Figure 5.5e, are very similar, showing that the evolution is equivalent using either kink or sausage waves.

For simulations MHD:anom1 and MHD:anom2, using anomalous resistivity, the kinetic, magnetic and internal energies are shown in Figure 5.3d and Figure 5.4d and Figure 5.5d, respectively, and the ohmic heating is shown in Figure 5.6d. Initially the two simulations are indistinguishable from the ideal case in MHD:ideal then the maximum current exceeds the threshold value and switches on the anomalous resistivity. This would enable the linear growth rate of the tearing mode to be tested for different values of  $\eta_{\text{anom}}$  in future work. It is found that the development of the instability does depend on the value of resistivity. The exact dependence of this needs further investigation. There is a small peak in the kinetic energy after the instability, at a time of  $t \sim 380$ , for simulation MHD:anom2 but no visible evidence of the magnetic energy being stored and so does not look like a second instability. The general dynamics of the anomalous simulations are analogous to the ones with background resistivity, except for the fact that in the former the magnetic energy is stored ideally and thus reaches a larger value before the instability.

In summary, the time that the instability develops varies a little as each parameter is varied, however the overall evolution is the same in each case. In the next section, we test the RMHD conditions using data from our reference full MHD simulation, simulation MHD:A.

### 5.3.2 Validity Tests of the RMHD Conditions

In this section, we check the conditions of RMHD, discussed in Section 3.4.1 and Oughton, Matthaeus, and Dmitruk 2017, using similar techniques used to measure anisotropy in Oughton et al. 2016 for full MHD turbulence with a guide field. We use data from simulation MHD:A in Table 5.1 on page 112. These validity tests will help to indicate whether RMHD is technically valid for the current system or not.

First, we check assumption (i) of RMHD:  $B_0^2 \gg b_\perp^2$ . We define the energy in each magnetic field component as

$$\langle \delta B_x^2 \rangle = \frac{1}{\langle B_0^2 \rangle} \int dV B_x^2, \quad \langle \delta B_y^2 \rangle = \frac{1}{\langle B_0^2 \rangle} \int dV B_y^2, \quad (5.9a)$$

$$\langle B_z^2 \rangle = \frac{1}{\langle B_0^2 \rangle} \int dV B_z^2, \quad \langle \delta B_z^2 \rangle = \frac{1}{\langle B_0^2 \rangle} \int dV B_z^2 - B_0^2, \quad (5.9b)$$

$$\langle B_0^2 \rangle = \int dV B_0^2, \quad (5.9c)$$

where  $B_0$  is the initial background magnetic field present at  $t = 0$ ,  $\delta B_z$  is the fluctuating part of the parallel field from the initial value,  $B_0$ ,  $B_z = B_0 + \delta B_z$  is the total parallel magnetic field which includes both the initial and fluctuating parts.  $\delta B_x$ ,  $\delta B_y$  are the  $x$  and  $y$  components of the magnetic field, which are zero initially. These quantities are plotted in Figure 5.7a on page 120. This shows that during the first stage, when magnetic energy is building up in the sheared magnetic field component,  $B_y$ , the amount of energy stored in this component reaches a maximum of about 90% of the initial magnetic field energy. It follows that the first assumption of RMHD cannot be satisfied once an appreciable amount of energy has been stored in the perpendicular components. Most of the injected energy is in  $B_y$  as the energy in  $B_x$  and  $\delta B_z$  remains small compared to  $B_0$ . After the stored energy has been released and the system reaches a steady state, the energy in the fluctuations is small compared to the initial field and this first RMHD condition may, again, be satisfied.

In Figure 5.7b on page 120,  $\delta p$  and  $\delta \rho$  are plotted. These are defined as the maximum variation from the initial uniform values, for example

$$\delta \rho = \max(\rho) - \rho_0. \quad (5.10)$$

There is a huge jump in the maximum of the density, giving  $\delta \rho \sim 4$ , after the instability and a large increase in the pressure (also evident in the internal energy plot in Figure 5.4a on page 115). When using RMHD changes in density and pressure are usually not considered. This may be arguable before and after the instability when these quantities remain relatively



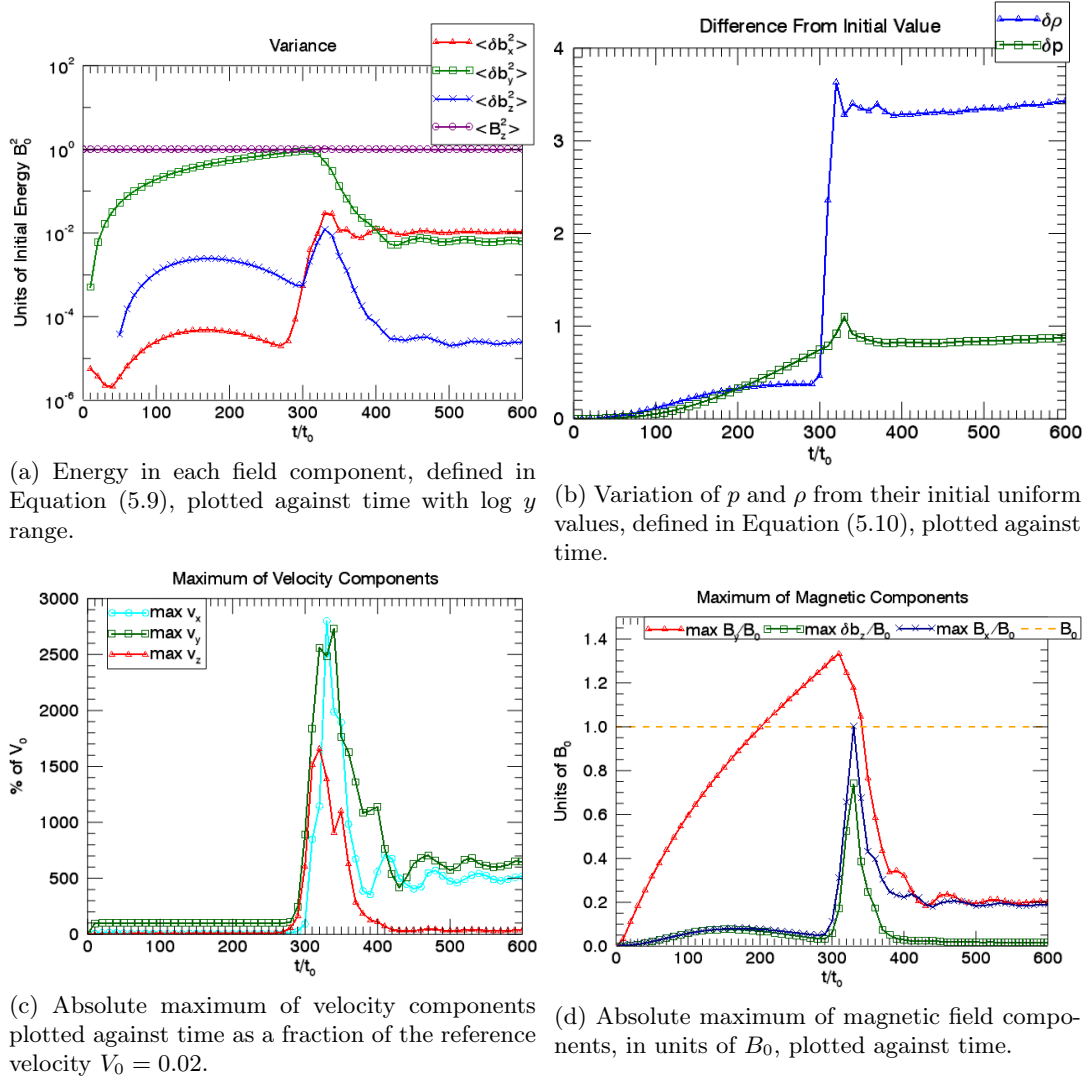


Figure 5.7: Tests of the RMHD conditions of a strong background field, variance anisotropy, negligible changes in density for simulation MHD:A in Table 5.1 on page 112.

constant in space, providing the pressure and density effects are not important for the dynamics, however the large change from the initial value would not be predicted.

Next, we test assumption (iii) of RMHD: variance anisotropy of the magnetic and velocity fields:  $b_z = v_z = 0$ . The absolute maximums of the field components are shown as functions of time in Figure 5.7d and Figure 5.7c on page 120, for magnetic and velocity components, respectively. The magnitude of the fluctuating parallel component of the magnetic field,  $\delta B_z$ , peaks about 70% of the initial field at  $t \sim 330$ , which occurs during the development of the instability and subsequent reconnection. This shows that there are significant variations in the parallel field which would be neglected in RMHD.  $B_x$  peaks at  $\sim 100\%$  of  $B_0$  and  $B_y \sim 130\%$ , showing that the magnitude of all of the components is similar to  $B_0$ . Ng, Lin, and Bhattacharjee 2012 also show that the magnitude of the perpendicular components is of the same order as the initial field in their RMHD simulations. The absolute maximum magnitude of the velocity components are much greater than the reference velocity,  $V_0 = 0.02$ . The parallel component of velocity,  $v_z$ , has a maximum

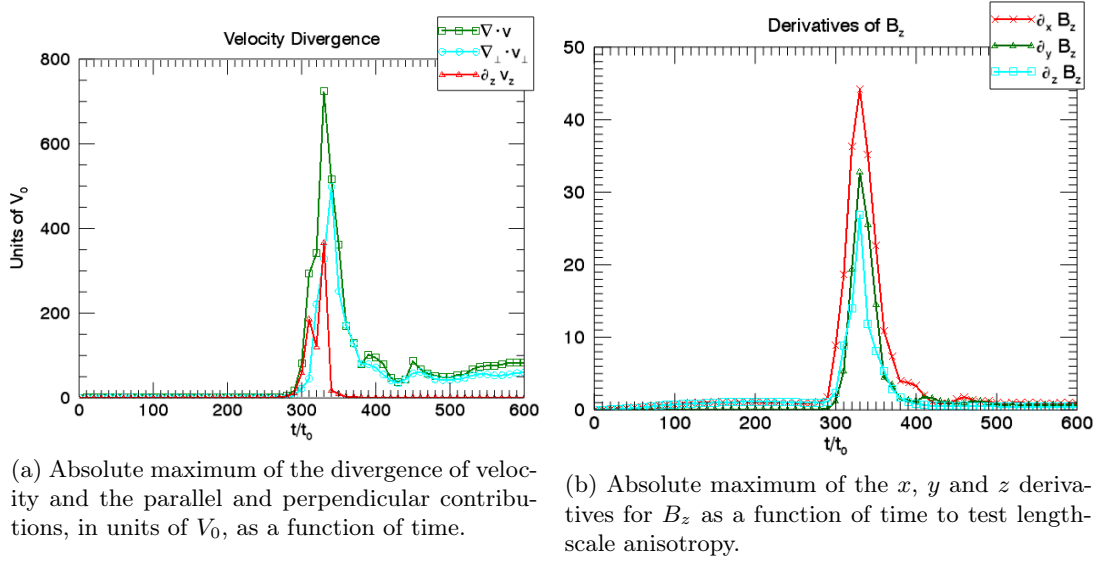


Figure 5.8: Tests of incompressibility and lengthscale anisotropy for simulation MHD:A in Table 5.1 on page 112.

magnitude about half of the perpendicular components. Thus, if parallel fluctuations are important in the evolution of the present system then the assumption of variance anisotropy would not be valid here.

One of the major simplifications of RMHD is the incompressibility of the velocity field in the perpendicular direction:  $\nabla_{\perp} \cdot \mathbf{v}_{\perp} = 0$ . To test the importance of compressible effects we plot the absolute maximum of  $\nabla \cdot \mathbf{v}$  normalised by the reference velocity,  $V_0$ , in Figure 5.8a on page 121. The divergence is split into its perpendicular and parallel contributions,  $\nabla_{\perp} \cdot \mathbf{v}_{\perp}$  and  $\frac{\partial v_z}{\partial z}$ . During the first phase, where magnetic energy is stored, the divergence is small, however it has been shown in Chapter 4 that the driver results in compression and expansion of the density and magnetic field. Thus, compressible effects are potentially still important during this phase but appear small in comparison to the compressible effects during the tearing evolution. Even when the system settles to a stationary state, at  $t > 400$ , the divergence is non-zero and is dominated by the perpendicular components, showing that even in the final state compressible effects may still be important.

In Figure 5.8b on page 121, we test assumption (ii) of RMHD: lengthscale anisotropy. This is done by plotting the absolute maximum of each of the derivatives of  $B_z$  as a function of time. It is clear that during most of the evolution the derivatives of  $B_z$  have approximately the same magnitude and so are roughly isotropic. Hence, any assumption that parallel variations are small compared to perpendicular ones is not valid for this system. The magnitude of the derivatives increases significantly during the growth of the instability and agrees with the large variation seen below for the parallel field.

In summary, the onset of the tearing mode results in dynamics that do not technically satisfy the RMHD conditions, even when the setup is valid in the RMHD formalism. However, it could be the case that the additional dynamical effects of compressibility and parallel fluctuations are small compared to the main processes in the system. A full inves-

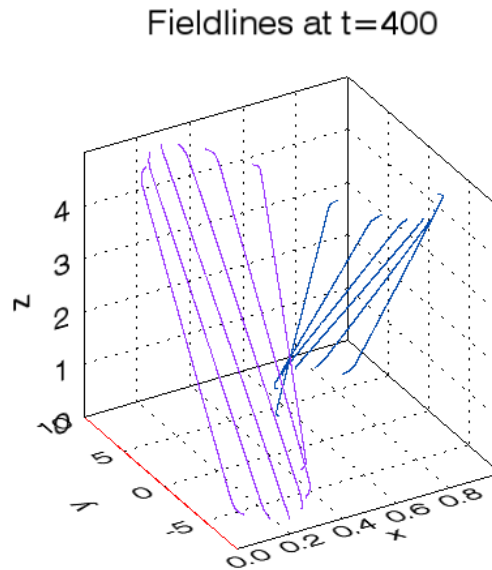


Figure 5.9: Magnetic fieldlines, traced from a 2D plane at  $z = 2.5$ , for simulation MHD:ideal in Table 5.1 on page 112. at  $t = 400$ . The  $y$  axis has been extended from  $[0, 1]$  to  $[-9, 9]$  to show the full fieldline displacement. This makes use of the periodic boundary conditions in  $y$ .

tigation of this will require direct comparisons of full MHD and RMHD simulations which will be done in the future. With these validity arguments in mind we outline qualitative comparisons of our full MHD simulations to the RMHD ones presented by Rappazzo, Velli, and Einaudi 2010 in the next section.

### 5.3.3 Qualitative Comparisons

Here we discuss some general aspects of our full MHD simulations and discuss similarities with the RMHD study done by Rappazzo, Velli, and Einaudi 2010.

Our kinetic and magnetic energies, in Figure 5.3 on page 114 and Figure 5.4 on page 115, show the same general characteristics found in their RMHD simulations, given in their Figures 1 and 2. Both methods illustrate that the evolution proceeds through three distinct phases: first the magnetic energy increases; second, the instability develops and magnetic energy is dissipated by reconnection processes and there is an increase in kinetic energy; lastly the system settles into a state where both magnetic and kinetic energies are approximately constant. A small, but noteworthy, difference in the final steady state is that our full MHD energies oscillate smoothly due to the choice of a smooth perturbation in the form of waves. In contrast, Rappazzo et al use a spatially random constant-time perturbation which results in a more unpredictable oscillation of the energies in the final steady state phase.

Another point is that the maximum stored magnetic energy for Rappazzo et al's RMHD results has almost reached the linear saturation limit imposed by nonzero resistivity. This shows that the magnetic field could not be driven much further. In contrast, our full MHD simulations are not near this linear threshold where the sheared magnetic field

saturates to a maximum. However, as shown in Figure 5.2b on page 113, the magnetic energy for MHD:shear is noticeably lower than MHD:ideal, hence the magnetic field has slipped a considerable amount when  $\eta$  is nonzero.

The evolution of the perpendicular magnetic field and  $|j|$  are also similar. This can be seen from Rappazzo et al's figure 3, which shows fieldlines and  $j_z$  in colour, and our full MHD figures for  $|j|$ , Figure 5.13 on page 128, and vector representation of the magnetic field in a plane perpendicular to the guide field, Figure 5.16 on page 133. In RMHD only the parallel current is nonzero, whereas, for full MHD, we have included all components. Rappazzo et al also retain the sign of  $j_z$ . It is clear that before the instability both methods predict fieldlines displaced in the sheared direction with strong concentrations of current. Rappazzo et al use a driver that creates many localised concentrations of current along the background field direction. There are not so many present in our full MHD simulations. Once the symmetry of this initial state is broken by the perturbation, the current reduces to localised patches of high current and "magnetic islands" form in 2D planes perpendicular to the initial field. Again, due to the different perturbations used, the RMHD results have many magnetic islands whereas there are not as many in our full MHD results.

Fieldline trajectories have been calculated for MHD:ideal in Figure 5.9 on page 122 and MHD:A in Figure 5.10 on page 125 and Figure 5.11 on page 126. Due to the nature of the footpoint motions and reconnection it is not possible to follow a single fieldline through its own unique evolution. Several fieldlines are plotted with initial points taken along  $y = 0$  at the midpoint in  $z$  ( $z = 2.5$ ) to give an impression of the overall evolution. Since the fieldlines undergo a large footpoint displacement in  $y$  they quickly move out of the simulation box in this direction. To show the full displacement the simulation box in Figure 5.9 and Figure 5.10 has been extended by several domain widths along the  $y$  direction. This is possible, since periodic boundary conditions are used in  $y$ . The simulation box in Figure 5.11 has been kept at its original dimensions to focus on the structure of fieldlines after the instability.

The final state, at  $t = 400$ , of the ideal case, MHD:ideal, is shown in Figure 5.9 on page 122. This shows how far the fieldlines are sheared when they do not reconnect. There is also evidence of the boundary layers, discussed in Chapter 4. This figure provides a 3D representation of the 2D figure, Figure 4.28 on page 99, which illustrates the compression and expansion of the magnetic field. Figure 5.10 on page 125 and Figure 5.11 on page 126 shows for four stages of the evolution of simulation MHD:A. At  $t = 200$ , in Figure 5.10a, fieldlines are sheared. At  $t = 300$ , in Figure 5.10b, the sheared fieldlines are distorted as the perturbation grows. At  $t = 350$ , in Figure 5.10c, the fieldlines reconnect and a new configuration is created. At  $t = 400$ , in Figure 5.10d, after the instability, it seems that fieldlines for MHD:A still have a large  $y$  component which appears to contradict the results in the previous section that the maximum of the  $y$  and  $x$  components are once again small compared to  $B_0$  after the instability. Figure 5.11d shows the same fieldlines looking down on the  $x - y$  plane. This shows that the  $x$  and  $y$  components have a similar magnitude which is smaller than the  $z$  component and so fieldlines are slightly twisted rather than sheared at the end. The fieldlines exit the box at the boundaries in  $x$ , and so the full fieldlines between the  $z$  boundaries are not followed.

Isosurfaces of  $|j|$  are also plotted for our full MHD simulation MHD:A in Figure 5.12 on page 127 at four simulation times, for two values of  $|j|$  indicated by the colourbar. These show that initially, at  $t = 200$  in Figure 5.12a, the current builds up in some regions, aligned with the  $z$  axis and along the  $y$  axis. This is the same as previously found in Chapter 4 in Figure 4.32 on page 101. Then, at  $t = 300$  in Figure 5.12b, the perturbation breaks the symmetry of the forming current structures. Then the energy is dissipated, at  $t = 350$  in Figure 5.12c, and, at  $t = 400$  in Figure 5.12d, the current is concentrated in smaller structures still aligned along  $z$  with small scale variations.

Similarly, contours of  $|j|$  are shown in Figure 5.13 on page 128 in the  $x - y$  plane at constant  $z = 2.5$ . At early times, in Figure 5.13a at  $t = 200$ , there are localised concentrations of strong current that extend along the initial field direction as indicated by the straight contour lines of constant  $|j|$  in the  $x - y$  plane and surfaces of constant  $|j|$  in Figure 5.12a, and in agreement with 2D surfaces of  $|j|$  in Chapter 4 in Figure 4.32 on page 101. At  $t = 300$  in Figure 5.13b and Figure 5.12b, these regions are perturbed by the waves and the current increases further in various smaller locations. During later times at  $t = 350$  in Figure 5.13c and  $t = 400$  in Figure 5.13d, the location of the large current agrees with the locations of reconnection sites as shown in the vector field in Figure 5.16 on page 133 where the energy is dissipated. During the evolution of the tearing mode the maximum magnitude of the current is about 200. This large value is reached very rapidly before rapidly decreasing. Thus, in order to provide a reasonable overview of the entire current evolution contours are plotted with values between 0 and 100.

These fieldlines and isosurfaces and contours of  $|j|$  can be qualitatively compared to figure 4 in Rappazzo et al for the steady state phase after the instability. RMHD also seems to predict twisted fieldlines but it is not possible to know whether the same amount of twist is present in both methods. The resulting current in RMHD still extends over the length in  $z$ . This may depend on the value of current plotted.

Rappazzo et al describe the process of the sheared field being a mapping of the boundary motion. They measure whether the field is a mapping or not by calculating the correlation length (their equation 36). This quantity was calculated for one of our full MHD simulations and showed similar behaviour to theirs. However, it is considered that this measurement overcomplicates the simple evolution of  $B_y$  which can be more easily understood by explicitly examining the sheared magnetic field itself as we describe in the next section.

In the next section we continue to discuss properties of the evolution in our full MHD simulations in more detail.

#### 5.3.4 MHD Dynamics

In this section, we discuss the dynamical evolution of the tearing instability in our reference full MHD simulation MHD:A. In order to capture the entire time evolution of the system, four simulation times have been chosen: a time of 200, before the instability, allows reference to be made to previous simulations in Chapter 4, a time of 300, just as the tearing instability develops, allows the growth of the perturbation to be seen and later times of 350 and 400

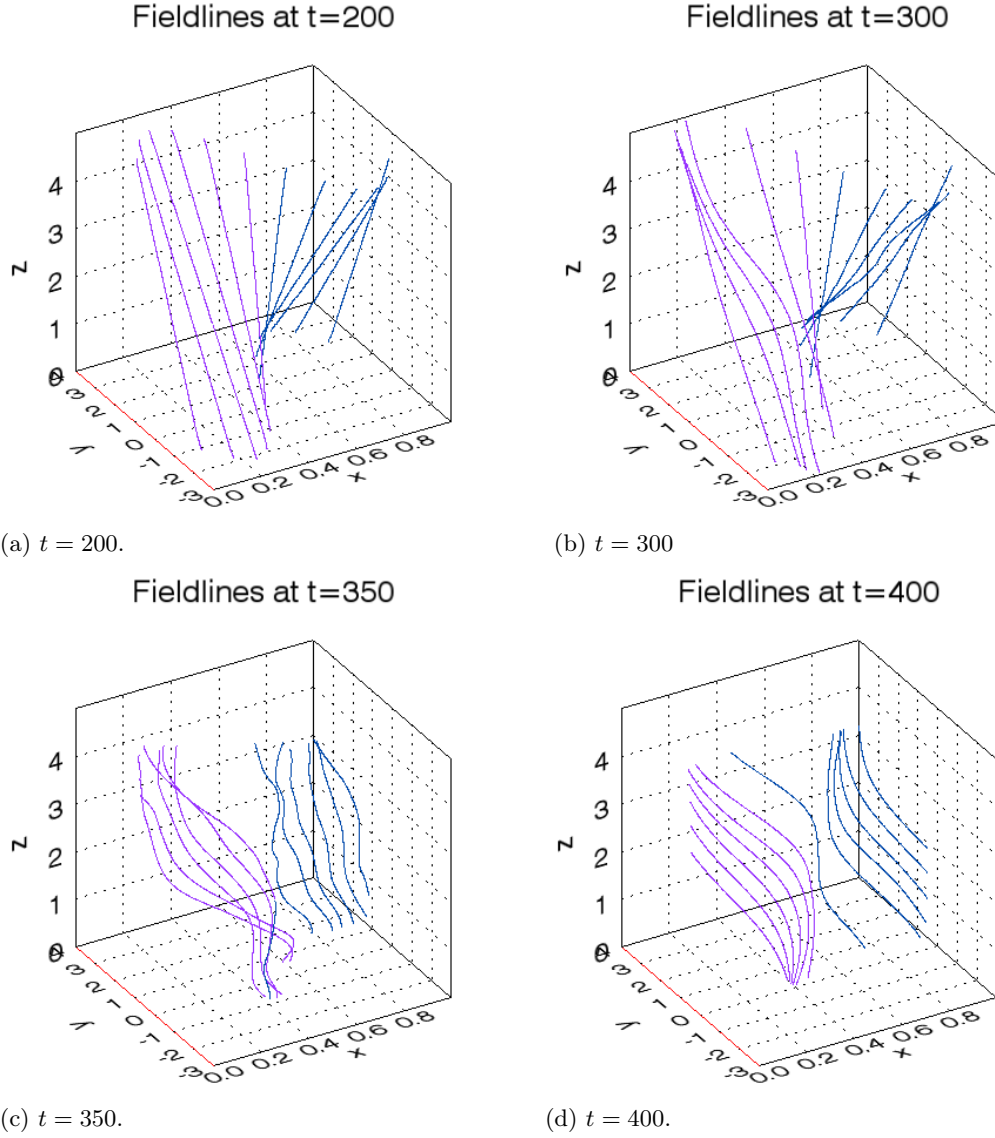


Figure 5.10: Magnetic fieldlines, traced from a 2D plane at  $z = 2.5$ , for simulation MHD:A in Table 5.1 on page 112, at selected times. The  $y$  axis has been extended from  $[0, 1]$  to  $[-3, 4]$  to show the full fieldline displacement. This makes use of the periodic boundary conditions in  $y$ . The actual direction of the fieldlines is unclear in Figure 5.10d, as it appears that there is a large  $y$  component. This is not the case, as shown in Figure 5.11, where a top view of fieldlines reveals that the fieldlines exit through the boundary in  $x$ .

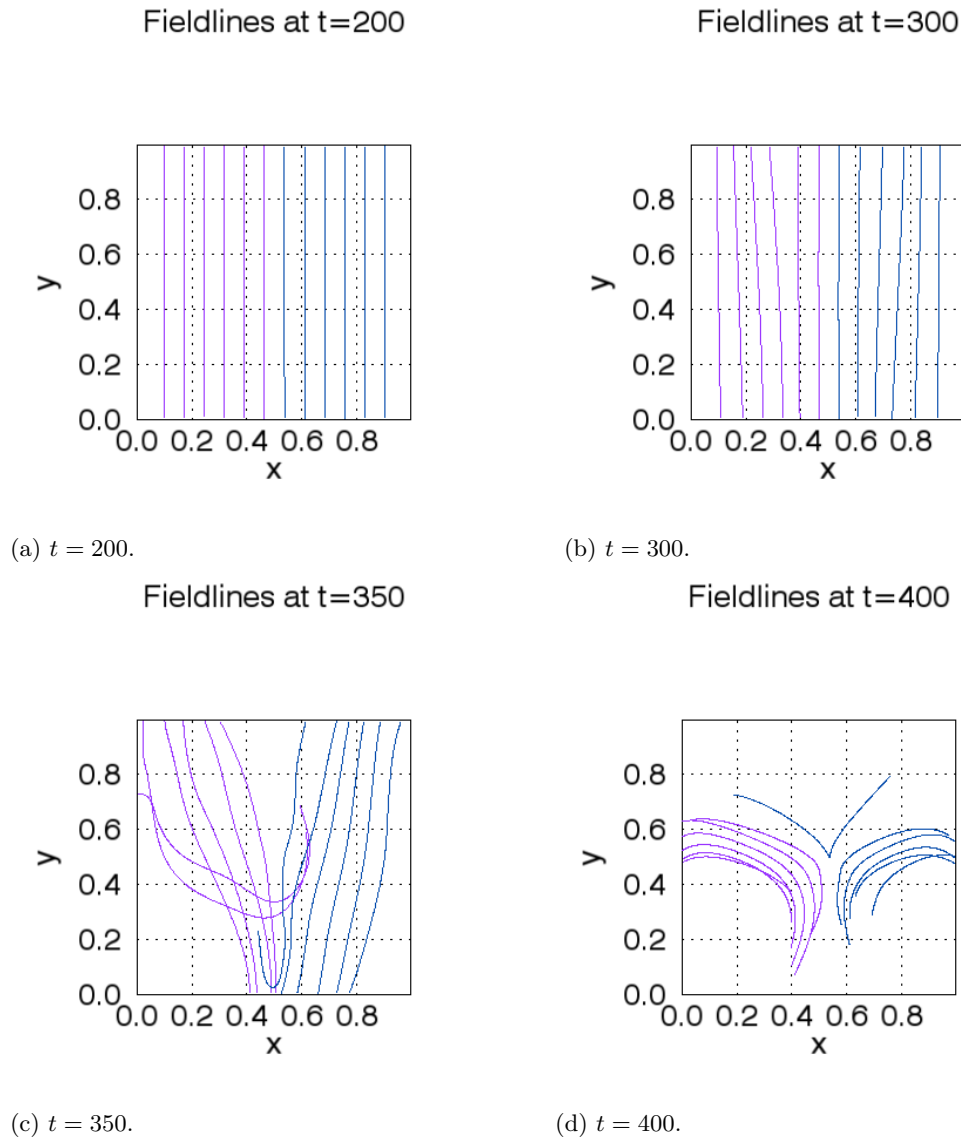


Figure 5.11: Top view of the fieldlines plotted in Figure 5.10. Here the  $x$  and  $y$  ranges have been kept to the actual box size of  $[0,1]$ . This view clarifies the direction of fieldlines at  $t=400$ , namely, that they exit the box through the  $x$  boundaries before reaching a boundary in  $z$ .

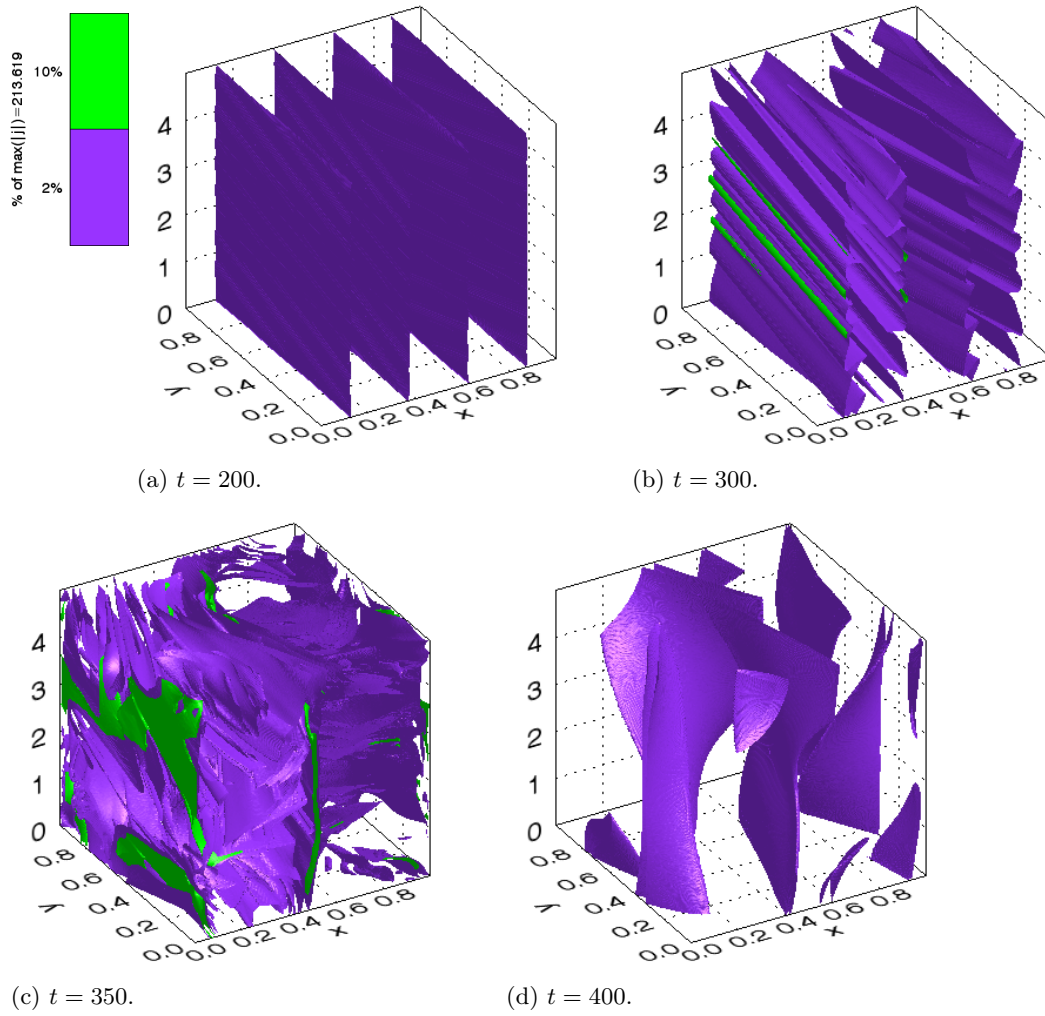


Figure 5.12: 3D isosurfaces of  $|j|$  for simulation MHD:A, in Table 5.1 on page 112, at selected times. The magnitude is given in the colourbar as a percentage of the overall maximum  $|j|$ .



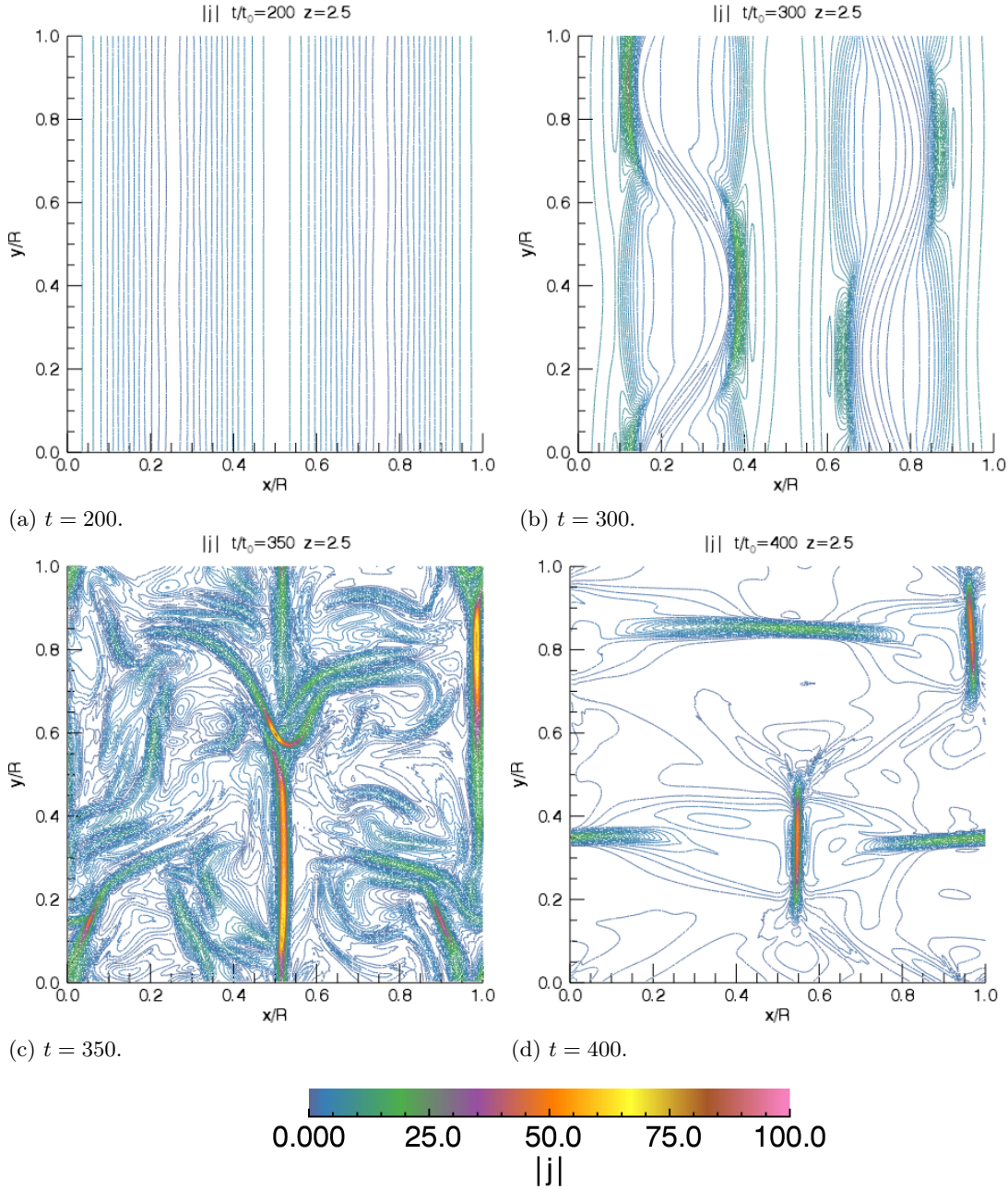


Figure 5.13: Contours of  $|j|$  in the  $x - y$  plane at the midpoint along the loop  $z = 2.5$  at different simulation times. Colours denote different magnitudes as given by the colourbar. This is for simulation MHD:A in Table 5.1 on page 112.

track the subsequent evolution after the instability. Important differences between RMHD and full MHD are noted where possible.

### Velocity

The evolution and growth of the perturbation as the tearing mode develops from the boundary driven kink waves can be seen from the  $x$  component of velocity. Plots of  $v_x$  are shown in Figure 5.14 on page 130 as a function of  $z$  at  $x = 0.25$  and  $y = 0.5$  for simulation MHD:A. This variable is plotted along this direction to show the evolution of the waves along the loop length. The  $y$  range has been adjusted at each timestep to clearly show the large variation in  $z$ . In RMHD variations along this direction are assumed to be slow, however in this setup this direction is where the perturbation grows, thus variations are likely to be large. Before the instability, at  $t = 200$  in Figure 5.14a, the waves in  $v_x$  are clearly seen propagating along in this direction. At  $t = 300$  in Figure 5.14b, the waves are distorted as the symmetry is broken and the instability develops. At  $t = 350$  in Figure 5.14c, the perturbation has increased to a magnitude about ten times larger than the driver amplitude,  $V_{0 \text{ shear}} = 0.02$ . After the instability, at  $t = 400$  when the system has settled to a steady state in Figure 5.14d, the perturbation has decreased in magnitude but is still greater than the driver amplitude in places. There is no evidence of the waves after the instability, even though they are still injected at the boundaries.

Similarly, the driving velocity,  $v_y$ , is plotted along the same line in Figure 5.15 on page 131 for simulation MHD:A. As shown before using linearisation in Section 4.2.5, Chapter 4, a linear analysis of this system predicts the driving velocity to be linear in  $z$  (Equation 4.23 on page 72  $z$  is  $y$  in 2.5D). This is indeed the case before the tearing instability at  $t = 200$ , shown in Figure 5.15a. After this time the symmetry of the system is broken and the instability begins to develop, becoming visible by  $t = 300$  in Figure 5.15b with a wavelength similar to the injected kink waves. The perturbation continues increasing in magnitude and at  $t = 350$  in Figure 5.15c is much larger than the boundary value of 0.02. The kinetic energy is subsequently dissipated and the magnitude of  $v_y$  greatly decreases by  $t = 400$  in Figure 5.15d. Note that once the symmetry is broken it is not recreated, and  $v_y$  does not have a completely linear dependence in  $z$  again, even though the driver is still switched on.

### Magnetic Vector Field

After the development of the tearing mode the magnetic field reconnects to form magnetic-island-type structures in 2D planes perpendicular to the guide field. A useful way to visualise this is to look at the magnetic vector field, which is shown in Figure 5.16 on page 133 for the  $x - y$  plane perpendicular to the background field taken at the midpoint along the loop at  $z = 2.5$ . This figure shows snapshots of the perpendicular vector field at different times during the simulation. The third magnetic field component,  $B_z$  is directed out of the plane of these figures. For early times,  $t = 200$  in Figure 5.16a and  $t = 300$  in Figure 5.16b, the dominant component in the  $x - y$  plane is the sheared field in the  $y$  direction, since the wave amplitude is small. Next the instability becomes visible when the component in

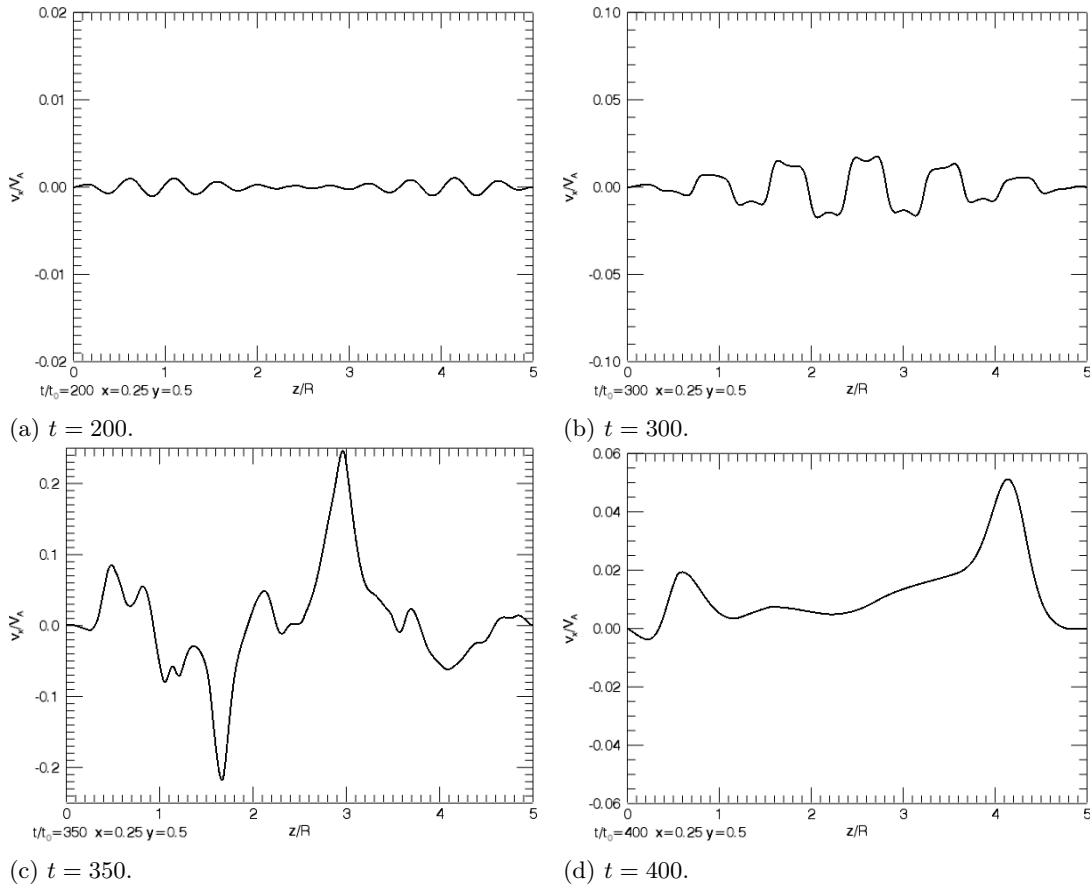


Figure 5.14: Plots of  $v_x$  as a function of  $z$  at  $y = 0.5$  and  $x = 0.25$  at various simulation times. This is for simulation MHD:A in Table 5.1 on page 112. The  $y$  range has been adjusted at each timestep to illustrate the large variation in  $v_x$  during the evolution. The  $y$  range at each time has been kept the same as in Figure 5.15 on page 131 for comparison of the magnitude of  $v_y$ .

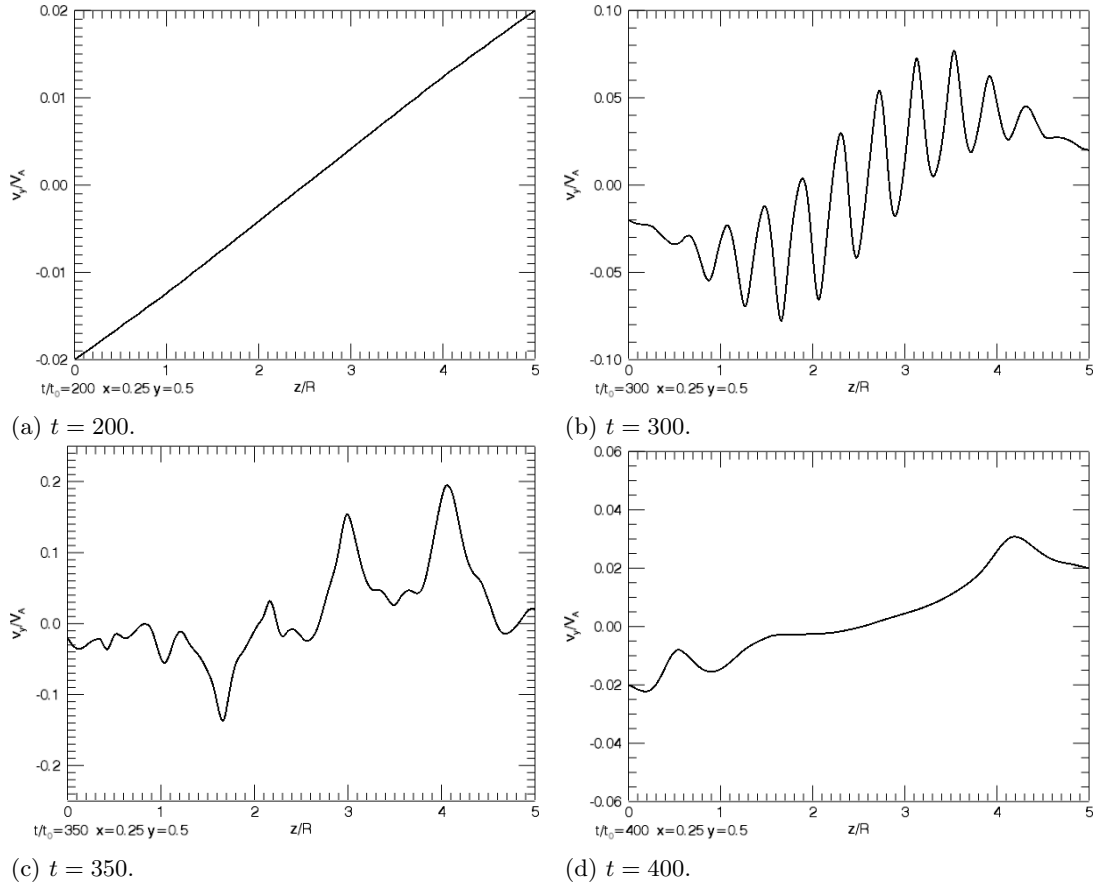


Figure 5.15: Plots of  $v_y$  as a function of  $z$  at  $y = 0.5$  and  $x = 0.25$  at various simulation times. This is for simulation MHD:A in Table 5.1 on page 112. The  $y$  range has been adjusted at each timestep to illustrate the large variation of  $v_y$  during the evolution. The  $y$  range at each timestep has been kept the same as in Figure 5.14 on page 130 for comparison of the magnitude of  $v_x$ .

$x$  grows at  $t = 350$ , shown in Figure 5.16c, and, at  $t = 400$ , shown in Figure 5.16d. The magnitude of  $B_x$  and  $B_y$  are now similar, forming a circular pattern. The growth continues and magnetic “islands” are formed as shown at and  $t = 400$  in Figure 5.16d. Note, that these are perpendicular cuts and there is a strong background field directed out of the page so the field is not truly zero at these X and O points, only the perpendicular components are zero at these points.

These figures indicate that the magnetic field reconnects in different places at different times. The magnetic field does not return to the initial state. It is suggested that this is because the magnetic field settles to a steady state where energy is continuously dissipated via turbulence type processes, which is subsequently maintained by the footpoint motions. Without this energy input the turbulence would decay and the magnetic field would relax back to the initial state. This theory may also explains why the magnetic energy cannot build up again: since the nature of turbulence is to continuously transfer energy from large spatial scales to small scales where it is dissipated through a direct cascade, the magnetic energy can no longer build up while nonlinearities are important.

### Magnetic Field Components

One way to illustrate this transition from a state where the magnetic field is able to store energy from the boundary motions to a turbulent state where energy is not stored, even though it is provided as before, is to consider the ideal MHD equations linearised to first order, as done in Section 4.2.5 in Chapter 4 for the viscous case. Neglecting viscosity in Equations 4.21 on page 72, this gives the Alfvén wave equation for  $B_y$  and  $v_y$  as

$$\begin{aligned}\frac{\partial v_y}{\partial t} &= \frac{\partial B_y}{\partial z}, \\ \frac{\partial B_y}{\partial t} &= \frac{\partial v_y}{\partial z}.\end{aligned}$$

Taking our shear velocity to be

$$v_y(x, y, z) = \frac{V_0 \text{ shear}}{L}(z - L) \sin(kx). \quad (5.11)$$

This satisfies our boundary conditions in Equations (5.4) and is analogous to the first order solution, Equation (4.23) on page 72. Using Equation (5.11) gives a sheared magnetic field of the form

$$B_y(x, y, z) = \frac{V_0 \text{ shear} t}{L} \sin(kx).$$

This is analogous to the first order solution for the sheared magnetic field, Equation 4.24 on page 73 with  $\nu = 0$ . Although this solution is for the simple ideal case, it can still be seen from this that the magnetic field is a smooth mapping of the boundary velocity:  $v_y \propto B_y \propto \sin(kx)$ . Nonideal effects only reduce the amplitude of the fields and not the spatial form of the relation between velocity and magnetic fields.

Plots of the sheared magnetic component,  $B_y$ , as a function of  $x$  at the midpoint

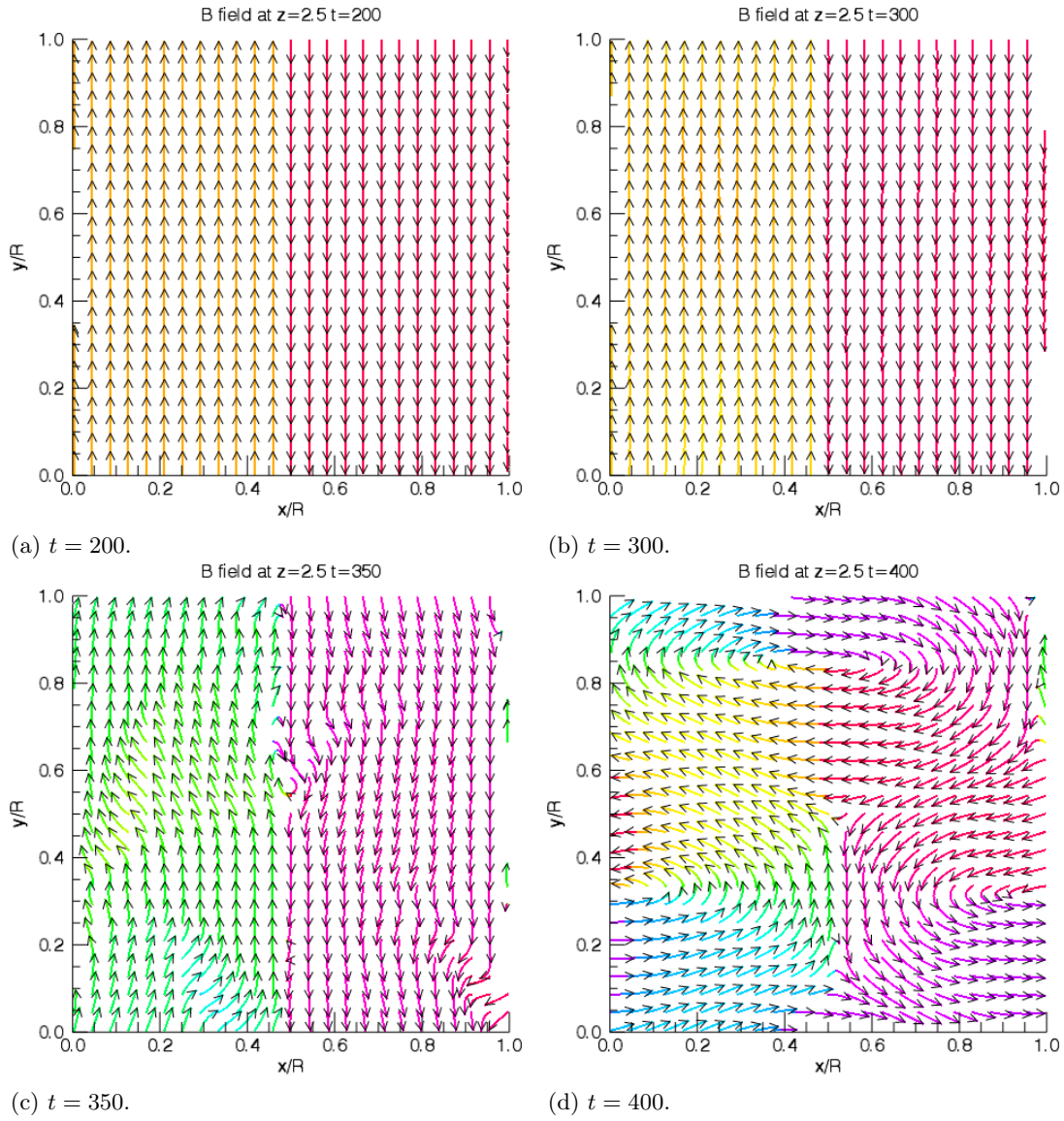


Figure 5.16: Magnetic vector field in the  $x-y$  plane at the midpoint along the loop  $z = 2.5$  at different simulation times. This is for simulation MHD:A in Table 5.1 on page 112. The colours indicate the direction of the field at each timestep.

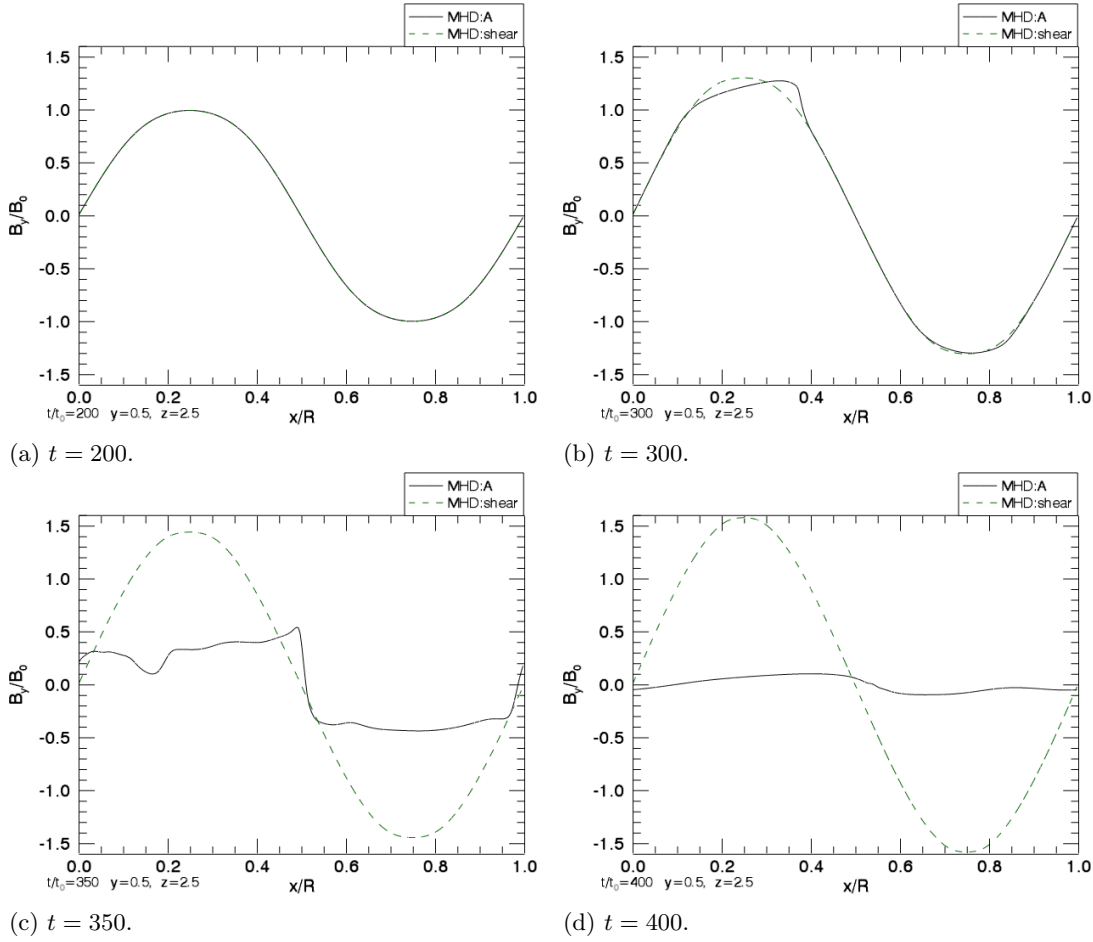


Figure 5.17: Plots of the sheared magnetic field,  $B_y$ , as a function of  $x$  at the midpoint in  $y = 0.5$  and  $z = 2.5$  at various simulation times. This is for simulations MHD:A and MHD:shear in Table 5.1 on page 112.

in  $y$  and  $z$  are shown in Figure 5.17 on page 134 for several times for simulations MHD:A and MHD:shear. Simulation MHD:shear is included, as this run only includes the shear velocity and not the perturbation at the boundary and so does not develop the instability. This allows us to identify the fluctuations in  $B_y$  that are due to the growth of the tearing mode by distinguishing them from the sheared field. In Figure 5.17a at  $t = 200$  the sheared magnetic field has a sinusoidal profile, as expected from the above argument. Hence,  $B_y$  is a smooth mapping of the driver and the two MHD simulations are identical. As discussed in Section 5.3.2, the maximum magnitude of  $B_y$  at  $t = 200$  is about one, which is the same as the initial field at  $t = 0$ . This means fluctuations are no longer small compared to the initial field and RMHD would not be applicable. The sinusoidal variation also agrees with the variation of the sheared field ( $B_z$  in  $2\frac{1}{2}D$ ) in Chapter 4 in Figure 4.6 on page 81. Figure 5.17b at  $t = 300$ , when the current starts to increase, the sheared field is no longer an exact smooth mapping and the symmetry of the driver has been broken. After the instability this component of the field has little resemblance to the smooth mapping that would otherwise develop as shown by simulation MHD:shear.

Similar plots for the initial magnetic field component,  $B_z$ , are shown in Figure 5.18

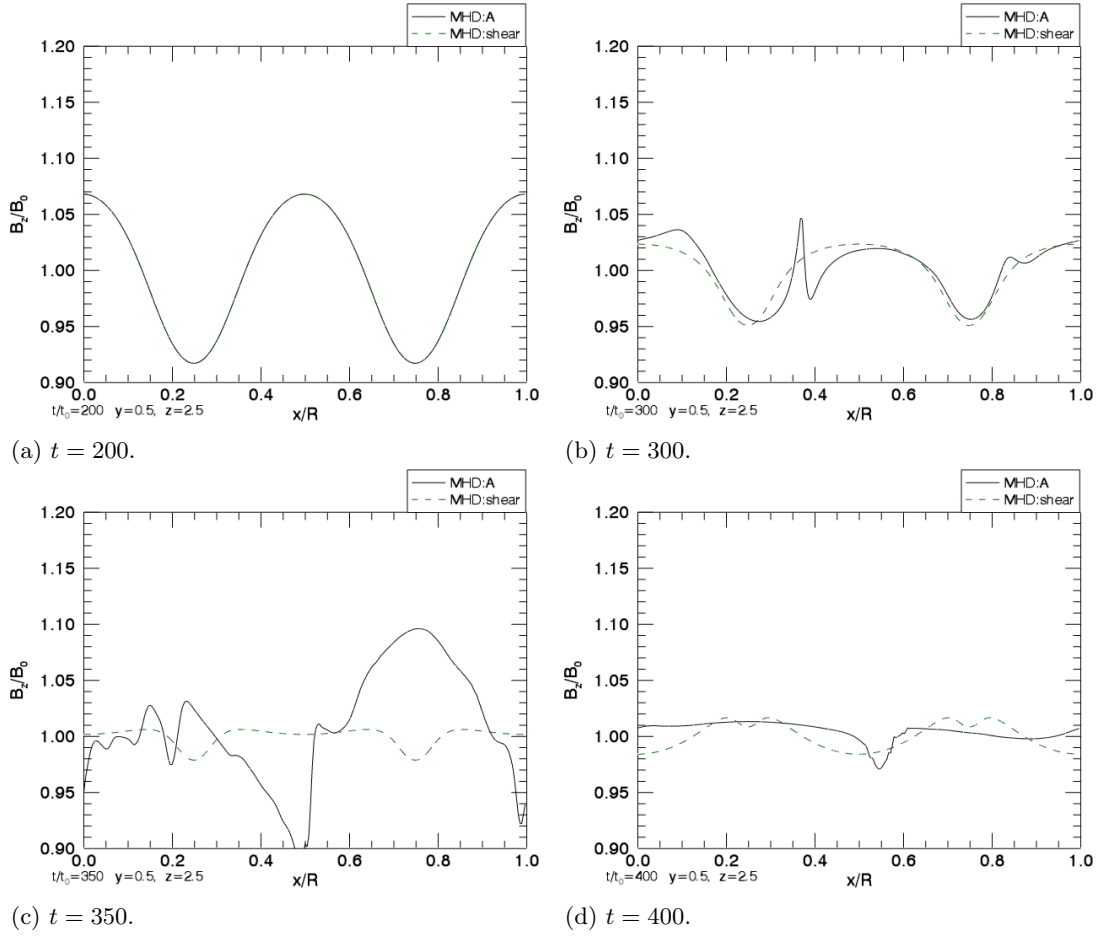


Figure 5.18: Plots of the magnetic field component,  $B_z$ , as a function of  $x$  at the midpoint in  $y = 0.5$  and  $z = 2.5$  at various simulation times. This is for simulations MHD:A and MHD:shear in Table 5.1 on page 112.

on page 135 for simulations MHD:A and MHD:shear. It was previously found for the 2.5D MHD case, in Chapter 4 in Figure 4.7 on page 82, that this magnetic field component is compressed in  $x$ . This is also the case in 3D before the instability at  $t = 200$  shown in Figure 5.18a. At  $t = 300$  in Figure 5.18b, the symmetry is broken as the perturbation grows. It is unclear why the magnitude decreases between these two times:  $t = 200$  and  $t = 300$  for both full MHD simulations. It is possibly due to resistive slippage of the fieldlines at the footpoints. At later times in Figure 5.18c and Figure 5.18d, after the instability, at  $t = 350$  and  $t = 400$ , there is evidence of variations at small scales in  $B_z$  which is indicative of turbulence.

RMHD assumes that  $B_z$  does not change from its constant value at  $t = 0$  as,  $B_z = B_0 = 1.0$ . This is obviously not the case in our full MHD simulations. RMHD would not predict any compression or expansion of the background field or the growth of the perturbation in the guide field that is found when using full MHD.



### Density and Pressure

The evolution of  $\rho$  and  $p$  as functions of  $x$  at the midpoint in  $y$  and  $z$  are shown in Figure 5.19 (page 137) and Figure 5.23 (page 141), respectively, for simulations MHD:A and MHD:shear. Contours of  $\rho$  in the  $x-z$  plane at  $y = 0.5$  and the  $x-y$  plane at  $z = 2.5$  are shown in Figure 5.20 (page 138) and Figure 5.21 (page 139) for simulation MHD:A.

Before the instability, at  $t = 200$  in Figure 5.19a and Figure 5.23a,  $\rho$  and  $p$  vary smoothly in  $x$ , corresponding to the compression and expansion of the magnetic field. This density profile also agrees with the density in Chapter 4 in Figure 4.11 on page 86 and the pressure profile is similar to Figure 4.10 on page 85. Then, at  $t = 300$  in Figure 5.19b and Figure 5.23b, the symmetry is broken as the perturbation grows. At later times,  $t = 350$  (Figure 5.19c and Figure 5.23c) and  $t = 400$  (Figure 5.19d and Figure 5.23d), the density and pressure have reached a roughly constant value with small scale variations due to the turbulent nature of the system. At the end of the simulation, the density has settled at a value smaller than the initial value at this position. The final value of the pressure has reached a value in some regions about an order of magnitude greater than its initial value, showing that the system has gone from fairly low  $\beta$  to high  $\beta$ . This follows from the fact that the Poynting flux is putting energy into the system but energy cannot be lost, since thermal effects are neglected here.

Contours of  $\rho$  in the  $x-y$  plane at the midpoint in  $z$  in Figure 5.20 show the evolution of density in this 2D plane. In Figure 5.20a, the density is invariant in  $y$  with a small smooth variation in  $x$ . This  $x$  variation has increased, at  $t = 300$  in Figure 5.20b. After the instability, at  $t = 350$ , in Figure 5.20c, the density is no longer invariant in  $y$  and variations are no longer smooth in  $x$  as the symmetry has been broken. At later times,  $t = 400$  in Figure 5.20d, the magnitude and variations of  $\rho$  are small.

Contours of  $\rho$  in the  $x-z$  plane at the midpoint in  $y$  are shown in Figure 5.21. Initially, at  $t = 200$  in Figure 5.21a, there is no visible variation of density. At  $t = 300$  in Figure 5.21b, the perturbation is visible in the density as a variation along  $x$  and  $z$ . After the instability, at  $t = 350$  in Figure 5.21c and  $t = 400$  in Figure 5.21d, the density has been redistributed and has collected at the boundaries in  $z$ , showing the density has been transported away from the loop centre. This explains the small magnitude of  $\rho$  at the midpoint in  $z$ , shown in Figure 5.19d and Figure 5.20d.

In order to further test this conclusion we calculate the integrated density in  $x-y$  planes as a function of  $z$  and  $t$

$$\rho_{\text{int}}(z, t) = \int dx dy \rho(x, y, z, t). \quad (5.12)$$

Contours of this expression are shown in Figure 5.22 for simulation MHD:A. It is clear from this that the density has collected in planes near the top and bottom of the loop. This could be due to the effect of the background field which forces the reconnection outflow to be parallel to  $B_0$ .

In summary, there are large variation of pressure and density in our MHD simulations as a result of the tearing instability. In studies of RMHD, the pressure and density are

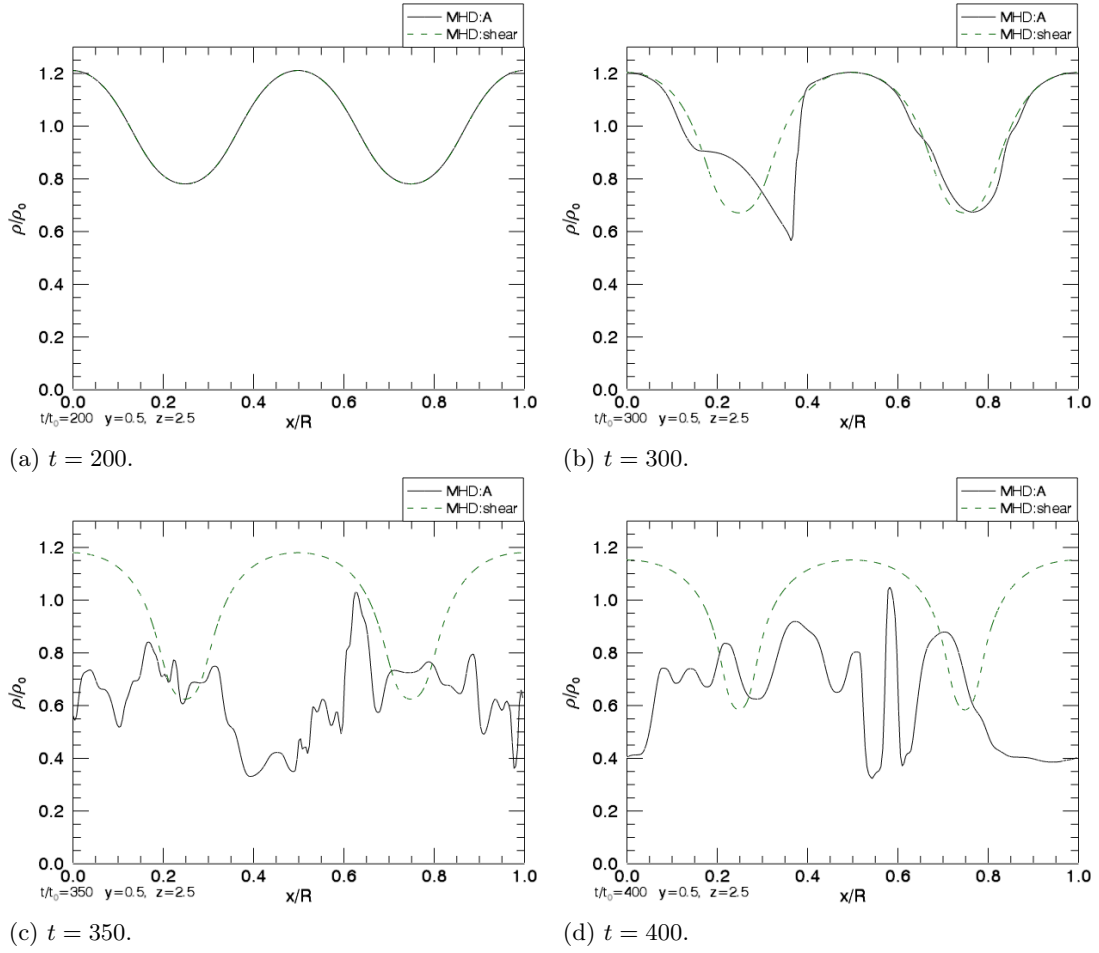


Figure 5.19: Plots of the density,  $\rho$ , as a function of  $x$  at the midpoint in  $y = 0.5$  and  $z = 2.5$  at various simulation times. This is for simulations MHD:A and MHD:shear in Table 5.1 on page 112.

not usually mentioned except to say that  $\beta \ll 1$ . These variables are not usually evolved and so RMHD makes no predictions for the evolution of  $\rho$  or  $p$ .

#### Total Pressure and Fieldline Angles

The maximum and minimum values of the total pressure  $p + \frac{1}{2}B^2$  are shown in Figure 5.24a on page 142 as a function of time. The difference between the maximum and minimum increases during the evolution until the variation decreases after the instability. Once the total pressure reaches an approximately constant spatial value, it can be seen that the total pressure also depends on time, as found in Chapter 4. The total pressure is not constant in space during the instability, indicating that the system is not in pressure balance. After the instability,  $t > 400$ , the maximum and minimum values are similar, showing that the system is close to an equilibrium. The evolution of the total pressure can be compared to the same quantity for the 2.5D MHD simulations in Chapter 4 in Figure 4.18 on page 91. In both cases the total energy increases in time, but when the perturbation and instability are present the total pressure has a greater spatial variation.

Figure 5.24b on page 142 shows the maximum angles,  $\theta_x$  and  $\theta_y$  between  $B_z$  and

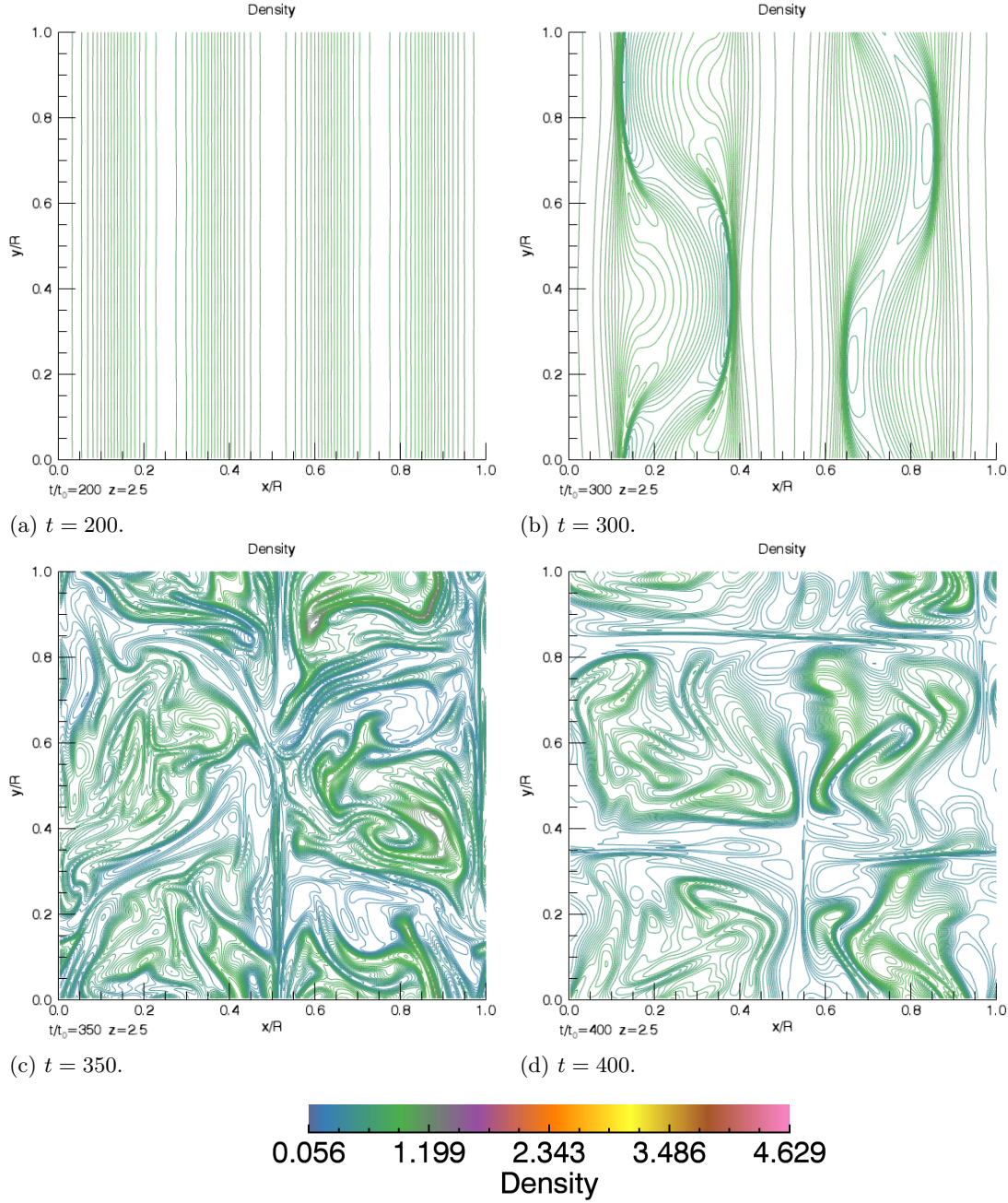


Figure 5.20: Contours of  $\rho$  in the  $x - y$  plane at the midpoint along the loop  $z = 2.5$  at different simulation times. This is for simulation MHD:A in Table 5.1 on page 112.



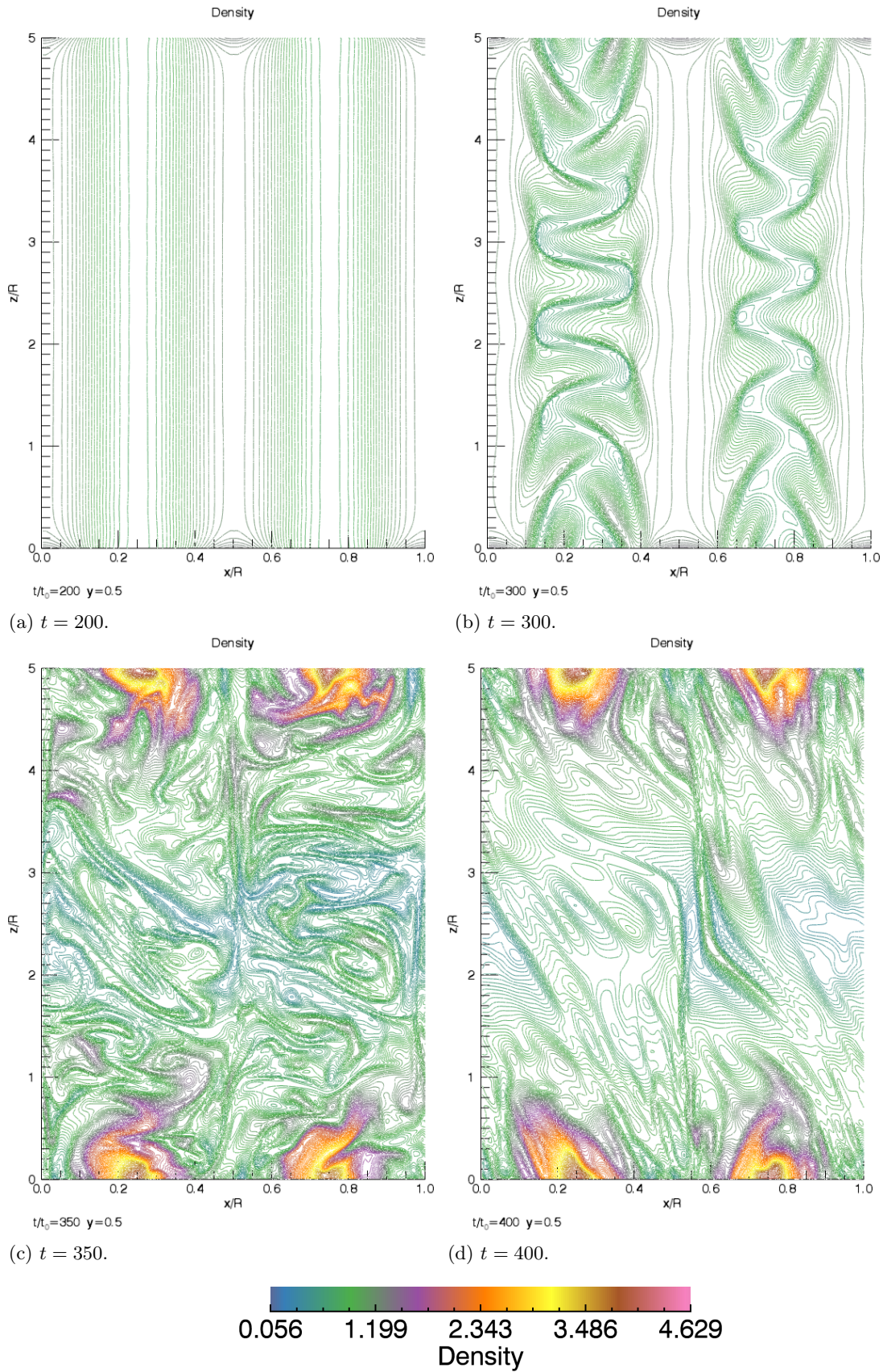


Figure 5.21: Contours of  $\rho$  in the  $x-z$  plane at the midpoint along  $y = 0.5$  at different simulation times: top left  $t = 200$ , top right  $t = 300$ , bottom left  $t = 350$ , bottom right  $t = 400$ . This is for simulation MHD:A in Table 5.1 on page 112.

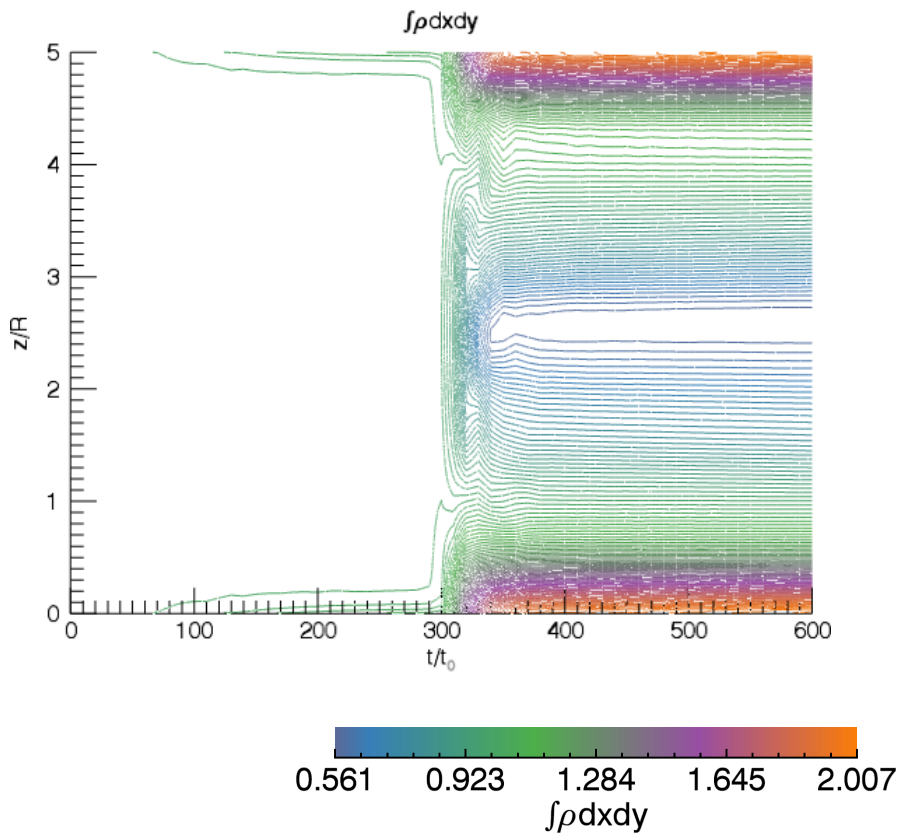


Figure 5.22: Contours of integrated density in  $x - y$  planes, defined in Equation (5.12), for simulation MHD:A in Table 5.1 on page 112. This illustrates that the density increases in the 2D planes near the  $z$  boundaries and decreases in the middle.

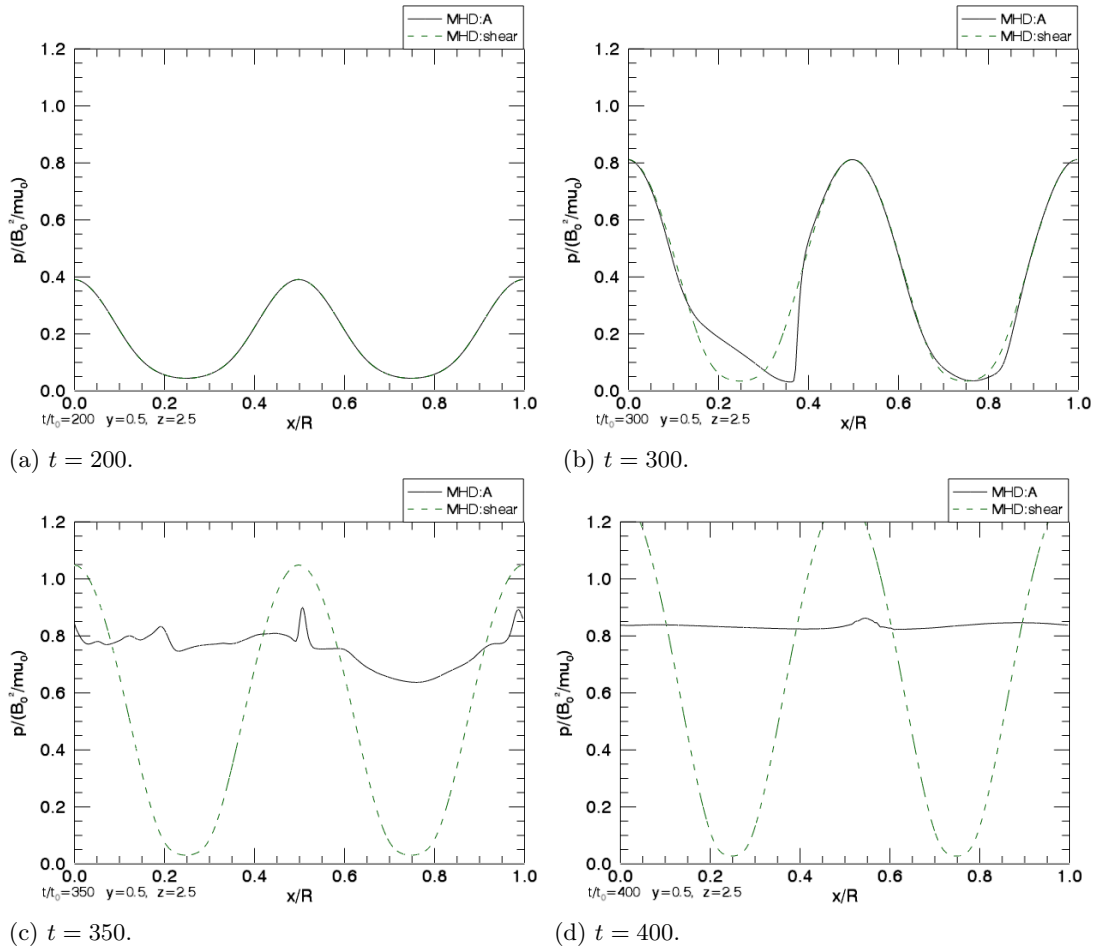


Figure 5.23: Plots of the pressure,  $p$ , as a function of  $x$  at the midpoint in  $y = 0.5$  and  $z = 2.5$  at various simulation times. This is for simulations MHD:A and MHD:shear in Table 5.1 on page 112.

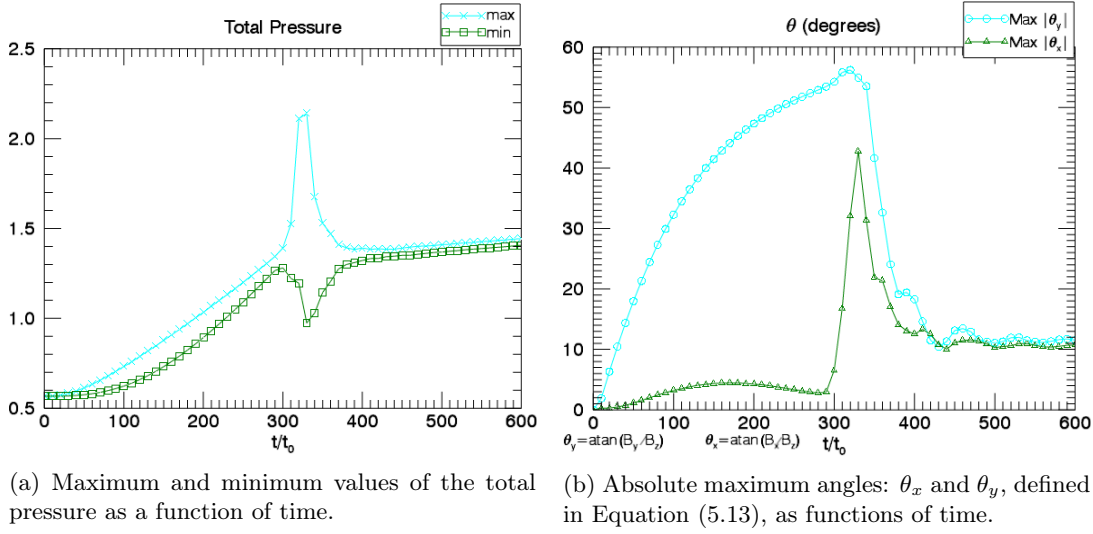


Figure 5.24: Plots of total pressure and magnetic field angles for simulation MHD:A in Table 5.1 on page 112.

$B_x$  and  $B_y$  respectively. These are

$$\theta_x = \frac{180}{\pi} \arctan\left(\frac{B_x}{B_z}\right), \quad (5.13a)$$

$$\theta_y = \frac{180}{\pi} \arctan\left(\frac{B_y}{B_z}\right). \quad (5.13b)$$

$\theta_y$  clearly increases to a maximum of  $\sim 60^\circ$  due to the shearing before the instability. In comparison  $\theta_x$  is small until the instability. Afterwards  $\theta_y$  decreases to a similar value to  $\theta_x$  of  $\sim 10$  deg. It follows that after reconnection has started at  $t > 400$ , fieldlines are slightly tilted in both  $x$  and  $y$ . Fieldlines shown in Figure 5.10d and Figure 5.11d agree with this idea. Further work is needed to investigate the relation between the shearing angle and the development of the instability.

In the next section we summarise the results of this chapter and motivate the following chapter.

## 5.4 Summary

In summary, we have investigated the validity of RMHD for the specific case of evolution of the tearing instability. Our study is very similar to that previously done by Rappazzo, Velli, and Einaudi 2010 using RMHD. Our full 3D compressible MHD simulations extend their main conclusion from RMHD to full MHD: a uniform background magnetic field subject to smooth footpoint motions and perturbed by a symmetry breaking fluctuation develops the tearing instability and suggests evolution into a state, where energy is not stored, akin to stationary turbulence, maintained by the footpoint motions that are present throughout. Unfortunately, we are unable to investigate the properties of this turbulence. An important point in both their study and ours is that the magnetic energy is not stored again after

the instability. However, it has been shown that although the tearing instability evolution is qualitatively similar in our full MHD simulations to those presented by Rappazzo, Velli, and Einaudi 2010, there are many aspects of the evolution where the validity of RMHD is questionable, including compressible effects, nonzero parallel fields, small scale variations along the  $z$  direction and large changes in density and pressure. These could be important to the dynamics of the full MHD system which are not predicted by RMHD. It may be arguable that RMHD is valid before and after the instability: before the stored magnetic energy becomes comparable to the background field and after this energy has been dissipated. It has been shown that once the instability develops, in full MHD, the fluctuations grow very rapidly in all three directions. On the other hand, RMHD assumes the parallel direction remains unchanged from the initial state. This is potentially a significant omission as the dynamics are essentially restricted to 2D planes. Although this is indeed the case for full 3D MHD in the limit of a strong enough background field, during the evolution the initial field no longer dominates the other components, hence this limit is not valid here. This restriction to essentially 2D dynamics could affect the evolution of the instability and subsequent reconnection and result in false conclusions being made.

Another issue regarding the use of RMHD is that it would not predict the large variation in density and pressure. This variation is found using full MHD, leading to regions of high and low temperature. These could be smoothed out by taking into account thermodynamic effects, such as conduction and radiation. Further work using full MHD in this direction would allow investigation of the heating ability of the tearing instability. This is the focus of the following chapter.



## Chapter 6

# Tearing Experiment: Thermodynamics

### 6.1 Introduction

In the previous chapter, it was shown that a model coronal loop subject to smooth continuous slow shearing motions and small velocity perturbations at its footpoints evolved through sequences of equilibria until the development of the tearing instability. After the instability, the system remained in a statistically steady turbulent-like state where the magnetic energy did not build up again even though the footpoint motions are still switched on. The same general qualitative evolution was reported for this system in Rappazzo, Velli, and Einaudi (2010) using RMHD. However, in the previous chapter, it was argued that RMHD is not valid for most of the development of the instability. This is a good illustration that a general conclusion may still hold true, despite the fact that the assumptions of the approximate method are not satisfied. This implies that the additional dynamics created by these non-RMHD effects are not too important in the resulting evolution, and it is appropriate to neglect them in this case. In general, it is unclear when these effects could become important. This emphasises the importance of considering validity of approximate methods for systems where it is unclear or unknown whether the assumptions are valid or not. Another essential aspect is to consider additional processes which cannot be included in the chosen approximate method. If such processes are overlooked important results could be missed. One example is thermodynamic process which are not included in RMHD, but are essential to understanding the coronal heating problem.

A complete model of coronal heating requires consideration of many processes, including: build up, storage and release of magnetic energy, conversion of this energy to heat and the response of the plasma to the resulting heating. For tractability each stage of this process is usually considered independently. The evolution of a magnetic field subject to footpoint motions is frequently investigated neglecting the additional thermodynamic processes. This simplification allows the potential use of many approximate MHD models, such as RMHD, as discussed in Chapter 4. However, in order to gain a more complete picture of coronal heating additional physics, such as optically thin radiation and thermal

conduction, needs to be taken into account. These effects are naturally included in the energy equation of full MHD, whereas, most approximate methods do not include such thermodynamical processes. For example, in the RMHD formalism, there is no internal energy equation. Thus, thermodynamical processes are not easily, or correctly, modelled in RMHD. In order to make progress in this direction, it is necessary to use full MHD to model the response of the plasma due to the heating from the instability.

Thermal conduction is expected to smooth out the large gradients along the guide magnetic field, that were seen in the final state for density and pressure in Chapter 5. Including radiation will give an indication of whether the Poynting flux and resulting plasma heating is capable of maintaining a constant temperature.

A similar final state has been shown to be obtained by applying either spatially-random footpoint motions Rappazzo et al. (2008), or as a result of the tearing instability in Rappazzo, Velli, and Einaudi (2010). The effect of the driving timescale are studied in Rappazzo et al. (2018) using RMHD. Thermal properties using the same setup of their simulations are studied using full MHD in Rappazzo et al. (2018), Dahlburg et al. (2016), and Dahlburg et al. (2018).

It is known that in such a system there are two competing modes: radiative and tearing, which can be modified by the presence of ohmic heating. The radiative mode is a thermal instability driven by optically thin radiation. The relationship between these modes and ohmic heating has been investigated in many studies (Steinolfson (1983), van Hoven, Steinolfson, and Tachi (1983), Tachi, Steinolfson, and van Hoven (1983), van Hoven, Tachi, and Steinolfson (1984), Steinolfson and van Hoven (1984), and Tachi, Steinolfson, and van Hoven (1985)). Here we only consider evolution through the tearing mode.

In Section 6.2, details of the full MHD equations, experiment setup and normalisation are given. Details and results of our full MHD simulations are presented in Section 6.3. A discussion of our results is given in Section 6.4.

## 6.2 Experiment Overview

The experiment setup is very similar to Chapter 5 but some details are repeated here for completeness.

### 6.2.1 MHD Equations

The full 3D MHD equations, given by Equations (2.9) on page 12 in Chapter 2, including radiation and conduction, are

$$\rho \frac{\partial \mathbf{v}}{\partial t} + \rho(\mathbf{v} \cdot \nabla) \mathbf{v} = -\nabla p + \mathbf{j} \times \mathbf{B} + \nabla \cdot \mathbf{S}, \quad (6.1)$$

$$\frac{\partial \rho}{\partial t} + \nabla \cdot (\rho \mathbf{v}) = 0, \quad (6.2)$$

$$\frac{\partial \mathbf{B}}{\partial t} = \nabla \times (\mathbf{v} \times \mathbf{B}) - \nabla \times (\eta \nabla \times \mathbf{B}), \quad (6.3)$$

$$\frac{\partial}{\partial t} \left( \frac{p}{\gamma - 1} \right) + \mathbf{v} \cdot \nabla \left( \frac{p}{\gamma - 1} \right) = -\frac{\gamma p}{\gamma - 1} \nabla \cdot \mathbf{v} - \mathcal{L}, \quad (6.4)$$

$$\mathcal{L} = \mathcal{L}_{\text{conduction}} + \mathcal{L}_{\text{radiation}} - \epsilon_{ij} S_{ij} - \eta j^2, \quad (6.5)$$

together with

$$\mathbf{j} = \frac{\nabla \times \mathbf{B}}{\mu}, \text{ and } \nabla \cdot \mathbf{B} = 0. \quad (6.6)$$

Conduction is given by  $\mathcal{L}_{\text{conduction}} = \nabla \cdot \mathbf{q}$ , where the conductive flux,  $\mathbf{q}$  is given in Equation (2.10). Radiative losses,  $\mathcal{L}_{\text{radiation}}$ , given by Equation (2.11) on page 12, are switched off if the plasma temperature is  $\leq 10000\text{K}$ . The viscous stress tensor is given by Equation (2.13) and the strain rate is given by Equation (2.14). A uniform background resistivity of  $\eta = 1 \times 10^{-4}$  is used in this chapter. The MHD equations are normalised in the same way as discussed in Section 4.2.1, Equation (4.2) on page 63. Inclusion of thermodynamic processes requires a carefully chosen normalisation.

### 6.2.2 Normalisation and Initial Conditions

As in Chapter 5, we consider a computational box of size  $0 \leq x, y \leq 2\ell$ , and  $0 \leq z \leq 2L$ , where  $\ell = 0.5$  and  $L = 2.5$ , with an initial, uniform magnetic field,  $\mathbf{B} = B_0 \hat{\mathbf{e}}_z$ , uniform density,  $\rho_0$  and uniform pressure,  $p_0$ . The magnetic field is line tied at the boundaries in  $z$ . Periodic boundary conditions are used in  $x$  and  $y$ .

For the normalisation values  $R = 10\text{Mm}$ ,  $\rho_0 = 1.67 \times 10^{-12} \text{kg m}^{-3}$  and  $B_0 = 3 \times 10^{-4} \text{tesla}$ , the Alfvén speed is  $V_A = 200 \text{km s}^{-1}$  and the Alfvén travel time along a unit of the box is  $t_0 = 48\text{s}$ . With this set, the normalised temperature is  $T_0 = 5.167\text{MK}$ . The dimensionless initial conditions for the magnetic field and internal energy density are chosen to be

$$B_{z\text{initial}} = 1.0, \quad e_{\text{initial}} = 0.4.$$

This gives a magnetic field of  $B_z = 3 \times 10^{-4} \text{T}$ . The resulting dimensionless initial temperature is  $T = 0.26$ , corresponding to  $T = 1.37\text{MK}$ . Our box has real dimensions of  $\ell = 5\text{Mm}$  and  $L = 25\text{Mm}$ .

As discussed before, there are many competing timescales in this system: Alfvén,

Table 6.1: Details of the two sets of initial conditions used for our full MHD simulations. Low density is for simulations A-D and high density is for simulations E-G in Table 6.2 on page 148.

IC Set	Name	$\rho_{\text{initial}}$	$\beta_{\text{initial}} = 2p_{\text{initial}}$	$e_{\text{initial}} = 3/2p_{\text{initial}}$
1	low density	0.25	2/15	0.4
2	high density	1.0	8/15	0.4

$\tau_A$ , sound,  $\tau_s$ , radiative,  $\tau_{\text{rad}}$ , conductive,  $\tau_{\text{cond}}$ , and diffusion,  $\tau_{\text{diff}}$ . An estimate of these timescales can be made for different regions. The diffusion time is given by  $\tau_{\text{diff}} \sim l/\eta = 1 \times 10^{11}\text{s}$ . For coronal plasma, take  $T = 1\text{MK}$ ,  $B = 0.001\text{T}$  and  $\rho = 1.67 \times 10^{-12}\text{kg m}^{-3}$ , giving  $\tau_A \sim 14\text{s}$ ,  $t_s \sim 85\text{s}$ . The radiative timescale is given by  $\tau_{\text{rad}} \sim \frac{p}{\gamma-1} (\rho^2 \chi T^\alpha)^{-1} \sim 730\text{s}$ . The conductive timescale can be calculated from  $\tau_{\text{cond}} \sim p (\kappa T^{7/2}/l^2)^{-1} \sim 140\text{s}$ . For plasma near the middle of the transition region  $T = 0.1\text{MK}$ ,  $\rho = 1.67 \times 10^{-11}\text{kg m}^{-3}$ , the timescales are  $\tau_A \sim 45\text{s}$ ,  $t_s \sim 268\text{s}$ ,  $\tau_{\text{rad}} \sim 1.6\text{s}$  and  $\tau_{\text{cond}} \sim 4.4 \times 10^5\text{s}$ . This shows that a lower temperature and higher density, radiation dominates conduction.

### 6.2.3 Experiment Setup

The setup is essentially identical to Chapter 5, Section 5.2.2. The driving velocity is given by Equation (5.4) and the perturbation, in the form of kink waves, is given by Equation (5.5). In the next section we discuss the results of our full MHD simulations.

## 6.3 Results

In this section we discuss the results of our full 3D MHD simulations. Optically thin radiative losses, Equation (2.11) on page 12, are proportional to  $\rho^2$  hence the initial density is critical for the evolution of the system. To illustrate this two sets of initial conditions, in Table 6.1 on page 147, are chosen. Set 2, referred to as “high density”, uses an initial value of  $\rho_{\text{initial}} = 1.0$  and Set 1, referred to as “low density”, uses an initial value of  $\rho_{\text{initial}} = 0.25$ . The choice of initial density affects the initial pressure and plasma beta, which are also summarised in Table 6.1. The first set of initial conditions is used for simulations A-D and the second set is used for simulations E-G, given in Table 6.2 on page 148. These initial conditions for density and pressure, along with the temperature and magnetic field given in the last section, can be used to estimate the dominant timescales. The high density initial conditions give  $\tau_A \sim 48\text{s}$ ,  $\tau_s \sim 73\text{s}$ ,  $\tau_{\text{cond}} \sim 66\text{s}$  and  $\tau_{\text{rad}} \sim 980\text{s}$ . The low density initial conditions give  $\tau_A \sim 24\text{s}$ ,  $\tau_s \sim 76\text{s}$ ,  $\tau_{\text{cond}} \sim 15\text{s}$  and  $\tau_{\text{rad}} \sim 3618\text{s}$ . The conduction time is longer for the high density case and the radiative time is shorter compared to the low density case. Since the same initial temperature is used for both cases the conductive timescale dominates radiation initially.  $\tau_s$  is similar in both cases, since the initial pressure decreases with the initial density. The high density initial conditions in Table 6.1 on page 147 provide a setup with fairly reasonable coronal quantities. As indicated above a high density is likely to have a dominant fast radiative timescale, and the plasma will cool until the instability develops. On the other hand, the low density initial conditions provide a setup where radiative losses are possibly balanced by the Poynting flux, allowing thermodynamic

Table 6.2: The values for our full MHD simulations.  $V_0 = 0.02$ . IC set is the set of initial conditions given in Table 6.1 on page 147. The last two columns refer to whether thermal conduction or radiative losses are switched on or off, respectively.

Simulation	IC Set	$\nu(10^{-4})$	$\eta_0(10^{-4})$	$V_0$ shear	$V_0$ waves	$\tau_{\text{waves}}$	Cond.	Rad.
A:thermal	1	1.0	1.0	$V_0$	$V_0/10$	4.0	on	on
A:nonthermal	1	1.0	1.0	$V_0$	$V_0/10$	4.0	off	off
B1:thermal	1	1.0	1.0	$V_0$	$V_0$	4.0	on	on
B2:thermal	1	1.0	1.0	$V_0$	$2V_0$	4.0	on	on
C:ideal	1	0.0	0.0	$V_0$	$V_0/10$	4.0	on	on
D:shear	1	1.0	1.0	$V_0$	0	-	on	on
E:thermal	2	1.0	1.0	$V_0$	$V_0/10$	4.0	on	on
E:conduct	2	1.0	1.0	$V_0$	$V_0/10$	4.0	on	off
E:nonthermal	2	1.0	1.0	$V_0$	$V_0/10$	4.0	off	off
F:ideal	2	0.0	0.0	$V_0$	$V_0/10$	4.0	on	on
G:shear	2	1.0	1.0	$V_0$	0	-	on	on

equilibrium to be reached, although the initial density is artificial.

Two initial tests are done to ensure the system evolves as expected when  $\nu = \eta = 0$  or when the perturbation is not present. This also highlights the important differences and similarities between the nonthermal simulations studied previously, in Chapter 5, and the thermal ones to be described in this chapter.

For the first test, an ideal simulation was performed with the driver, Equation (5.4) on page 110, and perturbation, Equation (5.5) on page 110, using both the high and low density initial conditions, simulations F:ideal and C:ideal in Table 6.2 on page 148, with thermal conduction and radiative losses switched on. A second test was also done for a case similar to simulations in Chapter 4, in which only the shear driver, Equation (5.4), is switched on and the perturbation is switched off. This is done with  $\nu = \eta \neq 0$  and for the high and low density initial conditions in simulations G:shear and D:shear in Table 6.2 on page 148.

The energies for these four simulations are shown in Figure 6.1. As before the tearing instability does not develop in these simulations. The kinetic energy is shown in Figure 6.1a. For the high density simulations, F:ideal and G:shear, the kinetic energy oscillates about a constant value throughout the evolution, with little difference between the shear and ideal cases. This is in agreement with results in Chapter 4 given in Figure 4.9 on page 84 and Chapter 5, given in Figure 5.2a on page 113. There are some large oscillations present for the low density cases, C:ideal and D:shear, especially for the latter case. This was not seen in previous cases and may be due to conduction as the internal energy is redistributed along the fieldlines.

The magnetic energy, in Figure 6.1b, builds up similarly to the previous experiments: Figure 4.8 on page 83 and Figure 5.2b on page 113. The magnetic energy in the shear cases, D:shear and G:shear, increases more slowly since viscosity and resistivity are nonzero for these simulations. The internal energy, in Figure 6.1c, decreases initially due to the radiative losses being dominant in all four of these simulations. Once the temperature reaches a threshold temperature of  $10^4\text{K}$  the radiative losses are switched off and the internal energy remains constant until the plasma is heated. The Poynting flux is smaller than

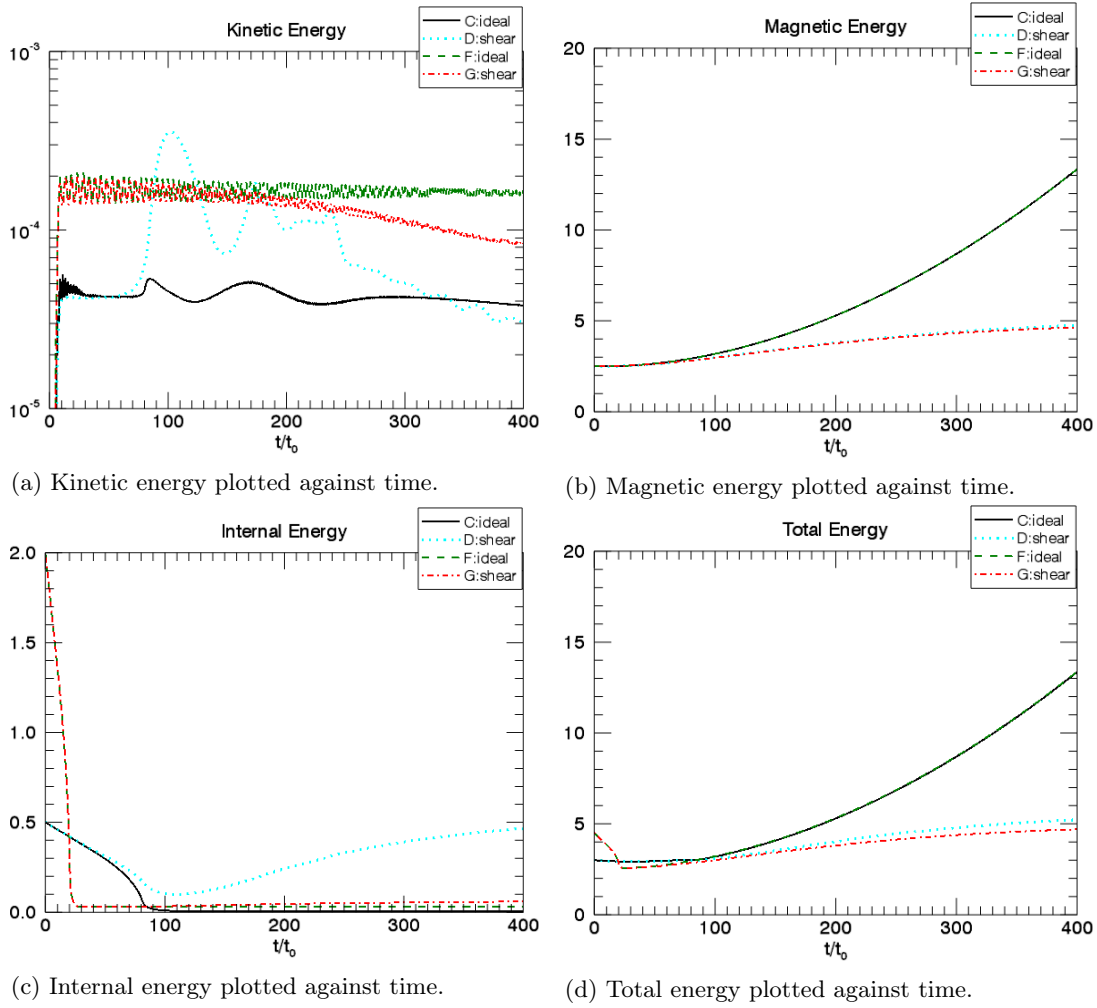


Figure 6.1: Plots of volume integrated instantaneous energy. The legends refer to the simulation names in Table 6.2 on page 148.

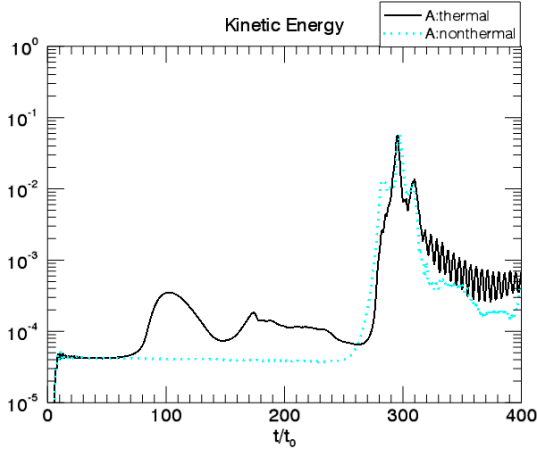
the radiative losses for both high density cases, F:ideal and G:shear, which results in the internal energy remaining at the threshold throughout the simulation. The internal energy for simulations, C:ideal and D:shear using the low density initial conditions in Table 6.1, decreases more slowly initially as radiative losses are smaller compared to the high density case. The ideal simulations do not include any heating hence once the internal energy reaches the threshold it cannot be heated. For simulation D:shear there is a turning point in the internal energy, about  $t = 120$ , as the cumulative Poynting flux equals the radiative losses and the internal energy subsequently increases slowly. This is possible in this case due to the lower radiative losses and nonzero dissipation.

Having investigated the effect of thermal conduction and radiative losses on these simple cases, we verified that the general evolution is in agreement with previous results, and the instability does not occur in an ideal evolution or when the magnetic field is sheared. We now turn our attention to simulations where the tearing instability develops.

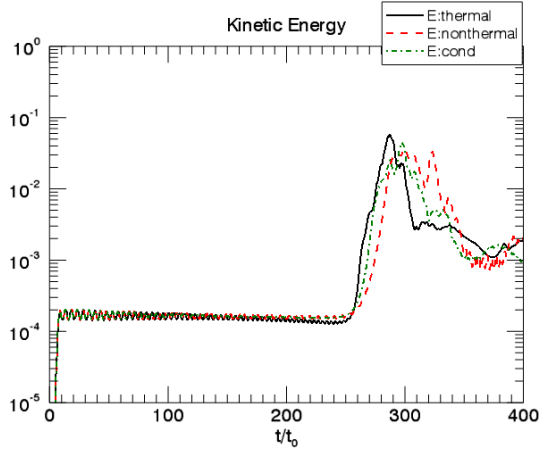
The effect of thermodynamic processes is investigated by evolving the same system in time with either radiation and conduction switched on or both radiation and conduction switched off. The parameters for these simulations are listed in Table 6.2 on page 148. Details are as follows. Simulations where both radiation and conduction are used will be denoted by “thermal”. Both sets of initial conditions in Table 6.1 are used. The low density and high density thermal simulations are A:thermal and E:thermal, respectively. Simulations with identical parameters except no radiative losses or conduction will be denoted by “nonthermal”. These are A:nonthermal and E:nonthermal. A simulation, E:cond, is also included with only conduction switched on and radiative losses switched off using the high density initial conditions in Table 6.1 on page 147. The perturbation amplitude,  $V_{0 \text{ waves}}$ , is varied relative to the driver amplitude,  $V_{0 \text{ shear}}$ , as in Chapter 5, with thermal effects. We performed simulations, B1:thermal and B2:thermal, where the amplitude of the kink waves and shearing are equal and where the wave amplitude is double the shear amplitude, respectively.

### Kinetic Energy

Figure 6.2, on page 151, shows the kinetic energy for all of the A, B and E simulations in Table 6.2 on page 148. The tearing instability develops in each case about a time of 270. The time at which the instability becomes visible varies slightly, as found in Chapter 5 and the general evolution of the kinetic energy is the same as in Figure 5.3 on page 114. Before the instability, the kinetic energy oscillates about a constant value, in agreement with the kinetic energy found in Chapter 4, Figure 4.9 on page 84. However, there are small differences between these previous results and those in this chapter. For the low density cases: A:thermal, B1:thermal and B2:thermal, (Figure 6.2c) there are large variations in the kinetic energy before the onset of the instability. These variations are not present in the nonthermal case, A:nonthermal. This could be a consequence of conduction. These variations are also not present in the high density cases; E:thermal, E:cond and E:nonthermal (Figure 6.2b). In this case the kinetic energy oscillates around a steady value, only decreasing slightly as found in Chapter 4 in Figure 4.9, until the instability develops. The kinetic energy, for simulations in Figure 6.2c, shows that increasing the wave speed causes a slight



(a) Low density initial conditions in Table 6.1 on page 147.



(b) High density initial conditions in Table 6.1 on page 147.

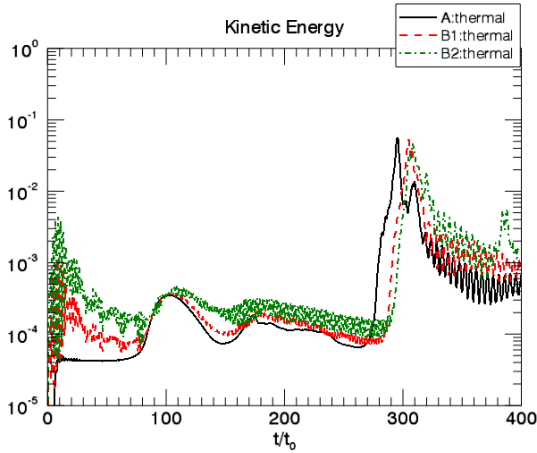
(c) Low density initial conditions in Table 6.1 on page 147. The perturbation amplitude,  $V_0$  waves, is varied.

Figure 6.2: Log plots of volume integrated instantaneous kinetic energy as a function of time. The legends refer to the simulations in Table 6.2 on page 148.



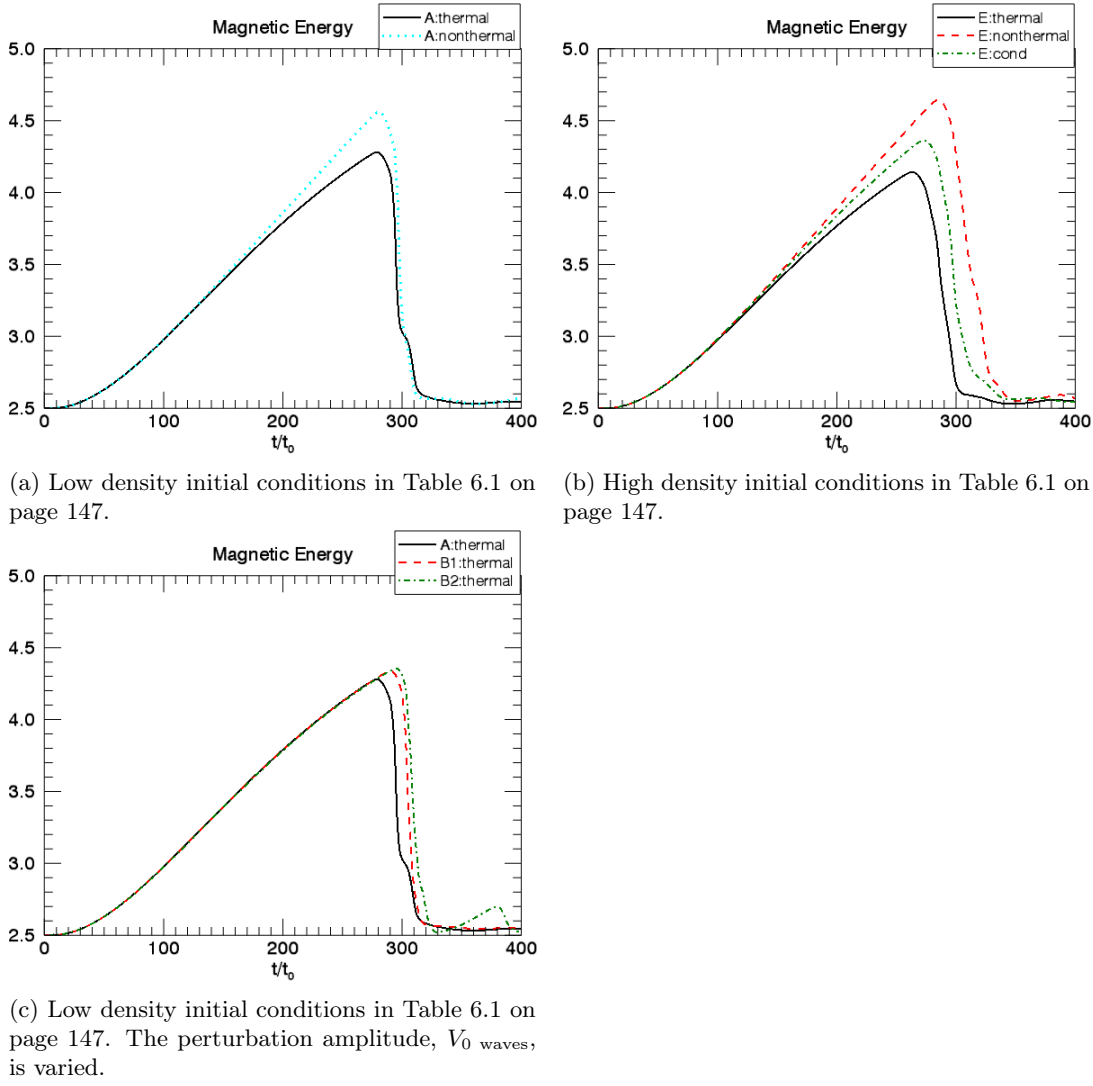
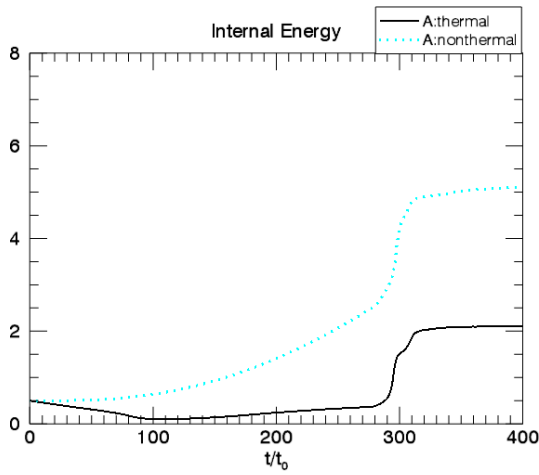


Figure 6.3: Plots of volume integrated instantaneous magnetic energy as functions of time. The legends refer to the simulations in Table 6.2 on page 148.

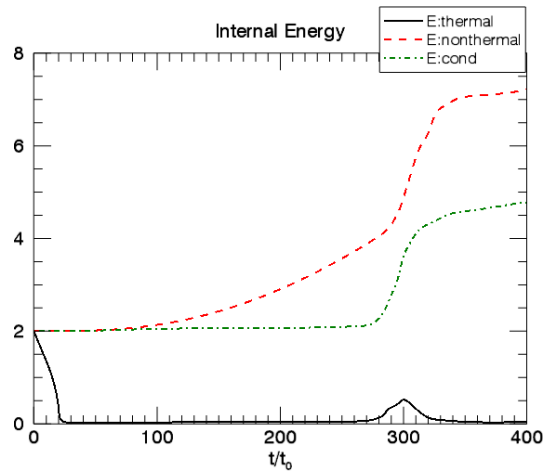
delay in the development of the tearing mode. There is also a second small increase in kinetic energy at a time of  $\sim 380$  for simulation B2:thermal.

### Magnetic Energy

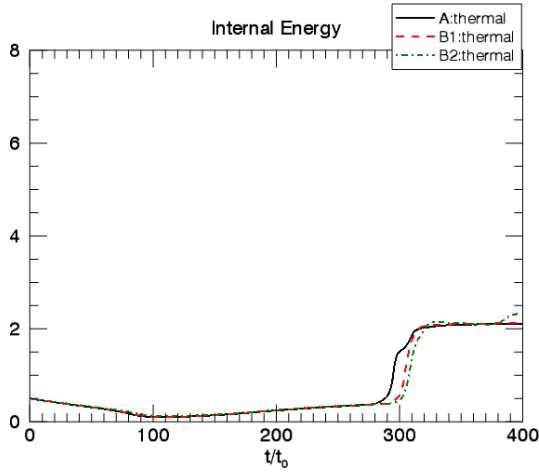
The magnetic energy is shown in Figure 6.3, on page 152, for each of the A, E and B simulations in Table 6.2 on page 148. All simulations have the same general evolution of the magnetic energy as seen in Chapter 5 in Figure 5.4 on page 115: build up of energy, followed by a sharp decrease to a steady state near the initial value. The initial build up of magnetic energy agrees with Chapter 4, Figure 4.8 on page 83. The high (Figure 6.3b) and low density (Figure 6.3a) initial conditions make little difference to the evolution of magnetic energy. When radiation and/or conduction are present the magnetic energy builds up more slowly than in the nonthermal case. This follows from the fact that energy is lost from radiation and any conductive flux through the boundaries in  $z$ . Varying the wave



(a) Low density initial conditions in Table 6.1 on page 147.



(b) High density initial conditions in Table 6.1 on page 147.



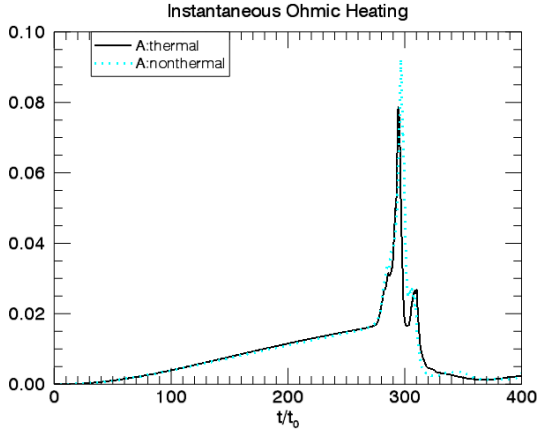
(c) Low density initial conditions in Table 6.1 on page 147. The perturbation amplitude,  $V_0$  waves, is varied.

Figure 6.4: Plots of volume integrated instantaneous internal energy as functions of time. The legends refer to the simulations in Table 6.2 on page 148.

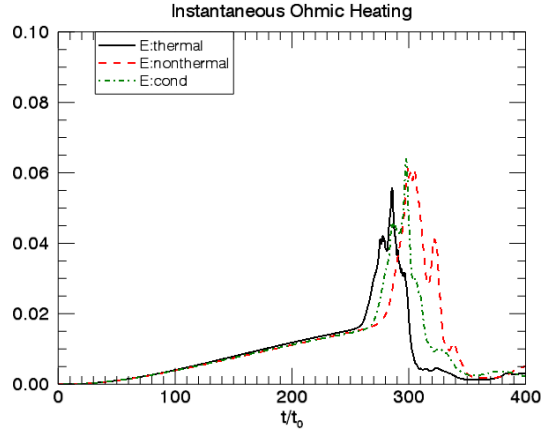
amplitude, shown in Figure 6.3c, makes little difference to the magnetic energy until the instability, where as mentioned there is a small delay in the onset of the instability which allows more magnetic energy to be stored. A second small but definite build up of magnetic energy occurs for simulation B2:thermal at about  $t = 380$  in Figure 6.3c.

### Internal Energy

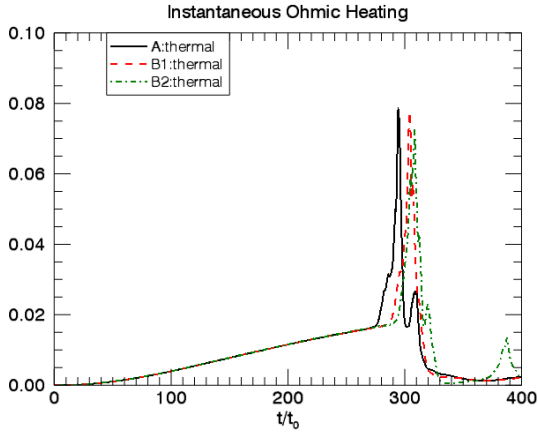
The internal energy is shown in Figure 6.4 on page 153 for all simulations. The internal energy in the two nonthermal cases, A:nonthermal and E:nonthermal, evolve similarly to the simulations in Chapter 5, shown in Figure 5.5 on page 116: the internal energy slowly increases from the initial value before a sudden increase, corresponding to the energy release of the tearing instability and reconnection, then an approximate constant value is attained again. For the rest of the simulations, which include thermal processes, the internal energy



(a) Low density initial conditions in Table 6.1 on page 147.



(b) High density initial conditions in Table 6.1 on page 147.



(c) Low density initial conditions in Table 6.1 on page 147. The perturbation amplitude,  $V_0$  waves, is varied.

Figure 6.5: Plots of volume integrated instantaneous ohmic heating as functions of time. The legends refer to the simulations in Table 6.2 on page 6.2.

decreases initially since radiative losses are greater than the Poynting flux. For the low density thermal cases in set A and B, the Poynting flux increases over time and becomes sufficient to balance the radiative losses, the plasma is compressed, as before, which heats the plasma a little due to adiabatic heating, before the onset of the tearing instability. The evolution of the internal energy is almost unaffected by increasing the wave amplitude, shown in Figure 6.4c, except for the second small sudden increase in simulation B2:thermal at  $t = 380$ . For the high density simulation, E:thermal in Figure 6.4b, radiative losses are greater than the Poynting flux throughout the evolution. Once the minimum temperature is reached the internal energy remains constant. There is a small increase in internal energy due to the instability about  $t = 300$  but the released energy is not enough to heat the plasma sufficiently and is quickly radiated away again.

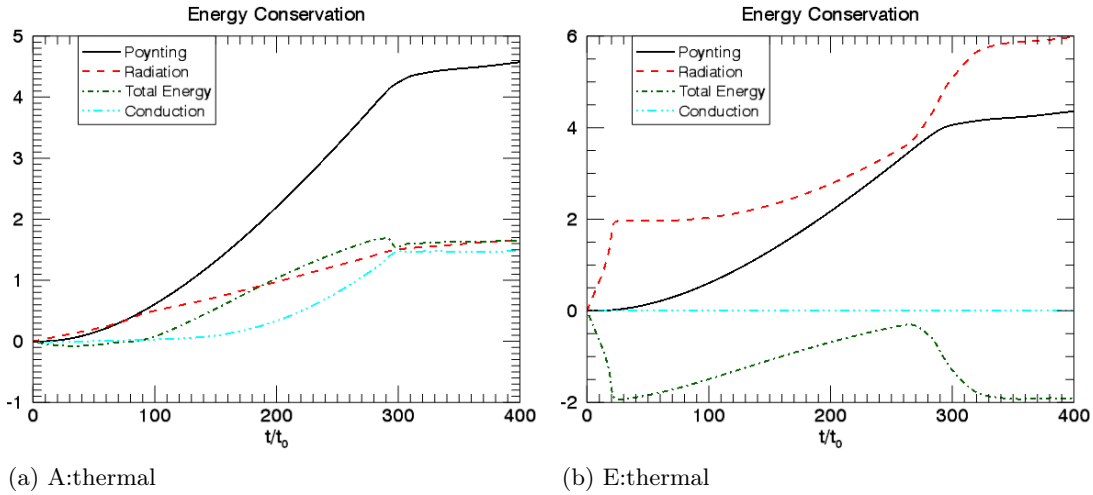


Figure 6.6: Plots of surface integrated, time integrated Poynting and conductive flux and optically thin radiative losses and volume integrated instantaneous total energy minus the initial energy at  $t = 0$ . The captions refer to the simulations in Table 6.2 on page 148.

### Ohmic heating

The instantaneous ohmic heating is shown in Figure 6.5 on page 154. All simulations show a similar evolution of the ohmic heating: a small amount, due to the build up of current, until the large release of energy at the instability. This evolution is similar to the time integrated ohmic heating found in Chapter 5 shown in Figure 5.6 on page 117. The largest magnitude of ohmic heating is found for A:nonthermal. This is because there are no losses due to radiation or conduction. There is, again, evidence of a second heating event for simulation B2:thermal at  $t = 380$  in Figure 6.5c.

### Energy Contributions

Energy balance between time and surface integrated Poynting flux and conductive flux through the boundaries in  $z$ , volume integrated optically thin radiative flux and total energy is shown in Figure 6.6, on page 155, for simulation A:thermal and E:thermal. It is clear, in Figure 6.6b, that the radiative losses always dominate the Poynting flux for the high density case, E:thermal. The radiative losses increase rapidly and become constant indicating that the temperature of the plasma has cooled to the threshold and radiative losses are switched off. Then there is some heating due to the tearing mode which immediately radiates away. The temperature remains smooth and slowly varying in space throughout this simulation, shown later in Figure 6.18 on page 169, resulting in very little conductive flux.

The evolution is very different for the low density simulation A:thermal. The Poynting flux is initially similar in magnitude and subsequently dominates the radiative losses. During the evolution there are three clear stages: first radiation dominates as the temperature decreases, these losses decrease, after the instability the plasma is heated, maintaining a density similar to the initial state, resulting in lower radiative losses. In this case there are very steep temperature gradients in  $x$ , which result in conductive flux at the boundaries. Here, the magnitude of the conductive flux is estimated. The conductive flux

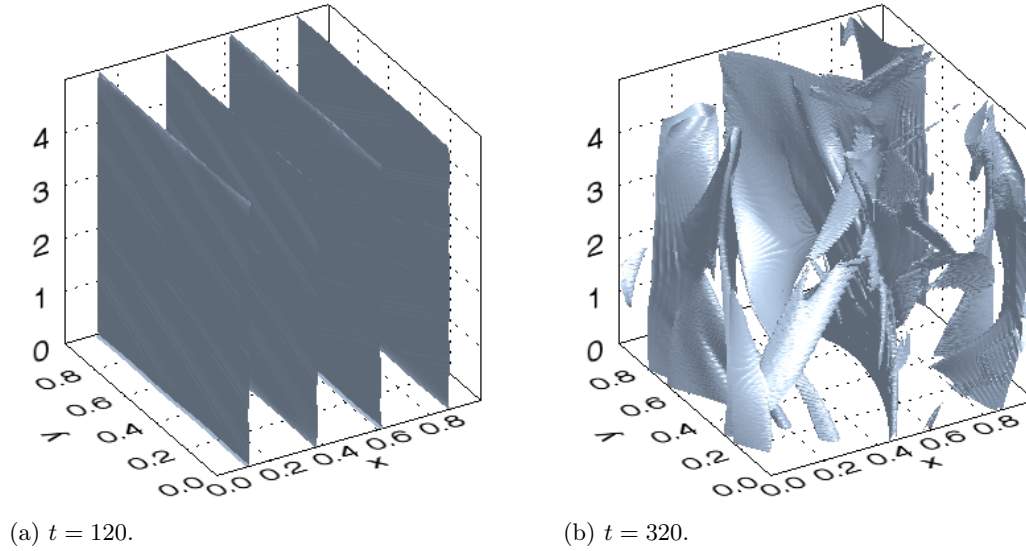


Figure 6.7: Isosurfaces of  $|j| = 3.0$  which is  $\sim 1\%$  of the maximum for simulation A:nonthermal in Table 6.2 on page 148.

increases rapidly in time once the instability occurs, corresponding to a small decrease in total energy. The temperature evolution, shown in Figure 6.17 on page 168, is discussed later.

#### Isosurfaces of Current

Examples of 3D isosurfaces of  $|j|$  before and after the instability are shown in Figure 6.7 for A:thermal. At early times  $t = 120$ , in Figure 6.7a, there are clear concentrations of current stretching along  $z$ . The build up of current is similar to the surfaces of  $|j|$  shown in Figure 4.32 on page 101 in Chapter 4 and isosurfaces of  $|j|$  in Figure 5.12a on page 127 in Chapter 5. These structures are subsequently distorted by the instability, shown in Figure 6.7b, at  $t = 320$ , showing a similar evolution to the nonthermal simulation MHD:A shown in Figure 5.12c on page 127 in Chapter 5.

#### Total Pressure

An interesting question is whether the system is in pressure balance. It has been previously shown, in Chapter 4, that the system is indeed in time-dependent pressure balance, shown in Figure 4.18 on page 91, and it was shown that the total pressure varies spatially during the development of the instability in Chapter 5, Figure 5.24a on page 142, but it is not known how thermal effects will affect this quantity. The total pressure is shown as a function of  $x$  at two times, one before and one after the instability, for A:thermal, A:nonthermal, E:thermal and E:nonthermal in Figure 6.8 on page 157. At early times,  $t = 120$ , the total pressure is constant for simulation A:thermal in Figure 6.8a. After the instability, at time  $t = 320$ , there is a small variation of total pressure. The same qualitative results are true for the nonthermal simulations. For A:thermal the total pressure increases in time while it decreases for E:thermal in Figure 6.8c.

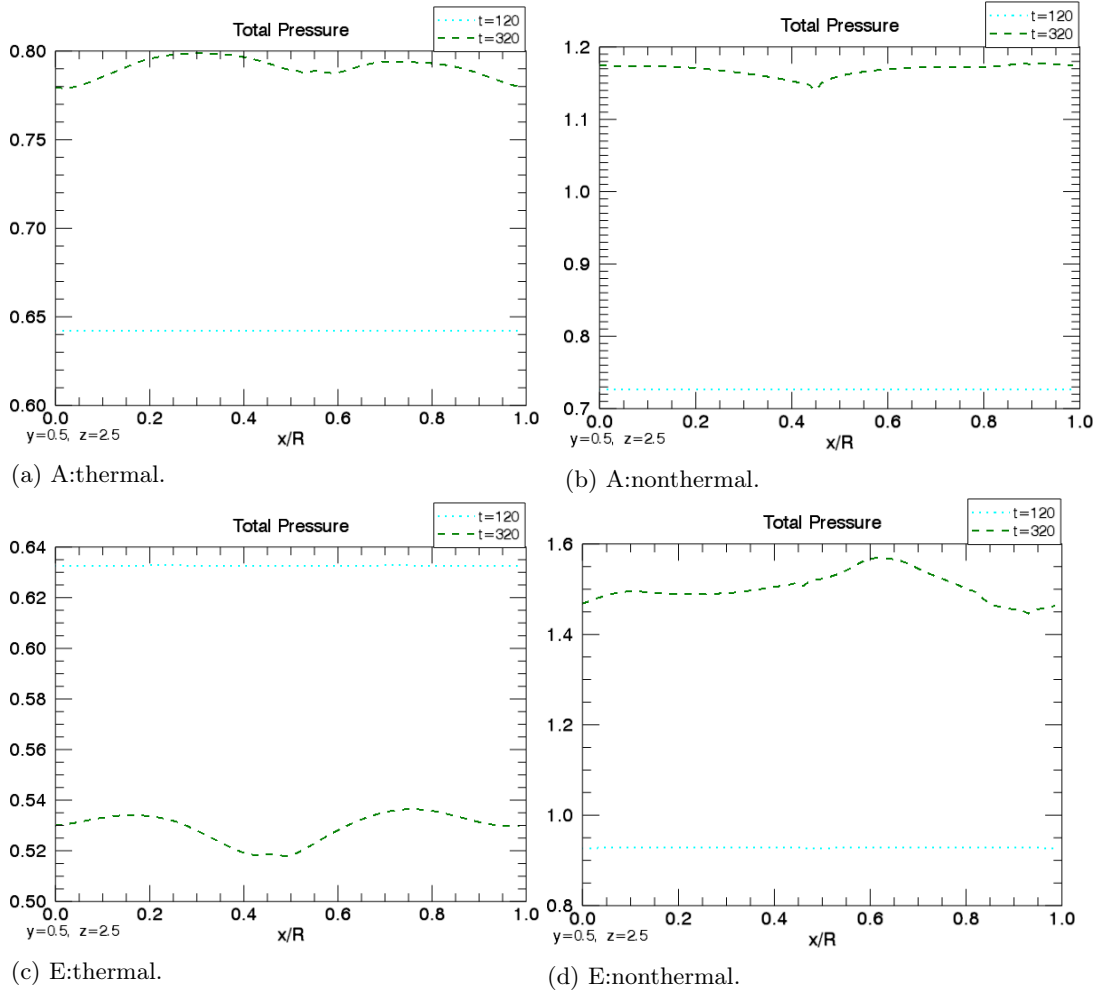


Figure 6.8: Plots of total pressure as a function of  $x$  at two times for the four main simulations in Table 6.2 on page 148. A different range has been used for the  $y$  axes for each simulation.

**Magnetic Field Component  $B_y$** 

The sheared magnetic field is shown in Figure 6.9 on page 159 and Figure 6.10 on page 160 for the low and high density cases respectively. The evolution of this component through the development of the instability is similar to that for the nonthermal simulations in Chapter 5 shown in Figure 5.17 on page 134. At early times,  $t = 80$  and  $t = 120$ ,  $B_y$  builds up with a sine profile that maps the shearing in Figure 6.9a and Figure 6.9b for low density simulations and Figure 6.10a and Figure 6.10b for high density simulations. This evolution is similar to that previously shown in Chapter 4 in Figure 4.6 on page 81 and Chapter 5 in Figure 5.17a on page 134, before the instability. The magnitude of  $B_y$  is  $\sim 1$  at  $t = 280$  before the instability, again showing that the perpendicular components are the same magnitude as the initial field. From Figure 6.9c it is found that, for the low density simulations, the symmetry of the sheared magnetic field is broken earlier when radiative processes are included. This can be seen by comparing  $B_y$  for A:thermal and A:nonthermal in this figure. This is not as clear for the high density case in Figure 6.10c. After the instability, at  $t = 320$ , in Figure 6.9d and Figure 6.10d, all simulations show a small variation in  $B_y$ . E:nonthermal still has a fairly large magnitude. Notably simulation E:thermal is comparatively constant.

**Magnetic Field Component  $B_z$** 

Figure 6.11 on page 161 and Figure 6.12 on page 162 show  $B_z$  as a function of  $x$  at the four simulation times for the low density and high density cases respectively. The background field,  $B_z$ , evolves similarly to the previous cases, shown in Chapter 4 in Figure 4.7 on page 82 and Chapter 5 in Figure 5.18 on page 135. The plasma is compressed in the middle and at the boundaries before the onset of the instability at early times for both high and low density, Figure 6.12a. This component in the thermal high density case, E:thermal, has a notably larger variation compared to the nonthermal case, E:nonthermal. This occurs because the temperature and pressure have decreased due to radiative losses, resulting in a smaller pressure force. The total force in the  $x$  direction is mainly due to the compression due to the magnetic pressure created by the shearing. In the thermal case, it is thought that the pressure force is smaller compared to the nonthermal case, resulting in the plasma being compressed more as a consequence of the unbalanced Lorentz force. This leads to a larger variation of  $B_z$  than in the nonthermal case. In contrast, the magnitude of  $B_z$  in the low density case is almost the same for the thermal and nonthermal cases at  $t = 80$ , Figure 6.11a. In this case radiative losses are not as large, leading to a slower decrease of pressure and the pressure force balances magnetic pressure. For  $t = 120$ , in Figure 6.11b, the thermal case has a larger variation plus an additional dip at the midpoint and boundaries. Between these two times:  $t = 80$  and  $t = 120$  the Poynting flux begins to dominate the radiative losses, as suggested in Figure 6.6a. While the pressure is decreasing everywhere due to radiative losses the plasma is still being compressed as a consequence of the driving motions. In the areas where the plasma is being compressed the pressure is increasing. When the Poynting flux dominates the radiative losses pressure is increasing more quickly than it is decreasing due to radiation. At the same time in

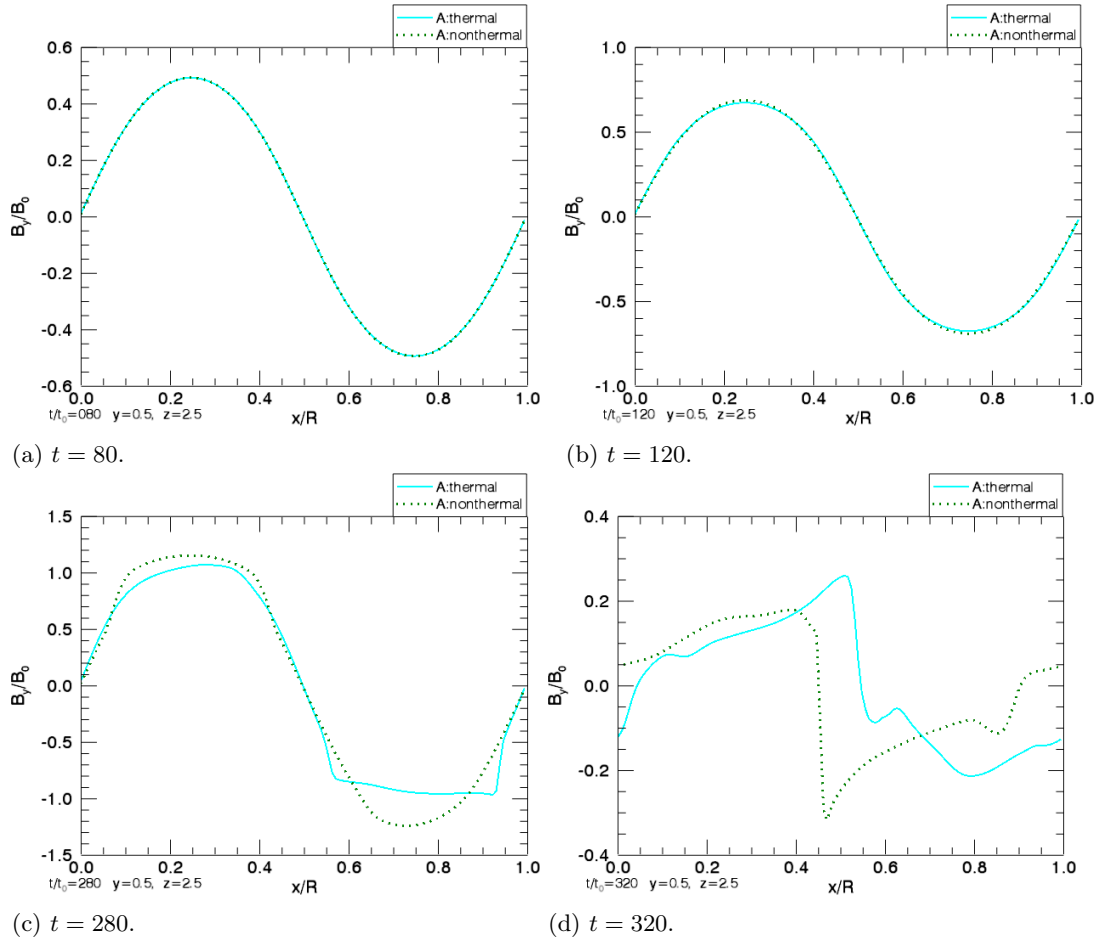


Figure 6.9: Plots of the sheared magnetic field,  $B_y$ , as a function of  $x$  at the midpoint in  $y$  and  $z$  for four simulation times. This is for the low density simulations A:thermal and A:nonthermal in Table 6.2 on page 6.2. The  $y$  range is different for each time.



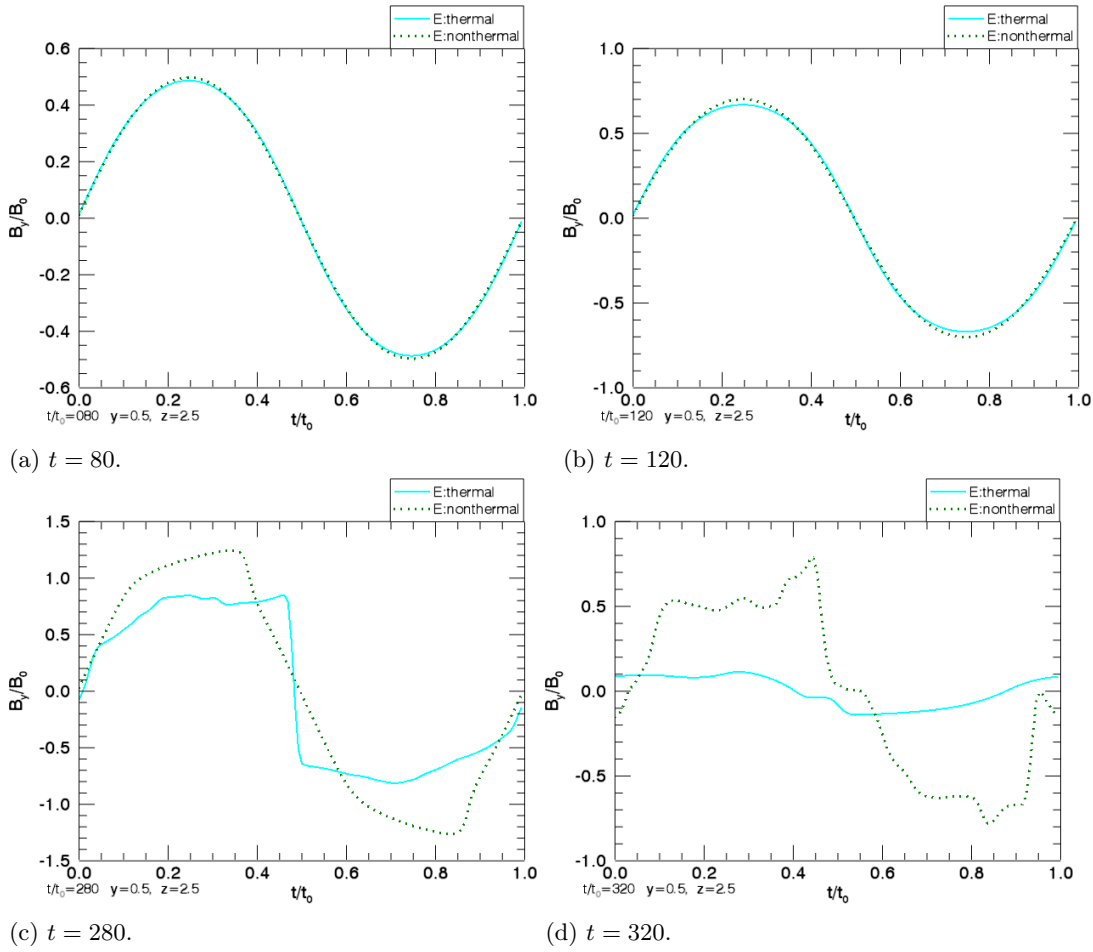


Figure 6.10: Plots of the sheared magnetic field,  $B_y$ , as a function of  $x$  at the midpoint in  $y$  and  $z$  for four simulation times. This is for the high density simulations E:thermal and E:nonthermal in Table 6.2 on page 148. The  $y$  range is different for each time.

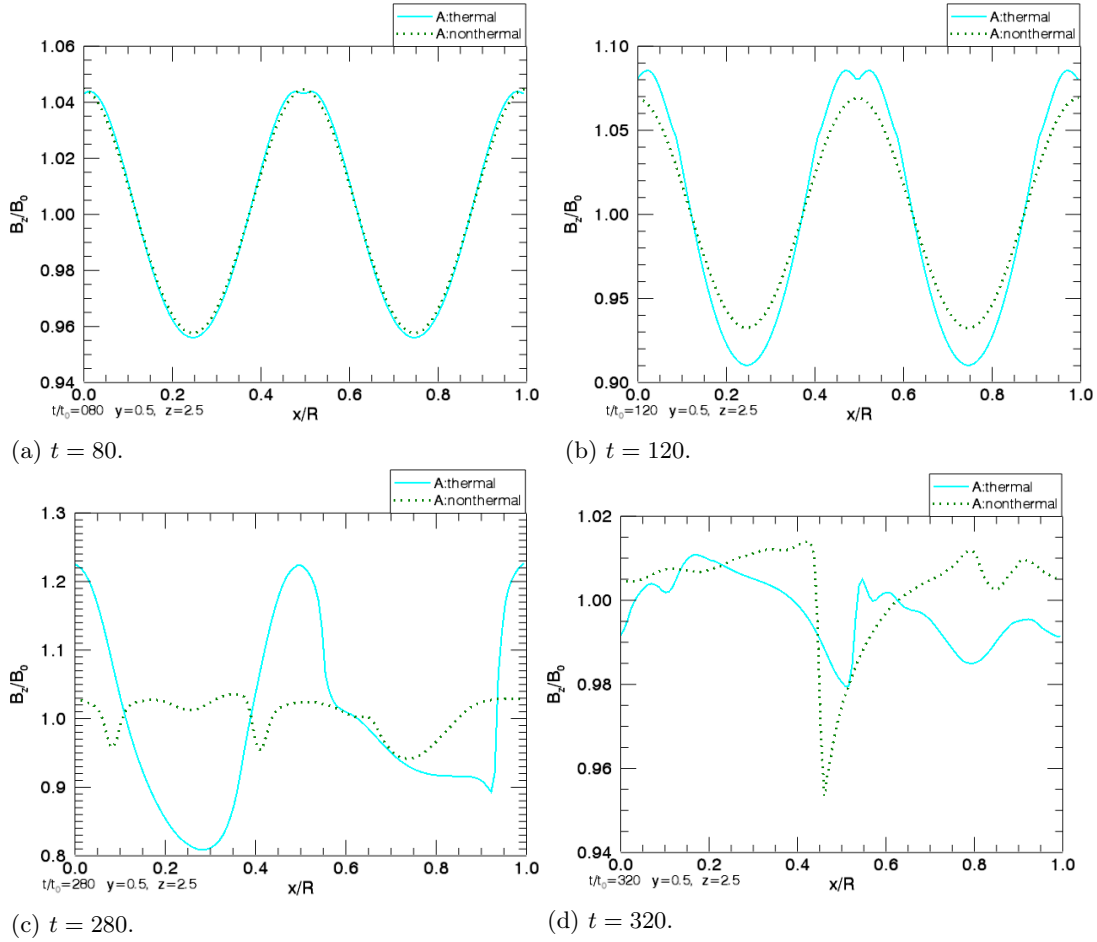


Figure 6.11: Plots of the magnetic field component,  $B_z$ , as a function of  $x$  at the midpoint in  $y$  and  $z$  for four simulation times. This is for the low density simulations A:thermal and A:nonthermal in Table 6.2 on page 148. The  $y$  range is different for each time.

areas where the plasma is expanding the pressure decreases due to expansion and radiation until the minimum temperature is reached and radiation switches off. This combination results in a steeper pressure gradient compared to the nonthermal case. This gradient is greatest around the midpoint and boundaries. This enhanced pressure gradient dominates the magnetic pressure from the driver in these small regions at the midpoint and boundaries. This results in the field being compressed either side of the midpoint and slightly away from the boundaries, which creates a little dip in  $B_z$  and  $\rho$  as is discussed later in this section. After the instability, at  $t = 320$ ,  $B_z$  is no longer smoothly varying for both high and low density cases, Figure 6.12d and Figure 6.11d. It is notable that this component is almost constant in the thermal high density case, E:thermal.

### Pressure

The pressure is shown as a function of  $x$  in Figure 6.13 on page 163 and Figure 6.14 on page 164 for the low and high density cases, respectively. The general evolution of the two nonthermal cases, A:nonthermal and E:nonthermal, are very similar to results in Chapter 5 for pressure shown in Figure 5.23 on page 141. Before the instability, at  $t = 80$ , shown

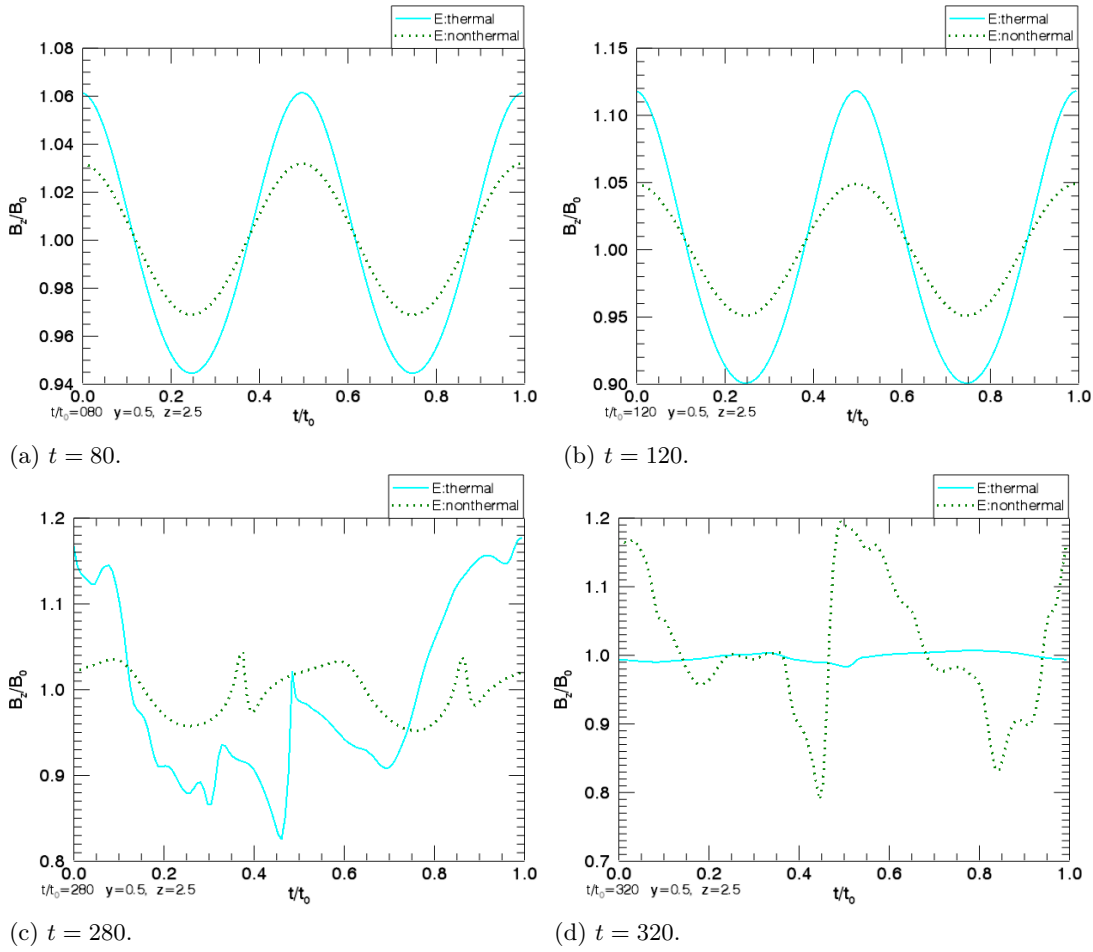


Figure 6.12: Plots of the magnetic field component,  $B_z$ , as a function of  $x$  at the midpoint in  $y$  and  $z$  for four simulation times. This is for the high density simulations E:thermal and E:nonthermal in Table 6.2 on page 148. The  $y$  range is different for each time.

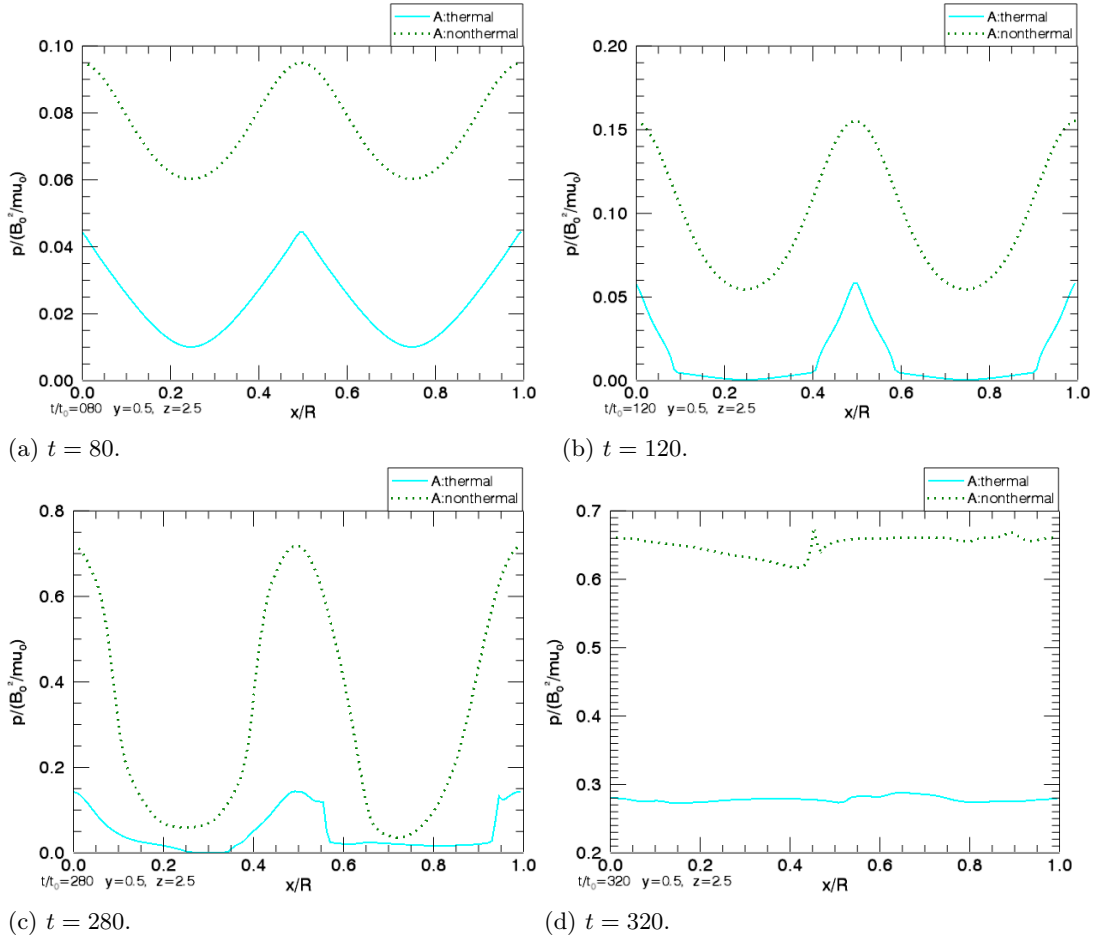


Figure 6.13: Plots of pressure,  $p$ , as a function of  $x$  at the midpoint in  $y$  and  $z$  for four simulation times. This is for the low density simulations A:thermal and A:nonthermal in Table 6.2 on page 148. The  $y$  range is different for each time.

in Figure 6.13a and Figure 6.14a, the pressure varies in  $x$  as the plasma compresses and expands. This agrees with the evolution of pressure in previous simulations in Chapter 4, Figure 4.10 on page 85 and Chapter 5, Figure 5.23a on page 141. At later times,  $t = 320$  in Figure 6.13d and Figure 6.14d, the magnitude of the pressure has increased, with small variations in some simulations. For E:thermal and A:thermal the final pressure is smaller than the nonthermal cases due to optically thin radiation cooling the plasma. In general, the pressure in simulation E:thermal is almost constant throughout the evolution. This agrees with the fact that in this simulation the plasma has cooled to the threshold. In contrast, although the pressure in simulation A:thermal also decreases initially, it then increases before the instability and has a similar profile to the nonthermal simulations, but with steeper and shallower gradients where the plasma is compressed and where it expands before the instability.

### Density

As in previous simulations, the density shows a similar variation to  $B_z$ .  $\rho$  as a function of  $x$  is shown in Figure 6.15 on page 166 and Figure 6.16 on page 167 for the low and high

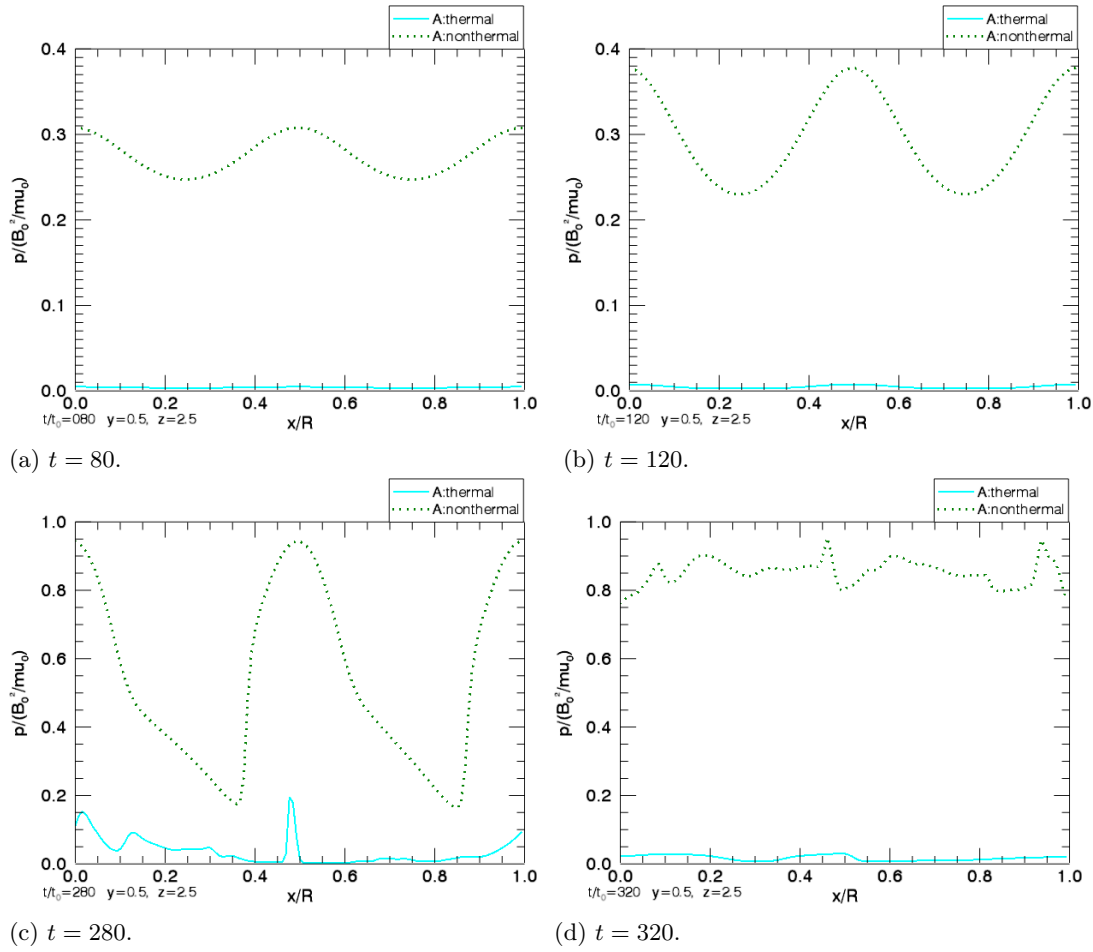


Figure 6.14: Plots of the pressure,  $p$ , as a function of  $x$  at the midpoint in  $y$  and  $z$  for four simulation times. This is for the high density simulations E:thermal and E:nonthermal in Table 6.2 on page 148. The  $y$  range is different for each time.

density cases respectively. The general evolution of  $\rho$  is very similar to Chapter 4, before the instability, and Chapter 5. Initially, at  $t = 80$ , the density is compressed at the midpoint and toward the boundaries in  $x$ , similar to Figure 4.11 on page 86 and Figure 5.19a on page 137. As described the plasma in the thermal high density case is being compressed more than the nonthermal case, resulting in a larger variation of  $\rho$  in  $x$  for  $t = 80$  and  $t = 120$  (Figures 6.15a, 6.15b, 6.16a and 6.16b). The low density thermal simulation, A:thermal, has a density slightly smaller than the nonthermal case for these early times. This is due to an asymmetry along the length of the loop in  $z$  due to conductive flux at the boundaries. Thus the density, pressure and temperature are larger at one end of the loop than the other. For both high and low density cases the instability is visible about  $t = 280$ , in Figure 6.16c and Figure 6.15c. The density in the thermal cases is smoother after the instability due to conduction compared to the nonthermal cases where there is no conduction, shown in Figures 6.16d and Figure 6.15d. At this time the two nonthermal cases still have large variations in  $\rho$ , which is smaller than the initial value. This agrees with the density evolution in the nonthermal simulations in Chapter 5 shown in Figure 5.19c. In contrast, simulation A:thermal settles to a value near the initial density of 0.25 and in E:thermal,  $\rho$  still has some variations at late times and the magnitude is much lower than the initial value of one.

### Temperature

The evolution of temperature is shown as a function of  $x$  in Figure 6.17 on page 168 and Figure 6.18 on page 169 for the low and high density cases, respectively. All of these simulations have an initial nondimensional temperature of 0.26 but evolve very differently. In the high density thermal simulation, E:thermal, in Figure 6.18a, the temperature decreases very quickly to the threshold value and remains there until the instability develops. Afterward, in Figure 6.18d, the temperature subsequently decreases again as the plasma cools. For the nonthermal cases, A:nonthermal and E:nonthermal, the temperature profile shows smooth large gradients in  $x$  as the plasma is compressed by the magnetic pressure, which are subsequently removed after the instability and replaced by small-scale variations. This evolution is similar to simulations in Chapter 5. In contrast, the thermal low density simulation, A:thermal, is very different. Initially, at  $t = 80$ , in Figure 6.17a, the temperature decreases but still has a variation in  $x$ , similar to A:nonthermal, but with steeper gradients around the midpoint and boundaries. This variation is further enhanced at  $t = 120$  in Figure 6.17b. This is due to localised heating in these positions due to the compression of the plasma, which is greater than the cooling caused by radiative losses. After the instability, at  $t = 320$ , in Figure 6.17d, the temperature increases and reaches a constant temperature, which is about four times the initial value of 0.26.

## 6.4 Discussion

In this chapter we have modelled the evolution of the tearing instability with inclusion of optically thin radiation and thermal conduction. Two types of initial conditions have been

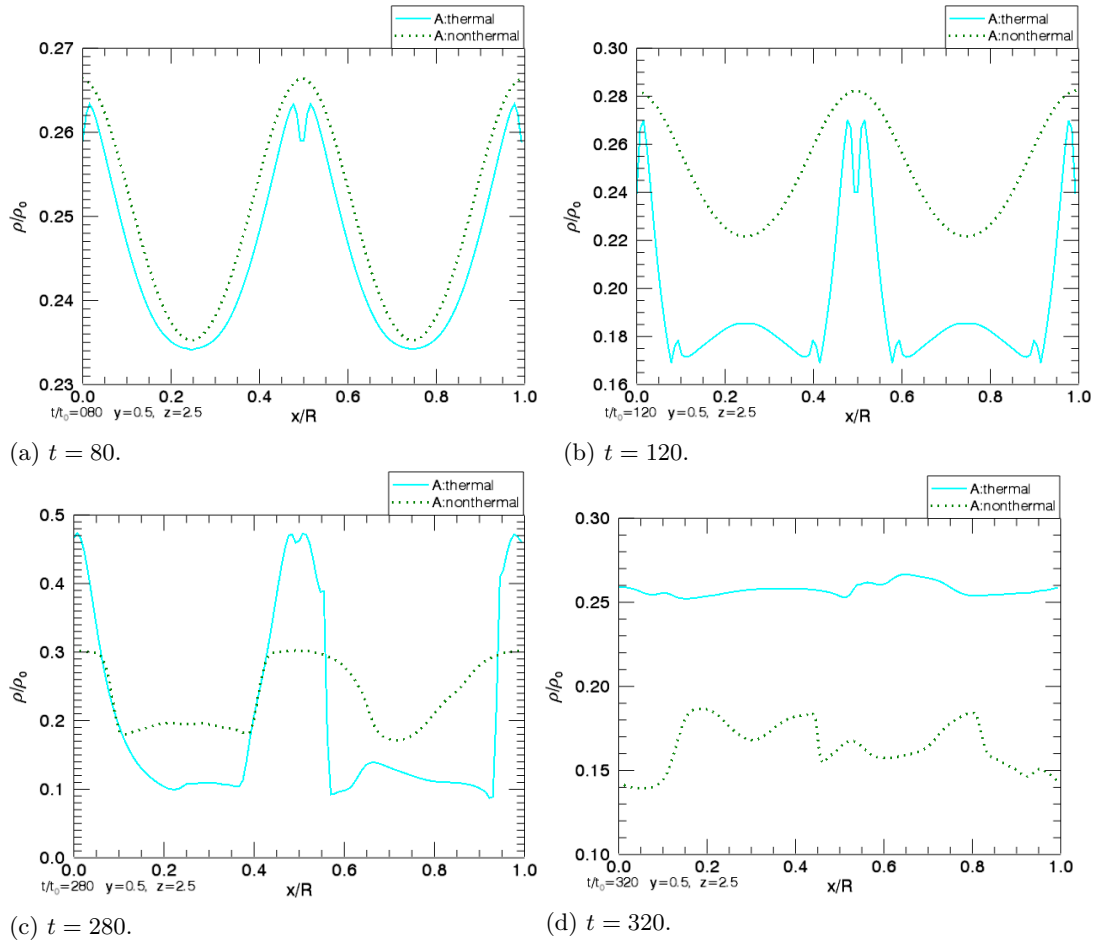


Figure 6.15: Plots of density,  $\rho$ , as a function of  $x$  at the midpoint in  $y$  and  $z$  for four simulation times. This is for the low density simulations A:thermal and A:nonthermal in Table 6.2 on page 148. The  $y$  range is different for each time.

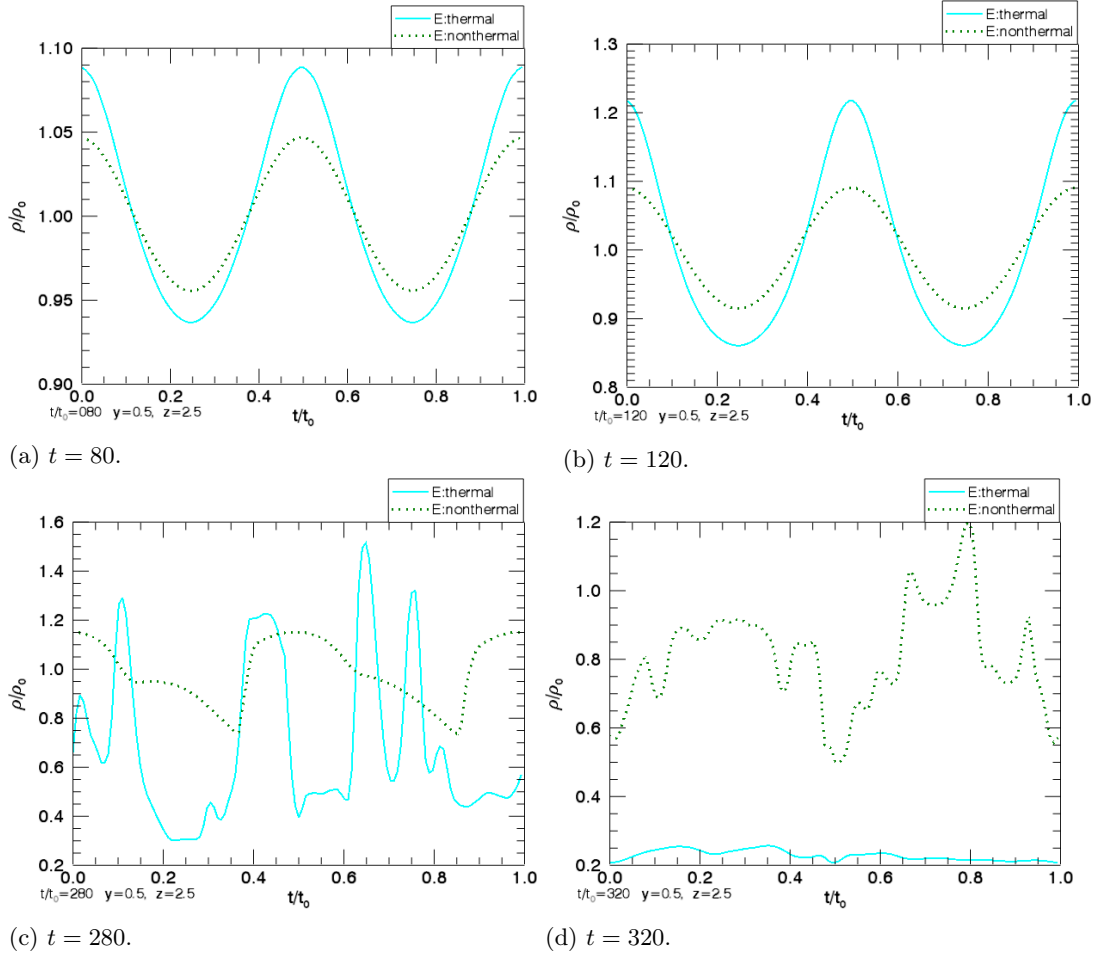


Figure 6.16: Plots of density,  $\rho$ , as a function of  $x$  at the midpoint in  $y$  and  $z$  for four simulation times. This is for the high density simulations E:thermal and E:nonthermal in Table 6.2 on page 148. The  $y$  range is different for each time.



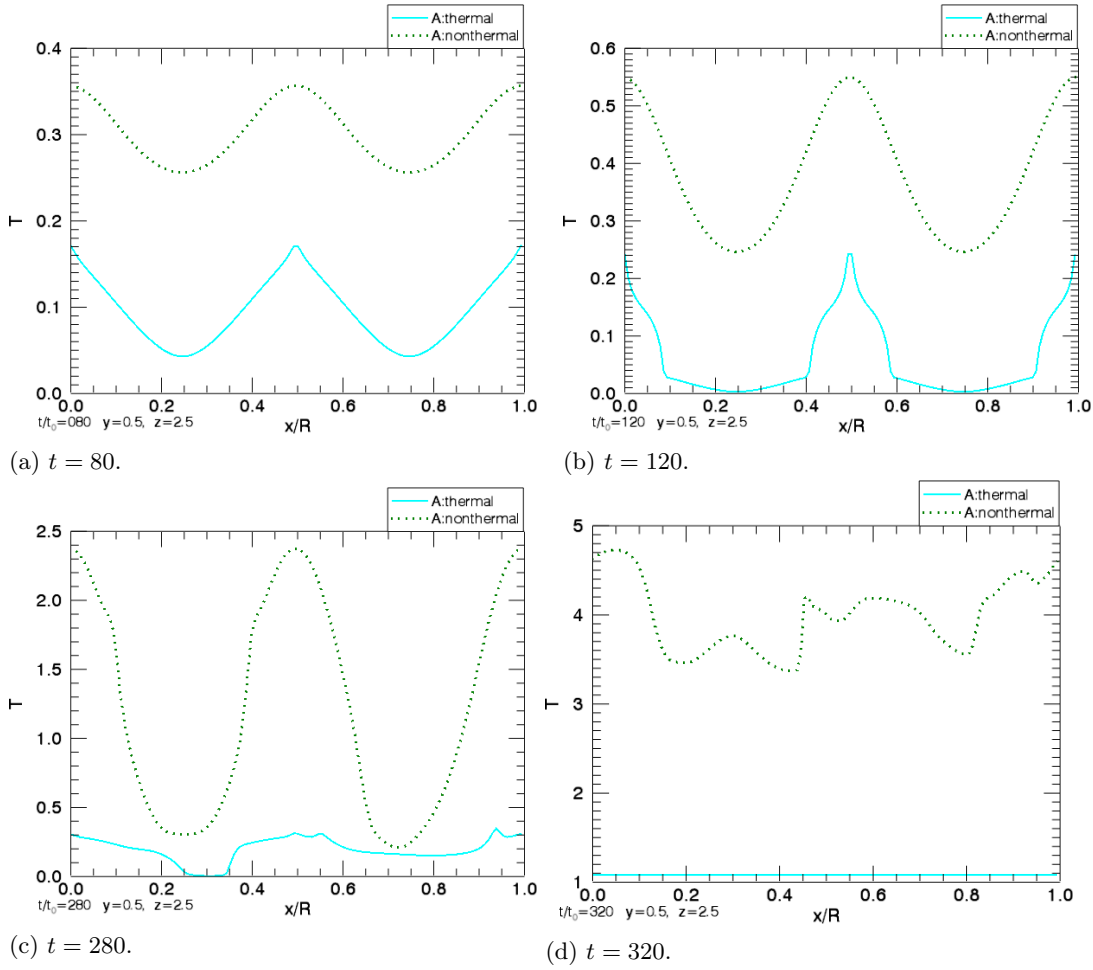


Figure 6.17: Plots of the temperature,  $T$ , as a function of  $x$  at the midpoint in  $y$  and  $z$  for four simulation times. This is for the low density simulations A:thermal and A:nonthermal in Table 6.2 on page 148. The  $y$  range is different for each time.

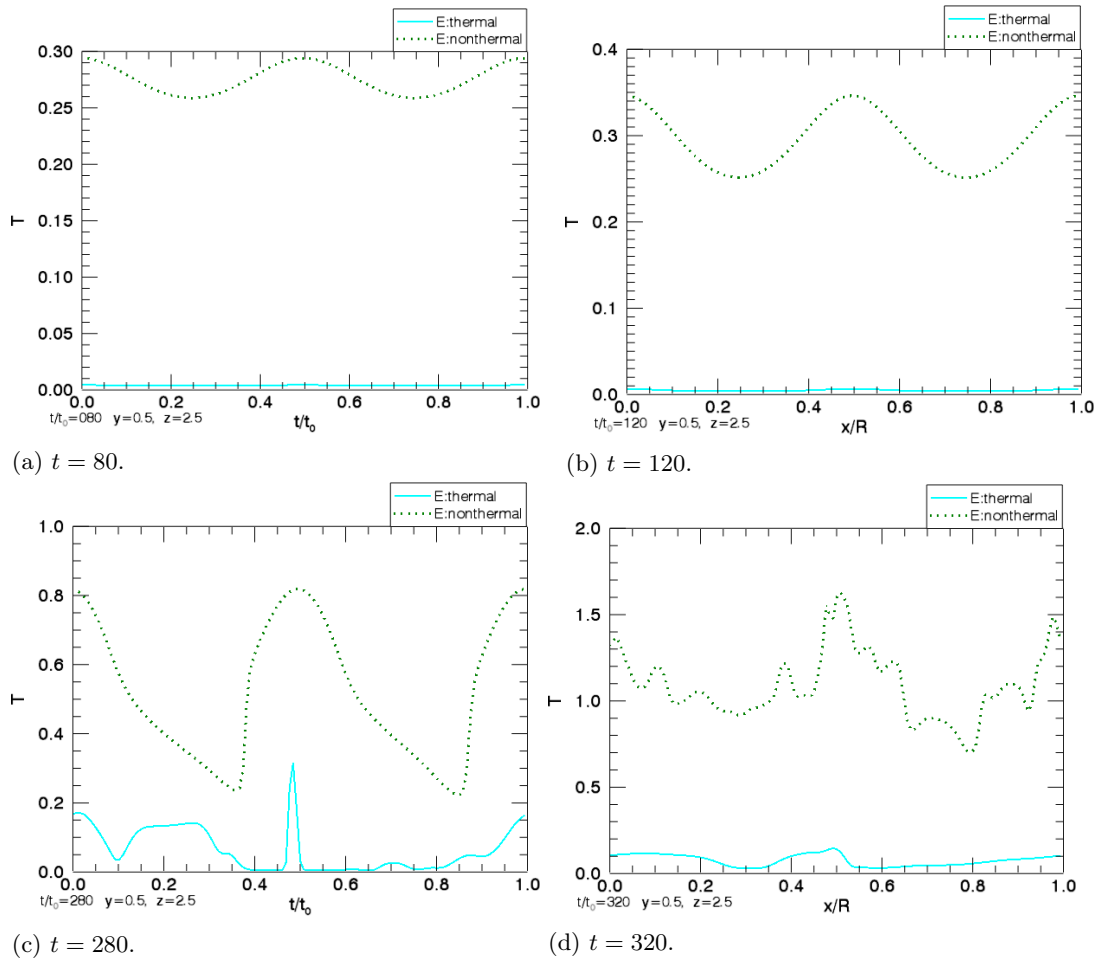


Figure 6.18: Plots of the temperature,  $T$ , as a function of  $x$  at the midpoint in  $y$  and  $z$  for four simulation times. This is for the high density simulations E:thermal and E:nonthermal in Table 6.2 on page 148. The  $y$  range is different for each time.

used, which involve very different timescales and evolutions.

A high density system, such as simulation E:thermal, results in very efficient radiation which is not balanced by the Poynting flux. This system radiates until the minimum temperature of  $\sim 1000\text{K}$  is reached. At this point the radiation process switches off and the system evolves similar to a nonradiative system, until the temperature exceeds this threshold and radiation switches back on. The heating produced by the tearing mode is quickly radiated away. The final temperature is two and a half times smaller than the initial value.

The high density nonthermal simulation, E:nonthermal, evolves similarly to the simulations in the previous chapter, Chapter 5. The temperature increases and decreases locally due to the compression resulting from the magnetic pressure generated by the shearing. After the instability the temperature distribution is very variable, since there is no thermal conduction in this system.

The temperature in the low density thermal case, A:thermal, decreases for about the first 100 Alfvén times. The radiative flux has a smaller magnitude due to the lower density. At this point the Poynting flux balances the radiative losses and starts to gradually heat the plasma. This heating could be due to compression which results from the magnetic pressure produced by the driver or ohmic and viscous heating. The final distribution of temperature is very different compared to the nonthermal case. Thermal conduction removes gradients in the temperature, resulting in a uniform temperature throughout the simulation box at the end. The final temperature is 1.13, corresponding to  $5.8\text{MK}$ . This gives a final temperature four times hotter than the initial temperature of 0.26.

During the 400 Alfvén times, equivalent to  $\sim 320$  minutes in our normalisation, the low density simulation, A:thermal, has a total energy input of  $\approx 4.6$  due to the Poynting flux through the two boundary surfaces. Over the same period the total volume integrated radiative losses are  $\approx 1.7$ , which is more than two and a half times smaller than the Poynting flux. This shows that there is more energy going into the system than is lost by radiation.

For the high density simulation, E:thermal, the total final Poynting flux through the boundary surfaces is slightly smaller at  $\approx 4.4$ . In this case, the final volume integrated radiative losses are greater than this Poynting flux, with a magnitude of  $\approx 6$ .

Here, there are many aspects of this system that could be investigated further. For example, a further extension to this study would be to use an anomalous or spatially dependent resistivity instead of a constant value. The period of the waves is held constant for all simulations present in this chapter and only one type of perturbation is used. These effects of varying these properties could be investigated further. Although this system has been evolved using the full MHD equations, there are still many areas of approximation. Here only the corona is modelled and the boundary motions are applied directly to the base of the coronal loop. It is expected that dynamics in the lower atmosphere are also likely to be important to the evolution of this system as has been shown in van Ballegooijen et al. 2011, using an adapted RMHD model, discussed in Appendix B.6. Another simplification is that only one coronal loop is considered. This does not allow for the interaction of many loops as would be the case in the corona.

In the final chapter, a summary of results and future work is discussed.

## Chapter 7

# Summary and Further Work

In summary, there are several aims of this study. The general purpose is to investigate the ability of footpoint motions to store and release magnetic energy to heat the solar corona. In carrying out this investigation, the importance of validity when considering applying an approximate method to a certain system is emphasised. In particular, we focus on the approximate MHD method of reduced MHD (RMHD).

The models of MHD and RMHD and the relevant properties were presented in Chapter 2 and Chapter 3. There are very few studies which have investigated validity, self-consistency and accuracy between RMHD and full MHD. This has resulted in considerable uncertainty and confusion about when RMHD is likely to be a good approximation to full MHD and when it is not. There are a wide range of studies that have been done using RMHD, yielding interesting and potentially useful and important conclusions, providing these results were also true for full MHD.

One such study, Rappazzo, Velli, and Einaudi (2010), concludes that a driven system in which magnetic energy is stored and subsequently released through the tearing instability only stores energy once, after the instability the system remains in a statistically steady state. This idea does not agree with the intuitive picture in full MHD, which expects this process of storing and releasing energy to occur in a cyclic manner.

The aim of this study is to investigate a similar system to Rappazzo, Velli, and Einaudi (2010) using full MHD and verify whether their conclusion is also true for full MHD. This is done in two parts.

First, a simple 2.5D model is developed in Chapter 4 where an initially uniform magnetic field is sheared by smooth footpoint motions, resulting in the build up of magnetic energy as the system evolves through sequences of equilibria. This system is used to illustrate the importance of validity by using four common approximate methods: magneto frictional relaxation, 1D approach, linearisation and RMHD, and full MHD to model the evolution of the magnetic field. The results from these models are compared to each other and their accuracy is judged against the full MHD results, which are taken to be the “exact” solution throughout. Linearisation and RMHD provide accurate approximations when the footpoint displacement is sufficiently small, independent of the plasma  $\beta$ . The 1D and relaxation methods provide a good approximation for the magnetic field for small plasma

$\beta$ , but not as good for pressure and density. An advantage of the 1D method is that it is the computationally fastest method used here.

In this first study, a ponderomotive type force due to viscous effects was found to be important as the plasma beta was decreased. The linearised MHD equations enabled useful insights into this phenomenon while the other approaches could not as they do not involve viscosity. RMHD is not valid for this 2.5D system. Each of the approximate methods was found to be valid for small footpoint motions. Some methods gave good results even when they were not expected to and some were not as accurate as expected. For example, the relaxation method provided excellent agreement for low  $\beta_0$  as expected since a force free system is assumed. Linearised MHD gave good results with only reasonable discrepancies for large values of  $D/L$ , despite being derived from assuming  $D/L \ll 1$ .

Second, in Chapter 5 the system is extended to 3D and small symmetry-breaking perturbations are added at the boundaries. This setup of a driver and perturbation allows investigation of the evolution of the tearing mode, using full MHD, by varying several parameters, including the type of perturbation and its amplitude and period. The main purpose of this chapter is to verify whether Rappazzo et al's RMHD conclusion, stating that the instability only occurs once in this setup rather than cyclically, is also true in full MHD or not. Qualitative comparisons are presented between Rappazzo, Velli, and Einaudi 2010 and our full MHD results. The main result of this chapter and project is that the tearing instability does indeed only occur once in full MHD. This conclusion extends Rappazzo et al's result from RMHD to full MHD.

The full MHD data is also analysed to check the assumptions of RMHD. It is concluded that qualitatively these studies give the same general evolution, despite the fact that the RMHD conditions are not satisfied during most of the evolution and the growth of the instability. This indicates that these additional effects are not important for the general evolution. For these simulations it seems reasonable to neglect them, however direct comparisons are still needed to verify this suggestion.

One limitation of RMHD is that thermal processes are neglected from the beginning, resulting in it not being possible to gain meaningful conclusions about the thermodynamic response of the plasma to coronal heating. As seen in Chapter 5, the tearing instability releases a substantial amount of energy. A natural next step is to investigate the heating potential of our system. This can be done using full MHD simulations by including thermal conduction and radiation in our setup. This first experiment in this direction and results are discussed in Chapter 6. Here two cases are studied. The first case has a higher initial density than the second. The temperature evolution in these two cases is surprisingly different considering the only difference is the initial density. The high density case is dominated by radiative losses. The final temperature attained after the tearing instability is two and a half times cooler than the initial temperature. The low density case is dominated by the Poynting flux created by the footpoint motions. The final temperature is four times hotter than the starting value.

There are a number of limitations to this study. An example is that only one system was investigated for validity of RMHD. There are many more tests that could be performed in the future to check validity of RMHD, it would be interesting to extend the

comparisons between RMHD and full MHD turbulence performed in Dmitruk, Matthaeus, and Oughton 2005 and the self-consistency checks undertaken in Oughton, Dmitruk, and Matthaeus 2004.

It is also essential to perform direct comparisons between RMHD and full MHD for the current system and investigate the properties of the final turbulent-like state. To do this using the same Lare data in cartesian coordinates, it would be necessary to develop a cartesian RMHD code since current RMHD codes are either written in cylindrical geometry for tokomaks or are psuedospectral codes designed for turbulence modelling. In order to conduct direct comparisons of any methods a technique to quantify the agreement would need to be chosen.

It would be interesting to investigate validity of the Alfvén wave turbulence models developed by Dmitruk et al (Dmitruk, Milano, and Matthaeus 2001) and Van Ballegooijen (van Ballegooijen et al. 2011) using adapted RMHD models. There are many related approximate methods, such as NIMHD (Appendix B.4 and Zank and Matthaeus 1993), 4fieldMHD (Appendix B.5 and Bhattacharjee, Ng, and Spangler 1998). The relation between these models, RMHD and full MHD could be considered. The “slow MHD” model derived by Zhukov 2001 in cylindrical coordinates and discussed in Appendix B.3, which includes slow waves in a model similar to RMHD could be derived in cartesian coordinates.

In the context of coronal heating, future extensions to this system would involve testing different driver and perturbation profiles, applying a more realistic lower atmosphere, photosphere and transition region. An important aspect is to investigate how different drivers result in different evolutions, some may involve numerous heating events and some only allow one, as was found in this study.

The main message is to be careful what you assume.

# Appendices

## Appendix A

# Alternative RMHD Derivations

### A.1 Zank and Matthaeus' Derivation

In this section we will follow the derivation of RMHD by Zank and Matthaeus 1992, which was summarised in Section 3.3.2. This is included since the equations are presented in terms of the velocity and magnetic fields, therefore giving a more physical interpretation of the assumptions compared to using the potentials as in Strauss' derivation (Strauss 1976) presented in Section 3.3.

This derivation is also more algebraically rigorous. They follow a procedure of separation of spatial and temporal scales in the compressible MHD equations, then the perpendicular and parallel components of these equations are considered. The final RMHD equations are found from the resulting equations after applying a few further arguments. The derivation for the  $\beta \ll 1$  regime is given here. Zank and Matthaeus also consider  $\beta \sim 1$  and  $\beta \gg 1$ .

We begin with the normalised compressible ideal MHD equations, Equation (2.17) on page 14. Applying the normalisation

$$t' = \frac{v_0 t}{L}, \quad \mathbf{v}' = \frac{\mathbf{v}}{v_0}, \quad \rho' = \frac{\rho}{\rho_0}, \quad \mathbf{B}' = \frac{\mathbf{B}}{B_0}, \quad \mathbf{x}' = \frac{\mathbf{x}}{L}, \quad p' = \frac{p}{p_0},$$

leaves the equations unchanged except for the momentum equation, Equation (2.17a). The momentum equation now has the form,

$$\rho \left( \frac{\partial}{\partial t} + \mathbf{v} \cdot \nabla \right) \mathbf{v} = -\frac{1}{v_0^2 \rho_0} \nabla p + \frac{1}{M_A^2} (\nabla \times \mathbf{B}) \times \mathbf{B},$$

where the Alfvénic mach number  $M_A = \frac{v_0^2}{V_A^2}$  and  $V_A^2 = \frac{B_0^2}{\mu \rho_0}$ . Here we assume a highly subsonic flow

$$v_0^2 \ll c_s^2 = \frac{\gamma p_0}{\rho_0}, \quad \text{and} \quad c_s^2 \leq V_A^2 \Rightarrow M_A = \varepsilon_{zm} \ll 1,$$



where  $\varepsilon_{zm}$  is a small parameter. Now the pressure term can be rewritten

$$\frac{1}{v_0^2 \rho_0} \nabla p = \frac{1}{\varepsilon_{zm}} \nabla \left( \frac{1}{\varepsilon_{zm}} \beta_0 \frac{p}{p_0} \right) = \frac{1}{\varepsilon_{zm}} \nabla p,$$

since  $\beta_0 = \frac{\mu p_0}{B_0^2} \ll 1$  and  $\beta \sim O(\varepsilon_{zm})$  is assumed the bracketed term is  $O(1)$ . Hence the momentum equation can be written as

$$\rho \left( \frac{\partial \mathbf{v}}{\partial t} + (\mathbf{v} \cdot \nabla) \right) \mathbf{v} = -\frac{1}{\varepsilon_{zm}} \nabla p + \frac{1}{\varepsilon_{zm}^2} (\nabla \times \mathbf{B}) \times \mathbf{B}. \quad (\text{A.1})$$

There are three relevant timescales in this system, namely

$$\text{convection: } \tau_c = L/v_0,$$

$$\text{acoustic: } \tau_s = \lambda_s/c_s,$$

$$\text{Alfvénic: } \tau_A = \lambda_A/V_A.$$

where  $L$  is a typical length,  $v_0$  is a typical velocity,  $\lambda_s$  and  $\lambda_A$  are typical sound and Alfvén wavelengths and  $C_s$  and  $V_A$  are the sound and Alfvén speeds, respectively. Since  $v_0 \ll c_s \ll V_A$  is assumed the convective timescale is slowest and the Alfvén timescale is the fastest. Here the dynamics of interest occur on the slow convective timescale and it is not necessary to follow the fast timescale dynamics. Hence we rescale the fast sound and Alfvén timescale by making them larger than the slow convective timescale. We define slow and fast time scales as

$$\text{slow time scale } \tau = t,$$

$$\text{fast time scale } \tau' = \frac{\tau}{\varepsilon_{zm}},$$

$$\Rightarrow \frac{\partial}{\partial t} = \frac{\partial}{\partial \tau} + \frac{1}{\varepsilon_{zm}} \frac{\partial}{\partial \tau'}. \quad (\text{A.2})$$

This will result in removing high frequency waves. The only waves that can still exist are those with extremely long wavelengths. A wave with such a long wavelength will vary very slowly in space and so the spatial scales must also be rescaled in order to investigate the interactions of such waves. The short and long spatial (wavelength) scales are defined as

$$\text{short lengthscale } \mathbf{X} = \hat{\mathbf{x}},$$

$$\text{long lengthscale } \mathbf{x} = \varepsilon_{zm} \hat{\mathbf{x}},$$

$$\Rightarrow \nabla_{\hat{\mathbf{x}}} = \nabla_{\mathbf{X}} + \varepsilon_{zm} \nabla_{\mathbf{x}}. \quad (\text{A.3})$$

Variables are expanded using the ansatz

$$\mathbf{v} = \mathbf{v}, \quad p = p_0 + \varepsilon_{zm} p_1, \quad \mathbf{B} = \mathbf{B}_0 + \varepsilon_{zm} \mathbf{B}_1, \quad \rho = 1 + \varepsilon_{zm} \rho_1. \quad (\text{A.4})$$

The initial background magnetic field is taken to be in the  $z$  direction and, ac-

cordingly, the remaining long-wavelength Alfvén waves will travel along this direction. For simplicity the slow spatial scale is taken to be only parallel to the background field direction. Only dynamics on the slow timescale,  $\tau$ , are kept so variations on the fast timescale,  $\tau'$ , are set to zero. This gives

$$\frac{\partial}{\partial \tau'} = 0, \quad \mathbf{B}_0 = (0, 0, B_0), \quad \nabla_{\mathbf{x}} = \left(0, 0, \frac{\partial}{\partial z}\right). \quad (\text{A.5})$$

We now expand each of the MHD equations using the ansatz, Equation (A.4), time and spatial scales, Equation (A.2) and Equation (A.3). Terms are then collected in each order of  $\varepsilon_{zm}$ .

As an example the continuity equation, Equation (2.17b) on page 14, is expanded as

$$\varepsilon_{zm} \frac{\partial \rho_1}{\partial \tau} + \frac{\partial \rho_1}{\partial \tau'} + \nabla_{\mathbf{x}} \cdot \mathbf{v} + \varepsilon_{zm} \nabla_{\mathbf{x}} \cdot (\rho_1 \mathbf{v}) + \varepsilon_{zm} \nabla_{\mathbf{x}} \cdot \mathbf{v} + \varepsilon_{zm}^2 \nabla_{\mathbf{x}} \cdot (\rho_1 \mathbf{v}) = 0.$$

The  $O(1)$  terms are

$$\frac{\partial \rho_1}{\partial \tau'} + \nabla_{\mathbf{x}} \cdot \mathbf{v} = 0, \quad \Rightarrow \quad \nabla_{\mathbf{x}} \cdot \mathbf{v} = 0.$$

Since derivatives on the fast timescale,  $\tau'$ , are zero this implies that  $\mathbf{v}$  is incompressible with respect to the short lengthscale,  $\mathbf{X}$ . Terms of  $O(\varepsilon_{zm})$  are

$$\frac{\partial \rho_1}{\partial \tau} + \mathbf{v} \cdot \nabla_{\mathbf{x}} \rho_1 = -\nabla_{\mathbf{x}} \cdot \mathbf{v} = -\frac{\partial v_z}{\partial z}, \quad (\text{A.6})$$

since  $\nabla_{\mathbf{x}} = (0, 0, \frac{\partial}{\partial z})$ .

The remaining term is of  $O(\varepsilon_{zm}^2)$

$$\nabla_{\mathbf{x}} \cdot (\rho_1 \mathbf{v}) = 0.$$

Expanding the momentum equation, Equation (A.1). gives the following terms in powers of  $\varepsilon_{zm}$ .

Terms of  $O\left(\frac{1}{\varepsilon_{zm}}\right)$  are

$$0 = (\mathbf{B}_0 \cdot \nabla_{\mathbf{x}}) \mathbf{B}_1 - \nabla_{\mathbf{x}} (\mathbf{B}_1 \cdot \mathbf{B}_0), \quad \Rightarrow \quad \nabla_{\mathbf{x}} B_{z1} = \frac{\partial}{\partial z} \mathbf{B}. \quad (\text{A.7})$$

Terms of  $O(1)$  give the equation

$$\begin{aligned} \frac{\partial \mathbf{v}}{\partial \tau} + (\mathbf{v} \cdot \nabla_{\mathbf{x}}) \mathbf{v} + \nabla_{\mathbf{x}} p_1 = & (\mathbf{B}_0 \cdot \nabla_{\mathbf{x}}) \mathbf{B}_1 - \nabla_{\mathbf{x}} (\mathbf{B}_1 \cdot \mathbf{B}_0) + (\mathbf{B}_1 \cdot \nabla_{\mathbf{x}}) \mathbf{B}_1 \\ & - \frac{1}{2} \nabla_{\mathbf{x}} (\mathbf{B}_1 \cdot \mathbf{B}_1). \end{aligned} \quad (\text{A.8})$$

Terms of  $O(\varepsilon_{zm})$  give the equation

$$\rho_1 \frac{\partial \mathbf{v}}{\partial \tau} + \rho_1 (\mathbf{v} \cdot \nabla_{\mathbf{x}}) \mathbf{v} + (\mathbf{v} \cdot \nabla_{\mathbf{x}}) \mathbf{v} + \nabla_{\mathbf{x}} p_1 = (\mathbf{B}_1 \cdot \nabla_{\mathbf{x}}) \mathbf{B}_1 - \frac{1}{2} \nabla_{\mathbf{x}} (\mathbf{B}_1 \cdot \mathbf{B}_1). \quad (\text{A.9})$$

The term of  $O(\varepsilon_{zm}^2)$  implies

$$\rho_1 (\mathbf{v} \cdot \nabla_{\mathbf{x}}) \mathbf{v} = 0, \quad \Rightarrow \quad \rho_1 v_z \frac{\partial \mathbf{v}}{\partial z} = 0. \quad (\text{A.10})$$

The induction equation, Equation (2.17c) on page 14, gives the following equations. The  $O(1)$  contribution results in

$$(\mathbf{B}_0 \cdot \nabla_{\mathbf{x}}) \mathbf{v} - \mathbf{B}_0 (\nabla_{\mathbf{x}} \cdot \mathbf{v}) = 0, \quad \Rightarrow \quad (\mathbf{B}_0 \cdot \nabla_{\mathbf{x}}) \mathbf{v} = B_0 \frac{\partial \mathbf{v}}{\partial Z} = 0.$$

since  $\mathbf{B}_0 (\nabla_{\mathbf{x}} \cdot \mathbf{v}) = 0$ . Therefore,  $\mathbf{v}$  is independent of the short parallel coordinate,  $Z$ . Terms of  $O(\varepsilon_{zm})$  give the equation

$$\frac{\partial \mathbf{B}_1}{\partial \tau} + (\mathbf{v} \cdot \nabla_{\mathbf{x}}) \mathbf{B}_1 = (\mathbf{B}_0 \cdot \nabla_{\mathbf{x}}) \mathbf{v} + (\mathbf{B}_1 \cdot \nabla_{\mathbf{x}}) \mathbf{v} - \mathbf{B}_0 (\nabla_{\mathbf{x}} \cdot \mathbf{v}). \quad (\text{A.11})$$

Lastly, the  $O(\varepsilon_{zm}^2)$  terms give the equation

$$(\mathbf{v} \cdot \nabla_{\mathbf{x}}) \mathbf{B}_1 = (\mathbf{B}_1 \cdot \nabla_{\mathbf{x}}) \mathbf{v} - \mathbf{B}_1 (\nabla_{\mathbf{x}} \cdot \mathbf{v}). \quad (\text{A.12})$$

Expanding the solenoidal constraint,  $\nabla \cdot \mathbf{B} = 0$ , gives the following equations. To  $O(\varepsilon_{zm})$  the perturbed magnetic field is incompressible in the short spatial coordinate,  $X$ ,

$$\nabla_{\mathbf{x}} \cdot \mathbf{B}_1 = 0.$$

The  $O(\varepsilon_{zm}^2)$  term

$$\frac{\partial B_{1z}}{\partial z} = 0,$$

shows that  $B_{1z}$  is independent of the long parallel coordinate,  $z$ .

The next step is to take the remaining equations which still need to be simplified and split them into the parallel and perpendicular components. Beginning with the  $O(1)$  momentum equation, Equation (A.8), the perpendicular and parallel components are

$$\begin{aligned} \frac{\partial \mathbf{v}_{\perp}}{\partial \tau} + (\mathbf{v}_{\perp} \cdot \nabla_{\mathbf{x}_{\perp}}) \mathbf{v}_{\perp} &= -\nabla_{\mathbf{x}_{\perp}} p_1 - \frac{1}{2} \nabla_{\mathbf{x}_{\perp}} (\mathbf{B}_{1\perp}) \\ &\quad + (\mathbf{B}_{1\perp} \cdot \nabla_{\mathbf{x}_{\perp}}) \mathbf{B}_{1\perp} + B_0 \frac{\partial \mathbf{B}_{1\perp}}{\partial z}, \end{aligned} \quad \star (\text{A.13})$$

$$\frac{\partial v_z}{\partial \tau} + (\mathbf{v}_{\perp} \cdot \nabla_{\mathbf{x}_{\perp}}) v_z = -\frac{\partial p_1}{\partial Z}, \quad (\text{A.14})$$

where  $\star$  means this is one of the final equations.

Next, the  $O(\varepsilon_{zm})$  momentum equation, Equation (A.9) the components are

$$\rho_1 \left( \frac{\partial \mathbf{v}_\perp}{\partial \tau} + (\mathbf{v}_\perp \cdot \nabla_{\mathbf{x}_\perp}) \mathbf{v}_\perp \right) + v_z \frac{\partial \mathbf{v}_\perp}{\partial z} = \mathbf{B}_{1z} \frac{\partial \mathbf{B}_{1\perp}}{\partial z}, \quad (\text{A.15})$$

$$\rho_1 \left( \frac{\partial v_z}{\partial \tau} + (\mathbf{v}_\perp \cdot \nabla_{\mathbf{x}_\perp}) v_z \right) + v_z \frac{\partial v_z}{\partial z} = - \frac{\partial p_1}{\partial z} - \frac{1}{2} \nabla_{\mathbf{x}} (\mathbf{B}_1^2). \quad (\text{A.16})$$

Now the  $O(\varepsilon_{zm})$  induction equation, Equation (A.11) can be written as

$$\frac{\partial}{\partial \tau} \mathbf{B}_1 + (\mathbf{v} \cdot \nabla_{\mathbf{x}}) \mathbf{B}_1 = B_0 \frac{\partial}{\partial z} \mathbf{v} + (\mathbf{B}_{1\perp} \cdot \nabla_{\mathbf{x}_\perp}) \mathbf{v} - B_0 \frac{\partial}{\partial z} v_z,$$

where the second last term has been updated to have perpendicular components only as  $\mathbf{v}$  was found to be independent of  $Z$ . The perpendicular and parallel components of this last equation are

$$\frac{\partial}{\partial \tau} \mathbf{B}_{1\perp} + (\mathbf{v} \cdot \nabla_{\mathbf{x}}) \mathbf{B}_{1\perp} = B_0 \frac{\partial}{\partial z} \mathbf{v}_\perp + (\mathbf{B}_{1\perp} \cdot \nabla_{\mathbf{x}_\perp}) \mathbf{v}_\perp, \quad (\text{A.17})$$

$$\frac{\partial}{\partial \tau} B_{1z} + (\mathbf{v} \cdot \nabla_{\mathbf{x}}) B_{1z} = (\mathbf{B}_{1\perp} \cdot \nabla_{\mathbf{x}_\perp}) v_z. \quad (\text{A.18})$$

The  $O(\varepsilon_{zm})$  induction equation, Equation (A.12) gives only an equation for the perpendicular components as

$$v_z \frac{\partial}{\partial z} \mathbf{B}_{1\perp} = B_{1z} \frac{\partial}{\partial z} \mathbf{v}_\perp - \mathbf{B}_{1\perp} \frac{\partial}{\partial z} v_z, \quad (\text{A.19})$$

The parallel component is zero since it was found that  $B_{1z}$  is independent of  $z$ .

These remaining equations, Equation (A.10), Equation (A.6) and Equations (A.13)-(A.19) are now in a form that we only require a few final arguments to obtain the equations of RMHD.

To satisfy the second order expansion of the momentum equation, Equation (A.10);  $\rho_1 v_z \frac{\partial}{\partial z} \mathbf{v} = 0$ , either  $\rho_1 = 0$ ,  $v_z = 0$  or  $\frac{\partial}{\partial z} \mathbf{v} = 0$ . It is chosen that  $\rho_1 = 0$  which immediately implies incompressibility.

Substituting  $\rho_1 = 0$  into the  $O(\varepsilon_{zm})$  continuity equation, Equation (A.6), leads to

$$\frac{\partial}{\partial z} v_z = 0, \quad \Rightarrow v_z = v_z(X, Y, \tau).$$

This implies that the parallel velocity is only a function of the short coordinates:  $X$  and  $Y$  and slow time coordinate,  $\tau$ .

Equation (A.16) now gives

$$\frac{\partial p_1}{\partial z} = - \frac{1}{2} \frac{\partial}{\partial z} (\mathbf{B}_{1\perp}^2). \quad \star (\text{A.20})$$

From Equations (A.19) and (A.15) we have

$$v_z \frac{\partial \mathbf{B}_{1\perp}}{\partial z} = B_{1z} \frac{\partial \mathbf{v}_\perp}{\partial z}, \quad B_{1z} \frac{\partial \mathbf{B}_{1\perp}}{\partial z} = v_z \frac{\partial \mathbf{v}_\perp}{\partial z}.$$

These last two equations imply that the parallel perturbed magnetic field is also a function of only the short spatial coordinates:  $X$  and  $Y$  and the slow time coordinate,  $\tau$ , as

$$v_z = \pm B_{1z} \Rightarrow B_{1z} = B_{1z}(X, Y, \tau).$$

Now taking  $\frac{\partial}{\partial Z}$  of Equation (A.18) gives

$$\left( \frac{\partial}{\partial Z} \mathbf{B}_{1\perp} \cdot \nabla_{\mathbf{x}_\perp} \right) v_z = 0.$$

It was suggested that this equation could be included as an additional constraint, however the authors felt there did not seem to be any advantage in doing so. Possible solutions are that  $\mathbf{B}_{1\perp}$  is independent of  $Z$  or that  $v_z$  is equal to a constant. The former is chosen but either solution arrives at the same result that  $v_z$  and  $B_{1z}$  are constant or zero. Perhaps if this term was retained it would allow the parallel components to be evolved.

Thus we have

$$\frac{\partial}{\partial Z} \mathbf{B}_{1\perp} = 0, \Rightarrow \mathbf{B}_{1\perp} = \mathbf{B}_{1\perp}(X, Y, z, \tau).$$

Hence Equation (A.17) becomes

$$\frac{\partial}{\partial \tau} B_{1\perp} + (\mathbf{v}_\perp \cdot \nabla_{\mathbf{x}_\perp}) \mathbf{B}_{1\perp} = B_0 \frac{\partial}{\partial z} \mathbf{v}_\perp + (\mathbf{B}_{1\perp} \cdot \nabla_{\mathbf{x}_\perp}) \mathbf{v}_\perp. \quad \star$$

It follows from Equation (A.20) that since  $\frac{\partial}{\partial Z} \mathbf{B}_{1\perp} = 0$  then  $p_1$  is independent of the short parallel coordinate,  $Z$ , as well.

$$p_1 = p_1(X, Y, z, \tau).$$

Since  $\mathbf{B}_1$  is independent of  $Z$  the  $O(\varepsilon_{zm}^{-1})$  momentum equation, Equation (A.7), now reads

$$\nabla_X B_{1z} = \nabla_{X_z} \mathbf{B} = 0, \Rightarrow \frac{\partial}{\partial X} B_{1z} = \frac{\partial}{\partial Y} B_{1z} = 0,$$

implying that  $B_{1z}$  is independent of the perpendicular short coordinates:  $X$  and  $Y$ . It has already been found that  $B_{1z}$  is independent of both the short and long parallel coordinates,  $Z$  and  $z$ , hence, at most  $B_{1z}$  is a function of the slow time coordinate,  $\tau$  as  $B_{1z} = B_{1z}(\tau)$ . It then follows that the same is true for the parallel velocity as  $v_z = v_z(\tau)$ .

Finally from Equation (A.14) we have

$$\frac{\partial}{\partial \tau} v_z = 0.$$

This gives the result that  $v_z$  and  $B_{1z}$  are constants which are assumed to be zero.

### Summary

The RMHD equations are given by

$$\begin{aligned} \nabla_{\mathbf{x}} \cdot \mathbf{v} &= 0, & \nabla_{\mathbf{x}} \cdot \mathbf{B} &= 0, & \mathbf{x} &= (x, y), \\ \frac{\partial \mathbf{v}}{\partial t} + (\mathbf{v} \cdot \nabla_{\mathbf{x}}) \mathbf{v} &= -\nabla_{\mathbf{x}} p - \frac{1}{2} \nabla_{\mathbf{x}} (\mathbf{B}^2) + (\mathbf{B} \cdot \nabla_{\mathbf{x}}) \mathbf{B} + \frac{B_0}{\varepsilon_{zm}} \frac{\partial}{\partial z} \mathbf{B}, \\ \frac{\partial \mathbf{B}}{\partial t} + (\mathbf{v} \cdot \nabla_{\mathbf{x}}) \mathbf{B} &= \frac{B_0}{\varepsilon_{zm}} \frac{\partial}{\partial z} \mathbf{v} + (\mathbf{B} \cdot \nabla_{\mathbf{x}}) \mathbf{v}, \\ \frac{\partial p}{\partial z} &= -\frac{1}{2} \frac{\partial \mathbf{B}^2}{\partial z}, \end{aligned}$$

where  $\mathbf{B} = (B_x(x, y, z, t), B_y(x, y, z, t))$  and  $\mathbf{v} = (v_x(x, y, z, t), v_y(x, y, z, t))$ .

## A.2 Montgomery's Derivation

Here we give the derivation of RMHD given by Montgomery 1982, which was summarised in Section 3.3.3. For this derivation the incompressible MHD equations are used from the outset. The system is considered to be permeated by a strong background magnetic field that is perturbed by fluctuations, hence the total magnetic field is  $\mathbf{B}_T = \mathbf{B}_0 + \mathbf{B}$ . The background magnetic field is assumed to be in the  $\hat{\mathbf{e}}_z$  direction. The author begins by assuming that the velocity and magnetic fluctuations are much smaller than the large constant background magnetic field. It follows that a small parameter,  $\varepsilon_m$ , can be introduced to show that the background field,  $\mathbf{B}_0$ , is much larger than the fluctuating field,

$$\varepsilon_m = \frac{b}{B_0}.$$

The total field can be written as

$$\mathbf{B}_T = \frac{\mathbf{B}_0}{\varepsilon_m} + \mathbf{B}.$$

Substituting the total magnetic field into the incompressible form of the momentum and induction equations, Equation (2.16a) and Equation (2.16c), gives

$$\frac{\partial \mathbf{v}}{\partial t} + \mathbf{v} \cdot \nabla \mathbf{v} = -\nabla p + \mathbf{B} \cdot \nabla \mathbf{B} + \frac{1}{\varepsilon_m} \mathbf{B}_0 \cdot \nabla \mathbf{B} + \nu \nabla^2 \mathbf{v}, \quad (\text{A.21})$$

$$\frac{\partial \mathbf{B}}{\partial t} + \mathbf{v} \cdot \nabla \mathbf{B} = \mathbf{B} \cdot \nabla \mathbf{v} + \frac{1}{\varepsilon_m} \mathbf{B}_0 \cdot \nabla \mathbf{v} + \eta \nabla^2 \mathbf{B}, \quad (\text{A.22})$$

The velocity and magnetic fields are now expanded as

$$\mathbf{B} = \mathbf{B}^{(0)} + \varepsilon_m \mathbf{B}^{(1)} + \varepsilon_m^2 \mathbf{B}^{(2)} \dots, \quad \mathbf{v} = \mathbf{v}^{(0)} + \varepsilon_m \mathbf{v}^{(1)} + \varepsilon_m^2 \mathbf{v}^{(2)} \dots.$$

The fields are taken to be incompressible at each order

$$\nabla \cdot \mathbf{v}^{(n)} = 0, \quad \nabla \cdot \mathbf{B}^{(n)} = 0 \quad n \geq 0.$$

Equations (A.21) and (A.22) involve terms for incompressible Alfvén waves. We are interested in the dynamics at  $O(1)$  and not on faster timescales hence time derivatives of interest are assumed to be  $O(1)$  as  $\frac{\partial \mathbf{v}^{(0)}}{\partial t} \sim \frac{\partial \mathbf{B}^{(0)}}{\partial t} \sim O(1)$ .

The  $O(\varepsilon_m^{-1})$  terms give

$$\mathbf{B}_0 \cdot \nabla \mathbf{B}^{(0)} = B_0 \frac{\partial \mathbf{B}^{(0)}}{\partial z} = 0,$$

$$\mathbf{B}_0 \cdot \nabla \mathbf{v}^{(0)} = B_0 \frac{\partial \mathbf{v}^{(0)}}{\partial z} = 0.$$

This does not necessarily imply that  $\mathbf{v}^{(0)}$  and  $\mathbf{B}^{(0)}$  are independent of  $z$  but shows that they are approximately constant in  $z$ , hence the variation could be over longer parallel scales. Thus at most these lowest order fluctuations depend weakly on  $z$  as  $\varepsilon_m z$ . Hence they vary in  $z$  much more slowly compared to the variations in the perpendicular  $x$  and  $y$  directions.

The incompressible condition at lowest order can now be written as

$$\nabla \cdot \mathbf{B}^{(0)} = 0 \quad \Rightarrow \quad \nabla_{\perp} \cdot \mathbf{B}_{\perp}^{(0)} = 0,$$

$$\nabla \cdot \mathbf{v}^{(0)} = 0 \quad \Rightarrow \quad \nabla_{\perp} \cdot \mathbf{v}_{\perp}^{(0)} = 0.$$

This does not mean that  $v_z^{(0)}$  or  $B_z^{(0)}$  are equal to zero or that they are independent of  $\varepsilon_m z$ . This implies that the perpendicular components are incompressible. This allows the fluctuating fields to be written in terms of potentials as

$$\mathbf{B}_{\perp}^{(0)} = \nabla \times \hat{\mathbf{e}}_z A = \nabla_{\perp} A \times \hat{\mathbf{e}}_z, \tag{A.23}$$

$$\mathbf{v}_{\perp}^{(0)} = \nabla \times \hat{\mathbf{e}}_z \phi = \nabla_{\perp} \phi \times \hat{\mathbf{e}}_z, \tag{A.24}$$

where  $A(x, y, \varepsilon_m z, t)$  is the magnetic potential and  $\phi(x, y, \varepsilon_m z, t)$  is the velocity stream function.

The evolution of the perpendicular fields,  $\mathbf{v}_{\perp}^{(0)}$  and  $\mathbf{B}_{\perp}^{(0)}$ , are given by the  $O(1)$

terms in the momentum and induction equation, Equation (A.21) and Equation (A.22), are

$$\begin{aligned} \frac{\partial \mathbf{v}_{\perp}^{(0)}}{\partial t} + \frac{\partial \mathbf{v}_{\perp}^{(1)}}{\partial t/\varepsilon_m} + \mathbf{v}_{\perp}^{(0)} \cdot \nabla_{\perp} \mathbf{v}_{\perp}^{(0)} = & -\nabla_{\perp} p^{(0)} + \mathbf{B}_{\perp}^{(0)} \cdot \nabla_{\perp} \mathbf{B}_{\perp}^{(0)} \\ & + B_0 \frac{\partial \mathbf{B}_{\perp}^{(0)}}{\partial(\varepsilon_m z)} + B_0 \frac{\partial \mathbf{B}_{\perp}^{(1)}}{\partial z} + \nu \nabla_{\perp}^2 \mathbf{v}_{\perp}^{(0)}, \end{aligned} \quad (\text{A.25})$$

$$\begin{aligned} \frac{\partial \mathbf{B}_{\perp}^{(0)}}{\partial t} + \frac{\partial \mathbf{B}_{\perp}^{(1)}}{\partial t/\varepsilon_m} + \mathbf{v}_{\perp}^{(0)} \cdot \nabla_{\perp} \mathbf{B}_{\perp}^{(0)} = & \mathbf{B}_{\perp}^{(0)} \cdot \nabla_{\perp} \mathbf{v}_{\perp}^{(0)} + B_0 \frac{\partial \mathbf{v}_{\perp}^{(0)}}{\partial(\varepsilon_m z)} \\ & + B_0 \frac{\partial \mathbf{v}_{\perp}^{(1)}}{\partial z} + \eta \nabla_{\perp}^2 \mathbf{B}_{\perp}^{(0)}. \end{aligned} \quad (\text{A.26})$$

The terms involving first order fields,  $\mathbf{v}_{\perp}^{(1)}$  and  $\mathbf{B}_{\perp}^{(1)}$ , relate to a fast Alfvén wave dependence on  $z$  and  $t/\varepsilon_m$ . The zeroth order terms vary on the slower variables  $\varepsilon_m z$  and  $t$ .

This fast variation is averaged out by averaging these equations over an interval  $\Delta z \Delta t / \varepsilon_m$  that is large enough that these terms drop out, while the interval is still small enough that there is no effect on the other terms which vary on the slow scales,  $\varepsilon_m z$  and  $t$ . This is an alternate method to applying multiple time scales but is equivalent to time scalings used by Zank and Matthaeus discussed in A.1 and Zank and Matthaeus 1992.

The averaged perpendicular equations are

$$\frac{\partial \mathbf{v}_{\perp}^{(0)}}{\partial t} + \mathbf{v}_{\perp}^{(0)} \cdot \nabla_{\perp} \mathbf{v}_{\perp}^{(0)} = -\nabla_{\perp} p^{(0)} + \mathbf{B}_{\perp}^{(0)} \cdot \nabla_{\perp} \mathbf{B}_{\perp}^{(0)} + B_0 \frac{\partial \mathbf{B}_{\perp}^{(0)}}{\partial(\varepsilon_m z)} + \nu \nabla_{\perp}^2 \mathbf{v}_{\perp}^{(0)}, \quad (\text{A.27})$$

$$\frac{\partial \mathbf{B}_{\perp}^{(0)}}{\partial t} + \mathbf{v}_{\perp}^{(0)} \cdot \nabla_{\perp} \mathbf{B}_{\perp}^{(0)} = \mathbf{B}_{\perp}^{(0)} \cdot \nabla_{\perp} \mathbf{v}_{\perp}^{(0)} + B_0 \frac{\partial \mathbf{v}_{\perp}^{(0)}}{\partial(\varepsilon_m z)} + \eta \nabla_{\perp}^2 \mathbf{B}_{\perp}^{(0)}. \quad (\text{A.28})$$

These equations are equivalent to the Strauss' RMHD equations, Equations (3.12) on page 34 discussed in Section 3.3.1. The equivalence is made explicit by using the potentials,  $A$  and  $\phi$ , as

$$\frac{\partial \omega}{\partial t} + \mathbf{v}_{\perp}^{(0)} \cdot \nabla_{\perp} \omega = \mathbf{B}_{\perp}^{(0)} \cdot \nabla_{\perp} j + B_0 \frac{\partial j}{\partial z} + \nu \nabla_{\perp}^2 \omega, \quad (\text{A.29})$$

$$\frac{\partial A}{\partial t} + \mathbf{v}_{\perp}^{(0)} \cdot \nabla_{\perp} A = B_0 \frac{\partial \phi}{\partial z} + \eta \nabla_{\perp}^2 A, \quad (\text{A.30})$$

where the  $z$  components of current and vorticity are given by  $j = \nabla^2 A$  and  $\omega = \nabla^2 U$ , respectively. A notable difference in this derivation is that the parallel fields,  $v_z$  and  $B_z$ , are not assumed to be constant.

The evolution of the lowest order parallel fluctuations,  $v_z^{(0)}$  and  $B_z^{(0)}$ , is given by

$$\frac{\partial v_z^{(0)}}{\partial t} + \mathbf{v}_{\perp}^{(0)} \cdot \nabla_{\perp} v_z^{(0)} = \mathbf{B}_{\perp}^{(0)} \cdot \nabla_{\perp} B_z^{(0)} + B_0 \frac{\partial B_z^{(0)}}{\partial z} + \nu \nabla_{\perp}^2 v_z^{(0)}, \quad (\text{A.31})$$

$$\frac{\partial B_z^{(0)}}{\partial t} + \mathbf{v}_{\perp}^{(0)} \cdot \nabla_{\perp} B_z^{(0)} = \mathbf{B}_{\perp}^{(0)} \cdot \nabla_{\perp} v_z^{(0)} + B_0 \frac{\partial v_z^{(0)}}{\partial z} + \eta \nabla_{\perp}^2 B_z^{(0)}. \quad (\text{A.32})$$



These equations are linear in  $B_z^{(0)}$  and  $v_z^{(0)}$  and only have coefficients of  $\mathbf{B}_\perp^{(0)}$  and  $\mathbf{v}_\perp^{(0)}$ . Hence the  $z$  component of the fluctuations is determined automatically once the perpendicular components are known. This behaviour is much like a 'passive scalar', as the parallel components do not affect the other quantities. This shows that it is not necessary to set  $v_z^{(0)} = 0$  or  $B_z^{(0)} = 0$ . The dynamics of  $\mathbf{v}_\perp^{(0)}$  and  $\mathbf{B}_\perp^{(0)}$  are unaffected by these assumptions since they are independent of  $v_z^{(0)}$  and  $B_z^{(0)}$ .

### A.3 Van Ballegooijen's Equilibrium Derivation of RMHD

Here we discuss an independent derivation of RMHD by van Ballegooijen 1985. Although the resulting equation for the velocity does not look like the classic equation of RMHD, the assumptions for this model are the same. This article is particularly interesting as the RMHD equations are derived from an entirely different perspective: from the point of view of equilibria. Here we shall continue to use the expansion parameters;  $\varepsilon_a$ ,  $\varepsilon_b$ , and generally the same notation used in the formal derivation of RMHD in Section 3.4.1. The magnetic field is expanded up to  $O(\varepsilon_a)$  as

$$\begin{aligned} \mathbf{B} &= \frac{B'_0}{\varepsilon_a} \hat{\mathbf{e}}_z + \mathbf{b}' + \varepsilon_a \mathbf{b}'_1, \\ &= \frac{B'_0}{\varepsilon_a} \hat{\mathbf{e}}_z + \nabla h \times \hat{\mathbf{e}}_z + \varepsilon_a \nabla \times (\nabla g \times \hat{\mathbf{e}}_z). \end{aligned} \quad (\text{A.33})$$

Thus  $h$  is the  $z$  component of the vector potential, the component traditionally used in RMHD and usually denoted by  $A$ .  $\nabla g \times \hat{\mathbf{e}}_z$  are the perpendicular components of the vector potential, which are higher order and usually neglected in RMHD.

The magnetic field components of Equation (A.33) are

$$\begin{aligned} B_x &= \frac{\partial h}{\partial y} + \varepsilon_a \varepsilon_b \frac{\partial^2 g}{\partial x \partial z}, \\ B_y &= -\frac{\partial h}{\partial x} + \varepsilon_a \varepsilon_b \frac{\partial^2 g}{\partial y \partial z}, \\ B_z &= \frac{B'_0}{\varepsilon_a} - \varepsilon_a \frac{\partial^2 g}{\partial x^2} - \varepsilon_a \frac{\partial^2 g}{\partial y^2}, \end{aligned}$$

where the slowly varying  $z$  coordinate,  $z/\varepsilon_b$  has been used as before. An immediate consequence of including the  $O(\varepsilon_a)$  and  $O(\varepsilon_a \varepsilon_b)$  terms is that there is a perpendicular current. A perpendicular current only comes in at higher order in RMHD. This is in contrast to the original RMHD model which keeps only lowest order terms and only has a parallel current component. The current is

$$j_x = \varepsilon_b \frac{\partial^2 h}{\partial x \partial z} + \varepsilon_a \frac{\partial f}{\partial y}, \quad j_y = \varepsilon_b \frac{\partial^2 h}{\partial y \partial z} - \varepsilon_a \frac{\partial f}{\partial x}, \quad j_z = -\left( \frac{\partial^2 h}{\partial x^2} + \frac{\partial^2 h}{\partial y^2} \right),$$

where  $f = \nabla_\perp^2 g$ .

As is common in RMHD pressure is neglected. The momentum equation, Equation (2.17a), is considered for the case of a force-free equilibrium. Using  $\mathbf{v} = \mathbf{p} = 0$ , the MHD equilibrium condition is then

$$\mathbf{j} \times \mathbf{B} = 0 \Rightarrow \mathbf{j} = \nabla \times \mathbf{B} = \alpha \mathbf{B}. \quad (\text{A.34})$$

$\alpha(x, y, z, t)$  is a measure of the twist of the magnetic fieldlines and  $\alpha \sim \frac{1}{l_{\parallel}}$ . Thus  $\alpha$  is rescaled as  $\alpha = \varepsilon_b \alpha'$ . In components Equation (A.34) is

$$\begin{aligned} \varepsilon_b \frac{\partial^2 h}{\partial x \partial z} + \varepsilon_a \frac{\partial f}{\partial y} &= \varepsilon_b \alpha' \left( \frac{\partial h}{\partial y} + \varepsilon_a \varepsilon_b \frac{\partial^2 g}{\partial x \partial z} \right), \\ \varepsilon_b \frac{\partial^2 h}{\partial y \partial z} - \varepsilon_a \frac{\partial f}{\partial x} &= \varepsilon_b \alpha' \left( -\frac{\partial h}{\partial x} + \varepsilon_a \varepsilon_b \frac{\partial^2 g}{\partial y \partial z} \right), \\ -\left( \frac{\partial^2 h}{\partial x^2} + \frac{\partial^2 h}{\partial y^2} \right) &= \varepsilon_b \alpha' \left( \frac{B'_0}{\varepsilon_a} - \varepsilon_a \frac{\partial^2 g}{\partial x^2} - \varepsilon_a \frac{\partial^2 g}{\partial y^2} \right). \end{aligned}$$

Keeping terms that are  $O(\varepsilon_a)$  or  $O(\varepsilon_b)$  and neglecting  $O(\varepsilon_a \varepsilon_b)$  or higher these reduce to

$$\varepsilon_b \frac{\partial^2 h}{\partial x \partial z} + \varepsilon_a \frac{\partial f}{\partial y} = \varepsilon_b \alpha' \left( \frac{\partial h}{\partial y} \right), \quad (\text{A.35})$$

$$\varepsilon_b \frac{\partial^2 h}{\partial y \partial z} - \varepsilon_a \frac{\partial f}{\partial x} = \varepsilon_b \alpha' \left( -\frac{\partial h}{\partial x} \right), \quad (\text{A.36})$$

$$-\left( \frac{\partial^2 h}{\partial x^2} + \frac{\partial^2 h}{\partial y^2} \right) = \varepsilon_b \alpha' \left( \frac{B'_0}{\varepsilon_a} \right), \quad (\text{A.37})$$

Differentiating Equation (A.35) with  $x$  and differentiating Equation (A.36) with  $y$  and adding them together and using Equation (A.37) gives the relation

$$\varepsilon_b \left( \frac{\varepsilon_b}{\varepsilon_a} B'_0 \right) \frac{\partial \alpha'}{\partial z} = \varepsilon_b \frac{\partial \alpha'}{\partial y} \frac{\partial h}{\partial x} - \varepsilon_b \frac{\partial \alpha'}{\partial x} \frac{\partial h}{\partial y}. \quad (\text{A.38})$$

The system can be evolved by taking the time derivative of Equation (A.38)

$$\begin{aligned} \varepsilon_b \left( \frac{\varepsilon_b}{\varepsilon_a} B'_0 \right) \frac{\partial}{\partial z} \frac{\partial \alpha'}{\partial t} &= \varepsilon_b \left( \frac{\partial}{\partial y} \frac{\partial \alpha'}{\partial t} \right) \frac{\partial h}{\partial x} - \varepsilon_b \left( \frac{\partial}{\partial x} \frac{\partial \alpha'}{\partial t} \right) \frac{\partial h}{\partial y} \\ &\quad + \varepsilon_b \frac{\partial \alpha'}{\partial y} \left( \frac{\partial}{\partial x} \frac{\partial h}{\partial t} \right) - \varepsilon_b \frac{\partial \alpha'}{\partial x} \left( \frac{\partial}{\partial y} \frac{\partial h}{\partial t} \right). \end{aligned} \quad (\text{A.39})$$

The integrated induction equation, Equation (2.17c), can be written in the same

way as RMHD, using  $\mathbf{v} = \nabla\phi \times \hat{\mathbf{e}}_z$ , as

$$\begin{aligned}\frac{\partial h}{\partial t} &= B_0 \left( \frac{\varepsilon_b}{\varepsilon_a} \right) \frac{\partial \phi}{\partial z} + \frac{\partial h}{\partial y} \frac{\partial \phi}{\partial x} - \frac{\partial h}{\partial x} \frac{\partial \phi}{\partial y} \\ &= B_0 \left( \frac{\varepsilon_b}{\varepsilon_a} \right) \frac{\partial \phi}{\partial z} + Q, \\ Q &= \frac{\partial h}{\partial y} \frac{\partial \phi}{\partial x} - \frac{\partial h}{\partial x} \frac{\partial \phi}{\partial y}.\end{aligned}\tag{A.40}$$

Finally, Equations (A.40) and (A.37) can be substituted into Equation (A.39) to get the final equation for  $\phi$  given by

$$\begin{aligned}\varepsilon_b \frac{\partial}{\partial z} \left( \frac{\partial}{\partial z} (D\phi) + DQ \right) - \varepsilon_b \left( \frac{\partial}{\partial y} \left( \frac{\partial}{\partial z} (D\phi) + DQ \right) \right) \frac{\partial h}{\partial x} \\ + \varepsilon_b \left( \frac{\partial}{\partial x} \left( \frac{\partial}{\partial z} (D\phi) + DQ \right) \right) \frac{\partial h}{\partial y} \\ + \varepsilon_b \frac{\partial \alpha'}{\partial y} \left( \frac{\partial}{\partial x} \left( \frac{\partial \phi}{\partial z} + Q \right) \right) - \varepsilon_b \frac{\partial \alpha'}{\partial x} \left( \frac{\partial}{\partial y} \left( \frac{\partial \phi}{\partial z} + Q \right) \right),\end{aligned}\tag{A.41}$$

where  $D = \nabla_\perp^2$  has been used.

This equation can be solved for  $\phi$  with boundary conditions at both loop ends  $\phi(x, y, 0, t)$  and  $\phi(x, y, L, t)$  and initial conditions for  $\alpha'$  and  $h$ . Once  $\phi$  is known for a certain  $t$  the magnetic field is evolved in time using Equation (A.40) and  $\alpha'$  is calculated from Equation (A.37). Since the final equation for  $\phi$  is  $O(\varepsilon_b)$  and considering that, when using this ordering, RMHD is normally taken to  $O(1)$ , it is clear that this provides a version of RMHD that is higher order. This form of the equation for  $\phi$  can only be derived when these higher order terms are retained. The central role of the force-free equilibrium condition makes this model appear very similar to other approximate models of MHD equilibria, namely magneto-frictional methods discussed in Section 4.2.3. The main difference in these models is that the velocity is made equal to the unbalanced Lorentz force and therefore is not evolved dynamically. It is also important to remember that magneto-frictional methods are used to solve a general field so no expansion about a strong background field or lengthscale considerations are needed. Further investigation into the validity of RMHD is necessary as well as the similarity between classic RMHD and magneto-frictional methods. Another aspect, which is common in RMHD is that the background field does not change. Although the field was initially expanded to  $O(\varepsilon_a)$  these terms create higher order terms in the equations which are subsequently neglected. It is shown in another study, Scheper and Hassam 1999, that the equations involving the next order for  $B_z$  are not compatible with line-tied boundary conditions. However, this only affects the parallel fluctuations, while perpendicular components remain unaffected at lower order. This is not an issue when these parallel fluctuations are neglected.

## Appendix B

### Similar Methods

#### B.1 Kruger et al: Generalised RMHD

In this section an overview of a general model of RMHD is given which was presented by Kruger, Hegna, and Callen 1998. This model is more general than RMHD as it does not require a large aspect ratio and does not assume a constant background magnetic field. Pressure and density are also evolved. This derivation uses a multiple-time scale method to separate the timescales related to the equilibrium and parallel and perpendicular wavenumbers. This allows for a more natural form of energy conservation than is found in the original derivation. Some higher order terms seem to be retained to achieve this. It is unclear if this is valid. This article also includes the total and electron stress tensors but these are neglected here for simplicity. This derivation aims to look at perpendicular modes which are small compared to the parallel equilibrium scale length

$$\frac{\lambda_{\perp}}{\lambda_{\parallel}} \sim \varepsilon_s.$$

Thus assuming lengthscale or spectral anisotropy. This is similar to Strauss' derivation (Strauss 1976 and Section 3.3.1) hence this is denoted by  $\varepsilon_s$ . Note, however that Strauss does define the small parameter to be the inverse aspect ratio of the system rather than the ratio of characteristic lengthscales or wavelengths.

All equilibrium quantities are  $O(1)$  and are functions of space and time, including the background magnetic field, as  $B_0 = B_0(\mathbf{x}, t)$ . The perturbed quantities will vary on different spatial and time scales. In contrast to previous approaches, the coordinates are scaled as

$$\mathbf{x} = \frac{\mathbf{x}_{\perp}}{\varepsilon_s} + x_{\parallel}, \quad t = \frac{t_{\perp}}{\varepsilon_s}.$$

Thus we define quantities of  $O(\varepsilon_s)$  as

$$\mathbf{v}_1 = \mathbf{v}_1 \left( \frac{\mathbf{x}_{\perp}}{\varepsilon_s}, x_{\parallel}, \frac{t_{\perp}}{\varepsilon_s}, t_{\parallel} \right).$$

Derivatives of these quantities are

$$\frac{\partial}{\partial t} \mathbf{v}_1 = \left( \frac{1}{\varepsilon_s} \frac{\partial}{\partial t_\perp} + \frac{\partial}{\partial t_\parallel} \right) \mathbf{v}_1, \quad \nabla \cdot \mathbf{v}_1 = \left( \frac{1}{\varepsilon_s} \nabla_\perp + \nabla_\parallel \right) \cdot \mathbf{v}_1.$$

This separates the different lengthscales and timescales, highlighting that the perpendicular variations are larger than parallel ones. The expansion

$$\rho = \rho_0 + \varepsilon_s \rho_1, \quad p = p_0 + \varepsilon_s p_1, \quad \mathbf{B} = \mathbf{B}_0 + \varepsilon_s \mathbf{B}_1, \quad \eta \sim \varepsilon_s^2, \quad \mathbf{v} = \varepsilon_s \mathbf{v}_1.$$

is applied to the MHD equations, Equations (2.9a)-(2.9d), with the right hand side of the energy equation equal to  $(\gamma - 1)\eta \mathbf{j}^2$ .

The final equations of this model are given by

$$\begin{aligned} \frac{d\rho_1}{dt_\parallel} + (\mathbf{v}_1 \cdot \nabla) \rho_0 + \rho_T \nabla \cdot \mathbf{v}_1 &= 0, \\ \frac{dp_1}{dt_\parallel} + (\mathbf{v}_1 \cdot \nabla) p_0 + \gamma p_T (\nabla \cdot \mathbf{v}) &= (\gamma - 1) \eta \left( J_{T\parallel}^2 + \frac{|\nabla p_T|^2}{B_0^2} \right), \\ \rho_T \frac{dv_\parallel}{dt_\parallel} &= -\mathbf{b}_0 \cdot \nabla p_1 - \mathbf{b}_1 \cdot \nabla p_T, \\ \frac{\partial \Psi}{\partial t_\parallel} - \mathbf{b}_T \cdot \nabla \phi &= \eta \tilde{j}_\parallel, \\ \nabla \cdot \left( \frac{\rho_T}{B_0} \frac{d}{dt_\parallel} \nabla \frac{\phi}{B_0} \right) &= (\mathbf{B}_0 \cdot \nabla) \frac{\tilde{j}_\parallel}{B_0} + (\mathbf{B}_1 \cdot \nabla) \frac{j_{T\parallel}}{B_0} \\ &\quad + \nabla \cdot \frac{\mathbf{B}_0 \times \nabla p_1}{B_0^2} + \nabla \cdot \frac{p_1 \mathbf{B}_0 \times \nabla p_T}{B_0^2}, \end{aligned}$$

where

$$\begin{aligned} \mathbf{B}_T &= \mathbf{B}_0 + \mathbf{B}_1, & \mathbf{b} &= \frac{\mathbf{B}_T}{B_0}, \\ j_{T\parallel} &= j_{\parallel 0} + \tilde{j}_\parallel = \mathbf{b}_0 \cdot (\nabla \times \mathbf{B}_0) + \nabla^2 \psi, & \Psi &= -\mathbf{A}_2 \cdot \mathbf{b}_0 = -A_{2\parallel}, \\ \rho_T &= \rho_0 + \rho_1, & p_T &= p_0 + p_1, \\ \mathbf{v}_1 &= \frac{\mathbf{B}_0 \times \nabla \phi}{B_0^2} + \frac{p_1 \mathbf{B}_0 \times \nabla \phi}{B_0^2} + v_\parallel \mathbf{b}_T - \eta \frac{\nabla p_T}{B_0^2}. \end{aligned}$$

$\phi$  is the electric potential and  $A_2$  is the magnetic potential given by

$$\begin{aligned} \phi &= \varepsilon_s^2 \phi, \\ \mathbf{A} &= \mathbf{A}_0 + \varepsilon_s^2 \mathbf{A}_2. \end{aligned}$$

The electric and magnetic fields in terms of these potentials as

$$\mathbf{E} = -\nabla\phi - \frac{\partial\mathbf{A}}{\partial t} = -\varepsilon_s\nabla_\perp\phi + \varepsilon_s^2\left(-\nabla_\parallel\phi - \frac{\partial\mathbf{A}_2}{\partial t_\parallel}\right),$$

$$\mathbf{B} = \nabla \times \mathbf{A} = \nabla \times \mathbf{A}_0 + \varepsilon_s\nabla_\perp \times \mathbf{A}_2.$$

## B.2 Gazol et al: RMHD including Alfvén dynamics

Here an overview of an extension of RMHD to include coupling to Alfvén waves, originally derived by Gazol, Passot, and Sulem 1999, is given. It is well known that a large constant background magnetic field has two effects. Firstly, Alfvén waves propagate along the field and secondly the large-scale transverse dynamics become two-dimensional. Generally these two consequences are treated separately, however, this study investigates a unified set of equations. The specific magnitude of  $\beta$  considered is not clear but this article is in the context of the interstellar medium. The Hall term is included in this study but is neglected here for simplicity and  $p = \rho^\gamma$  is assumed. The background magnetic field is assumed to be in the  $x$  direction,  $\mathbf{B}_0 = B_x\hat{\mathbf{e}}_x$ . The magnetic field consists of a strong magnetic field and small fluctuations. The expansion parameter is defined as  $\varepsilon = M_A^2$ . Since  $\varepsilon$  is the square of the Alfvén mach number the leading order perpendicular components of  $\mathbf{v}$  and  $\mathbf{B}$  are of order  $\varepsilon^{1/2}$ . This is equivalent to Zank and Matthaeus' small parameter,  $\varepsilon_{zm} = M_A$  (Zank and Matthaeus 1992 and Section 3.3.2).

Longitudinal components of  $\mathbf{v}$  and  $\mathbf{B}$  and fluctuations of density  $\rho_1$  are of order  $\varepsilon$ . This would be equivalent to  $\varepsilon_{zm}^2$  and is hence higher order and not usually included in RMHD. As usual this shows that variations parallel to the background field occur on a much larger scale and the time and spatial coordinates need to be rescaled accordingly. In order to investigate the balance between nonlinearities and dispersion for the Alfvén waves dynamics it is simplest to work in the reference frame travelling with the Alfvén phase velocity  $v_A = 1$ . Hence a coordinate transform is used of the form

$$X = \varepsilon(x - t), \quad Y = \varepsilon^{3/2}y, \quad Z = \varepsilon^{3/2}z, \quad \tau = \varepsilon^2t.$$

A similar transform is used in special relativity. It follows that derivatives have the form

$$\frac{\partial}{\partial x} = \varepsilon \frac{\partial}{\partial X} + \frac{\partial}{\partial t}, \quad \frac{\partial}{\partial t} = \frac{\partial}{\partial x} - \varepsilon \frac{\partial}{\partial X}, \quad \frac{\partial}{\partial y} = \varepsilon^{3/2} \frac{\partial}{\partial Y}, \quad \frac{\partial}{\partial z} = \varepsilon^{3/2} \frac{\partial}{\partial Z}.$$

The expansion is used

$$\begin{aligned} \rho &= 1 + \varepsilon\rho_1 + \varepsilon^2\rho_2 + \varepsilon^3\rho_3 \dots, & v_x &= \varepsilon v_{x1} + \varepsilon^2 v_{x2} + \varepsilon^3 v_{x3} \dots, \\ b_x &= 1 + \varepsilon b_{x1} + \varepsilon^2 b_{x2} + \varepsilon^3 b_{x3} \dots, & \mathbf{v}_\perp &= \varepsilon^{1/2} (\mathbf{v}_1 + \varepsilon \mathbf{v}_2 + \varepsilon^2 \mathbf{v}_3 \dots), \\ \mathbf{B}_\perp &= \varepsilon^{1/2} (\mathbf{B}_1 + \varepsilon \mathbf{B}_2 + \varepsilon^2 \mathbf{B}_3 \dots), \\ \mathbf{B}_\parallel &= B_y + iB_z, \quad \mathbf{v}_\parallel = v_y + iv_z, \end{aligned}$$

It is believed that this ordering is to separate the 2D perpendicular dynamics (i.e RMHD) and parallel Alfvén dynamics and keep them individual but coupled. To maintain the coupling the first order perpendicular fields are defined to include mean and fluctuating contributions.

$$\mathbf{B}_1 = \tilde{\mathbf{B}}_1(X, Y, Z, \tau) + \overline{\mathbf{B}}_1(Y, Z, \tau),$$

$$\mathbf{V}_1 = \tilde{\mathbf{v}}_1(X, Y, Z, \tau) + \overline{\mathbf{v}}_1(Y, Z, \tau),$$

where  $\tilde{\phantom{x}}$  denotes the fluctuations and overline donotes the mean contribution which are averaged over  $X$ . It is the large-scale mean values that follow the essentially 2D dynamics. These are equal to RMHD modes in the 2D limit: averaged over the parallel field direction. This is also done for the parallel fields,  $v_x$  and  $B_x$ .

### Summary

The final set of equations, renaming  $\mathbf{B} = \mathbf{B}_1$ ,  $\mathbf{v} = \mathbf{v}_1$ ,  $B_x = B_{x1}$  and  $v_x = v_{x1}$ , are The equations of this model are

$$\frac{\partial \tilde{\mathbf{B}}}{\partial \tau} + \frac{\partial}{\partial X} \left( \frac{1}{2} (\tilde{\mathbf{B}} + \overline{\mathbf{B}}) \tilde{P} + \left( \overline{v_x} + \frac{1}{2} \overline{B_x} - \frac{1}{2} \overline{\delta} \right) \tilde{\mathbf{B}} \right)$$

$$- \frac{1}{2} \nabla_{\perp} \tilde{P} + (\overline{\mathbf{v}} + \overline{\mathbf{B}}) \cdot \nabla_{\perp} \tilde{\mathbf{B}} + \frac{i}{2R_l} \frac{\partial^2 \tilde{\mathbf{B}}}{\partial X^2} = 0,$$

$$\frac{\partial \overline{v_x}}{\partial \tau} + \nabla_{\perp} \cdot (\overline{v_x} \overline{\mathbf{v}} - \overline{B_x} \overline{\mathbf{B}}) = \frac{1}{2} \left( \nabla_{\perp}^* \langle \tilde{\mathbf{B}} \tilde{P} \rangle + \nabla_{\perp} \langle \tilde{\mathbf{B}} \tilde{P} \rangle^* \right),$$

$$\frac{\partial \overline{\delta}}{\partial \tau} + \nabla_{\perp} \cdot (\overline{\delta} \overline{\mathbf{v}} + \overline{v_x} \overline{\mathbf{B}}) = 0,$$

$$\nabla_{\perp}^2 \left( (1 + \beta) \overline{B_x} + \beta \overline{\delta} + \left\langle \frac{|\tilde{\mathbf{B}}|^2}{2} \right\rangle \right) + \nabla_{\perp} \cdot (\overline{\mathbf{v}} \cdot \nabla_{\perp} \overline{\mathbf{v}} - \overline{\mathbf{B}} \cdot \nabla_{\perp} \overline{\mathbf{B}}) = 0,$$

$$\frac{\partial \overline{\mathbf{B}}}{\partial \tau} - \nabla_{\perp} \times (\overline{\mathbf{v}} \times \overline{\mathbf{B}}) = 0,$$

$$\frac{\partial \overline{\mathbf{v}}}{\partial \tau} + \overline{\mathbf{v}} \cdot \nabla_{\perp} \overline{\mathbf{v}} = -\nabla p + \overline{\mathbf{B}} \cdot \nabla_{\perp} \overline{\mathbf{B}},$$

$$\nabla_{\perp} \cdot \overline{\mathbf{v}} = 0, \quad \nabla_{\perp} \cdot \overline{\mathbf{B}} = 0,$$

These last three equations provide the 2D incompressible dynamics in planes perpendicular to the mean field. These are also related to RMHD when neglecting variations in the parallel direction.

The quantities used in these equations are

$$\begin{aligned}\tilde{P} &= \frac{1}{2(\beta - 1)} \left( 2\widetilde{B_{x1}} + |\widetilde{\mathbf{B}_1} + \overline{\mathbf{B}_1}|^2 - \langle |\widetilde{\mathbf{B}_1} + \overline{\mathbf{B}_1}|^2 \rangle \right). \\ \bar{\delta} &= \bar{\rho} - \overline{B_x}, \\ \nabla_{\perp} &= \frac{\partial}{\partial y} + i \frac{\partial}{\partial z}.\end{aligned}$$

In the next section a model including slow wave dynamics by Zhukov 2001 is summarised.

### B.3 Zhukov: RMHD including slow waves

Here an overview of an interesting model presented in Zhukov 2001 is given. This model is called a “slow” MHD model since it is argued to be equivalent to RMHD with allowance for slow magnetosonic waves. The interesting aspect of this model is that the final induction equation has the same form as in RMHD using a different approach that does not require the velocity to be incompressible. No fundamental assumptions about the velocity are made, thus allowing for slow waves. A cylindrical coordinate system  $(r, \phi, z)$  is used. A possible and interesting extension of this model would be to investigate whether it is possible to rederive these equations in cartesian coordinates.

A toroidal metric is chosen, given by

$$\begin{aligned}dl^2 &= dr^2 + r^2 d\phi^2 + g(r, \phi)^2 dz^2, \\ h_r &= 1 \quad h_{\phi} = r \quad h_z = g(r, \phi), \\ g(r, \phi) &= 1 + \frac{r}{R} \cos(\phi).\end{aligned}$$

Plasma bounded at  $r = 1$  is considered. The poloidal velocity and magnetic fields are denoted by  $\mathbf{V}$  and  $\mathbf{B}$  and the toroidal fields are given by  $V_z$  and  $B_z$ , where

$$B_z = \frac{g^{-1} \langle B_z \rangle}{\langle g^{-1} \rangle} + h_z,$$

The following ordering is taken

$$O(1) : \quad \nabla, \rho, \quad O(R^{-1}) : \quad \frac{\partial}{\partial z}, \frac{\partial}{\partial t}, \mathbf{V}, \mathbf{B}, V_z, \quad O(R^{-2}) : \quad h_z, \rho.$$

where here  $R$  is the ratio of the poloidal and toroidal magnetic fields. Solutions are found with accuracies of the order

$$O(R^{-2}) : \quad \mathbf{B}, \mathbf{V}, p \quad O(R^{-1}) : \quad \langle B_z \rangle, V_z, \rho.$$

$\nu$  and  $\eta$  are taken to be constant. It is also required that  $\nu$ ,  $\eta$  and  $\nabla g$  are less than or equal to  $O(R^{-1})$ .



The  $z$  component of the vector potential is defined as usual to give the magnetic and electric fields as

$$\mathbf{B} = \nabla \times (A \hat{\mathbf{e}}_z), \quad E_z = -\frac{\partial A}{\partial t}.$$

In summary, the final equations of this model, which is known as SMHD (slow MHD), are

$$\begin{aligned} \frac{\partial}{\partial r} (r (B_z V_r - B_r V_z)) + \frac{\partial}{\partial \phi} (B_z V_\phi - B_\phi V_z) &= 0, \\ \frac{\partial A}{\partial t} &= \frac{1}{B_z} (\mathbf{B} \cdot \nabla) \Phi + \eta \nabla_\perp^2 A, \\ \rho \left( \frac{\partial V_z}{\partial t} + (\mathbf{V} \cdot \nabla) V_z + \frac{V_z V_r}{g} \frac{\partial g}{\partial r} + \frac{V_z V_\phi}{gr} \frac{\partial g}{\partial \phi} \right) &= -\frac{1}{g} \frac{\partial}{\partial z} \left( p + \frac{B_r^2}{2} + \frac{B_\phi^2}{2} \right) \\ &\quad + j_r B_\phi - j_\phi B_r + \eta \nabla_\perp^2 V_z, \\ \rho \left( \frac{\partial V_r}{\partial t} + (\mathbf{V} \cdot \nabla) V_r - \frac{V_\phi^2}{r} \right) &= F_r, \\ \rho \left( \frac{\partial V_\phi}{\partial t} + (\mathbf{V} \cdot \nabla) V_\phi + \frac{V_r V_\phi}{r} \right) &= F_\phi, \\ \frac{1}{\gamma - 1} \left( \frac{\partial p}{\partial t} + \nabla (\mathbf{V} p) \right) &= -p \nabla \cdot \mathbf{V} + \eta j_z^2 + W_H, \\ \frac{\partial \rho}{\partial t} + \nabla (\mathbf{V} \rho) &= 0, \end{aligned}$$

$$\mathbf{F} = \rho V_z^2 \frac{1}{g} \nabla g - \nabla p - (\mathbf{j} \times \mathbf{B})_\perp + \eta \nabla_\perp^2 \mathbf{v}_\perp.$$

This model is simpler than full MHD as many resistive and viscous terms are not present in the equations but do include additional terms compared to RMHD.

In the next section the model known as nearly incompressible MHD (NIMHD) by Zank and Matthaeus 1993 is discussed.

## B.4 Zank and Matthaeus: Nearly Incompressible MHD

Here we summarise the model of nearly incompressible MHD (NIMHD) developed by Zank and Matthaeus 1993. This derivation begins by finding the equations of 2D incompressible MHD and then perturbing them to give nearly incompressible equations. One difference between NIMHD and RMHD is that NIMHD allows for high frequency waves which are not included in RMHD. This derivation is carried out for different values of  $\beta$ . Here we discuss only the case:  $\beta \ll 1$ . The compressible ideal MHD equation, Equation (2.17) are used. The adapted equation of motion, the details were discussed in Section A.1 and Zank and Matthaeus 1992, is given by Equation (A.1) on page 176. A large constant background

field,  $B_0$ , is assumed at first order, analogous to RMHD. The ansatz used is

$$p = p_0 + \varepsilon_{zm} p^i, \quad \mathbf{v} = \mathbf{v}^i, \quad \mathbf{B} = B_0 \hat{\mathbf{e}}_z + \varepsilon_{zm} \mathbf{B}^i, \quad \rho = 1.$$

The above form of the expansion ensures  $\frac{\partial \mathbf{v}}{\partial t}$  is bounded, meaning that all of the terms are of  $O(1)$  to lowest order. The superscript “i” means these quantities satisfy the 2D incompressible MHD equations given by

$$\begin{aligned} \nabla_{\perp} \mathbf{v}_{\perp}^i &= 0, \quad \nabla_{\perp} \mathbf{B}_{\perp}^i = 0, \\ \left( \frac{\partial}{\partial t} + \mathbf{v}_{\perp}^i \cdot \nabla_{\perp} \right) \mathbf{B}_{\perp}^i &= \mathbf{B}_{\perp}^i \cdot \nabla_{\perp} \mathbf{v}_{\perp}^i \\ \left( \frac{\partial}{\partial t} + \mathbf{v}_{\perp}^i \cdot \nabla_{\perp} \right) \mathbf{v}_{\perp}^i &= -\nabla_{\perp} p^i - \frac{1}{2} \nabla_{\perp} (\mathbf{B}_{\perp}^{i2}) + \mathbf{B}_{\perp}^i \cdot \nabla_{\perp} \mathbf{B}_{\perp}^i. \end{aligned}$$

Here there are three timescales to consider: Alfvén, magneto-acoustic and convective. To allow for weakly compressible effects we must rescale the momentum equation by  $\delta^2 = \varepsilon_{zm}$  thus equation (A.1) on page 176 becomes

$$\rho \left( \frac{\partial}{\partial t} + \mathbf{v} \cdot \nabla \right) \mathbf{v} = -\frac{1}{\delta^2} \nabla p + \frac{1}{\delta^4} (\nabla \times \mathbf{B}) \times \mathbf{B}.$$

We wish to keep magnetoacoustic frequencies while removing higher Alfvén frequencies. This is different from RMHD where all high frequencies are removed except very long wavelengths. We expand about the incompressible state as

$$\mathbf{v} = \mathbf{v}^i + \delta \mathbf{v}_1, \quad p = p_0 + \delta^2 (p^i + p^*), \quad \rho = 1 + \delta^2 \rho_*, \quad \mathbf{B} = \mathbf{B}_0 + \delta^2 (\mathbf{B}^i + \mathbf{B}_1) + \delta^4 \mathbf{B}^*.$$

The evolution of the weakly compressible quantities:  $p^*, \rho_*, \mathbf{B}^*$  and  $\mathbf{v}_1$  is the set of nearly incompressible equations

$$\frac{d\rho_*}{dt} + \frac{1}{\delta} \nabla \cdot \mathbf{v}_1 = 0, \tag{B.2a}$$

$$\frac{dp^*}{dt} + \frac{\gamma p_0}{\delta} \nabla \cdot \mathbf{v}_1 = -\frac{dp^i}{dt}, \tag{B.2b}$$

$$\begin{aligned} \frac{d\mathbf{v}_1}{dt} + \mathbf{v}_1 \cdot \nabla \mathbf{v}_{\perp}^i &= -\frac{1}{\delta} [\nabla p^* + \nabla (\mathbf{B}_0 \cdot \mathbf{B}^*) + \mathbf{B}_0 \cdot \nabla \mathbf{B}^*] \\ &\quad - \nabla (\mathbf{B}_{\perp}^i \cdot \mathbf{B}^*) + \mathbf{B}_{\perp}^i \cdot \nabla_{\perp} \mathbf{B}^* + \mathbf{B}^* \cdot \nabla \mathbf{B}_{\perp}^i, \end{aligned} \tag{B.2c}$$

$$\frac{d\mathbf{B}^*}{dt} - \mathbf{B}^* \cdot \nabla \mathbf{v}_{\perp}^i = \frac{1}{\delta} (\nabla \times \mathbf{v}_1 \times \mathbf{B}_{\perp}^i), \tag{B.2d}$$

$$(\mathbf{B}_0 \cdot \nabla) \mathbf{v}_1 = B_0 \nabla \cdot \mathbf{v}_1. \tag{B.2e}$$

$$\tag{B.2f}$$

Now we can apply a similar scaling of coordinates as in Section 3.3.2 to elucidate the similarities and differences between these NIMHD equations and those of RMHD. It can be shown that these equations give a wave equation for long wavelength acoustic waves. This

is a similar behaviour to that seen in RMHD for long wavelength Alfvén waves. The next model we discuss is a four-field system derived by Bhattacharjee, Ng, and Spangler 1998.

## B.5 Bhattacharjee et al: Four Field MHD

Here an overview of an approximate MHD model that was presented by Bhattacharjee, Ng, and Spangler 1998 is given.

The MHD equations are expanded using a general, spatially varying, background magnetic field,  $\mathbf{B}_0(x, y, z)$ . This results in a set of equations involving four variables: magnetic flux; parallel flow; vorticity and pressure. In the limit of a constant background magnetic field,  $\mathbf{B}_0 \rightarrow \hat{\mathbf{e}}_z$ , this system reduces to the original equations of RMHD. This derivation begins with the MHD equations, Equations (2.17b), Equation (2.17a) and Equation (2.16c) including resistivity and the RHS of the energy equation, Equation (2.17d)), is given by ohmic heating,  $\eta \mathbf{j}^2$ . After non-dimensionalisation, the induction and continuity equations remain unchanged. The momentum and energy equations are

$$\rho \left( \frac{\partial}{\partial t} + \mathbf{v} \cdot \nabla \right) \mathbf{v} = \frac{1}{\varepsilon^2} \left( -\nabla p + \frac{1}{\beta} (\nabla \times \mathbf{B}) \times \mathbf{B} \right), \quad (\text{B.3})$$

$$\frac{d}{dt} \left( \frac{p}{\rho^\gamma} \right) = \frac{\gamma - 1}{\beta \rho^\gamma} \eta |\mathbf{j}|^2, \quad (\text{B.4})$$

where the parameter,  $\varepsilon$ , is taken to be equal to the sound mach number as

$$\varepsilon = \gamma^{1/2} M, \quad M = \frac{v_0^2}{C_s^2}, \quad \beta = \frac{\rho_0 \mu_0}{B_0^2} = \frac{M_A^2}{\gamma M^2} = \frac{M_A^2}{\varepsilon^2}.$$

These parameters are typical values for the equilibrium state.

An asymptotic expansion is used of the form

$$\mathbf{B} = \mathbf{B}_0 + \mathbf{B}_1 \dots, \quad \mathbf{v} = \mathbf{v}_1 \dots, \quad \rho = \rho_0 + \rho_1 \dots, \quad p = p_0 + p_1 \dots,$$

The quantities with a “0” subscript denote the mean value of the quantities and the subscript “1” denotes the fluctuations.

The leading order terms of the dimensionless momentum equation, Equation (B.3), gives

$$\nabla p_0 = \frac{1}{\beta} (\nabla \times \mathbf{B}_0) \times \mathbf{B}_0. \quad (\text{B.5})$$

A solution to Equation (B.5) is

$$p_0 = 1, \quad \mathbf{B}_0 = \hat{\mathbf{e}}_z.$$

This is equivalent to the assumptions made in Zank and Matthaeus’ derivation of RMHD as given in Section 3.3.2, Appendix A.1 and Zank and Matthaeus 1992. Here more general

solutions of Equation (B.5) are explored.

By considering Equation (B.3) and Equation (B.5) the transformation

$$\begin{aligned}
 \mathbf{B} &\rightarrow \beta^{1/2} \mathbf{B} & \mathbf{B} &\sim O\left(\frac{1}{\beta^{1/2}}\right), \\
 \mathbf{j} &\rightarrow \varepsilon \beta^{1/2} \mathbf{j}, \\
 \eta &\rightarrow \frac{\eta}{\varepsilon^2}, \\
 \mathbf{v} &\rightarrow \frac{\mathbf{v}}{\varepsilon} & \mathbf{v} &\sim O(\varepsilon), \\
 \nabla &\rightarrow \varepsilon \nabla & \nabla &\sim O\left(\frac{1}{\varepsilon}\right),
 \end{aligned}$$

is applied to Equations (B.3), (B.5), (2.16c), (2.17b) and (B.4) to remove  $\varepsilon$  and  $\beta$ . The induction and continuity equations remain unchanged.

The momentum, 1st order momentum and energy equations, Equations (B.3), (B.5) and (B.4), give

$$\rho \left( \frac{\partial}{\partial t} + \mathbf{v} \cdot \nabla \right) \mathbf{v} = \nabla p + (\nabla \times \mathbf{B}) \times \mathbf{B}, \quad (\text{B.6a})$$

$$\nabla p_0 = (\nabla \times \mathbf{B}_0) \times \mathbf{B}_0, \quad (\text{B.6b})$$

$$\frac{d}{dt} \left( \frac{p}{\rho^\gamma} \right) = \frac{\gamma - 1}{\rho^\gamma} \eta |\mathbf{j}|^2. \quad (\text{B.6c})$$

Equation (B.6c) can be combined with the continuity equation, Equation (2.17b) as

$$\frac{\partial p}{\partial t} + \mathbf{v} \cdot \nabla p + \gamma p \nabla \cdot \mathbf{v} = (\gamma - 1) \eta |\mathbf{j}|^2.$$

Naturally, the mean and fluctuating values vary differently in time and space. The fluctuations vary much faster in space and time than the mean values. Since there is a large magnetic field,  $\mathbf{B}_0$ , the fluctuations will vary slowly along the direction parallel to the field and more quickly perpendicular to it. Fluctuations also vary faster in time. Hence, the following ordering is used for differentiating the mean and fluctuating quantities

mean	fluctuations
$\nabla \sim O(1)$	$\nabla_{\parallel} \sim O(1),$
	$\nabla_{\perp} \sim O\left(\frac{1}{\varepsilon}\right),$
$\frac{\partial}{\partial t} \sim O(\varepsilon^2)$	$\frac{\partial}{\partial t} \sim O(1).$

For example for a fluctuating and mean quantity,  $f_1$  and  $f_0$ , then  $\frac{\partial f_0}{\partial t} \sim O(\varepsilon^2)$  and  $\frac{\partial f_1}{\partial t} \sim O(\varepsilon)$ .

### Summary

The final equations for the four variables: magnetic flux,  $A$ , parallel flow,  $v_1$ , pressure,  $p_1$ , and parallel vorticity,  $\omega$ , are given by

$$\frac{dA}{dt} = \mathbf{B}_0 \cdot \nabla \phi + \eta \nabla_{\perp}^2 A, \quad (\text{B.7a})$$

$$\rho_0 \frac{d\omega}{dt} = DJ + 2\mathbf{b} \times \nabla P \cdot \nabla_{\perp} p_1 - J(\mathbf{b} \cdot \nabla \mathbf{B}_0^2), \quad (\text{B.7b})$$

$$\frac{dp_1}{dt} = -\mathbf{v}_1 \cdot \nabla p_0 + \frac{\gamma p_0}{\gamma p_0 + \mathbf{B}_0^2} (2\mathbf{v}_1 \cdot \nabla P + Dv_1 + \eta \nabla_{\perp}^2 p_1), \quad (\text{B.7c})$$

$$\rho_0 \frac{dv_1}{dt} = Dp_1 + \mathbf{B}_1 \cdot \nabla p_0, \quad (\text{B.7d})$$

where

$$\omega = -\nabla_{\perp}^2 \phi, \quad J = -\nabla_{\perp}^2 A, \quad P = p_0 + \mathbf{B}^2/2, \quad \mathbf{b} = \frac{\mathbf{B}_0}{B_0^2}$$

$$D = (\mathbf{B}_0 + \mathbf{B}_{1\perp}) \cdot \nabla, \quad \frac{d}{dt} = \frac{\partial}{\partial t} + \mathbf{v}_1 \cdot \nabla_{\perp}, \quad \rho_0 = p_0^{1/\gamma},$$

and the parallel components are defined as being locally parallel to  $\mathbf{B}_0$ . This set of equations is known as the four-field MHD equations.

### Limits

We can investigate the limits of a constant magnetic field and  $\beta \ll 1$  by assuming the following form for the background field

$$\mathbf{B}_0 = \frac{\hat{\mathbf{z}}}{\sqrt{\beta}} + \mathbf{B}(\mathbf{x}). \quad (\text{B.8})$$

Taking the limit  $\mathbf{B}(\mathbf{x}) \rightarrow 0$  or  $\beta \lll 1$  causes the equations for the parallel velocity, Equations (B.7d), and pressure, (B.7c), to decouple and the remaining equations for  $A$  and  $\omega$ , Equation (B.7a) and Equation (B.7b) become

$$\frac{dA}{dt} = \mathbf{B}_0 \cdot \nabla \phi + \eta \nabla_{\perp}^2 A,$$

$$\rho \frac{d\omega}{dt} = \mathbf{B} \cdot \nabla J,$$

where  $\mathbf{B} = \mathbf{B}_0 + \mathbf{B}_{1\perp}$ . These equations are equivalent to RMHD.

A further study, Bhattacharjee et al. 1999, was done to compare solutions of the 4field equations, NIMHD and RMHD. In the next section a model describing Alfvén wave turbulence developed by van Ballegoijen et al. 2011 is summarised.

## B.6 Van Ballegooijen et al: RMHD for Alfvén wave turbulence

Here a discussion is given of the development of a detailed model for coronal heating due to Alfvén wave dynamics that was first derived in van Ballegooijen et al. 2011.

The system consists of a kilogauss flux tube of length  $L$  including chromospheric and coronal regions. The tube is vertical in the chromosphere and curvature is neglected. The loop cross section varies with height as  $R(z)$ .  $R(z)$  must be smaller than  $L$ . Random footpoint motions are imposed on the boundaries at  $z = 0$  and  $L$ . The MHD equations are (2.17). Gravity is included in the lower atmosphere as  $\mathbf{g} = g_0(z)\hat{\mathbf{e}}_z$ . The velocity can be split into perpendicular and parallel parts as

$$\mathbf{v} = \mathbf{v}_\perp + v_\parallel \hat{\mathbf{B}}.$$

Quantities are written with mean and fluctuating components as  $\mathbf{B} = \mathbf{B}_0 + \mathbf{B}_1 \dots$ . The background field,  $\mathbf{B}_0$ , is nonuniform and varies on a lengthscale of

$$H_B = B_0(\hat{\mathbf{B}}_0 \cdot \nabla B_0)^{-1}.$$

Static equilibrium is assumed with  $\mathbf{v}_0 = 0$  and  $\nabla \times \mathbf{B}_0 = 0$ . This gives a force balance equation for mean quantities as

$$\nabla p_0 = \rho_0 \mathbf{g},$$

where  $p_0$  and  $\rho_0$  are functions of  $z$ . The radius  $R(z)$  is assumed to be smaller than the lengthscale of the background field,  $H_B$ . This is the first small parameter given by

$$\varepsilon_0(z) = \frac{R(z)}{|H_B(z)|} \ll 1.$$

The background field is written as

$$\mathbf{B}_0 = B_{00}\hat{\mathbf{e}}_z - \frac{1}{2} \frac{dB_{00}}{dz} (x\hat{\mathbf{x}} + y\hat{\mathbf{y}}) + O(B_{00}\varepsilon_0^2),$$

where  $B_{00}(z)$  is the magnetic field strength at the tube axis ( $x = y = 0$ ). The unit vector along the background field is

$$\hat{\mathbf{B}}_0 = \hat{\mathbf{e}}_z - \frac{1}{2H_B} (x\hat{\mathbf{x}} + y\hat{\mathbf{y}}) + O(\varepsilon_0^2),$$

where  $H_B(z) \approx B_{00}/\frac{dB_{00}}{dz}$ . Hence  $\nabla \cdot \mathbf{B}_0 = 0$  as required. Derivatives of this unit vector are

$$\frac{\partial \hat{\mathbf{B}}_0}{\partial x} = -\frac{\hat{\mathbf{x}}}{2H_B} + O(\varepsilon_0^2/R), \quad \frac{\partial \hat{\mathbf{B}}_0}{\partial y} = -\frac{\hat{\mathbf{y}}}{2H_B} + O(\varepsilon_0^2/R).$$

The wave amplitude is  $u_\perp(z) \ll v_A(z)$  and  $B_1 \ll B_{00}$ .

There are three parallel lengthscales: Alfvén wavelength  $v_A \tau$  ( $\tau$  is wave period); the lengthscale of the background field,  $|H_B|$  and the box length  $L$ . Thus, a parallel lengthscale is defined as the minimum of these quantities as

$$l_{\parallel} = \min(v_A \tau, |H_B|, L).$$

An additional requirement is that perpendicular lengthscales are  $l_{\perp} \ll l_{\parallel}$ .

A second small parameter is defined to be the maximum value of the ratio of typical velocities or lengthscales as

$$\varepsilon = \max\left(\frac{u_{\perp}}{v_A}, \frac{l_{\perp}}{l_{\parallel}}\right) \ll 1.$$

The magnetic and velocity fields are expanded as

$$\mathbf{B} = \mathbf{B}_0 + \mathbf{B}_1 + O(B_{00}\varepsilon^2), \quad \mathbf{v}_{\perp} = \mathbf{v}_{\perp 1} + \mathbf{v}_{\perp 2} + O(V_A\varepsilon^3),$$

Note  $v_{\parallel} \sim O(v_A\varepsilon^2)$ . As usual the leading order perturbed magnetic field is perpendicular to the background field, hence it can be written using a flux function,  $A$ .

$$\mathbf{A}_1 = h(\mathbf{r}, t)\mathbf{B}_0,$$

where  $h \sim l_{\perp}\varepsilon$ . The total magnetic field is written as

$$\mathbf{B} = \mathbf{B}_0 + \nabla_{\perp} h \times \mathbf{B}_0 + O(B_{00}^2\varepsilon^2).$$

The final equations of the Alfvén wave turbulence model can be written as

$$\frac{\partial h}{\partial t} = \hat{\mathbf{B}}_0 \cdot \nabla f + \frac{f}{H_B} + [f, h], \tag{B.9a}$$

$$\frac{\partial \omega}{\partial t} = -[\omega, f] + v_A^2 \left( \hat{\mathbf{B}}_0 \cdot \nabla \alpha + [\alpha, h] \right), \tag{B.9b}$$

$$\omega = -\nabla_{\perp}^2 f, \quad \alpha = -\nabla_{\perp}^2 h. \tag{B.9c}$$

where

$$[a, b] = \frac{\partial a}{\partial x} \frac{\partial b}{\partial y} - \frac{\partial a}{\partial y} \frac{\partial b}{\partial x}.$$

Although these equations are more general than RMHD, some limitations, such as incompressibility, are true in both models.

Next we summarise the coronal heating studies done using these equations. The above equations are used to model a one kilogauss flux tube with a circular cross section.

General conclusions from these studies are that the resulting field is twisted on very small perpendicular lengthscales ( $\sim 100\text{km}$ ) which are too small to be visible with current resolutions of observations. The perturbed field is very small  $\delta b_{rms}/B_0 \sim 0.025$  with an angle of  $1.4^\circ$ . Enough heating is produced when the magnetic field evolves dynamically

rather than quasi-statically.

This model is only an approximation to full MHD and there are a number of issues that would need full MHD to be modelled more accurately. The RMHD model does not allow for the interaction of multiple flux tubes and so only one is modelled at a time.

The effects of the resulting heating are not included as this is not part of the RMHD formalism.  $\beta$  is not always  $\ll 1$  in the model for the lower atmosphere and it is possible that the parallel lengthscale of the background field is less than the tube radius as  $H_B < R$ . This gives  $\varepsilon_0 > 1$  which means the thin tube approximation and RMHD are not valid in these areas. The ratio  $\delta b_{rms}/B_0 \sim 0.3$  for van Ballegooijen et al. 2011 so the first assumption of RMHD is only marginally satisfied.

This model is used to investigate the dependence of the heating rate in the corona and lower atmosphere regions on several system parameters, such as coronal loop length, magnetic field and pressure.

It is found that the heating rates in both regions increase with increasing magnetic field strength. The coronal heating decreases for small values of pressure whereas the heating rate in the lower atmosphere only depends weakly on the pressure.

After this initial study magnetic field extrapolation methods are used to calculate the magnetic field and height as functions of the position along the loop for two SDO/HMI observed active regions. This data is then used as the initial conditions for this model. First, Asgari-Targhi and van Ballegooijen 2012 look at 10 fieldlines traced from an active region observed on 5 May 2010. In this case the effects of gravity are included in the corona. Thermal equilibrium is assumed. It is concluded that the loops in the centre are in thermal equilibrium and have a temperature of 2-3MK and small temperature variations. The loops near the edge do not seem to be in equilibrium and do not produce realistic temperatures. Similarly in Asgari-Targhi et al. 2013 a similar study is done using an active region observed on 7 March 2012. The constraint of thermal equilibrium is not assumed in this study.

The debate between DC and AC heating models is addressed in van Ballegooijen, Asgari-Targhi, and Berger 2014 by considering both mechanisms. The input parameters are taken from one of the fieldlines in Asgari-Targhi and van Ballegooijen 2012. For an AC mechanism the magnetic field evolves dynamically whereas a DC one evolves quasi-statically.

It is concluded that a DC mechanism does not produce enough heating and it is important to include the lower atmosphere in the model.



## Appendix C

### Second order Solution

Here the second order linearised MHD solution used in Chapter 4 is derived.

The magnetic and velocity fields, density and pressure are expanded using Equations (4.20) on page 71 in the viscous MHD equations, Equations (4.1) on page 63 in Chapter 4, Section 4.2.5.

The full second order equations including all viscous terms are given by

$$\begin{aligned} \rho_0 \frac{\partial v_{2x}}{\partial t} = & -\frac{\partial}{\partial x} \left( p_2 + \frac{1}{2} B_{1z}^2 \right) + B_0 \left( \frac{\partial B_{2x}}{\partial y} - \frac{\partial B_{2y}}{\partial x} \right) \\ & + \rho_0 \nu \left( \frac{4}{3} \frac{\partial^2 v_{2x}}{\partial x^2} + \frac{\partial^2 v_{2x}}{\partial y^2} + \frac{1}{3} \frac{\partial^2 v_{2y}}{\partial x \partial y} \right), \end{aligned} \quad (\text{C.1})$$

$$\rho_0 \frac{\partial v_{2y}}{\partial t} = -\frac{\partial}{\partial y} \left( p_2 + \frac{1}{2} B_{1z}^2 \right) + \rho_0 \nu \left( \frac{\partial^2 v_{2y}}{\partial x^2} + \frac{4}{3} \frac{\partial^2 v_{2y}}{\partial y^2} + \frac{1}{3} \frac{\partial^2 v_{2x}}{\partial y \partial x} \right), \quad (\text{C.2})$$

$$\frac{\partial \rho_2}{\partial t} = -\rho_0 \left( \frac{\partial v_{2x}}{\partial x} + \frac{\partial v_{2z}}{\partial z} \right), \quad (\text{C.3})$$

$$\frac{\partial B_{2x}}{\partial t} = B_0 \frac{\partial v_{2x}}{\partial y}, \quad (\text{C.4})$$

$$\frac{\partial B_{2y}}{\partial t} = -B_0 \frac{\partial v_{2x}}{\partial x}, \quad (\text{C.5})$$

$$\frac{\partial p_2}{\partial t} = -\gamma p_0 \left( \frac{\partial v_{2x}}{\partial x} + \frac{\partial v_{2y}}{\partial y} \right) + (\gamma - 1) \rho_0 \nu \left( \left( \frac{\partial v_{1z}}{\partial x} \right)^2 + \left( \frac{\partial v_{1z}}{\partial y} \right)^2 \right). \quad (\text{C.6})$$

Taking the time derivative of the equation for  $v_{2x}$ , Equation (C.1), substituting the steady state expressions for  $v_{1z}$ , Equation (4.23), and  $B_{z1}$ , Equation (4.24) on page 73, which are given by

$$V_{1z} = \begin{cases} 0, & t < t_1, \\ \frac{V_{0y}}{L} \sin kx, & t_1 < t, \end{cases}$$

and

$$B_{1z} = \begin{cases} 0, & t < t_1, \\ B_0 \left( \frac{V_0(t-t_1)}{L} + \frac{\nu k^2 L V_0}{2V_A^2} \left( \frac{y^2}{L^2} - 1 \right) \right) \sin kx, & t_1 < t, \end{cases}$$

and simplifying gives

$$\begin{aligned} \rho_0 \frac{\partial^2 v_{2x}}{\partial t^2} &= - \frac{\partial}{\partial x} \left( \frac{\partial p_2}{\partial t} + \frac{1}{2} \frac{\partial B_{1z}^2}{\partial t} \right) - B_0 \frac{\partial}{\partial x} \frac{\partial B_{2y}}{\partial t} + B_0 \frac{\partial}{\partial y} \frac{\partial B_{2x}}{\partial t} \\ &\quad + \rho_0 \nu \frac{\partial}{\partial t} \left( \frac{4}{3} \frac{\partial^2 v_{2x}}{\partial x^2} + \frac{\partial^2 v_{2x}}{\partial y^2} + \frac{1}{3} \frac{\partial v_{2y}}{\partial x \partial y} \right), \\ \Rightarrow &= - \frac{\partial}{\partial x} \left( -\gamma p_0 \left( \frac{\partial v_{2x}}{\partial x} + \frac{\partial v_{2y}}{\partial y} \right) \right. \\ &\quad + (\gamma - 1) \rho_0 \nu \left( \frac{V_0^2 k^2 y^2}{L^2} \cos^2(kx) + \frac{V_0^2}{L^2} \sin^2(kx) \right) \\ &\quad + \frac{B_0^2}{2} \left( \frac{2V_0^2 t}{L^2} + \frac{\nu k^2 V_0^2}{V_A^2} \left( \frac{y^2}{L^2} - 1 \right) \right) \sin^2(kx) \\ &\quad + B_0^2 \left( \frac{\partial^2 v_{2x}}{\partial x^2} + \frac{\partial^2 v_{2x}}{\partial y^2} \right) \\ &\quad + \rho_0 \nu \frac{\partial}{\partial t} \left( \frac{4}{3} \frac{\partial^2 v_{2x}}{\partial x^2} + \frac{\partial^2 v_{2x}}{\partial y^2} + \frac{1}{3} \frac{\partial^2 v_{2y}}{\partial x \partial y} \right), \\ \Rightarrow &= \frac{\partial}{\partial x} \left( \gamma p_0 \left( \frac{\partial v_{2x}}{\partial x} + \frac{\partial v_{2y}}{\partial y} \right) \right. \\ &\quad + (\gamma - 1) \rho_0 \nu \left( -\frac{V_0^2 k^2 y^2}{2L^2} \cos(2kx) + \frac{V_0^2}{2L^2} \cos(2kx) \right) \\ &\quad + \frac{B_0^2}{4} \frac{\nu k^2 V_0^2}{V_A^2} \left( \frac{y^2}{L^2} - 1 \right) \cos(2kx) \Big) + B_0^2 \left( \frac{\partial^2 v_{2x}}{\partial x^2} + \frac{\partial^2 v_{2x}}{\partial y^2} \right) \\ &\quad - B_0^2 \frac{k V_0^2 t}{L^2} \sin(2kx) + \rho_0 \nu \frac{\partial}{\partial t} \left( \frac{4}{3} \frac{\partial^2 v_{2x}}{\partial x^2} + \frac{\partial^2 v_{2x}}{\partial y^2} + \frac{1}{3} \frac{\partial^2 v_{2y}}{\partial x \partial y} \right), \end{aligned} \tag{C.7}$$

Differentiating Equation (C.2) gives the following for  $v_{2y}$

$$\begin{aligned}
\rho_0 \frac{\partial^2 v_{2y}}{\partial t^2} &= -\frac{\partial}{\partial y} \left( \frac{\partial p_2}{\partial t} + \frac{1}{2} \frac{\partial B_{1z}^2}{\partial t} \right) + \rho_0 \nu \frac{\partial}{\partial t} \left( \frac{\partial^2 v_{2y}}{\partial x^2} + \frac{4}{3} \frac{\partial^2 v_{2y}}{\partial y^2} + \frac{1}{3} \frac{\partial^2 v_{2x}}{\partial y \partial x} \right), \\
\Rightarrow &= -\frac{\partial}{\partial y} \left( -\gamma p_0 \left( \frac{\partial v_{2x}}{\partial x} + \frac{\partial v_{2y}}{\partial y} \right) \right. \\
&\quad + (\gamma - 1) \rho_0 \nu \left( \frac{V_0^2 k^2 y^2}{L^2} \cos^2(kx) + \frac{V_0^2}{L^2} \sin^2(kx) \right) \\
&\quad + \frac{B_0^2}{2} \left( \frac{2V_0^2 t}{L^2} + \frac{\nu k^2 V_0^2}{V_A^2} \left( \frac{y^2}{L^2} - 1 \right) \right) \sin^2(kx) \Big) \\
&\quad + \rho_0 \nu \frac{\partial}{\partial t} \left( \frac{\partial^2 v_{2y}}{\partial x^2} + \frac{4}{3} \frac{\partial^2 v_{2y}}{\partial y^2} + \frac{1}{3} \frac{\partial^2 v_{2x}}{\partial y \partial x} \right), \\
\Rightarrow &= \frac{\partial}{\partial y} \left( \gamma p_0 \left( \frac{\partial v_{2x}}{\partial x} + \frac{\partial v_{2y}}{\partial y} \right) \right. \\
&\quad - (\gamma - 1) \rho_0 \nu \left( \frac{V_0^2 k^2 y^2}{2L^2} (1 + \cos(2kx)) + \frac{V_0^2}{2L^2} (1 - \cos(2kx)) \right) \\
&\quad - \frac{B_0^2}{4} \frac{\nu k^2 V_0^2}{V_A^2} \left( \frac{y^2}{L^2} - 1 \right) (1 - \cos(2kx)) \Big) \\
&\quad + \rho_0 \nu \frac{\partial}{\partial t} \left( \frac{\partial^2 v_{2y}}{\partial x^2} + \frac{4}{3} \frac{\partial^2 v_{2y}}{\partial y^2} + \frac{\partial^2 v_{2x}}{\partial y \partial x} \right). \tag{C.8}
\end{aligned}$$

From Equation (C.7) for  $V_{2x}$  we can assume

$$v_{2x}(x, y, t) = v_x(y, t) \sin(2kx).$$

Equation (C.7) and Equation (C.8) are now

$$\begin{aligned}
 \rho_0 \frac{\partial^2 v_x}{\partial t^2} \sin(2kx) = & \frac{\partial}{\partial x} \left( \gamma p_0 \left( 2k v_x \cos(2kx) + \frac{\partial v_{2y}}{\partial y} \right) \right. \\
 & + (\gamma - 1) \rho_0 \nu \left( -\frac{V_0^2 k^2 y^2}{2L^2} + \frac{V_0^2}{2L^2} \right) \cos(2kx) \\
 & + \frac{B_0^2}{4} \frac{\nu k^2 V_0^2}{V_A^2} \left( \frac{y^2}{L^2} - 1 \right) \cos(2kx) \Bigg) \\
 & + B_0^2 \left( -4k^2 v_x \sin(2kx) + \frac{\partial^2 v_x}{\partial y^2} \sin(2kx) \right) \\
 & - B_0^2 \frac{k V_0^2 t}{L^2} \sin(2kx) \\
 & + \rho_0 \nu \frac{\partial}{\partial t} \left( -4k^2 \frac{4}{3} v_x + \frac{\partial^2 v_x}{\partial y^2} \right) \sin(2kx) \\
 & + \frac{\rho_0 \nu}{3} \frac{\partial}{\partial t} \frac{\partial^2 v_{2y}}{\partial x \partial y}, \tag{C.9}
 \end{aligned}$$

$$\begin{aligned}
 \rho_0 \frac{\partial^2 v_{2y}}{\partial t^2} = & \frac{\partial}{\partial y} \left( \gamma p_0 \left( 2k v_x \cos(2kx) + \frac{\partial v_{2y}}{\partial y} \right) \right. \\
 & - (\gamma - 1) \rho_0 \nu \left( \frac{V_0^2 k^2 y^2}{2L^2} (1 + \cos(2kx)) \right. \\
 & + \left. \frac{V_0^2}{2L^2} (1 - \cos(2kx)) \right) - \frac{B_0^2}{4} \frac{\nu k^2 V_0^2}{V_A^2} \left( \frac{y^2}{L^2} - 1 \right) (1 - \cos(2kx)) \Bigg) \\
 & + \rho_0 \nu \frac{\partial}{\partial t} \left( 2k \frac{1}{3} \frac{\partial v_x}{\partial y} \cos(2kx) + \frac{\partial^2 v_{2y}}{\partial x^2} + \frac{4}{3} \frac{\partial^2 v_{2y}}{\partial y^2} \right). \tag{C.10}
 \end{aligned}$$

We can now take

$$v_{2y}(x, y, t) = v_y(y, t) \cos(2kx) + G(y, t). \tag{C.11}$$

Substituting into our current equation for  $v_{2y}$ , Equation (C.10), gives

$$\begin{aligned}
 \rho_0 \frac{\partial^2 v_y}{\partial t^2} \cos(2kx) + \rho_0 \frac{\partial^2 G}{\partial t^2} = & \frac{\partial}{\partial y} \left( \gamma p_0 \left( 2k v_x \cos(2kx) + \frac{\partial v_y}{\partial y} \cos(2kx) + \frac{\partial G}{\partial y} \right) \right. \\
 & - (\gamma - 1) \rho_0 \nu \left( \frac{V_0^2 k^2 y^2}{2L^2} (1 + \cos(2kx)) + \frac{V_0^2}{2L^2} (1 - \cos(2kx)) \right) \\
 & - \frac{B_0^2}{4} \frac{\nu k^2 V_0^2}{V_A^2} \left( \frac{y^2}{L^2} - 1 \right) (1 - \cos(2kx)) \Bigg) \\
 & + \rho_0 \nu \frac{\partial}{\partial t} \left( -4k^2 v_y \cos(2kx) + \frac{4}{3} \frac{\partial^2 (v_y \cos(2kx) + G)}{\partial y^2} \right. \\
 & + \left. 2k \frac{1}{3} \frac{\partial v_x}{\partial y} \cos(2kx) \right). \tag{C.12}
 \end{aligned}$$

Separating Equation (C.12) into two equations: one multiplied by  $\cos(2kx)$  and

one for  $G$ , gives

$$\begin{aligned} \rho_0 \frac{\partial^2 v_y}{\partial t^2} \cos(2kx) = & \frac{\partial}{\partial y} \left( \gamma p_0 \left( 2k v_x \cos(2kx) + \frac{\partial v_y}{\partial y} \cos(2kx) \right) \right. \\ & + (\gamma - 1) \rho_0 \nu \left( -\frac{V_0^2 k^2 y^2}{2L^2} \cos(2kx) + \frac{V_0^2}{2L^2} \cos(2kx) \right) \\ & + \frac{B_0^2}{4} \frac{\nu k^2 V_0^2}{V_A^2} \left( \frac{y^2}{L^2} - 1 \right) \cos(2kx) \Bigg) \\ & + \rho_0 \nu \frac{\partial}{\partial t} \left( -4k^2 v_y \cos(2kx) + \frac{4}{3} \frac{\partial^2 v_y}{\partial y^2} \cos(2kx) + 2k \frac{1}{3} \frac{\partial v_x}{\partial y} \cos(2kx) \right). \end{aligned} \quad (C.13)$$

$$\begin{aligned} \rho_0 \frac{\partial^2 G}{\partial t^2} = & \frac{\partial}{\partial y} \left( \gamma p_0 \frac{\partial G}{\partial y} - (\gamma - 1) \rho_0 \nu \left( \frac{V_0^2 k^2 y^2}{2L^2} + \frac{V_0^2}{2L^2} \right) - \frac{B_0^2}{4} \frac{\nu k^2 V_0^2}{V_A^2} \left( \frac{y^2}{L^2} - 1 \right) \right) \\ & + \rho_0 \frac{4}{3} \nu \frac{\partial}{\partial t} \frac{\partial^2 G}{\partial y^2}. \end{aligned} \quad (C.14)$$

It is possible to solve Equation (C.14) immediately for  $G$ .  $G$  is a function of  $y$  only. Integrating in  $y$  the equation can be solved

$$\begin{aligned} \frac{1}{\rho_0} \frac{\partial}{\partial y} \left( \gamma p_0 \frac{\partial G}{\partial y} - (\gamma - 1) \rho_0 \nu \left( \frac{V_0^2 k^2 y^2}{2L^2} + \frac{V_0^2}{2L^2} \right) - \frac{B_0^2}{4} \frac{\nu k^2 V_0^2}{V_A^2} \left( \frac{y^2}{L^2} - 1 \right) \right) &= 0. \\ \Rightarrow \frac{\gamma p_0}{\rho_0} \frac{\partial G}{\partial y} - (\gamma - 1) \nu \left( \frac{V_0^2 k^2 y^2}{2L^2} + \frac{V_0^2}{2L^2} \right) - \frac{B_0^2}{4\rho_0} \frac{\nu k^2 V_0^2}{V_A^2} \left( \frac{y^2}{L^2} - 1 \right) &= \lambda. \end{aligned}$$

The solution is

$$G(y) = \frac{\lambda \rho_0}{\gamma p_0} y + \frac{\rho_0}{\gamma p_0} (\gamma - 1) \nu \left( \frac{V_0^2 k^2 y^3}{6L^2} + \frac{V_0^2}{2L^2} y \right) + \frac{\rho_0}{\gamma p_0} \frac{B_0^2}{4\rho_0} \frac{\nu k^2 V_0^2}{V_A^2} \left( \frac{y^3}{3L^2} - y \right). \quad (C.15)$$

The constant  $\lambda$  can be found by applying boundary conditions at  $y = \pm L$  such that  $v_y(x, \pm L, t) = 0$ . Thus

$$\lambda = -\frac{V_0^2 \nu}{6} \left( \gamma k^2 - 2k^2 + \frac{3(\gamma - 1)}{L^2} \right). \quad (C.16)$$

Now  $G$  can be neatly written as

$$G(y) = -\frac{1}{6} \frac{\nu k^2 V_0^2 \rho_0 (\gamma - \frac{1}{2})}{\gamma p_0 L^2} y(L - y)(L + y). \quad (C.17)$$

Our remaining equations for  $v_x$  and  $v_y$ , after canceling the  $\sin(2kx)$  and  $\cos(2kx)$  coeffi-

cients, are

$$\begin{aligned} \rho_0 \frac{\partial^2 v_x}{\partial t^2} = & -2k \left( \gamma p_0 \left( 2k v_x + \frac{\partial v_y}{\partial y} \right) + (\gamma - 1) \rho_0 \nu \left( -\frac{V_0^2 k^2 y^2}{2L^2} + \frac{V_0^2}{2L^2} \right) \right. \\ & + \frac{B_0^2}{4} \frac{\nu k^2 V_0^2}{V_A^2} \left( \frac{y^2}{L^2} - 1 \right) \left. \right) + B_0^2 \left( -4k^2 v_x + \frac{\partial^2 v_x}{\partial y^2} \right) - \frac{B_0^2}{\mu} \frac{k V_0^2 t}{L^2} \\ & + \rho_0 \nu \frac{\partial}{\partial t} \left( -4k^2 \frac{4}{3} v_x + \frac{\partial^2 v_x}{\partial y^2} - 2k \frac{1}{3} \frac{\partial v_y}{\partial y} \right). \end{aligned} \quad (\text{C.18})$$

$$\begin{aligned} \rho_0 \frac{\partial^2 v_y}{\partial t^2} = & \frac{\partial}{\partial y} \left( \gamma p_0 \left( 2k v_x + \frac{\partial v_y}{\partial y} \right) + (\gamma - 1) \rho_0 \nu \left( -\frac{V_0^2 k^2 y^2}{2L^2} + \frac{V_0^2}{L^2} \right) \right. \\ & + \frac{B_0^2}{4} \frac{\nu k^2 V_0^2}{V_A^2} \left( \frac{y^2}{L^2} - 1 \right) \left. \right) + \rho_0 \nu \frac{\partial}{\partial t} \left( -4k^2 v_y + \frac{4}{3} \frac{\partial^2 v_y}{\partial y^2} + 2k \frac{1}{3} \frac{\partial v_x}{\partial y} \right). \end{aligned} \quad (\text{C.19})$$

$$(\text{C.20})$$

We can now propose the solution of the form

$$v_x = B(y)t + C(y),$$

$$v_y = F(y)t + E(y),$$

Considering Equation (C.19), for  $v_y$  now gives

$$\begin{aligned} \frac{\partial}{\partial y} \left( \frac{\gamma p_0}{\rho_0} \left( 2k(Bt + C) + \frac{\partial(Ft + E)}{\partial y} \right) + (\gamma - 1) \nu \left( -\frac{V_0^2 k^2 y^2}{2L^2} + \frac{V_0^2}{2L^2} \right) + \frac{B_0^2}{4\rho_0} \frac{\nu k^2 V_0^2}{V_A^2} \left( \frac{y^2}{L^2} - 1 \right) \right) \\ + \nu \frac{\partial}{\partial t} \left( -4k^2(Ft + E) + \frac{4}{3} \frac{\partial^2(Ft + E)}{\partial y^2} + 2k \frac{1}{3} \frac{\partial(Bt + C)}{\partial y} \right) = 0. \end{aligned} \quad (\text{C.21})$$

This gives two equations: one for the coefficient of  $t$  and one independent of  $t$ . The first is

$$\begin{aligned} \frac{\partial}{\partial y} \left( 2kB + \frac{\partial F}{\partial y} \right) &= 0, \\ \Rightarrow 2kB + \frac{\partial F}{\partial y} &= \alpha, \end{aligned} \quad (\text{C.22})$$

where  $\alpha$  is a constant to be determined.

The second is

$$\begin{aligned} \frac{\partial}{\partial y} \left( 2kC + \frac{\partial E}{\partial y} + \frac{(\gamma - 1) \rho_0 \nu}{\gamma p_0} \left( -\frac{V_0^2 k^2 y^2}{2L^2} + \frac{V_0^2}{2L^2} \right) \right. \\ + \frac{\rho_0}{\gamma p_0} \frac{B_0^2}{4\rho_0} \frac{\nu k^2 V_0^2}{V_A^2} \left( \frac{y^2}{L^2} - 1 \right) \left. \right) \\ + \frac{\rho_0}{\gamma p_0} \nu \left( -4k^2 F + \frac{4}{3} \frac{\partial^2 F}{\partial y^2} + 2k \frac{1}{3} \frac{\partial B}{\partial y} \right) = 0. \end{aligned} \quad (\text{C.23})$$

We can now write Equation (C.18) for  $v_x$  as

$$\begin{aligned} & -2k \frac{\gamma p_0}{\rho_0} \left( \left( 2k(Bt + C) + \frac{\partial(Ft + E)}{\partial y} \right) + \frac{(\gamma - 1)\nu\rho_0}{\gamma p_0} \left( -\frac{V_0^2 k^2 y^2}{2L^2} + \frac{V_0^2}{2L^2} \right) \right. \\ & + \frac{1}{\gamma p_0} \frac{B_0^2}{4} \frac{\nu k^2 V_0^2}{V_A^2} \left( \frac{y^2}{L^2} - 1 \right) \left. \right) + \frac{B_0^2}{\rho_0} \left( -4k^2(Bt + C) + \frac{\partial^2(Bt + C)}{\partial y^2} \right) \\ & - \frac{B_0^2}{\rho_0} \frac{k V_0^2 t}{L^2} + \nu \frac{\partial}{\partial t} \left( -4k^2 \frac{4}{3}(Bt + C) + \frac{\partial^2(Bt + C)}{\partial y^2} - 2k \frac{1}{3} \frac{\partial(Ft + E)}{\partial y} \right) = 0. \end{aligned}$$

Separating this equation as two equations for the coefficient of  $t$  and a constant-time equation. The first is

$$\begin{aligned} & -2k \frac{\gamma p_0}{\rho_0} \left( 2kB + \frac{\partial F}{\partial y} \right) + \frac{B_0^2}{\rho_0} \left( -4k^2 B + \frac{\partial^2 B}{\partial y^2} \right) - \frac{B_0^2}{\rho_0} \frac{k V_0^2}{L^2} = 0, \\ \Rightarrow & -2k \frac{\gamma p_0}{\rho_0} \alpha + \frac{B_0^2}{\rho_0} \left( -4k^2 B + \frac{\partial^2 B}{\partial y^2} \right) - \frac{B_0^2}{\rho_0} \frac{k V_0^2}{L^2} = 0, \end{aligned} \quad (C.24)$$

where Equation (C.22) was substituted in the second line.

The second is

$$\begin{aligned} & -2k \frac{\gamma p_0}{\rho_0} \left( \left( 2kC + \frac{\partial E}{\partial y} \right) + \frac{(\gamma - 1)\rho_0 \nu}{\gamma p_0} \left( -\frac{V_0^2 k^2 y^2}{2L^2} + \frac{V_0^2}{L^2} \right) \right. \\ & + \frac{\rho_0}{\gamma p_0} \frac{B_0^2}{4\rho_0} \frac{\nu k^2 V_0^2}{V_A^2} \left( \frac{y^2}{L^2} - 1 \right) \left. \right) \\ & + \frac{B_0^2}{\rho_0} \left( -4k^2 C + \frac{\partial^2 C}{\partial y^2} \right) + \nu \left( -4 \frac{4}{3} k^2 B + \frac{\partial^2 B}{\partial y^2} - 2k \frac{1}{3} \frac{\partial F}{\partial y} \right) = 0, \end{aligned} \quad (C.25)$$

In summary our system of equations for the functions:  $B(y)$ ,  $C(y)$ ,  $E(y)$  and  $F(y)$ , are

$$-2k \frac{\gamma p_0}{\rho_0} \alpha + \frac{B_0^2}{\rho_0} \left( -4k^2 B + \frac{\partial^2 B}{\partial y^2} \right) - \frac{B_0^2}{\rho_0} \frac{k V_0^2}{L^2} = 0, \quad (C.26)$$

$$2kB + \frac{\partial F}{\partial y} = \alpha, \quad (C.27)$$

$$\begin{aligned} & -2k \frac{\gamma p_0}{\rho_0} \left( \left( 2kC + \frac{\partial E}{\partial y} \right) + \frac{(\gamma - 1)\rho_0 \nu}{\gamma p_0} \left( -\frac{V_0^2 k^2 y^2}{2L^2} + \frac{V_0^2}{2L^2} \right) + \frac{\rho_0}{\gamma p_0} \frac{B_0^2}{4\rho_0} \frac{\nu k^2 V_0^2}{V_A^2} \left( \frac{y^2}{L^2} - 1 \right) \right) \\ & + \frac{B_0^2}{\rho_0} \left( -4k^2 C + \frac{\partial^2 C}{\partial y^2} \right) + \nu \left( -4k^2 \frac{4}{3} B + \frac{\partial^2 B}{\partial y^2} - 2k \frac{1}{3} \frac{\partial F}{\partial y} \right) = 0, \end{aligned} \quad (C.28)$$

$$\begin{aligned} & \frac{\partial}{\partial y} \left( 2kC + \frac{\partial E}{\partial y} + \frac{(\gamma - 1)\rho_0 \nu}{\gamma p_0} \left( -\frac{V_0^2 k^2 y^2}{2L^2} + \frac{V_0^2}{2L^2} \right) + \frac{\rho_0}{\gamma p_0} \frac{B_0^2}{4\rho_0} \frac{\nu k^2 V_0^2}{V_A^2} \left( \frac{y^2}{L^2} - 1 \right) \right) \\ & + \frac{\rho_0}{\gamma p_0} \nu \left( -4k^2 F + \frac{4}{3} \frac{\partial^2 F}{\partial y^2} + 2k \frac{1}{3} \frac{\partial B}{\partial y} \right) = 0. \end{aligned} \quad (C.29)$$

These four equations derived from the momentum equations for  $v_{2x}$  and  $v_{2y}$  form a system of equation that can be solved to give solutions for  $B(y)$ ,  $C(y)$ ,  $F(y)$  and  $E(y)$ .

The first, Equation (C.26), can be solved for  $B(y)$  as

$$\begin{aligned} -4k^2 B + \frac{\partial^2 B}{\partial y^2} &= \frac{kV_0^2}{L^2} + 2k \frac{\gamma p_0}{\rho_0} \frac{\rho_0}{B_0^2} \alpha = k\delta, \\ \Rightarrow B(y) &= \frac{\delta}{4k} \left( \frac{\cosh(2ky)}{\cosh(2kL)} - 1 \right), \end{aligned} \quad (\text{C.30})$$

where  $\delta$  is substituted for the RHS to simplify notation.

Now we can solve the second equation, Equation (C.27), for  $F(y)$

$$\begin{aligned} \frac{\partial F}{\partial y} &= \alpha - 2kB, \\ \Rightarrow &= \alpha - \frac{\delta}{2} \left( \frac{\cosh(2ky)}{\cosh(2kL)} - 1 \right), \\ \Rightarrow F(y) &= \left( \alpha + \frac{\delta}{2} \right) y - \frac{\delta}{4k} \frac{\sinh(2ky)}{\cosh(2kL)}. \end{aligned} \quad (\text{C.31})$$

Applying boundary conditions:  $F(\pm L) = 0$ , gives  $\alpha$

$$\alpha = \frac{\delta}{4kL} \tanh(2kL) - \frac{\delta}{2}. \quad (\text{C.32})$$

The fourth equation, Equation (C.29), can be simplified now

$$\begin{aligned} &\left( 2kC + \frac{\partial E}{\partial y} + \frac{(\gamma - 1)\rho_0\nu}{\gamma p_0} \left( -\frac{V_0^2 k^2 y^2}{2L^2} + \frac{V_0^2}{2L^2} \right) + \frac{\rho_0}{\gamma p_0} \frac{B_0^2}{4\rho_0} \frac{\nu k^2 V_0^2}{V_A^2} \left( \frac{y^2}{L^2} - 1 \right) \right), \\ &= \int \frac{\rho_0}{\gamma p_0} \nu 4k^2 \left( \alpha + \frac{\delta}{2} \right) y \, dy, \\ &= \frac{\rho_0}{\gamma p_0} \nu 2k^2 \left( \alpha + \frac{\delta}{2} \right) y^2 + \nu\kappa, \end{aligned} \quad (\text{C.33})$$

where  $\kappa$  is a constant.

The RHS of the third equation, Equation (C.28) can now be written as

$$\begin{aligned} &-2k \frac{\gamma p_0}{\rho_0} \left( \frac{\rho_0}{\gamma p_0} \nu 2k^2 \left( \alpha + \frac{\delta}{2} \right) y^2 + \nu\kappa \right) + \frac{B_0^2}{\rho_0} \left( -4k^2 C + \frac{\partial^2 C}{\partial y^2} \right) \\ &= -\nu \left( -4\frac{4}{3}k^2 B + \frac{\partial^2 B}{\partial y^2} - 2k \frac{1}{3} \frac{\partial F}{\partial y} \right), \\ &= -\nu k \left( \delta - \frac{2}{3}\alpha \right). \end{aligned}$$



Rearranging the equation for  $C(y)$  is

$$\begin{aligned} \frac{B_0^2}{\rho_0} \left( -4k^2 C + \frac{\partial^2 C}{\partial y^2} \right) &= 2k \frac{\gamma p_0}{\rho_0} \left( \frac{\rho_0}{\gamma p_0} \nu 2k^2 \left( \alpha + \frac{\delta}{2} \right) y^2 + \nu \kappa \right) - \nu k \left( \delta - \frac{2}{3} \alpha \right) \\ &= 2k \nu 2k^2 \left( \alpha + \frac{\delta}{2} \right) y^2 + k \left( 2 \frac{\gamma p_0}{\rho_0} \nu \kappa - \nu \left( \delta - \frac{2}{3} \alpha \right) \right), \\ \Rightarrow -4k^2 C + \frac{\partial^2 C}{\partial y^2} &= 2k \frac{\rho_0}{B_0^2} \nu 2k^2 \left( \alpha + \frac{\delta}{2} \right) y^2 + \frac{\rho_0}{B_0^2} k \left( 2 \frac{\gamma p_0}{\rho_0} \nu \kappa - \nu \left( \delta - \frac{2}{3} \alpha \right) \right). \end{aligned}$$

The solution,  $C(y)$ , is

$$\begin{aligned} C(y) &= \frac{\nu}{2k} \frac{\rho_0}{B_0^2} \left( \alpha + \frac{\delta}{2} \right) \left( \frac{\cosh(2ky)}{\cosh(2kL)} (2k^2 L^2 + 1) - (2k^2 y^2 + 1) \right) \\ &\quad + \frac{1}{4k} \frac{\rho_0}{B_0^2} \left( 2 \frac{\gamma p_0}{\rho_0} \nu \left( \kappa - \left( \delta - \frac{2}{3} \alpha \right) \right) \right) \left( \frac{\cosh(2ky)}{\cosh(2kL)} - 1 \right). \end{aligned} \quad (C.34)$$

We can finally substitute for  $C(y)$  in Equation (C.33) to give

$$\begin{aligned} \frac{\partial E}{\partial y} \frac{\rho_0}{\gamma p_0} \nu 2k^2 \left( \alpha + \frac{\delta}{2} \right) y^2 - \frac{(\gamma - 1) \rho_0 \nu}{\gamma p_0} \left( -\frac{V_0^2 k^2 y^2}{2L^2} + \frac{V_0^2}{2L^2} \right) - \frac{\rho_0}{\gamma p_0} \frac{B_0^2}{4\rho_0} \frac{\nu k^2 V_0^2}{V_A^2} \left( \frac{y^2}{L^2} - 1 \right) \\ - 2kC + \nu \kappa \\ = \frac{\rho_0}{\gamma p_0} \nu 2k^2 \left( \alpha + \frac{\delta}{2} \right) y^2 - \frac{(\gamma - 1) \rho_0 \nu}{\gamma p_0} \left( -\frac{V_0^2 k^2 y^2}{2L^2} + \frac{V_0^2}{2L^2} \right) - \frac{\rho_0}{\gamma p_0} \frac{B_0^2}{4\rho_0} \frac{\nu k^2 V_0^2}{V_A^2} \left( \frac{y^2}{L^2} - 1 \right) \\ - \nu \frac{\rho_0}{B_0^2} \left( \alpha + \frac{\delta}{2} \right) \left( \frac{\cosh(2ky)}{\cosh(2kL)} (2k^2 L^2 + 1) - (2k^2 y^2 + 1) \right) \\ - \frac{1}{2} \frac{\rho_0}{B_0^2} \left( 2 \frac{\gamma p_0}{\rho_0} \nu \left( \kappa - \left( \delta - \frac{2}{3} \alpha \right) \right) \right) \left( \frac{\cosh(2ky)}{\cosh(2kL)} - 1 \right) + \kappa \end{aligned} \quad (C.35)$$

The solution for  $E(y)$  is

$$\begin{aligned} E(y) &= \frac{\rho_0}{\gamma p_0} \nu 2k^2 \left( \alpha + \frac{\delta}{2} \right) \frac{y^3}{3} - \frac{(\gamma - 1) \rho_0 \nu}{\gamma p_0} \left( -\frac{V_0^2 k^2 y^3}{6L^2} + \frac{V_0^2}{2L^2} y \right) - \frac{\rho_0}{\gamma p_0} \frac{B_0^2}{4\rho_0} \frac{\nu k^2 V_0^2}{V_A^2} \left( \frac{y^3}{3L^2} - y \right) \\ &\quad - \nu \frac{\rho_0}{B_0^2} \left( \alpha + \frac{\delta}{2} \right) \left( \frac{\sinh(2ky)}{2k \cosh(2kL)} (2k^2 L^2 + 1) - \left( 2k^2 \frac{y^3}{3} + y \right) \right) \\ &\quad - \frac{1}{2} \frac{\rho_0}{B_0^2} \left( 2 \frac{\gamma p_0}{\rho_0} \nu \left( \kappa - \left( \delta - \frac{2}{3} \alpha \right) \right) \right) \left( \frac{\sinh(2ky)}{2k \cosh(2kL)} - y \right) + \nu \kappa y \end{aligned} \quad (C.36)$$

This solution for  $E(y)$  can be written

$$\begin{aligned}
 E(y) = & \left( -\frac{1}{2}\nu \left( \alpha + \frac{\delta}{2} \right) (2L^2k^2 + 1) - \frac{1}{4} \left( 2c_s^2\nu \left( \kappa - \left( \delta - \frac{2}{3}\alpha \right) \right) \right) \right) \frac{\sinh(2ky)}{kV_A^2 \cosh(2kL)} \\
 & + \left( \frac{2}{3} \frac{k^2\nu \left( \alpha + \frac{\delta}{2} \right)}{c_s^2} - \frac{1}{12} \frac{k^2V_0^2\nu}{c_s^2L^2} + \frac{2}{3} \frac{\nu k^2 \left( \alpha + \frac{\delta}{2} \right)}{V_A^2} + \frac{1}{6} \frac{(\gamma - 1)\rho_0\nu k^2V_0^2}{\gamma p_0L^2} \right) y^3 \\
 & + \left( \frac{1}{4} \frac{\nu k^2V_0^2}{c_s^2} + \frac{\nu \left( \alpha + \frac{\delta}{2} \right)}{V_A^2} + \frac{1}{2} \frac{2c_s^2\nu(\kappa - (\delta - \frac{2}{3}\alpha))}{V_A^2} + \nu\kappa - \frac{1}{2} \frac{(\gamma - 1)\rho_0\nu V_0^2}{\gamma p_0L^2} \right) y.
 \end{aligned} \tag{C.37}$$

Thus the boundary conditions are satisfied by setting

$$\begin{aligned}
 \nu\kappa = & -\frac{2}{3} \frac{1}{\gamma p_0LB_0^2 \left( -\frac{1}{2}\gamma p_0 \tanh(2kL) + kL(\gamma p_0 + B_0^2) \right)} \times \\
 & \left( \rho_0\nu \left( -\frac{3}{2}\gamma \left( \alpha k^2 (\gamma p_0 + B_0^2) L^2 + \frac{1}{2} \left( V_0^2k^2 + \frac{4}{3}\alpha \right) B_0^2 \right) Lp_0 \tanh(2kL) \right. \right. \\
 & + k \left( k^2\alpha (\gamma p_0 + B_0^2)^2 L^4 + \frac{1}{4}B_0^2 (V_0^2 ((B_0^2 + p_0)\gamma + 2B_0^2) k^2 + 8\alpha\gamma p_0) L^2 \right. \\
 & \left. \left. \left. - \frac{3}{4}B_0^4V_0^2(\gamma - 1) \right) \right) \right)
 \end{aligned} \tag{C.38}$$

In summary the full solutions for  $v_{2x}$  and  $v_{2y}$  are

$$v_{2x}(x, y, t) = (B(y)t + C(y)) \sin(2kx), \tag{C.39}$$

$$v_{2y}(x, y, t) = (F(y)t + E(y)) \cos(2kx) + G(y), \tag{C.40}$$

where

$$G(y) = -\frac{1}{6} \frac{\nu k^2 V_0^2 \rho_0 (\gamma - \frac{1}{2})}{\gamma p_0 L^2} y(L-y)(L+y), \quad (\text{C.41})$$

$$B(y) = \frac{\delta}{4k} \left( \frac{\cosh(2ky)}{\cosh(2kL)} - 1 \right), \quad (\text{C.42})$$

$$C(y) = \frac{\nu}{2k} \frac{\rho_0}{B_0^2} \left( \alpha + \frac{\delta}{2} \right) \left( \frac{\cosh(2ky)}{\cosh(2kL)} (2k^2 L^2 + 1) - (2k^2 y^2 + 1) \right) \\ + \frac{1}{4k} \frac{\rho_0}{B_0^2} \left( 2 \frac{\gamma p_0}{\rho_0} \kappa - \nu \left( \delta - \frac{2}{3} \alpha \right) \right) \left( \frac{\cosh(2ky)}{\cosh(2kL)} - 1 \right), \quad (\text{C.43})$$

$$F(y) = \left( \alpha + \frac{\delta}{2} \right) y - \frac{\delta}{4k} \frac{\sinh(2ky)}{\cosh(2kL)}, \quad (\text{C.44})$$

$$E(y) = \left( -\frac{1}{2} \nu \left( \alpha + \frac{\delta}{2} \right) (2L^2 k^2 + 1) - \frac{1}{4} \left( 2C_s^2 \kappa - \nu \left( \delta - \frac{2}{3} \alpha \right) \right) \right) \frac{\sinh(2ky)}{k V_A^2 \cosh(2kL)} \\ + \left( \frac{2}{3} \frac{k^2 \nu (\alpha + \frac{\delta}{2})}{C_s^2} - \frac{1}{12} \frac{k^2 V_0^2 \nu}{C_s^2 L^2} + \frac{2}{3} \frac{\nu k^2 (\alpha + \frac{\delta}{2})}{V_A^2} + \frac{1}{6} \frac{(\gamma - 1) \rho_0 \nu k^2 V_0^2}{\gamma p_0 L^2} \right) y^3 \\ + \left( \frac{1}{4} \frac{\nu k^2 V_0^2}{C_s^2} + \frac{\nu (\alpha + \frac{\delta}{2})}{V_A^2} + \frac{1}{2} \frac{2C_s^2 \kappa - \nu (\delta - \frac{2}{3} \alpha)}{V_A^2} + \kappa - \frac{1}{2} \frac{(\gamma - 1) \rho_0 \nu k^2 V_0^2}{\gamma p_0 L^2} \right) y, \quad (\text{C.45})$$

$$\delta = \frac{V_0^2}{L^2} + 2 \frac{C_s^2}{V_A^2} \alpha. \quad (\text{C.46})$$

The boundary conditions:  $\mathbf{v}_2(x, \pm L, z, t) = 0$  are automatically satisfied for  $v_{2x}$  and are ensured for  $v_{2y}$  by the definitions of  $\alpha$ ,  $\lambda$ , and  $\kappa$  Equations (C.32), (C.16) and (C.38).

We can now derive expressions for  $\rho_0$  and  $p$ .

$$\frac{\partial p_2}{\partial t} = -\gamma p_0 \left( \frac{\partial v_{2x}}{\partial x} + \frac{\partial v_{2y}}{\partial y} \right) + (\gamma - 1) \nu \rho_0 \left( \left( \frac{\partial v_{z1}}{\partial x} \right)^2 + \left( \frac{\partial v_{z1}}{\partial y} \right)^2 \right), \\ = -\gamma p_0 \left( 2k(Bt + C) \cos(2kx) + \frac{\partial((Ft + E) \cos(2kx) + G)}{\partial y} \right) \\ + (\gamma - 1) \rho_0 \nu \left( \frac{V_0^2 k^2 y^2}{L^2} \cos^2(kx) + \frac{V_0^2}{L^2} \sin^2(kx) \right) \\ = -\gamma p_0 \left( \left( 2kB + \frac{\partial F}{\partial y} \right) t \cos(2kx) + \left( 2kC + \frac{\partial E}{\partial y} \right) \cos(2kx) + \frac{\partial G}{\partial y} \right) \\ + (\gamma - 1) \rho_0 \nu \left( \frac{V_0^2 k^2 y^2}{2L^2} (1 + \cos(2kx)) + \frac{V_0^2}{2L^2} (1 - \cos(2kx)) \right) \\ \Rightarrow p_2 = -\gamma p_0 \left( \left( (2kB(y) + F'(y)) \frac{t^2}{2} + (2kC(y) + E'(y)) t \right) \cos(2kx) + G'(y) t \right) \\ + \rho_0 (\gamma - 1) \nu \left( \frac{V_0^2 k^2 y^2}{2L^2} (1 + \cos(2kx)) + \frac{V_0^2}{2L^2} (1 - \cos(2kx)) \right) t \\ + J_1(y) \cos(2kx) + J_2(y) \quad (\text{C.47})$$

where  $J_1(y)$  and  $J_2(y)$  are functions to be determined.

The equation for  $\rho_2$  is similar so

$$\rho_2 = -\rho_0 \left( \left( (2kB(y) + F'(y)) \frac{t^2}{2} + (2kC(y) + E'(y)) t \right) \cos(2kx) + G'(y)t \right). \quad (\text{C.48})$$

The solutions for  $B_{2x}$  and  $B_{2y}$  are

$$\begin{aligned} \frac{\partial B_{2x}}{\partial t} &= B_0 \frac{\partial v_{2x}}{\partial y}, \\ &= B_0 \frac{\partial(Bt + C)}{\partial y} \sin(2kx), \\ \Rightarrow B_{2x} &= B_0 \left( B'(y) \frac{t^2}{2} + C'(y)t \right) \sin(2kx) + M(y) \sin(2kx). \end{aligned} \quad (\text{C.49})$$

$$\begin{aligned} \frac{\partial B_{2y}}{\partial t} &= -B_0 \frac{\partial v_{2x}}{\partial x}, \\ &= -B_0(Bt + C)2k \cos(2kx), \\ \Rightarrow B_{2y} &= -B_0 \left( B(y) \frac{t^2}{2} + C(y)t \right) 2k \cos(2kx) + H(y) \cos(2kx). \end{aligned} \quad (\text{C.50})$$

where  $M(y)$  and  $H(y)$  can be determined.

Currently these solutions satisfy the equations including viscosity for the coefficients of  $t$ , i.e  $F$  and  $B$ . The undetermined functions  $J_1(y)$ ,  $J_2(y)$ ,  $M$  and  $H$  can be determined by considering the original equations.

The equation for  $v_{2y}$  is

$$\begin{aligned} \rho_0 \frac{\partial v_{2y}}{\partial t} &= -\frac{\partial}{\partial y} (p_2 + B_{1z}^2) + \rho_0 \nu \left( \frac{\partial^2 v_{2y}}{\partial x^2} + \frac{4}{3} \frac{\partial^2 v_{2y}}{\partial y^2} + \frac{2k}{3} \frac{\partial v_{2x}}{\partial y} \right), \\ \rho_0 \frac{\partial((Ft + E) \cos(2kx) + G)}{\partial t} &= -\frac{\partial}{\partial y} (p_2 + B_{1z}^2) \\ &+ \rho_0 \nu \left( \frac{\partial^2((Ft + E) \cos(2kx) + G)}{\partial x^2} + \frac{4}{3} \frac{\partial^2((Ft + E) \cos(2kx) + G)}{\partial y^2} \right. \\ &\left. + \frac{2k}{3} \frac{\partial(Bt + C)}{\partial y} \right). \end{aligned}$$

Separating this equation into coefficients of powers of  $t$  gives

$$\begin{aligned}
 t^2 \quad 0 &= -\frac{\partial}{\partial y} \left( p_2 - \frac{B_0^2 V_0^2}{4\mu L^2} \right), \\
 t \cos(2kx) \quad 0 &= -\frac{\partial}{\partial y} \left( p_2 - \frac{B_0^2 \nu k^2 V_0^2}{4\mu V_A^2} \left( \frac{y^2}{L^2} - 1 \right) \right) \\
 &\quad + \rho_0 \nu \left( -4k^2 F + \frac{4}{3} \frac{\partial^2 F}{\partial y^2} + \frac{2k}{3} \frac{\partial B}{\partial y} \right), \\
 \cos(2kx) \quad \rho_0 F &= -\frac{\partial}{\partial y} \left( J_1 - \frac{B_0^2 \nu^2 V_0^2 L^2 k^4}{4\mu 4V_A^4} \left( \frac{y^2}{L^2} - 1 \right)^2 \right) \\
 &\quad + \rho_0 \nu \left( -4k^2 E + \frac{4}{3} \frac{\partial^2 E}{\partial y^2} + \frac{2k}{3} \frac{\partial C}{\partial y} \right), \\
 t^0 \quad 0 &= -\frac{\partial}{\partial y} \left( J_2 + \frac{B_0^2 \nu^2 V_0^2 L^2 k^4}{4\mu 4V_A^4} \left( \frac{y^2}{L^2} - 1 \right)^2 \right) + \rho_0 \nu \frac{4}{3} \frac{\partial^2 G}{\partial y^2}.
 \end{aligned}$$

Substituting the appropriate terms of  $p_2$  show that the first and second equations are satisfied already. The fourth is solved by setting

$$J_2(y) = \rho_0 \nu \frac{4}{3} G'(y) - \frac{B_0^2 k^4 \nu^2 V_0^2 L^2}{4\mu 4V_A^4} \left( \frac{y^2}{L^2} - 1 \right)^2. \quad (\text{C.51})$$

The third equation written in full is

$$\frac{\partial}{\partial y} \left( J_1 - \frac{B_0^2 \nu^2 k^4 V_0^2 L^2}{4\mu 4V_A^4} \left( \frac{y^2}{L^2} - 1 \right)^2 \right) = -\rho_0 F + \rho_0 \nu \left( -4k^2 E + \frac{4}{3} \frac{\partial^2 E}{\partial y^2} + \frac{2k}{3} \frac{\partial C}{\partial y} \right). \quad (\text{C.52})$$

Integrating gives

$$\begin{aligned}
 j_1(y) &= \frac{\rho_0 \nu^2 k^4 V_0^2 L^2}{4 4V_A^2} \left( \frac{y^2}{L^2} - 1 \right)^2 + \rho_0 \nu \left( \frac{4}{3} E'(y) + \frac{2k}{3} C(y) \right) \\
 &\quad - \int (\rho_0 F(y) + \rho_0 \nu 4k^2 E(y)) dy.
 \end{aligned}$$

Similarly the coefficients of terms in the momentum equation for  $v_{2x}$  are

$$\begin{aligned}
 t^2 \sin(2kx) \quad 0 &= 2k \left( p_2 - \frac{B_0^2}{4\mu} \frac{V_0^2 k^2}{L^2} \right) + \frac{B_0}{\mu} \left( \frac{\partial B_x}{\partial y} + 2kB_y \right), \\
 t \sin(2kx) \quad 0 &= 2k \left( p_2 - \frac{B_0^2}{4\mu} \frac{\nu V_0^2 k^2}{V_A^2} \left( \frac{y^2}{L^2} - 1 \right) \right) + \frac{B_0}{\mu} \left( \frac{\partial B_x}{\partial y} + 2kB_y \right) \\
 &\quad + \nu \rho_0 \left( -4\frac{4}{3}k^2 B + \frac{\partial^2 B}{\partial y^2} - \frac{2k}{3} \frac{\partial D}{\partial y} \right) \\
 \sin(2kx) \quad \rho_0 B &= 2k \left( J_1 - \frac{B_0^2}{4\mu} \frac{\nu^2 k^4 V_0^2 L^2}{4V_A^4} \left( \frac{y^2}{L^2} - 1 \right)^2 \right) + \frac{B_0}{\mu} \left( \frac{\partial M}{\partial y} + 2kH \right) \\
 &\quad + \rho_0 \nu \left( -4k^2 \frac{4}{3} C + \frac{\partial^2 C}{\partial y^2} - \frac{2k}{3} \frac{\partial E}{\partial y} \right). \tag{C.53}
 \end{aligned}$$

The first two equations are already satisfied. The third can be solved for  $M(y)$  and  $H(y)$ . These functions are related by using the solenoidal constraint

$$\frac{\partial H}{\partial y} = -2kM \tag{C.54}$$

Differentiating by  $x$  (remember this is multiplied by  $\sin(2kx)$  so simply multiply by  $2k$ .)

$$\begin{aligned}
 \frac{B_0}{\mu} \left( -4k^2 H - \frac{\partial}{\partial y} 2kM \right) &= 4k^2 \left( J_1 - \frac{B_0^2}{4\mu} \frac{\nu^2 k^4 V_0^2 L^2}{4V_A^4} \left( \frac{y^2}{L^2} - 1 \right) \right) \\
 &\quad + \rho_0 \nu 2k \left( -4k^2 \frac{4}{3} C + \frac{\partial^2 C}{\partial y^2} - \frac{2k}{3} \frac{\partial E}{\partial y} \right) - \rho_0 2kB \\
 \Rightarrow -4k^2 H + \frac{\partial^2 H}{\partial y^2} &= \frac{4k^2 B_0}{\rho_0 V_A^2} \left( J_1 - \frac{B_0^2}{4\mu} \frac{\nu^2 k^4 V_0^2 L^2}{4V_A^4} \left( \frac{y^2}{L^2} - 1 \right) \right) \\
 &\quad + \frac{\nu 2kB_0}{V_A^2} \left( -4k^2 \frac{4}{3} C + \frac{\partial^2 C}{\partial y^2} - \frac{2k}{3} \frac{\partial E}{\partial y} \right) - \frac{2kB_0}{V_A^2} B. \tag{C.55}
 \end{aligned}$$

Once  $H(y)$  is known,  $M(y)$  can be determined from

$$M(y) = -\frac{1}{2k} H'(y). \tag{C.56}$$

### Summary

The full solutions for  $p_2$ ,  $\rho_2$ ,  $B_{2x}$  and  $B_{2y}$  are of the form.

$$p_2(x, y, t) = p(x, y, t) + J_1(y) \cos(2kx) + J_2(y),$$

$$\rho_2(x, y, t) = \rho(x, y, t)$$

$$B_{2x}(x, y, t) = B_x(x, y, t) + M(y) \sin(2kx),$$

$$B_{2y}(x, y, t) = B_y(x, y, t) + H(y) \cos(2kx),$$

where

$$p_2(x, y, t) = -\gamma p_0 \left( \left( (2kB(y) + F'(y)) \frac{t^2}{2} + (2kC(y) + E'(y)) t \right) \cos(2kx) + G'(y)t \right) \\ + \rho_0(\gamma - 1)\nu \left( \frac{V_0^2 k^2 y^2}{2L^2} (1 + \cos(2kx)) + \frac{V_0^2}{2L^2} (1 - \cos(2kx)) \right) t,$$

$$\rho_2(x, y, t) = -\rho_0 \left( \left( (2kB(y) + F'(y)) \frac{t^2}{2} + (2kC(y) + E'(y)) t \right) \cos(2kx) + G'(y)t \right) \\ + \rho_0(\gamma - 1)\nu \left( \frac{V_0^2 k^2 y^2}{2L^2} (1 + \cos(2kx)) + \frac{V_0^2}{2L^2} (1 - \cos(2kx)) \right) t,$$

$$B_x(x, y, t) = B_0(B'(y) \frac{t^2}{2} + C'(y)t) \sin(2kx),$$

$$B_y(x, y, t) = -B_0(B(y) \frac{t^2}{2} + C(y)t) 2k \cos(2kx),$$

$$J_1(y) = \frac{\rho_0 \nu^2 k^4 V_0^2 L^2}{4 V_A^2} \left( \frac{y^2}{L^2} - 1 \right)^2 + \rho_0 \nu \left( \frac{4}{3} E'(y) + \frac{2k}{3} C(y) \right) - \int (\rho_0 F(y) + \rho_0 \nu 4k^2 E(y)) dy,$$

$$J_2(y) = \rho_0 \nu \frac{4}{3} A'(y) - \frac{B_0^2 k^4 \nu^2 V_0^2 L^2}{4\mu V_A^4} \left( \frac{y^2}{L^2} - 1 \right)^2.$$

$M(y)$  and  $H(y)$  satisfy the equations

$$-4k^2 H + \frac{\partial^2 H}{\partial y^2} = \frac{4k^2 B_0}{\rho_0 V_A^2} \left( J_1 - \frac{B_0^2 \nu^2 k^4 V_0^2 L^2}{4\mu V_A^4} \left( \frac{y^2}{L^2} - 1 \right) \right) \\ + \frac{\nu 2k B_0}{V_A^2} \left( -4k^2 \frac{4}{3} C + \frac{\partial^2 C}{\partial y^2} - \frac{2k}{3} \frac{\partial E}{\partial y} \right) - \frac{2k B_0}{V_A^2} B \\ M(y) = -\frac{1}{2k} H'(y)$$

# Bibliography

- Alexakis, A. (2011). “Two-dimensional behavior of three-dimensional magnetohydrodynamic flow with a strong guiding field”. In: *Phys. Rev. E* 84.5, 056330, p. 056330. DOI: [10.1103/PhysRevE.84.056330](https://doi.org/10.1103/PhysRevE.84.056330). arXiv: [1109.2039 \[physics.flu-dyn\]](https://arxiv.org/abs/1109.2039).
- Alexakis, A. et al. (2007). “Anisotropic fluxes and nonlocal interactions in magnetohydrodynamic turbulence”. In: *Phys. Rev. E* 76.5, 056313, p. 056313. DOI: [10.1103/PhysRevE.76.056313](https://doi.org/10.1103/PhysRevE.76.056313). arXiv: [0708.0765 \[physics.flu-dyn\]](https://arxiv.org/abs/0708.0765).
- Arber, T.D. et al. (2001). “A Staggered Grid, Lagrangian–Eulerian Remap Code for 3-D MHD Simulations”. In: *Journal of Computational Physics* 171.1, pp. 151–181. ISSN: 0021-9991. DOI: [http://dx.doi.org/10.1006/jcph.2001.6780](https://doi.org/10.1006/jcph.2001.6780). URL: <http://www.sciencedirect.com/science/article/pii/S0021999101967804>.
- Asgari-Targhi, M. and A. A. van Ballegooijen (2012). “Model for Alfvén Wave Turbulence in Solar Coronal Loops: Heating Rate Profiles and Temperature Fluctuations”. In: *ApJ* 746, 81, p. 81. DOI: [10.1088/0004-637X/746/1/81](https://doi.org/10.1088/0004-637X/746/1/81).
- Asgari-Targhi, M. et al. (2013). “The Spatial and Temporal Dependence of Coronal Heating by Alfvén Wave Turbulence”. In: *ApJ* 773, 111, p. 111. DOI: [10.1088/0004-637X/773/2/111](https://doi.org/10.1088/0004-637X/773/2/111). arXiv: [1306.6038 \[astro-ph.SR\]](https://arxiv.org/abs/1306.6038).
- Bhattacharjee, A. and C. S. Ng (2001). “Random Scattering and Anisotropic Turbulence of Shear Alfvén Wave Packets”. In: *ApJ* 548, pp. 318–322. DOI: [10.1086/318692](https://doi.org/10.1086/318692).
- Bhattacharjee, A., C. S. Ng, and S. R. Spangler (1998). “Weakly Compressible Magnetohydrodynamic Turbulence in the Solar Wind and the Interstellar Medium”. In: *ApJ* 494, pp. 409–418. DOI: [10.1086/305184](https://doi.org/10.1086/305184).
- Bhattacharjee, A and CS Ng (1999). “Reduced Models of Magnetohydrodynamic Turbulence in the Interstellar Medium and the Solar Wind”. In: *Nonlinear MHD Waves and Turbulence*, pp. 182–197.
- Bhattacharjee, A. et al. (1999). “A comparative study of four-field and fully compressible magnetohydrodynamic turbulence in the solar wind”. In: *J. Geophys. Res.* 104, pp. 24835–24844. DOI: [10.1029/1999JA900327](https://doi.org/10.1029/1999JA900327).
- Biskamp, Dieter (1993). *Nonlinear Magnetohydrodynamics*. Cambridge Monographs on Plasma Physics. Cambridge University Press. DOI: [10.1017/CB09780511599965](https://doi.org/10.1017/CB09780511599965).
- Bowness, R., A. W. Hood, and C. E. Parnell (2013). “Coronal heating and nanoflares: current sheet formation and heating”. In: *A&A* 560, A89, A89. DOI: [10.1051/0004-6361/201116652](https://doi.org/10.1051/0004-6361/201116652).
- Boyd, T. J. M. and J. J. Sanderson (2003). *The Physics of Plasmas*. Cambridge University Press. DOI: [10.1017/CB09780511755750](https://doi.org/10.1017/CB09780511755750).
- Browning, P. K. and A. W. Hood (1989). “The shape of twisted, line-tied coronal loops”. In: *Sol. Phys.* 124, pp. 271–288. DOI: [10.1007/BF00156270](https://doi.org/10.1007/BF00156270).



- Dahlburg, R. B., A. F. Rappazzo, and M. Velli (2010). “Turbulence, Energy Transfers and Reconnection in Compressible Coronal Heating Field-line Tangling Models”. In: *Twelfth International Solar Wind Conference* 1216, pp. 40–43. DOI: [10.1063/1.3395890](#). arXiv: [0912.1063 \[astro-ph.SR\]](#).
- Dahlburg, R. B. et al. (2012). “Turbulent coronal heating mechanisms: coupling of dynamics and thermodynamics”. In: *A&A* 544, L20, p. L20. DOI: [10.1051/0004-6361/201219752](#). arXiv: [1208.2459 \[astro-ph.SR\]](#).
- Dahlburg, R. B. et al. (2016). “Observational Signatures of Coronal Loop Heating and Cooling Driven by Footpoint Shuffling”. In: *ApJ* 817, 47, p. 47. DOI: [10.3847/0004-637X/817/1/47](#). arXiv: [1512.03079 \[astro-ph.SR\]](#).
- Dahlburg, R. B. et al. (2018). “Dependence of Coronal Loop Temperature on Loop Length and Magnetic Field Strength”. In: *ApJ* 868, 116, p. 116. DOI: [10.3847/1538-4357/aae535](#).
- Denton, R. E., B. Rogers, and W. Lotko (2007). “Reduced magnetohydrodynamic equations with coupled Alfvén and sound wave dynamics”. In: *Physics of Plasmas* 14.10, 102906, p. 102906. DOI: [10.1063/1.2786060](#).
- Dmitruk, P. and D. Gómez (1997). “Two-dimensional magnetohydrodynamics and turbulent coronal heating”. In: *Two-Dimensional Turbulence in Plasmas and Fluids*. Ed. by R. L. Dewar and R. W. Griffiths. Vol. 414. American Institute of Physics Conference Series, pp. 205–211. DOI: [10.1063/1.54430](#).
- Dmitruk, P. and D. O. Gómez (1999). “Scaling Law for the Heating of Solar Coronal Loops”. In: *ApJ* 527, pp. L63–L66. DOI: [10.1086/312390](#). eprint: [astro-ph/9910329](#).
- Dmitruk, P., D. O. Gómez, and E. E. DeLuca (1998). “Magnetohydrodynamic Turbulence of Coronal Active Regions and the Distribution of Nanoflares”. In: *ApJ* 505, pp. 974–983. DOI: [10.1086/306182](#).
- Dmitruk, P. and W. H. Matthaeus (2003a). “Low-Frequency Waves and Turbulence in an Open Magnetic Region: Timescales and Heating Efficiency”. In: *ApJ* 597, pp. 1097–1105. DOI: [10.1086/378636](#).
- (2003b). “The timescales and heating efficiency of MHD wave-driven turbulence in an open magnetic region”. In: *Solar Wind Ten*. Ed. by M. Velli et al. Vol. 679. American Institute of Physics Conference Series, pp. 347–350. DOI: [10.1063/1.1618610](#).
- Dmitruk, P., W. H. Matthaeus, and S. Oughton (2005). “Compressible MHD and reduced MHD turbulence: direct numerical comparisons”. In: *AGU Fall Meeting Abstracts*.
- Dmitruk, P., L. J. Milano, and W. H. Matthaeus (2001). “Wave-driven Turbulent Coronal Heating in Open Field Line Regions: Nonlinear Phenomenological Model”. In: *ApJ* 548, pp. 482–491. DOI: [10.1086/318685](#).
- Dmitruk, P. et al. (2001). “Conditions for sustainment of magnetohydrodynamic turbulence driven by Alfvén waves”. In: *Physics of Plasmas* 8, pp. 2377–2384. DOI: [10.1063/1.1344563](#).
- Dmitruk, P. et al. (2002). “Coronal Heating Distribution Due to Low-Frequency, Wave-driven Turbulence”. In: *ApJ* 575, pp. 571–577. DOI: [10.1086/341188](#). eprint: [astro-ph/0204347](#).
- Einaudi, G. and F. Rubini (1986). “Resistive instabilities in a flowing plasma: I. Inviscid case”. In: *The Physics of Fluids* 29.8, pp. 2563–2568. DOI: [10.1063/1.865548](#). eprint: [https://aip.scitation.org/doi/pdf/10.1063/1.865548](#). URL: [https://aip.scitation.org/doi/abs/10.1063/1.865548](#).

- Einaudi, G. et al. (1996). “Energy Release in a Turbulent Corona”. In: *ApJ* 457, p. L113. DOI: [10.1086/309893](https://doi.org/10.1086/309893).
- Einaudi, Giorgio and Franco Rubini (1989). “Resistive instabilities in a flowing plasma. II. Effects of viscosity”. In: *Physics of Fluids B: Plasma Physics* 1.11, pp. 2224–2228. DOI: [10.1063/1.859038](https://doi.org/10.1063/1.859038). eprint: <https://doi.org/10.1063/1.859038>. URL: <https://doi.org/10.1063/1.859038>.
- Furth, H. P., J. Killeen, and M. N. Rosenbluth (1963). “Finite-Resistivity Instabilities of a Sheet Pinch”. In: *Physics of Fluids* 6, pp. 459–484. DOI: [10.1063/1.1706761](https://doi.org/10.1063/1.1706761).
- Galsgaard, K. and Å. Nordlund (1996). “Heating and activity of the solar corona 1. Boundary shearing of an initially homogeneous magnetic field”. In: *J. Geophys. Res.* 101, pp. 13445–13460. DOI: [10.1029/96JA00428](https://doi.org/10.1029/96JA00428).
- Gazol, A., T. Passot, and P. L. Sulem (1999). “Coupling between nonlinear Alfvén waves and reduced magnetohydrodynamics for compressible fluids”. In: *Physics of Plasmas* 6, pp. 3114–3122. DOI: [10.1063/1.873551](https://doi.org/10.1063/1.873551).
- (2000). “On the Reduced MHD for Compressible Fluids”. In: *Revista Mexicana de Astronomia y Astrofisica Conference Series*. Ed. by S. J. Arthur, N. S. Brickhouse, and J. Franco. Vol. 9. Revista Mexicana de Astronomia y Astrofisica, vol. 27, pp. 80–82.
- Goldreich, P. and S. Sridhar (1995). “Toward a theory of interstellar turbulence. 2: Strong alfvénic turbulence”. In: *ApJ* 438, pp. 763–775. DOI: [10.1086/175121](https://doi.org/10.1086/175121).
- Goldstraw, E. E. et al. (2018). “Comparison of methods for modelling coronal magnetic fields”. In: *A&A* 610, A48, A48. DOI: [10.1051/0004-6361/201731069](https://doi.org/10.1051/0004-6361/201731069). arXiv: [1711.07458 \[astro-ph.SR\]](https://arxiv.org/abs/1711.07458).
- Gomez, D. O., P. A. Dmitruk, and L. J. Milano (2000). “Recent theoretical results on coronal heating”. In: *Sol. Phys.* 195, pp. 299–318. DOI: [10.1023/A:1005283923956](https://doi.org/10.1023/A:1005283923956).
- Gómez, D. O. et al. (2001). “Magnetic Reconnection in Reduced Magnetohydrodynamics”. In: *Magnetic Fields Across the Hertzsprung-Russell Diagram*. Ed. by G. Mathys, S. K. Solanki, and D. T. Wickramasinghe. Vol. 248. Astronomical Society of the Pacific Conference Series, p. 157.
- Gómez, Daniel O, Swadesh M Mahajan, and Pablo Dmitruk (2008). “Hall magnetohydrodynamics in a strong magnetic field”. In: *Physics of Plasmas* 15.10, p. 102303.
- Hesse, M. and J. Birn (1993). “On the energy budget in the current disruption region”. In: *Geophys. Res. Lett.* 20, pp. 1451–1454. DOI: [10.1029/93GL01587](https://doi.org/10.1029/93GL01587).
- Huang, Y.-M. and E. G. Zweibel (2009). “Effects of line tying on resistive tearing instability in slab geometry”. In: *Physics of Plasmas* 16.4, 042102, p. 042102. DOI: [10.1063/1.3103789](https://doi.org/10.1063/1.3103789). arXiv: [0812.3190 \[physics.plasm-ph\]](https://arxiv.org/abs/0812.3190).
- Kadomtsev, B. B. and O. P. Pogutse (1974). “Nonlinear helical perturbations of a plasma in the tokamak”. In: *JETP* 38.2, p. 283.
- Kinney, R. and J. C. McWilliams (1997). “Magnetohydrodynamic equations under anisotropic conditions”. In: *Journal of Plasma Physics* 57, pp. 73–82. DOI: [10.1017/S0022377896005284](https://doi.org/10.1017/S0022377896005284).
- Kinney, R. M. and J. C. McWilliams (1998). “Turbulent cascades in anisotropic magnetohydrodynamics”. In: *Phys. Rev. E* 57, pp. 7111–7121. DOI: [10.1103/PhysRevE.57.7111](https://doi.org/10.1103/PhysRevE.57.7111).
- Klimchuk, J. A., S. Patsourakos, and P. J. Cargill (2008). “Highly Efficient Modeling of Dynamic Coronal Loops”. In: *ApJ* 682, pp. 1351–1362. DOI: [10.1086/589426](https://doi.org/10.1086/589426). arXiv: [0710.0185](https://arxiv.org/abs/0710.0185).
- Klimchuk, J. A. and P. A. Sturrock (1992). “Three-dimensional force-free magnetic fields and flare energy buildup”. In: *ApJ* 385, pp. 344–353. DOI: [10.1086/170943](https://doi.org/10.1086/170943).

- Kruger, S. E., C. C. Hegna, and J. D. Callen (1998). “Generalized reduced magnetohydrodynamic equations”. In: *Physics of Plasmas* 5, pp. 4169–4182. DOI: [10.1063/1.873152](https://doi.org/10.1063/1.873152).
- Longcope, D. W. and R. N. Sudan (1994). “Evolution and statistics of current sheets in coronal magnetic loops”. In: *ApJ* 437, pp. 491–504. DOI: [10.1086/175013](https://doi.org/10.1086/175013).
- Lothian, R. M. and A. W. Hood (1989). “Twisted magnetic flux tubes - Effect of small twist”. In: *Sol. Phys.* 122, pp. 227–244. DOI: [10.1007/BF00912994](https://doi.org/10.1007/BF00912994).
- Mackay, D. H. and A. A. van Ballegooijen (2006a). “Models of the Large-Scale Corona. I. Formation, Evolution, and Liftoff of Magnetic Flux Ropes”. In: *ApJ* 641, pp. 577–589. DOI: [10.1086/500425](https://doi.org/10.1086/500425).
- (2006b). “Models of the Large-Scale Corona. II. Magnetic Connectivity and Open Flux Variation”. In: *ApJ* 642, pp. 1193–1204. DOI: [10.1086/501043](https://doi.org/10.1086/501043).
- Mason, J. et al. (2012). “Numerical simulations of strong incompressible magnetohydrodynamic turbulence”. In: *Physics of Plasmas* 19.5, pp. 055902–055902. DOI: [10.1063/1.3694123](https://doi.org/10.1063/1.3694123). arXiv: [1202.3474](https://arxiv.org/abs/1202.3474) [physics.plasm-ph].
- Mellor, C. et al. (2005). “Numerical Simulations of the Flux Tube Tectonics Model for Coronal Heating”. In: *Sol. Phys.* 227, pp. 39–60. DOI: [10.1007/s11207-005-1713-2](https://doi.org/10.1007/s11207-005-1713-2).
- Meyer, K. A., D. H. Mackay, and A. A. van Ballegooijen (2012). “Solar Magnetic Carpet II: Coronal Interactions of Small-Scale Magnetic Fields”. In: *Sol. Phys.* 278, pp. 149–175. DOI: [10.1007/s11207-011-9924-1](https://doi.org/10.1007/s11207-011-9924-1). arXiv: [1211.3924](https://arxiv.org/abs/1211.3924) [astro-ph.SR].
- Meyer, K. A. et al. (2011). “Solar Magnetic Carpet I: Simulation of Synthetic Magnetograms”. In: *Sol. Phys.* 272, pp. 29–58. DOI: [10.1007/s11207-011-9809-3](https://doi.org/10.1007/s11207-011-9809-3). arXiv: [1108.1080](https://arxiv.org/abs/1108.1080) [astro-ph.SR].
- (2013). “Solar Magnetic Carpet III: Coronal Modelling of Synthetic Magnetograms”. In: *Sol. Phys.* 286, pp. 357–384. DOI: [10.1007/s11207-013-0272-1](https://doi.org/10.1007/s11207-013-0272-1). arXiv: [1303.1342](https://arxiv.org/abs/1303.1342) [astro-ph.SR].
- Milano, L. J. et al. (1999). “Quasi-Separatrix Layers in a Reduced Magnetohydrodynamic Model of a Coronal Loop”. In: *ApJ* 521, pp. 889–897. DOI: [10.1086/307563](https://doi.org/10.1086/307563).
- Moffatt, H. K. (1967). “On the suppression of turbulence by a uniform magnetic field”. In: *Journal of Fluid Mechanics* 28.3, pp. 571–592. DOI: [10.1017/S0022112067002307](https://doi.org/10.1017/S0022112067002307).
- Montgomery, D. (1982). “Major disruptions, inverse cascades, and the Strauss equations”. In: *Physica Scripta Volume T* 2, pp. 83–88. DOI: [10.1088/0031-8949/1982/T2A/009](https://doi.org/10.1088/0031-8949/1982/T2A/009).
- Montgomery, D. and L. Turner (1981). “Anisotropic magnetohydrodynamic turbulence in a strong external magnetic field”. In: *Physics of Fluids* 24, pp. 825–831. DOI: [10.1063/1.863455](https://doi.org/10.1063/1.863455).
- Murawski, K. and M. Goossens (1994). “Excitation of nonlinear MHD waves by foot-point motions”. In: *A&A* 286, pp. 952–961.
- Ng, C. S., L. Lin, and A. Bhattacharjee (2012). “High-Lundquist Number Scaling in Three-dimensional Simulations of Parker’s Model of Coronal Heating”. In: *ApJ* 747, 109, p. 109. DOI: [10.1088/0004-637X/747/2/109](https://doi.org/10.1088/0004-637X/747/2/109). arXiv: [1106.0515](https://arxiv.org/abs/1106.0515) [astro-ph.SR].
- Oughton, S. (1996). “Ion parallel viscosity and anisotropy in MHD turbulence”. In: *Journal of Plasma Physics* 56, pp. 641–657. DOI: [10.1017/S0022377800019504](https://doi.org/10.1017/S0022377800019504).
- Oughton, S., P. Dmitruk, and W. H. Matthaeus (2003). “Coronal Heating and Reduced MHD”. In: *Turbulence and Magnetic Fields in Astrophysics*. Ed. by E. Falgarone and T. Passot. Vol. 614. Lecture Notes in Physics, Berlin Springer Verlag, pp. 28–55.
- Oughton, S., W. H. Matthaeus, and P. Dmitruk (2017). “Reduced MHD in Astrophysical Applications: Two-dimensional or Three-dimensional?” In: *ApJ* 839. DOI: [10.3847/1538-4357/aa67e2](https://doi.org/10.3847/1538-4357/aa67e2).

- Oughton, S., E. R. Priest, and W. H. Matthaeus (1994). “The influence of a mean magnetic field on three-dimensional magnetohydrodynamic turbulence”. In: *Journal of Fluid Mechanics* 280, pp. 95–117. DOI: [10.1017/S00222112094002867](#).
- Oughton, S. et al. (2016). “Variance anisotropy in compressible 3-D MHD”. In: *Journal of Geophysical Research (Space Physics)* 121, pp. 5041–5054. DOI: [10.1002/2016JA022496](#).
- Oughton, Sean, Pablo Dmitruk, and William H Matthaeus (2004). “Reduced magnetohydrodynamics and parallel spectral transfer”. In: *Physics of Plasmas* 11.5, pp. 2214–2225.
- Perez, J. C. et al. (2012). “On the Energy Spectrum of Strong Magnetohydrodynamic Turbulence”. In: *Physical Review X* 2.4, 041005, p. 041005. DOI: [10.1103/PhysRevX.2.041005](#). arXiv: [1209.2011 \[astro-ph.SR\]](#).
- Priest, E. R. (1984). *Solar magneto-hydrodynamics*.
- Priest, Eric (2014). *Magnetohydrodynamics of the Sun*.
- Rappazzo, A. F. (2015). “Equilibria, Dynamics, and Current Sheet Formation in Magnetically Confined Coronae”. In: *ApJ* 815, 8, p. 8. DOI: [10.1088/0004-637X/815/1/8](#). arXiv: [1505.04370 \[astro-ph.SR\]](#).
- Rappazzo, A. F. and E. N. Parker (2013). “Current Sheets Formation in Tangled Coronal Magnetic Fields”. In: *ApJ* 773, L2, p. L2. DOI: [10.1088/2041-8205/773/1/L2](#). arXiv: [1306.6634 \[astro-ph.SR\]](#).
- Rappazzo, A. F. and M. Velli (2011). “Magnetohydrodynamic turbulent cascade of coronal loop magnetic fields”. In: *Phys. Rev. E* 83.6, 065401, p. 065401. DOI: [10.1103/PhysRevE.83.065401](#). arXiv: [1005.1640 \[astro-ph.SR\]](#).
- Rappazzo, A. F., M. Velli, and G. Einaudi (2008). “The Parker Scenario for Coronal Heating as an MHD Turbulence Problem”. In: *Subsurface and Atmospheric Influences on Solar Activity*. Ed. by R. Howe et al. Vol. 383. Astronomical Society of the Pacific Conference Series, p. 353. arXiv: [1002.2631 \[astro-ph.SR\]](#).
- (2010). “Shear Photospheric Forcing and the Origin of Turbulence in Coronal Loops”. In: *ApJ* 722, pp. 65–78. DOI: [10.1088/0004-637X/722/1/65](#). arXiv: [1003.3872 \[astro-ph.SR\]](#).
- (2013). “Field Lines Twisting in a Noisy Corona: Implications for Energy Storage and Release, and Initiation of Solar Eruptions”. In: *ApJ* 771, 76, p. 76. DOI: [10.1088/0004-637X/771/2/76](#). arXiv: [1301.7678 \[astro-ph.SR\]](#).
- Rappazzo, A. F. et al. (2006). “Nonlinear interactions in coronal heating”. In: *Advances in Space Research* 37, pp. 1335–1341. DOI: [10.1016/j.asr.2005.12.015](#).
- Rappazzo, A. F. et al. (2007). “Coronal Heating, Weak MHD Turbulence, and Scaling Laws”. In: *ApJ* 657, pp. L47–L51. DOI: [10.1086/512975](#). eprint: [astro-ph/0701872](#).
- (2008). “Nonlinear Dynamics of the Parker Scenario for Coronal Heating”. In: *ApJ* 677, 1348–1366, pp. 1348–1366. DOI: [10.1086/528786](#). arXiv: [0709.3687](#).
- Rappazzo, A. F. et al. (2012). “Interchange Reconnection in a Turbulent Corona”. In: *ApJ* 758, L14, p. L14. DOI: [10.1088/2041-8205/758/1/L14](#). arXiv: [1209.1388 \[astro-ph.SR\]](#).
- Rappazzo, A. F. et al. (2018). “Subresolution activity in solar and stellar coronae from magnetic field line tangling”. In: *MNRAS* 478, pp. 2257–2266. DOI: [10.1093/mnras/sty1132](#). arXiv: [1805.00480 \[astro-ph.SR\]](#).

- Ritchie, M. L., A. L. Wilmot-Smith, and G. Hornig (2016). “The Dependence of Coronal Loop Heating on the Characteristics of Slow Photospheric Motions”. In: *ApJ* 824, 19, p. 19. DOI: [10.3847/0004-637X/824/1/19](https://doi.org/10.3847/0004-637X/824/1/19). arXiv: [1508.05001](https://arxiv.org/abs/1508.05001) [astro-ph.SR].
- Romeou, Z., M. Velli, and G. Einaudi (2004). “Long Time Incompressible 2D MHD Simulations of Coronal Loop Heating: the Role of Photospheric Time-Scales”. In: *SOHO 15 Coronal Heating*. Ed. by R. W. Walsh et al. Vol. 575. ESA Special Publication, p. 523.
- (2007). “A Reduced MHD Turbulence Numerical Approach On Coronal Loop Heating: Deriving Scaling Laws”. In: *Second Solar Orbiter Workshop*. Vol. 641. ESA Special Publication, p. 78.
- (2009). “A MHD-turbulence model for solar corona”. In: *Advances in Space Research* 43, pp. 612–617. DOI: [10.1016/j.asr.2008.10.014](https://doi.org/10.1016/j.asr.2008.10.014).
- Rosenbluth, M. N. et al. (1976). “Numerical studies of nonlinear evolution of kink modes in Tokamaks”. In: *Physics of Fluids* 19, pp. 1987–1996. DOI: [10.1063/1.861430](https://doi.org/10.1063/1.861430).
- Ruffolo, D. and W. H. Matthaeus (2013). “Theory of magnetic field line random walk in noisy reduced magnetohydrodynamic turbulence”. In: *Physics of Plasmas* 20.1, 012308, p. 012308. DOI: [10.1063/1.4789606](https://doi.org/10.1063/1.4789606).
- (2015). “Dynamical Field Line Connectivity in Magnetic Turbulence”. In: *ApJ* 806, 233, p. 233. DOI: [10.1088/0004-637X/806/2/233](https://doi.org/10.1088/0004-637X/806/2/233).
- Schekochihin, A. A. et al. (2009). “Astrophysical Gyrokinetics: Kinetic and Fluid Turbulent Cascades in Magnetized Weakly Collisional Plasmas”. In: *ApJS* 182, pp. 310–377. DOI: [10.1088/0067-0049/182/1/310](https://doi.org/10.1088/0067-0049/182/1/310). arXiv: [0704.0044](https://arxiv.org/abs/0704.0044).
- Scheper, R. A. and A. B. Hassam (1999). “Line-Tying and the Reduced Equations of Magnetohydrodynamics”. In: *ApJ* 511, pp. 976–980. DOI: [10.1086/306702](https://doi.org/10.1086/306702).
- Servidio, S. et al. (2014). “Complexity and Diffusion of Magnetic Flux Surfaces in Anisotropic Turbulence”. In: *ApJ* 785, 56, p. 56. DOI: [10.1088/0004-637X/785/1/56](https://doi.org/10.1088/0004-637X/785/1/56).
- Shalchi, A. and M. Hussein (2014). “Perpendicular Diffusion of Energetic Particles in Noisy Reduced Magnetohydrodynamic Turbulence”. In: *ApJ* 794, 56, p. 56. DOI: [10.1088/0004-637X/794/1/56](https://doi.org/10.1088/0004-637X/794/1/56). arXiv: [1409.2470](https://arxiv.org/abs/1409.2470) [astro-ph.SR].
- Shebalin, J. V., W. H. Matthaeus, and D. Montgomery (1983). “Anisotropy in MHD turbulence due to a mean magnetic field”. In: *Journal of Plasma Physics* 29, pp. 525–547. DOI: [10.1017/S0022377800000933](https://doi.org/10.1017/S0022377800000933).
- Steinolfson, R. S. (1983). “Energetics and the resistive tearing mode: Effects of Joule heating and radiation”. In: *The Physics of Fluids* 26.9, pp. 2590–2602. DOI: [10.1063/1.864450](https://doi.org/10.1063/1.864450). eprint: <https://aip.scitation.org/doi/pdf/10.1063/1.864450>. URL: <https://aip.scitation.org/doi/abs/10.1063/1.864450>.
- Steinolfson, R. S. and G. van Hoven (1984). “Radiative tearing - Magnetic reconnection on a fast thermal-instability time scale”. In: *ApJ* 276, pp. 391–398. DOI: [10.1086/161623](https://doi.org/10.1086/161623).
- Strauss, H. R. (1976). “Nonlinear, three-dimensional magnetohydrodynamics of noncircular tokamaks”. In: *The Physics of Fluids* 19.1, pp. 134–140. DOI: [10.1063/1.861310](https://doi.org/10.1063/1.861310). eprint: <http://aip.scitation.org/doi/pdf/10.1063/1.861310>. URL: <http://aip.scitation.org/doi/abs/10.1063/1.861310>.
- Strauss, H. R. (1977). “Dynamics of high beta Tokamaks”. In: *Physics of Fluids* 20, pp. 1354–1360. DOI: [10.1063/1.862018](https://doi.org/10.1063/1.862018).



- (1980). “Stellarator equations of motion”. In: *Plasma Physics* 22, pp. 733–745. DOI: [10.1088/0032-1028/22/7/010](https://doi.org/10.1088/0032-1028/22/7/010).
- (1988). “Turbulent reconnection”. In: *ApJ* 326, pp. 412–417. DOI: [10.1086/166104](https://doi.org/10.1086/166104).
- (1990). “Three-dimensional driven reconnection in magnetic loops”. In: *J. Geophys. Res.* 95, pp. 17145–17151. DOI: [10.1029/JA095iA10p17145](https://doi.org/10.1029/JA095iA10p17145).
- (1997). “Reduced MHD in nearly potential magnetic fields”. In: *Journal of Plasma Physics* 57, pp. 83–87. DOI: [10.1017/S0022377896005296](https://doi.org/10.1017/S0022377896005296).
- Strauss, H. R. and W. S. Lawson (1989). “Computer simulation of Alfvén resonance in a cylindrical, axially bounded flux tube”. In: *ApJ* 346, pp. 1035–1040. DOI: [10.1086/168086](https://doi.org/10.1086/168086).
- Strauss, HR (1982). “Reduced MHD equations for mirror machines”. In: *Nuclear Fusion* 22.7, p. 893.
- Tachi, T., R. S. Steinolfson, and G. van Hoven (1983). “The effects of Ohmic heating and stable radiation on magnetic tearing”. In: *Physics of Fluids* 26, pp. 2976–2982. DOI: [10.1063/1.864019](https://doi.org/10.1063/1.864019).
- (1985). “Radiative and reconnection instabilities - Compressible and viscous effects”. In: *Sol. Phys.* 95, pp. 119–140. DOI: [10.1007/BF00162641](https://doi.org/10.1007/BF00162641).
- Teaca, B. et al. (2009). “Energy transfer in anisotropic magnetohydrodynamic turbulence”. In: *Phys. Rev. E* 79 (4), p. 046312. DOI: [10.1103/PhysRevE.79.046312](https://doi.org/10.1103/PhysRevE.79.046312). URL: <https://link.aps.org/doi/10.1103/PhysRevE.79.046312>.
- Tolman, Elizabeth A., Nuno F. Loureiro, and Dmitri A. Uzdensky (2018). “Development of tearing instability in a current sheet forming by sheared incompressible flow”. In: *Journal of Plasma Physics* 84.1, p. 905840115. DOI: [10.1017/S002237781800017X](https://doi.org/10.1017/S002237781800017X).
- Uzdensky, D. A. and N. F. Loureiro (2016). “Magnetic Reconnection Onset via Disruption of a Forming Current Sheet by the Tearing Instability”. In: *Phys. Rev. Lett.* 116 (10), p. 105003. DOI: [10.1103/PhysRevLett.116.105003](https://doi.org/10.1103/PhysRevLett.116.105003). URL: <https://link.aps.org/doi/10.1103/PhysRevLett.116.105003>.
- van Ballegooijen, A. A. (1985). “Electric currents in the solar corona and the existence of magnetostatic equilibrium”. In: *ApJ* 298, pp. 421–430. DOI: [10.1086/163626](https://doi.org/10.1086/163626).
- van Ballegooijen, A. A., M. Asgari-Targhi, and M. A. Berger (2014). “On the Relationship Between Photospheric Footpoint Motions and Coronal Heating in Solar Active Regions”. In: *ApJ* 787, 87, p. 87. DOI: [10.1088/0004-637X/787/1/87](https://doi.org/10.1088/0004-637X/787/1/87).
- van Ballegooijen, A. A. et al. (2011). “Heating of the Solar Chromosphere and Corona by Alfvén Wave Turbulence”. In: *ApJ* 736, 3, p. 3. DOI: [10.1088/0004-637X/736/1/3](https://doi.org/10.1088/0004-637X/736/1/3). arXiv: [1105.0402 \[astro-ph.SR\]](https://arxiv.org/abs/1105.0402).
- van Hoven, G. (1979). “The energetics of resistive magnetic tearing”. In: *ApJ* 232, pp. 572–581. DOI: [10.1086/157315](https://doi.org/10.1086/157315).
- van Hoven, G., R. S. Steinolfson, and T. Tachi (1983). “Energy dynamics in stressed magnetic fields - The filamentation and flare instabilities”. In: *ApJ* 268, pp. 860–864. DOI: [10.1086/161008](https://doi.org/10.1086/161008).
- van Hoven, G., T. Tachi, and R. S. Steinolfson (1984). “Radiative and reconnection instabilities - Filaments and flares”. In: *ApJ* 280, pp. 391–398. DOI: [10.1086/162004](https://doi.org/10.1086/162004).
- Velli, M. and A. W. Hood (1989). “Resistive tearing in line-tied magnetic fields - Slab geometry”. In: *Sol. Phys.* 119, pp. 107–124. DOI: [10.1007/BF00146216](https://doi.org/10.1007/BF00146216).
- Wan, M. et al. (2014). “Dissipation and Reconnection in Boundary-driven Reduced Magnetohydrodynamics”. In: *ApJ* 797, 63, p. 63. DOI: [10.1088/0004-637X/797/1/63](https://doi.org/10.1088/0004-637X/797/1/63).

- Wilmot-Smith, A. L. (2015). “An overview of flux braiding experiments”. In: *Philosophical Transactions of the Royal Society of London Series A* 373, pp. 20140265–20140265. DOI: [10.1098/rsta.2014.0265](#). arXiv: [1411.2490 \[astro-ph.SR\]](#).
- Yang, W.-H. (1989). “Expansion of solar-terrestrial low-beta plasmoid”. In: *ApJ* 344, pp. 966–972. DOI: [10.1086/167864](#).
- (1990). “Expanding force-free magnetized plasmoid”. In: *ApJ* 348, pp. L73–L76. DOI: [10.1086/185634](#).
- (1992). “Self-similar evolution of magnetized plasmas. I - Quasi-static solution”. In: *ApJ* 392, pp. 465–469. DOI: [10.1086/171446](#).
- Yang, W. H., P. A. Sturrock, and S. K. Antiochos (1986). “Force-free magnetic fields - The magneto-frictional method”. In: *ApJ* 309, pp. 383–391. DOI: [10.1086/164610](#).
- Zank, G. P. and W. H. Matthaeus (1992). “The equations of reduced magnetohydrodynamics”. In: *Journal of Plasma Physics* 48, pp. 85–100. DOI: [10.1017/S002237780001638X](#).
- (1993). “Nearly incompressible fluids. II - Magnetohydrodynamics, turbulence, and waves”. In: *Physics of Fluids* 5, pp. 257–273. DOI: [10.1063/1.858780](#).
- Zank, GP and WH Matthaeus (1992). “Waves and turbulence in the solar wind”. In: *Journal of Geophysical Research: Space Physics* 97.A11, pp. 17189–17194.
- Zhdankin, V., S. Boldyrev, and C. H. K. Chen (2016). “Intermittency of energy dissipation in Alfvénic turbulence”. In: *MNRAS* 457, pp. L69–L73. DOI: [10.1093/mnras1/slv208](#). arXiv: [1512.07355 \[physics.plasm-ph\]](#).
- Zhdankin, V. et al. (2017). “Universal small-scale structure in turbulence driven by magnetorotational instability”. In: *MNRAS* 467, pp. 3620–3627. DOI: [10.1093/mnras/stx372](#). arXiv: [1702.02857 \[astro-ph.HE\]](#).
- Zhukov, VP (2001). “Reduced MHD equations with allowance for slow magnetosonic waves”. In: *Plasma Physics Reports* 27.7, pp. 591–597.